

Cranfield University

Engineering Photonics  
School of Engineering

PhD Thesis

Sahar A Chowdhury

Fibre optic hydrogen sensing for long term use in  
explosive environments

Supervisors: Dr. Jane Hodgkinson and Prof. Ralph Tatam

September 2015

# Cranfield University

Engineering Photonics  
School of Engineering

PhD Thesis

2015

Sahar A Chowdhury

Fibre optic hydrogen sensing for long term use in  
explosive environments

Supervisors: Dr. Jane Hodgkinson and Prof. Ralph Tatam

September 2015

This thesis is submitted in partial fulfilment of the requirements for the degree of Doctor of Philosophy

© Cranfield University, 2015. All rights reserved. No part of this publication may be reproduced without the written permission of the copyright holder

# Abstract

Hydrogen is an explosive and flammable gas with a lower explosive limit of just 4% volume in air. It is important to monitor the concentration of hydrogen in a potentially hazardous environment where hydrogen may be released as a by-product in a reaction or used as a principal gas/liquid.

A fibre optic based hydrogen sensor offers an intrinsically safe method of monitoring hydrogen concentration. Previous research studies have demonstrated a variety of fibre optic based techniques for hydrogen detection. However the long-term stability of the hydrogen sensor and interrogation system has not yet been assessed and is the focus of this study. In the case of sensor heads being permanently installed in-situ, they cannot be removed for regular replacement, making long-term stability and reliability of results an important feature of the hydrogen sensor.

This thesis describes the investigation and characterisation of palladium coated fibre optic sensor heads using two designs of self-referenced refractometer systems with the aim of finding a system that is stable in the long term (~6 months). Palladium was the chosen sensing material owing to its selective affinity for absorbing hydrogen. Upon hydrogen absorption, palladium forms a palladium-hydride compound that has a lower refractive index and lower reflectivity than pure palladium. The refractometers measured the changes in the reflectivity to enable calculation of the concentration of hydrogen present. A low detection limit of 10ppm H<sub>2</sub> in air was demonstrated, with a response time of 40s for 1000ppm H<sub>2</sub> in air.

A further aspect to sensor stability was investigated in the form of sensor heads that had a larger area for palladium coverage. Hydrogen induced cracking in palladium is a common failure mechanism. A hypothesis is presented that a larger sensor area can reduce the probability of catastrophic failure resulting from cracks, which may improve the predictability of the sensor's performance. Two sensor head designs have been proposed – fibre with a ball lens at the tip and fibre with a GRIN lens at the tip, both of which potentially offer a larger area than the core of a singlemode optical fibre. The limit of detection and response times of the sensor heads were characterised in hydrogen. For long term stability assessment of the sensor head and the interrogation unit, the system was left running for a period of 1 to 4 weeks and the noise and drift in the system was quantified using an Allan deviation plot.

# Acknowledgements

I would like to thank the following people for their contributions:

My academic supervisors Jane Hodgkinson and Ralph Tatam for their guidance, patience and support throughout the course; Jane's morale boosting pep-talks over coffee breaks and generally always being available during times of distress; Dan Francis for his assistance during the difficult first few months and lending a critical eye to the project; Ricardo Correia and Edmund Chehura for giving me technical advice on optics, sensor development and work in general and Steve Staines with his imaginative insights towards developing solutions for mechanical problems.

I would also like to thank Ben Jones, Simon Brooks and Alex Thompson from AWE plc for useful discussions concerning the palladium-hydrogen system and assistance in coating test fibres with palladium.

I am very grateful to all my family and friends for their love, understanding, constant encouragement and patience through the difficult phases of the PhD.

And I would finally like to thank all members of Engineering Photonics, past and present, who made this PhD experience memorable, bearable and enjoyable.

# Table of Contents

|   |               |
|---|---------------|
| Abstract.....   | i             |
| Acknowledgements .....  | ii            |
| Table of Contents.....  | iii           |
| List of figures .....   | vii           |
| List of tables .....  | x             |
| List of symbols and abbreviations .....                             | xi            |
| <br><b>1. Introduction.....</b>                                     | <br><b>1</b>  |
| 1.1 Hydrogen gas .....  | 2             |
| 1.2 Hydrogen sensor .....   | 3             |
| 1.2.1 <i>Detection mechanism</i> .....                              | 4             |
| 1.2.2 <i>Research novelty</i> .....                                 | 5             |
| 1.3 Thesis outline .....  | 5             |
| 1.4 References.....   | 7             |
| <br><b>2. Hydrogen detection.....</b>                               | <br><b>9</b>  |
| 2.1 Palladium – hydrogen system .....                               | 10            |
| 2.1.1 <i>Hysteresis</i> .....                                       | 12            |
| 2.1.2 <i>Changes in electrical and optical properties</i> .....     | 14            |
| 2.1.3 <i>Effects of contamination</i> .....                         | 14            |
| 2.1.4 <i>Palladium alloys</i> .....                                 | 15            |
| 2.2 Hydrogen detection technologies.....                            | 16            |
| 2.3 Fibre optic sensors .....                                       | 18            |
| 2.3.1 <i>Intensity based - Micromirrors</i> .....                   | 19            |
| 2.3.2 <i>Intensity based - Evanescent waves</i> .....               | 20            |
| 2.3.3 <i>Surface plasmon resonance (SPR)</i> .....                  | 23            |
| 2.3.4 <i>Interferometer based</i> .....                             | 25            |
| 2.3.5 <i>Fibre grating based</i> .....                              | 27            |
| 2.3.6 <i>Other</i> .....  | 31            |
| 2.4 Conclusion .....  | 32            |
| 2.5 References.....   | 35            |
| <br><b>3. Experimental study of Pd film and instabilities .....</b> | <br><b>41</b> |
| 3.1 Sensor coatings .....   | 42            |

|           |   |           |
|-----------|---|-----------|
| 3.1.1     | Pure palladium film thickness and reflectivity.....                                   | 42        |
| 3.1.2     | Adhesion of the palladium film .....  | 44        |
| 3.1.3     | Protection of the palladium film .....  | 45        |
| 3.2       | Multilayer coating stability .....  | 47        |
| 3.2.1     | Sputter coating deposition .....  | 47        |
| 3.2.2     | Coating stability tests in hydrogen .....   | 48        |
| 3.3       | Palladium film cracking under high hydrogen pressure.....                             | 52        |
| 3.3.1     | Discussion- Pd cracking under high hydrogen pressure .....                            | 55        |
| 3.4       | Statistical analysis of the cracking .....  | 59        |
| 3.5       | Conclusion .....  | 61        |
| 3.6       | References.....   | 63        |
| <b>4.</b> | <b>Fresnel Refractometer .....</b>  | <b>65</b> |
| 4.1       | Fresnel Refractometer .....   | 66        |
| 4.1.1     | Background.....   | 66        |
| 4.2       | Method 1: Single source, 2 paths and cleaved fibre in oil .....                       | 69        |
| 4.2.1     | Results 1: Single source, 2 paths and cleaved fibre in oil.....                       | 71        |
| 4.2.2     | Discussion 1: Single source, 2 paths and cleaved fibre in oil.....                    | 73        |
| 4.3       | Method 2: Single source, 2 paths and Pd coated cleaved fibre in H <sub>2</sub> .....  | 74        |
| 4.3.1     | Results 2: Single source, 2 paths and Pd coated cleaved fibre in H <sub>2</sub> ..... | 75        |
| 4.3.2     | Discussion 2: Single source, 2 paths, Pd coated cleaved fibre .....                   | 76        |
| 4.4       | Conclusion .....  | 79        |
| 4.5       | References.....   | 81        |
| <b>5.</b> | <b>Probe sensor heads.....</b>  | <b>82</b> |
| 5.1       | Optical fibre probe sensor heads .....  | 83        |
| 5.1.1     | Background.....   | 83        |
| 5.2       | Ball lens sensor head.....  | 86        |
| 5.2.1     | Theory of Gaussian beam expansion .....   | 86        |
| 5.2.2     | Ball lens preparation A: Manual .....   | 88        |
| 5.2.3     | Ball lens preparation B: Automated .....  | 91        |
| 5.3       | Method 1: Single source, 2 paths and ball lens in oil.....                            | 96        |
| 5.3.1     | Results 1: Single source, 2 paths and ball lens in oil.....                           | 96        |
| 5.4       | Method 2: Single source, 2 paths and Pd coated ball lens in H <sub>2</sub> .....      | 97        |
| 5.4.1     | Results 2: Single source, 2 paths and Pd coated ball lens in H <sub>2</sub> .....     | 98        |
| 5.4.2     | Discussion 2: Single source, 2 paths and Pd coated ball lens in H <sub>2</sub> .....  | 100       |

|           |  |            |
|-----------|--|------------|
| 5.4.3     | Data modelling to find $n_{Pd}$ of $PdH_x$ .....                                       | 101        |
| 5.5       | Method 3: Single source, 2 paths and GRIN lens in oil .....                            | 103        |
| 5.5.1     | Results 3: Single source, 2 paths and GRIN lens in oil .....                           | 104        |
| 5.6       | Method 4: Single source, 2 paths and Pd coated GRIN lens in $H_2$ .....                | 105        |
| 5.6.1     | Results 4: Single source, 2 paths and Pd coated GRIN lens in $H_2$ .....               | 106        |
| 5.7       | Conclusion .....   | 107        |
| 5.8       | References.....  | 110        |
| <b>6.</b> | <b>Advanced Fresnel Refractometer .....</b>  | <b>111</b> |
| 6.1       | Introduction.....  | 112        |
| 6.2       | Method 1: Dual wavelength, common path, GRIN lens and filter in oil .....              | 113        |
| 6.2.1     | Sensor head: GRIN lens and filter .....  | 116        |
| 6.3       | Method 2: Dual wavelength, common path, FBG and bare fibre in oil .....                | 119        |
| 6.3.1     | Summing operational amplifier .....  | 122        |
| 6.3.2     | Calculation of refractive index .....  | 124        |
| 6.3.3     | Results 2: Dual wavelength, common path, FBG and bare fibre in oil .....               | 125        |
| 6.3.4     | Discussion 2: Dual wavelength, common path, FBG and bare fibre in oil .....            | 126        |
| 6.4       | Method 3: Dual wavelength, common path, FBG and Pd coated ball lens in $H_2$ .....     | 127        |
| 6.4.1     | Results 3: Dual wavelength, common path, FBG and Pd coated ball lens in $H_2$ .....    | 128        |
| 6.4.2     | Discussion 3: Dual wavelength, common path, FBG and Pd coated ball lens in $H_2$ ..... | 131        |
| 6.5       | Conclusion .....   | 132        |
| 6.6       | References.....  | 134        |
| <b>7.</b> | <b>Long term stability tests .....</b>   | <b>135</b> |
| 7.1       | Allan deviation.....   | 136        |
| 7.1.1     | Background.....  | 136        |
| 7.2       | Single source, 2 paths and Pd coated cleaved fibre (24 hours) .....                    | 138        |
| 7.3       | Single SLD source, 2 paths and Pd coated ball lens (4 days) .....                      | 140        |
| 7.4       | Dual wavelength, common path and Pd coated ball lens (4 days) .....                    | 142        |
| 7.5       | One month stability of the final system (4 weeks).....                                 | 145        |
| 7.6       | Conclusion .....   | 147        |
| 7.7       | References.....  | 148        |
| <b>8.</b> | <b>Conclusions and future work .....</b>   | <b>149</b> |
| 8.1       | Summary .....  | 150        |

|   |   |            |
|---|---|------------|
| 8.2   | Conclusions.....                                    | 154        |
| 8.3   | Future work.....                                    | 154        |
| 8.3.1   | <i>Dual wavelength and common path system</i> ..... | 154        |
| 8.3.2   | <i>Sensor heads</i> .....                           | 155        |
| 8.3.3   | <i>Packaging</i> .....                              | 159        |
| 8.4   | Summary.....  | 159        |
| 8.5   | References.....                                     | 160        |
| <b>List of Publications .....</b>                     |   | <b>161</b> |
| <b>Appendix A. Refractive index calculation .....</b> |   | <b>162</b> |



# List of figures

|   |    |
|---|----|
| <b>Figure 1.1-</b> Testing vessel where materials testing is carried out. ....  | 3  |
| <b>Figure 2.1-</b> Face-centred cubic (fcc) model of the palladium lattice. ....  | 10 |
| <b>Figure 2.2-</b> Palladium Pressure-Concentration-Temperature (PCT) graph.....  | 12 |
| <b>Figure 2.3-</b> Hysteresis effects in palladium lattice.....   | 13 |
| <b>Figure 2.4-</b> Micromirror sensor head. ....  | 19 |
| <b>Figure 2.5-</b> Evanescent wave based H <sub>2</sub> sensor on an exposed etched fibre core coated with Pd.....                        | 21 |
| <b>Figure 2.6-</b> Evanescent wave based H <sub>2</sub> sensor on a tapered fibre region coated with Pd. ....                             | 21 |
| <b>Figure 2.7-</b> Evanescent wave based H <sub>2</sub> sensor with mismatched core diameters .....                                       | 22 |
| <b>Figure 2.8-</b> Evanescent wave based H <sub>2</sub> sensor formed on a side-polished fibre coated with Pd .....                       | 23 |
| <b>Figure 2.9-</b> Generation of surface plasmon waves (SPW). ....  | 24 |
| <b>Figure 2.10-</b> Mach-Zehnder interferometer .....   | 26 |
| <b>Figure 2.11-</b> Extrinsic Fabry-Perot cavity.....   | 26 |
| <b>Figure 2.12-</b> Photonic crystal fibre (PCF) based H <sub>2</sub> sensor .....  | 27 |
| <b>Figure 2.13-</b> Fibre Bragg gratings (FBG) based H <sub>2</sub> sensor. ....  | 28 |
| <b>Figure 2.14-</b> In-line Mach-Zehnder interferometer (MZI) and FBG coated with Pd.....   | 29 |
| <b>Figure 2.15-</b> Long period grating (LPG) based H <sub>2</sub> sensor. ....   | 30 |
| <b>Figure 3.1-</b> a) Micromirror sensor head with a thin film of palladium deposited at the tip .....                                    | 42 |
| <b>Figure 3.2-</b> Reflectivity of a palladium film. ....   | 43 |
| <b>Figure 3.3-</b> Response of PdAg film to 500ppm H <sub>2</sub> in N <sub>2</sub> with and without the presence of O <sub>2</sub> ..... | 45 |
| <b>Figure 3.4-</b> Rate of hydrogen uptake by 10nm Pd film.....   | 46 |
| <b>Figure 3.5-</b> SEM image of a cross-section through Ni and Pd layer deposited on a glass substrate .....                              | 48 |
| <b>Figure 3.6-</b> Unusual inverted hydrogen response from a Ni/Pd coated cleaved fibre.....  | 49 |
| <b>Figure 3.7-</b> Response sizes from cleaved SMF tips coated in Pd, Ni/Pd, Ni/Pd/Au and Pd/Au. ....                                     | 50 |
| <b>Figure 3.8-</b> Gas chamber for high H <sub>2</sub> pressure and concentration tests .....   | 52 |
| <b>Figure 3.9-</b> Cracks in coated glass substrates in high H <sub>2</sub> pressure and concentration.....                               | 53 |
| <b>Figure 3.10-</b> Cracks, wrinkles and pin-holes on film surface .....  | 54 |
| <b>Figure 3.11-</b> Pd coated glass substrate observed at 2, 4, 10, 22 and 40 hours .....   | 56 |
| <b>Figure 3.12-</b> Ni/Pd coated glass substrate observed at 2, 4, 10, 22 and 40 hours .....  | 57 |
| <b>Figure 3.13-</b> Ni/Pd/Au coated glass substrate observed at 2, 4, 10, 22 and 40 hours .....   | 58 |
| <b>Figure 3.14-</b> Magnified image of a cracked 40nm Pd film on glass substrate. ....  | 59 |
| <b>Figure 3.15-</b> Histogram analysis of cracked image.....  | 60 |
| <b>Figure 3.16-</b> Designs of micromirror sensor heads with increasing sensing area. ....  | 61 |
| <b>Figure 4.1-</b> Theory of reflection, refraction and transmission .....  | 66 |
| <b>Figure 4.2-</b> Concept of a ratiometric fibre optic refractometer .....   | 67 |

|   |     |
|---|-----|
| <b>Figure 4.3-</b> Single source and 2 path configuration .....   | 69  |
| <b>Figure 4.4-</b> Spectrum of broadband SLD and DFB LD. ....   | 70  |
| <b>Figure 4.5-</b> Noise frequencies detected using an electrical spectrum analyser. ....   | 71  |
| <b>Figure 4.6-</b> Oil calibration chart using SLD or LD and 2 path configuration. ....   | 72  |
| <b>Figure 4.7-</b> Comparison of noise levels in reflectivity using SLD and LD.....   | 73  |
| <b>Figure 4.8-</b> Trial vessel used to supply test gases .....   | 74  |
| <b>Figure 4.9-</b> Change in reflectivity vs H <sub>2</sub> concentration graph using cleaved fibre coated with 40nm Pd.....      | 76  |
| <b>Figure 4.10-</b> Demonstration of effects of temperature fluctuations on measurements. ....                                    | 77  |
| <b>Figure 4.11-</b> Controlling temperature fluctuations using an insulating polystyrene box. ....                                | 78  |
| <b>Figure 4.12-</b> Demonstration of how the box helps reduce fluctuations in temperature in the short term. ....                 | 79  |
|   |     |
| <b>Figure 5.1-</b> Multimode fibre (MMF) with a tapered section and a ball lens .....   | 83  |
| <b>Figure 5.2-</b> Singlemode fibre (SMF) followed by an air gap and then a ball lens .....                                       | 84  |
| <b>Figure 5.3-</b> Interferometric technique using a ball lens and a mirror.....  | 85  |
| <b>Figure 5.4-</b> Gaussian beam propagation inside a ball lens .....   | 86  |
| <b>Figure 5.5-</b> Change in ball lens radius and the wavefront radius with increasing propagation distance, z. ....              | 87  |
| <b>Figure 5.6-</b> The beam waist radius increase with propagation distance, z. ....  | 88  |
| <b>Figure 5.7-</b> Fabricating ball lenses manually with fibre positioned 500µm to left of electrodes .....                       | 89  |
| <b>Figure 5.8-</b> Fabricating ball lenses manually with fibre positioned at centre of electrodes .....                           | 89  |
| <b>Figure 5.9-</b> Fabricating ball lenses manually with fibre positioned 1000µm to right of centre of electrodes.....            | 89  |
| <b>Figure 5.10-</b> Reflected light intensity vs ball lens diameter.....  | 90  |
| <b>Figure 5.11-</b> Parameters that define the geometry of a ball lens .....  | 91  |
| <b>Figure 5.12-</b> SMF28 ball lens with/without core in the ball and pure silica ball lens .....                                 | 92  |
| <b>Figure 5.13-</b> Automated process for production of pure silica ball lens .....   | 92  |
| <b>Figure 5.14-</b> Pure silica ball lens formed at the tip of a single mode fibre. ....  | 93  |
| <b>Figure 5.15-</b> Spot size image comparison between SMF28 and ball lens.....   | 95  |
| <b>Figure 5.16-</b> Ball lens oil calibration chart using single SLD and 2 path system .....                                      | 96  |
| <b>Figure 5.17-</b> Hydrogen cycling graphs using 40nm Pd coated ball lens .....  | 98  |
| <b>Figure 5.18-</b> Change in reflectivity vs H <sub>2</sub> concentration plot using 40nm Pd coated ball lens over 6 months .... | 99  |
| <b>Figure 5.19-</b> Long term recovery of sensor head in air.....   | 100 |
| <b>Figure 5.20-</b> Modelling palladium-hydride's change in the complex refractive index. ....                                    | 103 |
| <b>Figure 5.21-</b> GRIN lens sensor head assembly .....  | 104 |
| <b>Figure 5.22-</b> Oil calibration chart using the GRIN lens. ....   | 105 |
| <b>Figure 5.23-</b> Metallic palladium coated GRIN lens as a hydrogen sensor head. ....   | 106 |
| <b>Figure 5.24-</b> Inverted response to H <sub>2</sub> from a Ni/Pd coated GRIN lens. ....                                       | 107 |
|   |     |
| <b>Figure 6.1-</b> Hydrogen sensor configuration using GRIN lens. ....  | 112 |
| <b>Figure 6.2-</b> Dual wavelength, common path system. ....  | 113 |
| <b>Figure 6.3-</b> DFB laser diode spectra at 1533nm and 1569nm.....  | 114 |
| <b>Figure 6.4-</b> Time division multiplexing sequence .....  | 115 |

|  |      |
|--|------|
| <b>Figure 6.5-</b> Filter transmission spectrum .....  | 116  |
| <b>Figure 6.6-</b> GRIN sensor head assembly for the double wavelength, common path system .....                   | 116  |
| <b>Figure 6.7-</b> Reflectivity measurements from GRIN lens using an OBR.....                                      | 117  |
| <b>Figure 6.8-</b> GRIN lens sensor head assembly with matching 8° cuts on the filter.....                         | 118  |
| <b>Figure 6.9-</b> Modified dual wavelength configuration that uses a high modulation frequency.....               | 119  |
| <b>Figure 6.10-</b> FBG spectra and effects of temperature on the FBG .....  | 121  |
| <b>Figure 6.11-</b> Returned optical power from broadened 1533nm LD and FBG. ....                                  | 122  |
| <b>Figure 6.12-</b> Circuit diagram of the summing operational amplifier. ....                                     | 123  |
| <b>Figure 6.13-</b> Output from the summing amplifier.....   | 123  |
| <b>Figure 6.14-</b> Transmission spectrum of the FBG with a reflectivity dip centred at 1533.9nm .....             | 124  |
| <b>Figure 6.15-</b> Oil calibration chart using cleaved fibre and FBG.....   | 126  |
| <b>Figure 6.16-</b> Hydrogen response from 40nm coated ball lens and FBG as sensor head .....                      | 129  |
| <b>Figure 6.17-</b> Change in reflectivity vs H <sub>2</sub> concentration from the 40nm Pd coated ball lens ..... | 130  |
| <br>   |      |
| <b>Figure 7.1-</b> Reflectivity signals displaying an upward drift.....  | 136  |
| <b>Figure 7.2-</b> Interpreting an Allan deviation chart. ....   | 138  |
| <b>Figure 7.3-</b> Time series data from the single SLD source and 2 path interrogation system (24 hours). ....    | 139  |
| <b>Figure 7.4-</b> Allan deviation plot of the single source (SLD and LD) and 2 path system (24 hours).....        | 140  |
| <b>Figure 7.5-</b> Time series data from the single SLD source and 2 path interrogation system (4 days).....       | 141  |
| <b>Figure 7.6-</b> Allan deviation plot of the single SLD source and 2 path system (4days).....                    | 142  |
| <b>Figure 7.7-</b> Time series data from the dual wavelength, common path system (4 days) .....                    | 143  |
| <b>Figure 7.8-</b> Allan deviation plot of the dual wavelength, common path system (4days).....                    | 144  |
| <b>Figure 7.9-</b> Time series data from the single SLD source and 2 paths system (4 weeks) .....                  | 146  |
| <b>Figure 7.10-</b> Allan deviation plot of single SLD source and 2 path system (4 weeks). ....                    | 146  |
| <br>   |      |
| <b>Figure 8.1-</b> Modulating the source output wavelength near the edge of the filter .....                       | 155  |
| <b>Figure 8.2-</b> CO <sub>2</sub> laser beam melting an optical fibre .....                                       | 156  |
| <b>Figure 8.3-</b> Ball lens with a polished end to match the wavefront curvature.....                             | 157  |
| <b>Figure 8.4-</b> Integrating solid geometry sensor head ideas.....   | 157  |
| <b>Figure 8.5-</b> Schematic of a wire grid polariser.....   | 158  |
| <b>Figure 8.6-</b> Sensors in a protective housing.....  | 159  |
| <br>   |      |
| <b>Figure A.1-</b> Modelling light reflectivity at interfaces in the GRIN lens and filter sensor head .....        | 1623 |

# List of tables

|   |     |
|---|-----|
| <b>Table 1-1</b> – Hydrogen sensor specifications .....   | 4   |
| <b>Table 2-1</b> – The palladium-hydride phases.....  | 11  |
| <b>Table 2-2</b> – Comparison of hydrogen permeability of various Pd-alloy films to pure Pd film.....                       | 16  |
| <b>Table 2-3</b> – Summary of existing hydrogen sensing techniques.....   | 17  |
| <b>Table 2-4</b> – Summary of fibre optic hydrogen detection techniques .....   | 33  |
| <b>Table 3-1</b> – Response from Pd, Ni/Pd, Ni/Pd/Au and Pd/Au coated cleaved fibres .....                                  | 50  |
| <b>Table 4-1</b> – Signal to noise analysis from reference and probe fibres using different sources .....                   | 73  |
| <b>Table 4-2</b> – Fresnel reflected intensities at different interfaces .....  | 74  |
| <b>Table 4-3</b> – Summary of source properties and corresponding sensitivity results .....                                 | 80  |
| <b>Table 5-1</b> – Summary of ball lens sizes and their reflected power relative to a cleaved control fibre .....           | 90  |
| <b>Table 5-2</b> – MM125 ball lenses of varying diameter and their reflectivities. ....                                     | 94  |
| <b>Table 5-3</b> – Summary of ball lens testing conditions over 6 months .....  | 97  |
| <b>Table 5-4</b> – Normalised change in reflectivity, $\Delta R/R_{\text{air}}$ for a range of hydrogen concentrations..... | 100 |
| <b>Table 7-1</b> – Summary of long term experiments.....  | 147 |
| <b>Table 8-1</b> – Summary of hydrogen detection techniques and their limits of detection .....                             | 150 |

# List of symbols and abbreviations

|              |   |                  |                              |
|--------------|---|------------------|------------------------------|
| $[H_2]$      | Hydrogen concentration                              | Ag               | Silver                       |
| A            | Average   | Ar               | Argon                        |
| $a$          | Lattice constant                                    | Au               | Gold                         |
| $b$          | Distance between splice end and centre of ball lens | B                | Boron                        |
| $c$          | Free space velocity of light                        | C                | Carbon                       |
| $d$          | Core radius   | Ce               | Cerium                       |
| $f$          | frequency   | CH <sub>4</sub>  | Methane                      |
| $i$          | $\sqrt{-1}$   | CO               | Carbon monoxide              |
| I            | Intensity   | CO <sub>2</sub>  | Carbon dioxide               |
| $K_s$        | Sievert's constant                                  | Cu               | Copper                       |
| $k_{sp}$     | Surface plasmon wave propagation constant           | Fe               | Iron                         |
| $l_c$        | Coherence length                                    | H                | Hydrogen atom                |
| $n$          | Refractive index                                    | H <sub>2</sub>   | Hydrogen gas                 |
| $n^*$        | Complex refractive index                            | HeNe             | Helium Neon                  |
| $n_{eff}$    | Effective refractive index                          | N <sub>2</sub>   | Nitrogen                     |
| $n_1$        | Imaginary refractive index                          | Ni               | Nickel                       |
| $n_R$        | Real refractive index                               | O <sub>2</sub>   | Oxygen                       |
| $p_{H_2}$    | Partial pressure of hydrogen                        | O <sub>2</sub>   | Oxygen                       |
| $r$          | Fresnel reflection coefficient                      | Pd               | Palladium                    |
| R            | Fresnel reflectivity                                | PdH <sub>x</sub> | Palladium hydride            |
| $R(z)$       | Radius of wavefront curvature as a function of $z$  | Pt               | Platinum                     |
| $R_{norm}$   | Normalisation factor                                | Rh               | Rhodium                      |
| T            | Temperature   | Ru               | Rubium                       |
| $t$          | Time  | Si               | Silicon                      |
| V            | Fresnel reflection voltage                          | SiO <sub>2</sub> | Silicon dioxide              |
| $V_A$        | Sound velocity in silica                            | Ti               | Titanium                     |
| $x$          | Atomic ratio of H and Pd                            | WO <sub>3</sub>  | Tungsten oxide               |
| $z$          | Propagation in direction $z$                        | Y                | Yttrium                      |
| $\alpha$     | Phase of palladium/palladium hydride                |                  |                              |
| $\beta$      | Phase of palladium hydride                          | BL               | Ball lens                    |
| $\delta$     | Phase shift   | DAQ              | Data acquisition adapter     |
| $\Delta R$   | Change in Fresnel reflectivity                      | ESA              | Electrical spectrum analyser |
| $\epsilon_d$ | Dielectric constant of dielectrics                  | FPI              | Fabry-Perot Interferometer   |

|              |  |
|--------------|--|
| $\epsilon_m$ | Dielectric constant of metals          |
| $\theta$     | Angle                                  |
| $\lambda$    | Wavelength                             |
| $\Lambda$    | Grating period                         |
| $\lambda_B$  | Bragg wavelength                       |
| $\mu_0$      | Permeability of free space             |
| $\nu$        | Normalised wave number                 |
| $\nu_B$      | Brillouin shift in frequency           |
| $\sigma$     | Standard deviation                     |
| $\sigma^2$   | Variance                               |
| $\sigma_e$   | Conductivity of metal                  |
| $\tau$       | Integration time                       |
| $\varphi$    | Diameter                               |
| $\omega$     | Angular frequency                      |
| $\omega(z)$  | Gaussian beam waist as a function of z |
| $\omega_0$   | Gaussian beam waist at z=0             |

|      |                               |
|------|-------------------------------|
| FBG  | Fibre Bragg grating           |
| FWHM | Full width half maximum       |
| GRIN | Graded Index                  |
| LD   | Laser diode                   |
| LED  | Light emitting diode          |
| LIA  | Lock-in amplifier             |
| LPG  | Long period grating           |
| MZI  | Mach-Zehnder Interferometer   |
| MMF  | Multimode fibre               |
| OSA  | Optical spectrum analyser     |
| ppb  | Parts per billion (by volume) |
| ppm  | Parts per million (by volume) |
| PD   | Photodetector amplifier       |
| PCF  | Photonic crystal fibre        |
| RIU  | Refractive index unit         |
| RMS  | Root mean square              |
| SEM  | Scanning electron microscope  |
| SMF  | Singlemode fibre              |
| SLD  | Superluminescent diode        |
| TM   | Transverse magnetic           |

# Chapter 1

## Introduction

This chapter gives a description to the background of the research project. This is followed by the sensor development specifications, the choice of technique for the development and the novelty of this research. Finally an outline of the thesis is presented.

## 1.1 Hydrogen gas

Hydrogen gas exists in the atmosphere in trace levels ( $\leq 1$ ppm by volume), however elemental hydrogen is the most abundant element on Earth and occurs chiefly in combination with oxygen in water and in hydrocarbons [1]. Hydrogen has a large energy content of 142kJ/g [2], and therefore can play a key role as an energy carrier for renewable energy sources in the future. It is considered a potential alternative to the depleting availability of fossil fuels [3, 4]. Hydrogen as a fuel can be produced from high temperature steam being passed over heated carbon, decomposition of hydrocarbons with heat or electrolysis of water [1]. It is an environmentally friendly energy source because hydrogen combines with oxygen to generate electricity and produces water as a by-product.

Hydrogen gas has applications in several industries. It is used in liquid states for propulsion of rockets; in cryogenic research in superconductivity studies; in refining petroleum; for metal extraction from their ores [5]; during heat treatment of metals during atomic hydrogen welding, cutting and coating [6]; in heat treatment of glass and fibre optic pre-forms [7] and for processing food and production of plastics, polyester and nylon [8].

Despite its usefulness, hydrogen is a hazardous and flammable gas. Properties of hydrogen that makes it potentially dangerous are:

- It is a colourless and odourless gas, making a leak difficult to detect
- It has a low LEL (lower explosive limit) of 4% volume in air and an upper explosive limit of 75% volume in air [9].
- It has a low minimum ignition energy of only 0.017mJ, so that a small spark is sufficient to ignite a mixture where hydrogen is present in abundance.

Constant monitoring of hydrogen concentration in air, well below the lower explosive limit, is essential where hydrogen is being produced, stored, transported or used in applications to prevent explosions. The explosion at the Fukushima Daichii nuclear power plant in Japan in 2011 indicates the consequences of a hydrogen leakage [10].



## 1.2 Hydrogen sensor

Hydrogen's low minimum ignition energy and high heat of combustion requires an intrinsically safe hydrogen sensor that can be used in potentially explosive environments. A particular industrial application for this research is for AWE's Material Science and Research Division to build a prototype of a highly stable, intrinsically safe, micro-dimensional sensor head that can be permanently installed in a materials testing vessel and make in-situ hydrogen concentration measurements. Intrinsically safe means that the technology does not have enough stored or transmitted energy to raise the temperature of any surface above the auto ignition temperature of the gas mixture in the vessel. For optical fibre sensors this also requires the transmitted intensity to be below 30mW [11].

The testing vessel is shown in Figure 1.1a, which comprises of detachable metal discs that make up the tower. A schematic diagram of one of the rings with a sensor fitted in the middle is shown in Figure 1.1b. The vessel is 12cm in diameter. Once the vessel is sealed, the sensor cannot be removed frequently for calibration and cleaning to avoid disturbing the sealed atmosphere. This means that the sensor head and the interrogation system must maintain long term stability (over ~1 month) in terms of accuracy of measurement readings.

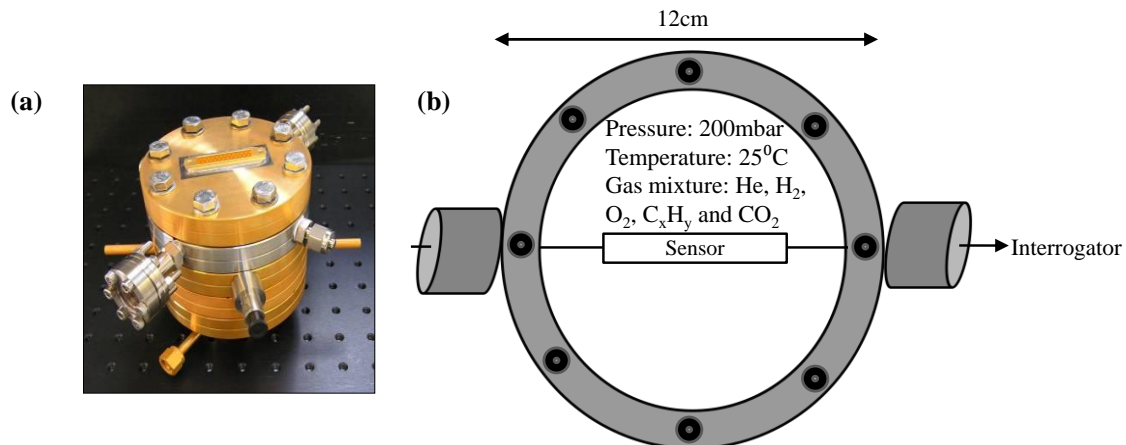


**Figure 1.1- a) Testing vessel where materials testing is carried out; b) schematic diagram of a metal disc where the proposed sensor head would be fitted. The diameter of the discs is 12cm.**

The gas composition in the vessel would consist mainly of helium with trace levels of hydrogen, oxygen, carbon dioxide and hydrocarbons at 200mbar and held at a temperature of 25°C. The sensor will be interrogated by a lab based interrogation system. The sensor specifications for this application are summarised in Table 1-1. There are no commercial sensors currently available to meet these specifications nor has any research work met the long term stability requirement.

**Table 1-1 – Hydrogen sensor specifications**

| <b>Criterion</b>                         | <b>Sensor head<br/>(and connection)</b>                    | <b>Interrogator</b> |
|--|--|---------------------|
| Range                                    | 0-4% volume hydrogen                                       |                     |
| Repeatability                            | 1-10ppm*   |                     |
| Accuracy                                 | $\pm 1\sigma$  |                     |
| Drift                                    | Maintain accuracy OR characterised for calibration         |                     |
| Response Time                            | -  | 30-90s              |
| Repeatability                            | Maintain accuracy over lifetime                            |                     |
| Max. Dimensions                          | 10x10x20mm   | 450x450x200mm       |
| Temperature                              | 25°C   |                     |
| Pressure                                 | 0.01 – 1065mbar  | 790 – 1065mbar      |
| Operating Life<br>(between calibrations) | 6 months   | 1 year              |
| Electricity                              | No electrical pathway through Faraday cages                |                     |
| Energy                                   | Temperature / Power intrinsically safe with test unit      |                     |
| Sampling                                 | Non-invasive, i.e. does not perturb the gas being measured |                     |

\*Unless otherwise stated, all values in this project are quoted as ppm by volume

### ***1.2.1 Detection mechanism***

Fibre optic technology has been identified as the most suitable to provide an intrinsically safe solution for the following reasons:

- Relatively unaffected by electromagnetic interference
- Electrical isolation, eliminating many sources of ignition that may lead to an explosion
- Micro-dimensional in size and can be embedded in operation
- Low loss optical fibres allow transmission of optical signals over many kilometres, making possible remote control

Palladium, Pd is often used as the sensing element in a hydrogen sensor due to its high catalytic activity and selective affinity for hydrogen with high solubility. It reacts with hydrogen to form palladium hydride, which has a larger lattice constant than pure palladium. The palladium lattice expands as hydrogen atoms fill the interstitial gaps and defect locations and the refractive index reduces. This leads to a reduction in palladium's surface reflectivity, with a change in reflected intensity that is related to the amount of hydrogen absorbed by the film.

Optical fibre refractometers have been designed to make use of the change in reflected intensity from the junction between an optical fibre end and the testing species. Butler [12] used a micromirror chemical sensor head with a 10nm thin Pd film deposited at the end of a multi-mode fibre and detected hundreds of ppm hydrogen in nitrogen. This approach was adapted in this study due to its

simplistic design, thought to be advantageous towards developing a system that will possess long term stability.

### ***1.2.2 Research novelty***

Hysteresis effects take place during hydrogenation and dehydrogenation and can cause irreversible deformations that are manifested as cracks, pin-holes and peeling of the film. This can lead to reduced reflectivity due to surface delamination and thus deterioration in sensor performance. Use of a restricted sensor area, for example the core of a singlemode fibre (8.2 $\mu$ m), can lead to catastrophic failure if such flaws coincide with the active area. The hypothesis that a larger sensor area will allow greater coverage for the palladium deposition, which could reduce the probability of catastrophic sensor failure resulting from cracks and improve the performance predictability is quantified in this study. This has been investigated with the development of a novel sensor head in the shape of a spherical ball lens and a GRIN lens with a larger surface area at the tip of a single mode fibre. The work of Butler [12] mentioned above used a GRIN lens coated with Pd for hydrogen sensing. Commercial GRIN lenses have a face diameter typically between 1 and 2mm.

Various other approaches have been reported to increase the active area of Fresnel based hydrogen sensors. A fibre optic bundle with multiple singlemode fibre ends has also been used for refractive index measurement [13]. Multimode fibres have been used by Butler *et al* for hydrogen sensing [12] and by Suhadolnik *et al* for refractometry of liquids [14], however such sensors may be subject to mode noise in the fibre that may impact the sensor head's measurement uncertainty.

Significant requirements for the sensor head, summarised in Table 1-1, are- low limit of detection, fast response time and stability over 6 months. Previous research studies have demonstrated fibre optic sensors detecting hydrogen down to parts-per-billion level (20ppb using a Mach-Zehnder interferometric setup [15], described in section 2.3.4, page 25) and achieving fast response (5s for 4% hydrogen in air [16]). The long-term stability of the interrogation system has not yet been assessed. The novelty of this research lies in the stability study of the complete sensing unit including the sensor head and the interrogation system. A statistical analysis of the Allan deviation of the data collected from the system left running over a prolonged period of time (1 to 4 weeks), was used to quantify the noise and drift in the system. This approach to evaluating fibre optic sensor head performance has been applied for the first time.

## **1.3 Thesis outline**

Chapter 2 examines the palladium-hydrogen reaction and the changes in refractive index, electrical, physical and mechanical properties in comparison to pure palladium. A summary of existing

techniques that transform these changes into an electrical signal to determine the concentration of hydrogen in the surrounding environment is presented. The bulk of this chapter then focusses on fibre optic techniques. From this chapter, it was established that a micromirror system that measures the reflected light intensity would be suitable for a stability study owing to its simplicity of design and lack of additional stress on the Pd film.

Chapter 3 focuses on palladium film and its instabilities. The ideal coating structure for the sensor head composition is discussed, in terms of optimum thickness of the palladium film, using an adhesive layer between the palladium and the substrate and using a protective capping layer for the palladium. The stability of the films in hydrogen is also presented. A statistical analysis of images of cracked palladium films is completed to quantify the hypothesis that the performance of a larger sensor head will be more predictable because the ratio of cracked to unaffected area is more likely to be consistent.

Chapter 4 is an experimental chapter that describes the design of a simple micromirror Fresnel refractometer using a single source and 2 paths, one holding the probe fibre and the second a reference fibre to compensate for time varying optical fluctuations. Characterisation of the refractometer using oils of known refractive indices is described. Results of a palladium coated cleaved fibre capable of detecting low levels of hydrogen concentration is demonstrated. The various design stages of the refractometer for enhanced performance are also presented.

Chapter 5 reports the various stages of producing ball lenses and a sensor head consisting of a GRIN lens. Gaussian beam propagation as a theoretical model is described for ball lenses and used to analyse the optimum geometry to maximise reflected light back into the core. Results of successful implementation of a palladium coated ball lens as a hydrogen sensor head is reported. Long term tests over a period of six months are also shown. Reports of mechanical issues with the fabrication of GRIN lens as a sensor head are discussed.

Chapter 6 investigates an advanced refractometer design that uses two time-division multiplexed sources and a common path for the probe and reference signal to compensate for temperature fluctuations and time dependent optical variations. Various design stages for enhanced performance are also described. Characterisation of the system using an uncoated ball lens immersed in oils of known refractive indices is presented, followed by a demonstration of a palladium coated ball lens as hydrogen sensor.

Chapter 7 describes a statistical approach used to study the stability of the two systems, from Chapters 4 and 6, using analysis of Allan deviation. Each of the systems developed in this thesis was assessed over a period of a week and the results compared. The final sensing unit is proposed in this chapter and the performance assessed over a period of 4 weeks.

Chapter 8 contains the conclusion of this thesis along with suggestions for further work in this area.

This is followed by a list of publications arising from this thesis and appendices.

## 1.4 References

- [1] Lide, D. R. (2013), *CRC Handbook of Chemistry and Physics*, 94th ed, CRC Press, Florida, US.
- [2] Hübert, T., Boon-Brett, L., Black, G. and Banach, U. (2011), "Hydrogen sensors - a review", *Sensors and Actuators, B: Chemical*, vol. 157, no. 2, pp. 329-352.
- [3] Elam, C. C., Padró, C. E. G., Sandrock, G., Luzzi, A., Lindblad, P. and Hagen, E. F. (2003), "Realizing the hydrogen future: the International Energy Agency's efforts to advance hydrogen energy technologies", *International Journal of Hydrogen Energy*, vol. 28, no. 6, pp. 601-607.
- [4] Lubitz, W. and Tumas, W. (2007), "Hydrogen: an overview", *Chemical Reviews*, vol. 107, no. 10, pp. 3900-3903.
- [5] Luidold, S. and Antrekowitsch, H. (2007), "Hydrogen as a reducing agent: State-of-the-art science and technology", *Journal of Metals*, vol. 59, no. 6, pp. 20-26.
- [6] Durgutlu, A. (2004), "Experimental investigation of the effect of hydrogen in argon as a shielding gas on TIG welding of austenitic stainless steel", *Materials & Design*, vol. 25, no. 1, pp. 19-23.
- [7] Auguste, J. L., Humbert, G., Leparmentier, S., Kudinova, M., Martin, P. O., Delaizir, G., Schuster, K. and Litzkendorf, D. (2014), "Modified powder-in-tube technique based on the consolidation processing of powder materials for fabricating specialty optical fibers", *Materials*, vol. 7, no. 8, pp. 6045-6063.
- [8] EU Commission (2008), *Report from the Commission on dietary food additive intake*, [http://ec.europa.eu/food/fs/sfp/addit\\_flavor/flav15\\_en.pdf](http://ec.europa.eu/food/fs/sfp/addit_flavor/flav15_en.pdf).
- [9] The Institution of Gas Engineers (1998), *Dealing with reported gas escapes*, IGE/SR/20 Edition 2, Institution of Gas Engineers and Managers, Kegworth, UK.
- [10] International Atomic Energy Agency (02 March 2011), *Fukushima nuclear accident update log*, available at: <https://www.iaea.org/newscenter/news/fukushima-nuclear-accident-update-log-21> (accessed 03 March 2015).
- [11] British Standards Institution (2007), *Explosive atmospheres - Part 28: Protection of equipment and transmission systems using optical radiation*, BSI EN 60079-28:2007, Cenelec, UK.
- [12] Butler, M. A., Sanchez, R. and Dulleck, G. (1996), *Fiber Optic Hydrogen Sensor*, Sandia Reports SAND96-113, Sandia National Laboratories, Albuquerque, US.
- [13] Degamber, B. and Fernando, G. F. (2002), "Process monitoring of fiber-reinforced polymer composites", *MRS Bulletin*, vol. 27, no. 5, pp. 370-380.
- [14] Suhadolnik, A., Babnik, A. and Možina, J. (1995), "Optical fiber reflection refractometer", *Sensors and Actuators B: Chemical*, vol. 29, no. 1-3, pp. 428-432.

- [15] Butler, M. A. and Ricco, A. J. (1988), "Chemisorption-induced reflectivity changes in optically thin silver films", *Applied Physics Letters*, vol. 53, no. 16, pp. 1471-1473.
- [16] Monzón-Hernández, D., Luna-Moreno, D. and Martínez-Escobar, D. (2009), "Fast response fiber optic hydrogen sensor based on palladium and gold nano-layers", *Sensors and Actuators, B: Chemical*, vol. 136, no. 2, pp. 562-566.

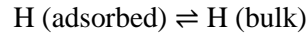
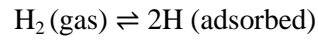
# Chapter 2

## Hydrogen detection

Palladium is commonly used in hydrogen detection techniques as the sensing element due to its selective affinity for absorbing hydrogen, which was first discovered by Thomas Graham in 1866 [1]. The metal can absorb up to 900 times its own volume of hydrogen at room temperature and atmospheric pressure [2]. As the metal absorbs hydrogen, it forms a palladium hydride with associated changes in its physical, electrical and optical properties. The palladium hydride system has been subjected to extensive research as reported by Lewis [3] and Wicke [4]. Several hydrogen sensor techniques have been developed to date that can detect these changes, which are dependent on the hydrogen concentration present in the surrounding environment. The resulting changes in palladium properties and methods of detection are discussed in this chapter.

## 2.1 Palladium – hydrogen system

Pure Palladium, Pd has a face-centred cubic (fcc) lattice structure with a lattice parameter of 0.3890nm at room temperature (298K) [5]. The unit cell is shown in Figure 2.1. With hydrogen absorption the palladium lattice expands isotropically but retains its fcc structure. Palladium's reaction to hydrogen is thought to happen in two stages [6].



First the gas molecules are adsorbed onto the Pd surface where they dissociate into two hydrogen atoms. The atoms then diffuse into the bulk lattice structure forming a palladium-hydride. Hydrogen atoms settle into an octahedral interstitial site present in each unit cell (see Figure 2.1), and are held loosely in the lattice by weak van der Waals forces [7].

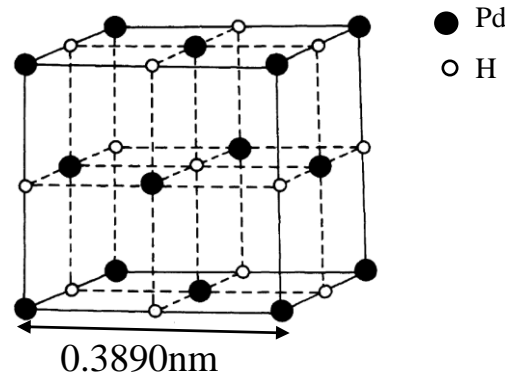


**Figure 2.1- Face-centred cubic (fcc) model showing the positions of hydrogen in the palladium lattice. Taken from [5].**

The compound has a general composition  $\text{PdH}_x$  where  $x$  is the atomic ratio of the constituents H and Pd and has values in the range  $0 \leq x \leq 1$ . This ratio can be measured directly by weighing a bulk sample or indirectly by measuring the change in the dimensions of a hydride sample [3, 8]. For low hydrogen content between  $0 \leq x \leq 0.03$ , the palladium-hydride is said to exist in the  $\alpha$ -phase and has a maximum lattice parameter of 0.3894nm ( $\alpha_{\text{max}}$ ) at room temperature (298K) [5]. Frazier [8] found that a 100nm thick annealed palladium film at 27°C existed in the  $\alpha$  phase for a hydrogen partial pressure  $\leq 2\text{kPa}$  or 2% hydrogen by volume. The relationship between  $x$  and the partial pressure of hydrogen,  $p_{\text{H}_2}$  is defined by equation (2.1) [9], where  $T$  is the temperature in Kelvin and  $p_{\text{H}_2}$  is measured in Torr.

$$\log(p_{\text{H}_2}^{1/2}) = \log x + 4.2 - \frac{521.9}{T} - \frac{926x}{T - 215} \quad (2.1)$$



Equation (2.1) can be simplified for  $x \leq 0.004$  (when  $p_{H_2} \sim 1$  Torr or  $\sim 100$  Pa or  $\sim 0.1\%$  volume) to Sievert's law as shown by equation (2.2) [9].

$$x = K_S \sqrt{p_{H_2}} \quad (2.2)$$

Where  $K_S$  is Sievert's constant, which is dependent only on temperature for a given material and is approximately  $350 \text{ Torr}^{-0.5}$  for annealed Pd at room temperature.

For higher hydrogen content the behaviour of the metal-hydrogen system is more complex. There is a marked increase in the lattice parameter as the film stretches to accommodate more hydrogen atoms. When maximum solubility in the  $\alpha$ -phase has been reached for  $x > 0.015$ , a new phase starts to nucleate – the  $\beta$ -phase, which has a lattice parameter of  $0.4025 \text{ nm}$  ( $\beta_{\min}$ ) and also exists in an fcc structure. Both the  $\alpha$ - and the  $\beta$ -phases coexist in a homogenous mixture within an fcc matrix for  $0.015 < x < 0.6$  under an invariant hydrogen partial pressure, called the plateau pressure region [10].

With increasing hydrogen content the  $\alpha$ -phase disappears completely and there is a substantial increase in the hydrogen partial pressure. At  $x = 0.7$ ,  $100 \text{ kPa}$  (100% hydrogen) and room temperature the lattice constant increases to  $0.4040 \text{ nm}$  ( $\beta_{\max}$ ) [5, 11, 12], making the volume expansion from the  $\alpha_{\max}$  to the  $\beta_{\max}$  phase 11.7%. The palladium-hydride phases are summarised in Table 2-1.

**Table 2-1 – The palladium-hydride phases occurring at various values of  $x$ , (H/Pd ratio) with corresponding lattice constant sizes,  $a$  at room temperature and for a 100nm palladium film. Data taken from [5] and [8].**

| Phase                                   | $[H_2]^\dagger$ | $x$                     | $a$                                 |
|---|-----------------|-------------------------|-------------------------------------|
| $\alpha$ phase                          | 0 - 2%          | $0 \leq x \leq 0.015$   | $\alpha_{\min} = 0.3890 \text{ nm}$ |
|   |                 |                         | $\alpha_{\max} = 0.3894 \text{ nm}$ |
| $\alpha$ - $\beta$ phase in coexistence | 2%*             | $0.015 \leq x \leq 0.6$ | $\beta_{\min} = 0.4025 \text{ nm}$  |
| $\beta$ phase                           | 100%            | $0.6 \leq x \leq 0.7$   | $\beta_{\max} = 0.4040 \text{ nm}$  |

<sup>†</sup> Hydrogen concentration \* Equilibrium pressure at plateau region

For increasing temperature, the  $\alpha_{\max}$  phase occurs for higher hydrogen content while the  $\beta_{\min}$  occurs for lower  $x$  until the critical temperature of  $295.3^\circ \text{C}$  is reached at  $x = 0.27$  [3, 13], above which only one phase exists. The different phases are shown in the well cited pressure-concentration-temperature (PCT) diagram in Figure 2.2a, where the dashed envelope connects the  $\alpha_{\max}$  and  $\beta_{\min}$  for successive isotherms [3].

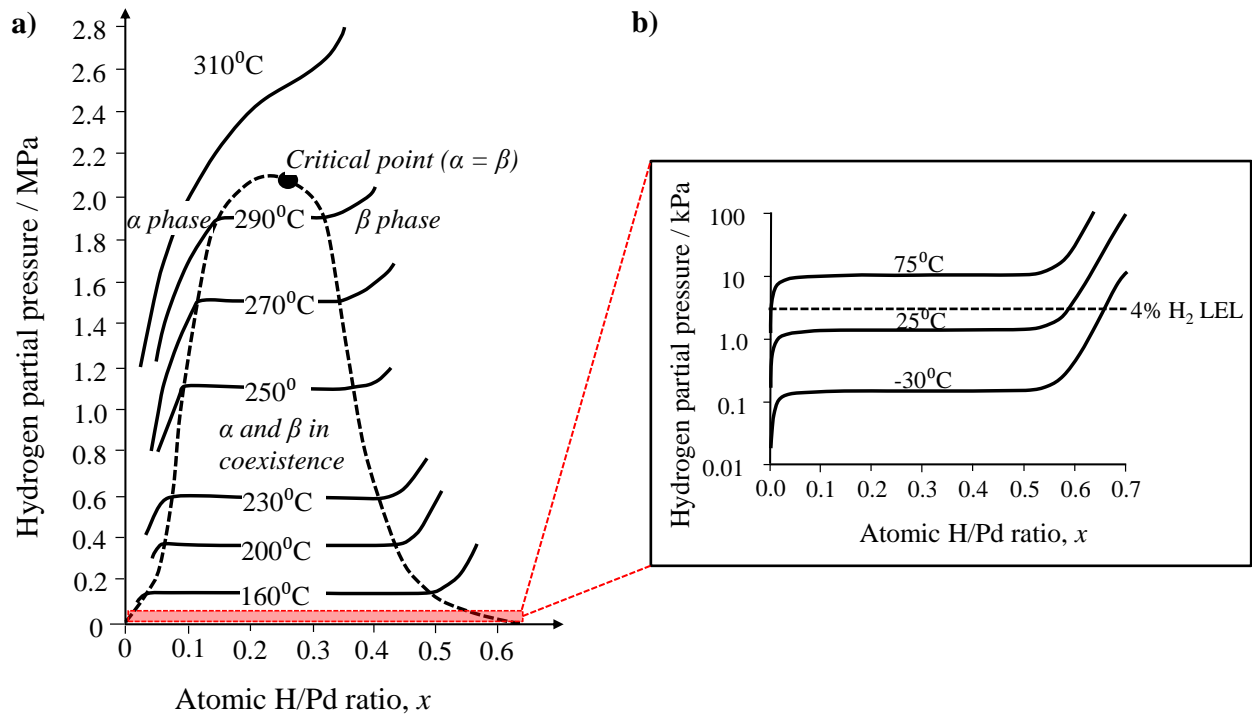


**Figure 2.2-** a) Pressure-concentration-temperature (PCT) graph indicating the formation of the two phases,  $\alpha$  and  $\beta$ , and the region of homogenous coexistence of the two phases. Above the critical temperature of  $\sim 300^\circ\text{C}$ , only one phase exists. The dashed black line shows the envelope connecting the  $\alpha_{\max}$  and  $\beta_{\min}$  of the plateau pressure region for successive isotherms [3, 14]. b) Inset – PCT graph for 100nm palladium film at low temperatures [15].

The value of the H/Pd atomic ratio,  $x$  is generally explained using the electron distribution in  $\text{PdH}_x$ . Palladium is a transition metal with an atomic number of 46 and has two bands of available electron states, the 4d (ten electrons per atom) and 5s (two electrons per atom), and these bands overlap [13]. The two bands are not completely filled and there are 0.6 unoccupied states or holes per Pd atom [13, 16]. This means that 60% of palladium's interstitial sites are available for H atoms [4]. Hydrogen is soluble in Pd until the 4d band (with a high density of states) is filled, which occurs when the ratio of H:Pd is 0.6. For temperatures below  $80^\circ\text{C}$ ,  $x$  can be greater than 0.6 as the low density states in the 5s band become available [16, 44, 17]. For example, at  $0^\circ\text{C}$ , the maximum concentration,  $x$  tends to unity [16].

### 2.1.1 Hysteresis

Transition from one phase to another is associated with a hysteresis effect that is characteristic of metal hydrides. The palladium-hydride system is one system where the hysteresis effect has been studied widely [18]. The lattice expansion during nucleation of the  $\beta$ -phase leads to strain and disorder in the plateau pressure region of coexistence between the two phases. The hydrogen pressure needed for hydrogen absorption is higher than that for desorption at the same temperature [17, 5]. This causes irreversible plastic deformation of the lattice with loss of heat between the cycles [5].

Figure 2.3 adapted from Lewis [19] shows hysteresis loops in the pressure-composition-temperature diagram where  $T_3$  is greater than the critical temperature and  $T_3 > T_2 > T_1$ . The region marked by AB represents low hydrogen content when the system is in the  $\alpha$ -phase and the absorption and desorption is reversible. In the closed loop BCDEGH, higher hydrogen content shows path separation between the absorption and desorption cycles when the phases are in coexistence. For even higher hydrogen concentration, region EF shows reversible effects.

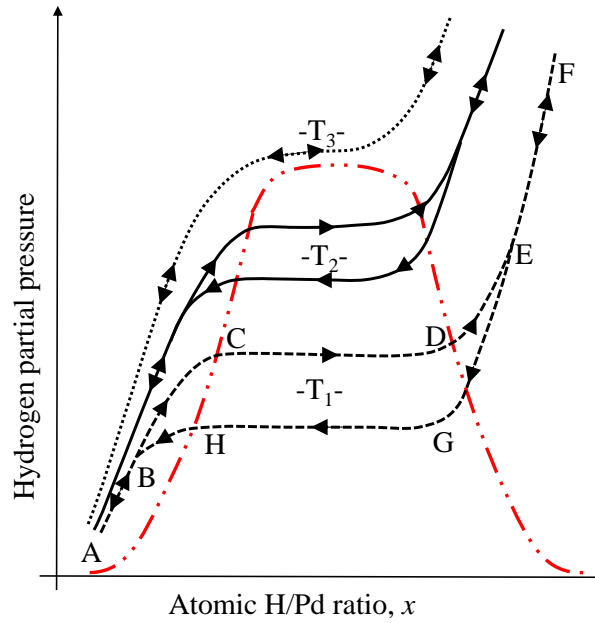


**Figure 2.3- Hysteresis loops opening around the plateau pressure region. The hysteretic differences get smaller for higher temperatures,  $T_3 > T_2 > T_1$ . Redrawn from [19].**

The PCT diagram described thus far is for bulk palladium films with thicknesses greater than 100nm but Frazier [8, 20] shows evidence that the PCT diagram is also dependent on film thickness. For thinner films, the plateau pressure slope appears to increase slightly and  $\alpha_{\max}$  occurs for higher  $x$ . It is estimated from Frazier's graphs that the plateau pressure of an annealed palladium film of thickness  $\geq 100\text{nm}$  at  $27^\circ\text{C}$  is at 15 Torr ( $\sim 2\%$  hydrogen by volume) and consistent with the bulk PCT diagram. But a 75nm film doesn't really show a plateau but a slowly increasing slope where the point of inflection is estimated to be at 17 Torr ( $\sim 2.3\%$  hydrogen by volume) whilst the 52nm is at 18 Torr ( $\sim 2.4\%$  hydrogen by volume). Frazier [20] also noted that a film thicker than 120nm stands a higher likelihood of peeling as it enters the  $\beta$ -phase due to the formation of cracks and blisters. We might suppose that thinner films are therefore more robust but a palladium layer thinner than 25nm may not be reproducibly continuous and could lead to an inconsistent response from the film. Thus it is important to decide on the appropriate thickness of the palladium film where the delamination is minimised and the sensor response is stable. For this project, a 40nm thickness for the palladium layer was chosen and explained in chapter 3, section 3.1, page 42. The problem of hysteresis can also be alleviated by using alloys of palladium as described in section 2.1.4, page 15.

### 2.1.2 Changes in electrical and optical properties

As palladium expands, the density of free electrons decreases and so does the electron mobility which leads to a reduction in the electrical conductivity [16]. Palladium hydride has a higher electrical resistance than pure palladium and the rise in resistance is proportional to the amount of hydrogen absorbed, as reported by Cheng *et al* [21], when experimenting using a 100nm Pd(92%)Ni(8%) film at 22°C at 5% H<sub>2</sub> in N<sub>2</sub>. Hysteresis effects have been also been observed in measurements of resistance during cycling at high concentrations of hydrogen that induce the formation of the  $\beta$ -phase [22]. With the Pd 4d band filled by electrons, the Fermi energy level shifts upwards reducing the number of empty states above the Fermi level available to participate in optical transitions [23, 4]. The real and imaginary refractive index decreases, causing the reflectivity of the surface to decrease as well. The dependence of changes in optical properties on the material conductivity can be seen from the Kramers-Kronig relationship in equation (2.3) as used by Maier *et al* [24]

$$n^* = \frac{c\sqrt{2\omega\mu_0\sigma_e}}{\omega}(1 - i) \quad (2.3)$$

where  $n^*$  is the complex refractive index of the material,  $c$  is the free space velocity of light,  $\omega$  is the angular frequency of the wave,  $\mu_0$  is the permeability of free space and  $\sigma_e$  is the conductivity of the metal. The complex refractive index is made of a real part,  $n_R$  and an imaginary part,  $n_I$  and shown by equation (2.4).

$$n^* = n_R - in_I \quad (2.4)$$

Palladium's complex refractive index at 1550nm is 2.95 -  $i$ 8.33 [25]

Using the real and the imaginary parts of the complex refractive index, the reflectivity,  $R$  of the metal surface can be calculated [14]:

$$R = \frac{(n_R - 1)^2 + n_I^2}{(n_R + 1)^2 + n_I^2} \quad (2.5)$$

Changes in refractive index can be detected as changes in resistance or changes in reflected light intensity. The methods of detection are discussed in detail in section 2.3, page 18.

### 2.1.3 Effects of contamination

Despite palladium's selective affinity for dissolving hydrogen, several compounds are known to interfere with the surface adsorption.

1. O<sub>2</sub> – Palladium acts as a catalyst for the chemisorption of oxygen and hydrogen, which can then form desorbable water on the palladium surface [21, 26]. This reaction leads to reduced hydrogen partial pressure at the Pd surface, thus reducing the dissolved concentration and

hence the response of the sensor. The blocking of adsorption sites by water also increases the response time since it limits the access of hydrogen. Butler [27] investigated the rate of hydrogen uptake of a 10nm thick palladium film for hydrogen in two carrier gases, N<sub>2</sub> and air. Butler defined the rate of uptake as the time taken to reach the maximum change in reflectivity with H<sub>2</sub> exposure. In N<sub>2</sub>, the uptake rate was proportional to the concentration, whereas in the presence of oxygen in air a reduced rate for 0-10% H<sub>2</sub> in air was observed with a square law dependence on hydrogen concentration (see chapter 3, Figure 3.4, page 46 for more details). Pure palladium exposed to air for long periods can also form an oxide layer. The metal will need to be flushed with a few cycles of hydrogen to allow complete reduction of the oxide.

2. CO – Whilst the effect of oxygen on the palladium layer is reversible at room temperature, the adsorption of carbon monoxide is irreversible at room temperature as it can displace the adsorbed hydrogen and poison the sensing layer by blocking adsorption sites [28]. This was found to be an issue for CO concentration >5 mol%. To remedy CO poisoning the film can be heated at high temperature, 200°C in oxygen so that the CO becomes oxidised to CO<sub>2</sub>, which is then desorbed [21]. Carbon has a similar poisoning effect on the palladium surface; it forms primarily through the decomposition of a hydrocarbon, (CH<sub>4</sub> = C+2H<sub>2</sub>) [28].

Exposure of the transducer to oxygen and carbon may poison the active sensing layer and reduce the response to atmospheric hydrogen, so care must be taken to minimise exposure to hands, air, solvents etc during construction and installation. Butler [29] used a 10nm layer of Ni as an adhesive layer between the PdAg coating and substrate to prevent film delamination and a 25nm Pt capping layer to minimise oxidation of the silver and contamination and therefore improve sensor lifetime.

### 2.1.4 Palladium alloys

Alloys of Pd have been shown to inhibit the phase  $\alpha$ - $\beta$  transition, leading to reduced hysteresis. Binary palladium alloys that use Ag, Au, Cu, Ce and Y as the alloying metal have a larger unit cell than pure palladium and are capable of absorbing more hydrogen. The plateau pressures near the  $\alpha$ - $\beta$  transition are lower than in the Pd-H system because the strain energy needed for expansion of the Pd lattice to accommodate the hydrogen atoms is smaller [30]. Hydrogen permeability (in cm<sup>3</sup> cm<sup>-2</sup> s<sup>-1</sup>) is correlated to the average bond distance of alloys [31]. This is expected because with bigger atomic distance more atomic hydrogen can diffuse into the lattice and this is shown in Table 2-2, taken from Yun *et al* and Knapton [31, 32]. The permeability also depends on the alloy metal used. For example 5% of Au alloy in Pd has increased permeability compared to 40% Au alloy metal in Pd.

Palladium alloys that use Fe, Ni, Ru, Rh and B suffer from lower permeability than pure palladium as the lattice unit cell shrinks with fewer interstitial sites to occupy. Nanometre sized palladium particles

that have an fcc cubooctahedral lattice structure, have been used to show faster permeability of hydrogen. The lattice has a higher density of dislocations and allows for increased binding sites [28, 33].

**Table 2-2 – Comparison of hydrogen permeability of various Pd-alloy films to pure Pd film. The data is taken from Knapton[32], where the experiments were conducted on films that were 25µm thick at 350°C and 300psi.**

| Pd-Alloy                              | % of alloy metal | Average bond distance <sup>a</sup> /nm | Permeability ratio of H <sub>2</sub> in Pd-alloy <sup>b</sup> /Pd |
|---------------------------------------|------------------|--|---|
| Increased H <sub>2</sub> permeability |                  |  |   |
| Pd                                    | 0                | 0.275                                  | 1   |
| Pd-Au                                 | 5                | 0.275                                  | 1.06  |
| Pd-Cu                                 | 40               | 0.275                                  | 1.1   |
| Pd-Ce                                 | 7.7              | 0.28                                   | 1.6   |
| Pd-Ag                                 | 23               | 0.278                                  | 1.7   |
| Pd-Y                                  | 10               | 0.284                                  | 3.8   |
| Reduced H <sub>2</sub> permeability   |                  |  |   |
| Pd-Ni                                 | 10               | -                                      | 0.19  |
| Pd-Au                                 | 40               | 0.270                                  | 0.42  |
| Pd-Cu                                 | 10               | 0.272                                  | 0.48  |
| Pd-B                                  | 0.5              | -                                      | 0.94  |

<sup>a</sup> The bond distances of the metals are - Pd(0.275nm), Y(0.355nm), Ag(0.289nm), Ce(0.365nm), Cu(0.256nm) and Au(0.288nm). Taken from [31]

<sup>b</sup> Permeability of H<sub>2</sub> in pure Pd is 1.43 cm<sup>3</sup>/cm<sup>2</sup>/s.

Alloying can alleviate embrittlement problems too by reducing hysteresis. The relative difference in lattice size between  $\alpha$  and  $\beta$  decreases so there is less distortion between hydrogen adsorption and desorption cycles [31]. It is therefore desirable to have a combination of palladium and an alloy metal with increased changes in lattice constant on uptake of H<sub>2</sub>. Some alloys offer better resistance to poisoning too, for example PdAu is resistant to sulphur poisoning [29] and PdNi is resistant to oxygen and sulphur poisoning [21].

The use of palladium alloys was not within the scope of this project. Since the primary focus was to characterise the stability of the sensor head and the interrogation system, a palladium coating was chosen to maintain simplicity.

## 2.2 Hydrogen detection technologies

The development of a stable, intrinsically safe and reliable hydrogen sensor is essential as a safety measure in hazardous environments since hydrogen has a wide explosive range of 4-75% volume in air [34]. Interaction of hydrogen with a hydrogen sensitive material, commonly palladium, can cause changes in temperature, the material's refractive index, electrical, physical and mechanical properties. A transducer is needed to transform these changes into an electrical signal. There are several

hydrogen detection technologies that have been described including semi-conducting metal oxide sensors, work-function based sensors, electrochemical cells, catalytic sensors, spectroscopic methods, optical fibre based sensors. Many of these sensor techniques are rendered unsuitable for application in an explosive environment for reasons that are summarised in Table 2-3. Many techniques require the passage of electricity to the sensor head, which could ignite a spark and cause an explosion, whilst other techniques involve equipment that cannot be miniaturised or are not suitable for long term stability studies due to the need for frequent calibration. Although these techniques can be made EU ATEX (describes what equipment and protective systems are permitted for use in potentially explosive environments) [35] compliant, this tends to increase the sensor size.

**Table 2-3 – Summary of existing hydrogen sensing techniques and discussion of their merits for this application.**

| Sensor                     | Physical change                                  | Lod*   | Discussion   | Suitable? | Ref          |
|----------------------------|--|--------|--|-----------|--------------|
| Semiconducting metal-oxide | Resistance                                       | 1 ppm  | Fast, low cost, low power, moderate stability but not selective, electrical operation, needs oxygen to operate               | No        | [36-38]      |
| Metallic resistor          | Resistance                                       | 25ppm  | Fast, stable and selective but needs electricity and is affected by temperature  | No        | [21, 22, 39] |
| Schottky diodes            | Work function voltage                            | 100ppm | Fast, small size, low cost but susceptible to drift and needs electricity  | No        | [36, 40, 41] |
| MOSFET <sup>a</sup>        | Work function voltage                            | 10ppm  | Fast, accurate, small size and stable but susceptible to drift and needs electricity   | No        | [38, 40, 42] |
| MOS capacitor              | Capacitance                                      | 10ppm  | Selective, fast, low power, low cost, operates at room temperature and stable but needs electricity                          | No        | [36, 43]     |
| Electrochemical cells      | Current, electrode potential                     | 1ppm   | Operates at room temperature, low power and resistant to poisoning but needs passage of electricity                          | No        | [37, 44, 45] |
| Pyroelectric               | Electrode potential                              | 40ppm  | Needs electricity, acts as energy storage medium   | No        | [46, 47]     |
| Piezoelectric              | Resonant frequency                               | 100ppm | Operates at room temperature but cross-sensitive, temperature dependent and needs electricity, acts as energy storage medium | No        | [36, 48-50]  |
| SAW <sup>b</sup>           | Frequency, intensity, phase shift, wave velocity | 10ppm  | Low power, operates at room temperature but needs electricity  | No        | [51, 52]     |
| Catalytic pellistors       | Temperature, resistance                          | 50ppm  | Fast and stable but not selective, needs oxygen to operate and electrical operation  | No        | [36, 37]     |

| Sensor               | Physical change                                   | Lod*  | Discussion   | Suitable? | Ref                     |
|----------------------|---|-------|--|-----------|-------------------------|
| Thermal conductivity | Temperature, resistance                           | -     | Low cost, robust and stable but is temperature dependent and needs electricity   | No        | [36, 37]                |
| Fibre Optics         | Transmission, reflection, wavelength, phase shift | ~ppb  | Electrical isolation, remote operation, small size, relatively unaffected by electromagnetic interference but susceptible to drift and sulphur poisoning | Yes       | Section 2.3 for details |
| CRDS <sup>c</sup>    | Decay time, intensity                             | ~ppb  | Difficult to align light into cavity; need high reflectivity and large mirrors and cannot be miniaturised  | No        | [53-57]                 |
| Raman spectroscopy   | Intensity   | 30ppm | Stability and reproducibility issues   | No        | [58-60]                 |
| PAS <sup>d</sup>     | Intensity   | 1ppm  | High sensitivity but is temperature dependent and needs high powered lasers  | No        | [60, 61]                |
| Mass spectrometry    | Time of flight, current                           | <1ppm | Selective and sensitive but needs electricity, calibration and vacuum chamber. Samples extracted and sent to MS currently                                | No        | [37]                    |

\* Limit of detection

*a* Metal-Oxide-Semiconductor Field Effect Transistor

*b* Surface Acoustic Wave

*c* Cavity Ring Down Spectroscopy

*d* Photo Acoustic Spectroscopy

## 2.3 Fibre optic sensors

The particular interest in fibre optics arises due to the intrinsic safety offered by fibre optic based sensors. Fibre optic sensors are also relatively unaffected by electromagnetic interference. The sensor interrogation is based on dielectric materials and contains no energy storing elements. The optical beam used to interrogate the fibre optic network is much lower than the power limit of 30mW set by the EU ATEX directive [35] for use in explosive environments and thus insufficient to raise the temperature of any surface above the auto ignition temperature of the gas mixture in the testing chamber. The sensor heads are small in size and can be embedded in operation, allowing remote operation.

Fibre optic based sensors are commonly coated with a palladium coating. When exposed to hydrogen the metal coating expands and changes the palladium lattice as explained in section 2.1, page 10. The volume of free electrons decreases which causes both the real and imaginary parts of the complex refractive index of the palladium coating (equation (2.4)) to decrease as well.

Different types of responses can occur from changes in the complex refractive index [7]:



1. Change in the imaginary part of the refractive index,  $n_I$  alters the absorption of light and can be detected by monitoring the intensity of the transmitted/reflected signal
2. Change in the real part of the refractive index,  $n_R$  alters the optical pathlength/phase of light and this can be detected using interferometric techniques.

Some fibre optic sensor configurations for hydrogen detection that employ these changes are discussed in this section and are based on an excellent review article by Silva [7] in 2012 and updated with the latest research. Reviewing these existing methods and weighing their pros and cons led to the choice of technique selected for this project.

### 2.3.1 Intensity based - Micromirrors

Micromirrors typically consist of a thin film of palladium or palladium alloy that is coated onto the tip of a cleaved optical fibre, as originally reported by Butler [62]. This sensor has a simple configuration as shown in Figure 2.4.

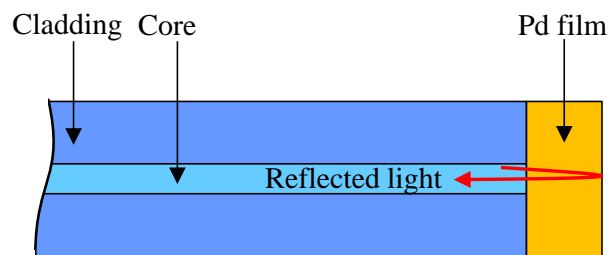


**Figure 2.4- Micromirror sensor head. Fibre tip coated with a film of palladium. Measurements are made of changes in reflectivity of the Pd film as a function of hydrogen concentration.**

A portion of the incident light is reflected at the surface of the Pd film, which acts as a partial mirror, and reflected light intensity is recorded using a photodiode detector. The reflectivity of the coating decreases upon hydrogenation, and the change in reflectance is dependent on the hydrogen concentration. Butler [62] used a 10nm palladium film deposited at the tip of a multimode fibre (MMF, 50 $\mu$ m core/125 $\mu$ m cladding). He measured the reflectivity change using an LED at 860nm modulated at 10kHz and drew a calibration chart for proportional change in reflectivity versus hydrogen concentration. Butler concluded that the sensor was able to detect hydrogen concentration in the range 0.2% to 100% H<sub>2</sub> in N<sub>2</sub> at room temperature. Butler noticed a rapid decrease in the absolute reflectivity around 2% H<sub>2</sub> in N<sub>2</sub> that led him to believe that the compound had reached the mixed phase region, where a large change in the hydride composition occurs for small changes in hydrogen concentration. The sensor became less responsive for higher concentrations as the hydride composition changed to the saturated  $\beta$ -phase. Butler [29] further developed a commercial micromirror sensor to detect hydrogen in transformer oil, where the sensor head was a GRIN lens attached to a MMF (50 $\mu$ m core/125 $\mu$ m cladding) and coated with a 10nm Ni adhesive layer, an

optically thick 150nm PdAg sensing layer followed by 25nm Pt protective capping layer. The interrogation system employed a common optical network and two LEDs at 880nm and 810nm. A high pass filter coating between the GRIN lens and the MMF separated the wavelengths into probe and reference intensities so that the reflectivity change measurements could be normalised to compensate for time varying optical fluctuations and thermal changes. Details of the sensor head and the interrogation system are described in chapter 6, section 6.1, page 112. Butler was able to detect 50ppm H<sub>2</sub> in transformer oil at room temperature.

The reflectivity of the palladium surface also depends on its thickness. Butler's paper in 1994 [63] observed that a palladium film remained optically thin up to 40nm thickness when the reflectivity responded to surface reactions. Whilst thin films had a fast response time, they were less sensitive. Thicker films were more prone to suffer from delamination and cracking. To choose the optimum thickness of the sensing layer for a specific application, the reflectivity of the palladium film was modelled from the thin film interference model and is described in chapter 3.

Bevenot *et al* [64] used this concept to develop an improved sensor that could be used to detect hydrogen leakage from the engine of a rocket. The instrumentation was simplified by eliminating lock-in amplifiers, and the sensor reproducibility was improved by using a 13nm palladium film on a 400µm MMF core. The palladium film was optically heated with a high powered laser diode (up to 5W) at 815nm to broaden the range of temperatures that the sensor could operate in, between -196°C and 23°C. They were able to detect between 1-17% H<sub>2</sub> in N<sub>2</sub> with a response time smaller than 5s.

### ***2.3.2 Intensity based - Evanescent waves***

When light is totally internally reflected at a boundary separating two media, evanescent waves form at the boundary with the intensity decaying exponentially with distance from the boundary [65]. According to Maxwell's equations there cannot be an abrupt discontinuity in the electric and magnetic fields between the two media and a portion of the light is transmitted as evanescent waves. The evanescent wave is at its most intense within one third of a wavelength from boundary. Tabib-Azar *et al* in 1999 [65] were the first to develop an evanescent wave hydrogen sensor by stripping a 1.5cm length of the cladding from a MMF (50µm core/125µm cladding) and coating the exposed and etched fibre core with a 10nm film of palladium, as shown in Figure 2.5.

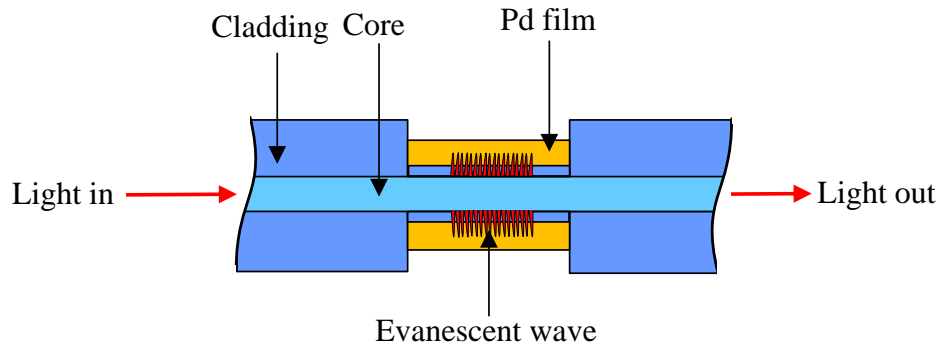


**Figure 2.5- Evanescent wave based  $H_2$  sensor. An exposed etched fibre core is coated with a palladium film. Due to the formation of palladium hydride with lower refractive index, the evanescent wave intensity is attenuated as a function of adsorbed hydrogen. Diagram adapted from [54]**

The palladium layer changes refractive index upon absorbing hydrogen, which attenuates the evanescent wave intensity. This could be detected as a change in transmittance of the fibre. A monochromator at 650nm was used to detect 0.2-0.6%  $H_2$  in  $N_2$  with respective response times of 30-20s at room temperature. Although the sensitivity and response times of this configuration could be improved by controlling the length and thickness of the sensing area, unlike the micromirror configuration which has a fixed sensing area, the sensors were fragile. The authors found sensor handling and packaging challenging for deployment on a space vehicle. This method has the advantage of being able to sample gas concentrations along the length of the fibre rather than just at the tip of the fibre.

An alternative method of accessing the evanescent waves is by using a tapered fibre as shown by the schematic in Figure 2.6. Villatoro *et al* [66] first used a tapered single mode fibre (SMF), which was formed by stretching the SMF whilst heating under a controlled oscillating flame. The 15mm long tapered region with a  $20\mu m$  waist diameter was coated in 12nm palladium. Using a low powered LED, ( $3\mu W$ ) centred at 1600nm operating wavelength, the authors were able to detect between 1.8% and 10%  $H_2$  in  $N_2$ . It was observed that the sensitivity increased for longer wavelengths.

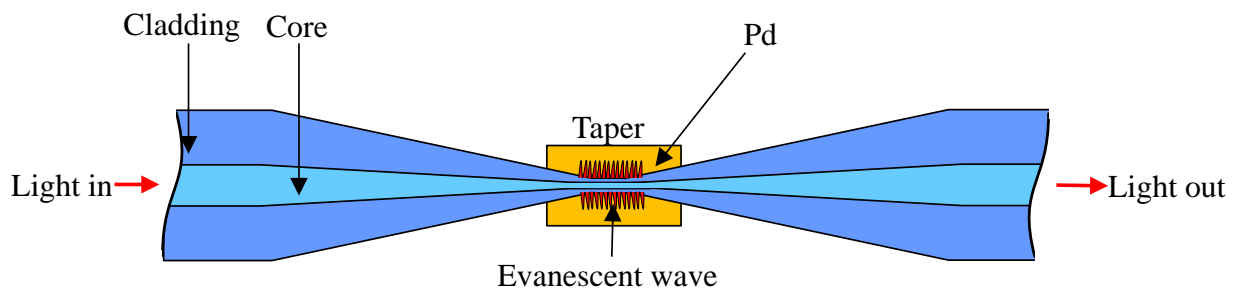


**Figure 2.6- Evanescent wave based  $H_2$  sensor on a tapered fibre region coated with palladium. Schematic adapted from [66] and not to scale.**

A few years later, Villatoro *et al* [67] implemented the concept on a multimode fibre with taper waists of 30µm and 60µm and a length of 10mm coated with a 14nm palladium film. Owing to noise in the signal, these sensors were able to detect between 0.3 and 3.5% H<sub>2</sub> in N<sub>2</sub> before signal saturation. The sensor with the narrowest waist gave a bigger response but they both responded in similar times, ~30s for 2% H<sub>2</sub> in N<sub>2</sub>. The authors reported that the sensors were easy to handle and simple to produce, but the stretching of the fibre weakened it and made it fragile. Villatoro *et al* [68] further improved the performance and response time of tapered fibres by producing nano tapers on single mode fibres. The waist diameter was 1300nm (smaller than the operating laser diode wavelength of 1500nm) and a 2mm length of the tapered region was coated with a 4nm palladium film. The sensor was able to detect between 0.05%-5% H<sub>2</sub> in N<sub>2</sub> at room temperature with a ~10s response for 3.9% H<sub>2</sub> in N<sub>2</sub>.

A heterostructure core-mismatch sandwich design was developed by Luna-Moreno *et al* [69], where a 5mm single mode fibre stub, SMF-28 (9µm core/125µm cladding) coated in 10nm Pd(60%)Au(40%) was spliced between two multimode fibres (62.5µm core/125µm cladding). The schematic is shown in Figure 2.7.

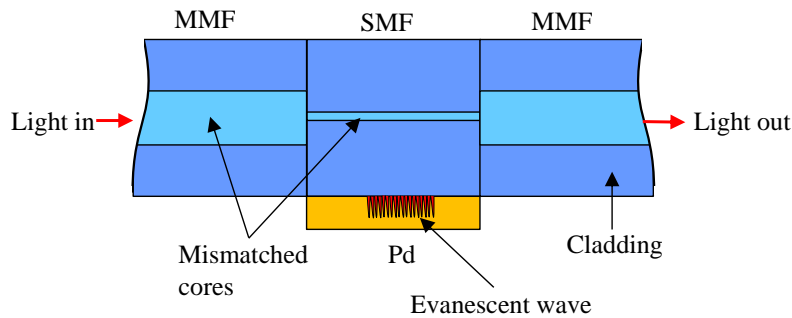


**Figure 2.7- Evanescent wave based H<sub>2</sub> sensor with mismatched core diameters. A SMF is sandwiched between two MMFs and coated with palladium. Core modes of first MMF couple with cladding modes of SMF and to evanescent waves. Schematic adapted from [69]**

The core modes of the first MMF were coupled to the core and cladding modes of the SMF. The second MMF re-coupled the core and the SMF cladding modes. The modes that propagated through the SMF cladding generated evanescent waves that interacted with a palladium sensing layer. These modes were perturbed by changes to the palladium caused by hydrogenation. The sensors were able to detect between 0.2% and 5% H<sub>2</sub> in N<sub>2</sub>. The response time to 4% H<sub>2</sub> in N<sub>2</sub> was 15s, whilst the recovery was 200s. Hernandez *et al* [70] used the same configuration but used alternate layers of 1.4nm Pd and 0.6nm Au to build a layered structure. They were able to make improvements to the sensor performance and response time. For a 4 stacked structure of 8nm total thickness, the sensor responded in 6s and 10s for 4% and 2% H<sub>2</sub> in N<sub>2</sub> respectively with a recovery time of ~13s, and a limit of detection of 0.8%. The sensor size increased with the number of repeated stacked layers. The sensors were simple to produce and had good mechanical strength.

Kim *et al* [71] used a side polished SMF coated with a 40nm palladium film and embedded the fibre in a quartz block, with a 50cm radius of curvature. The schematic is shown in Figure 2.8.

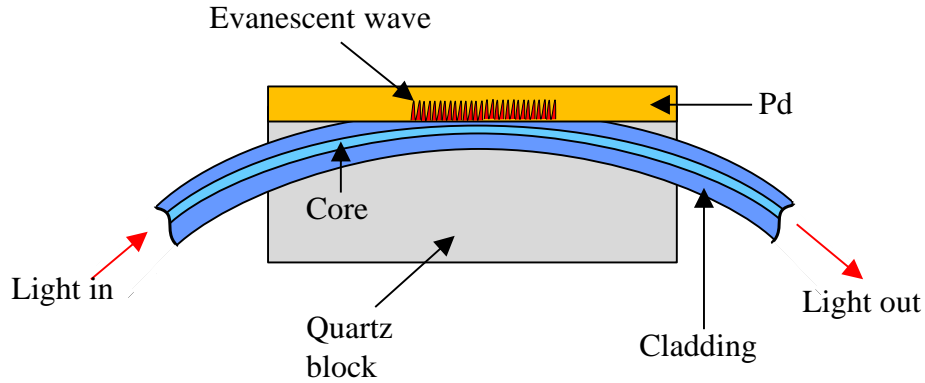


**Figure 2.8-** Evanescent wave based  $H_2$  sensor formed on a side-polished fibre coated with palladium. Schematic adapted from [54]

Using a transverse magnetic (TM) polarised input at 1550nm, the authors recorded a big change of 32% in the transmitted optical power when exposed to 4%  $H_2$  in  $N_2$ . The response time for that concentration was 100s and recovery 150s.

### 2.3.3 Surface plasmon resonance (SPR)

Plasmons can be described as the oscillation of the free electron density cloud in a metal. When the metal is subjected to an external electric field, the free electrons are driven by the force of attraction towards the fixed positive ions in the metal lattice and at the same time the electrons feel an opposite force from the Coulomb repulsion between like-charges [72, 73]. The electrons thus move back and forth in so-called plasma oscillations. Surface plasmons are electromagnetic waves that propagate parallel to a metal-dielectric boundary [73]. The surface plasmon wave propagation constant  $k_{sp}$  is continuous through the metal-dielectric and the dispersion relation is given by equation (2.6) [72], where  $\omega$  is the frequency of incident light;  $c$  is the velocity of light;  $\epsilon_m$  is the dielectric constant of a metal and  $\epsilon_d$  is the dielectric constant of a dielectric material (eg – glass prism, air or silicon dioxide optical fibre). For metals  $\epsilon_m < 0$  and for dielectrics  $\epsilon_d > 0$ , so the surface plasmons will only be excited if  $\epsilon_d > \epsilon_m$ .

$$k_{sp} = \frac{\omega}{c} \sqrt{\frac{\epsilon_d \epsilon_m}{\epsilon_d + \epsilon_m}} \quad (2.6)$$

The maximum propagation constant of a transverse magnetic (TM) or p-polarised incident light (same polarisation state as the surface plasmon wave) hitting a metal-dielectric boundary at angle  $\theta$  is given by equation (2.7) [72, 74].

$$k_l = \frac{\omega}{c} \sqrt{\epsilon_d} \sin \theta \quad (2.7)$$

Comparing equations (2.6) and (2.7),  $k_{sp} > k_l$  and hence direct light cannot excite the surface plasmons instantly. But if the p-polarised light, with their plane of polarisation parallel to the plane of incidence, is passed through a dielectric medium (typically a glass prism) at an angle that supports total internal reflection, evanescent waves will be generated at the boundary and interact with the plasmons to create surface plasmon waves. The arrangement of the setup is shown in Figure 2.9a.

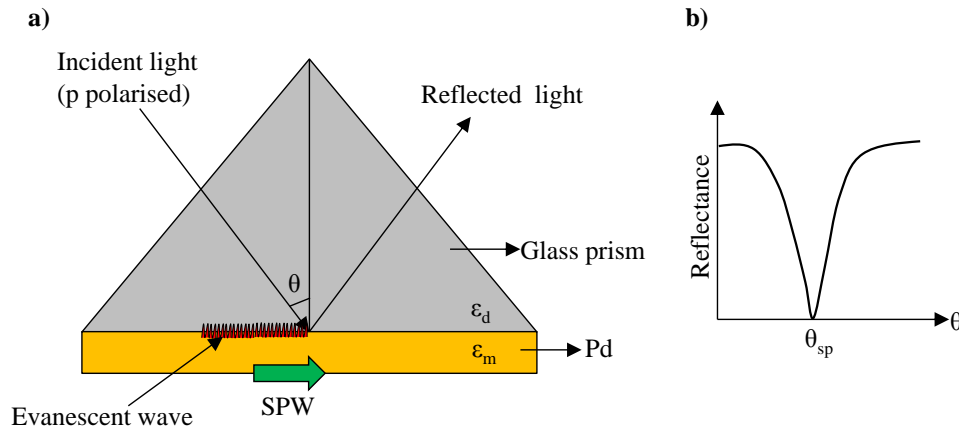


**Figure 2.9- Generation of surface plasmon waves (SPW).** a) Incident light is totally internally reflected and evanescent waves form at the glass prism and metal boundary, due to a difference in their dielectric constants,  $\epsilon_d$  and  $\epsilon_m$  respectively. The evanescent waves excite SPW and change the intensity of reflected light. b) Dip in the intensity of reflected light at resonant angle of incidence,  $\theta_{sp}$ . Diagram adapted from [72].

These waves are sensitive to changes in the metal surface characteristics. At a resonance angle  $\theta_{sp}$ , maximum energy from incident photons is transferred to the surface plasmons and there is a dip in the intensity of reflected light (Figure 2.9b). An SPR sensor can be intensity based, where the changes in reflectivity light intensity is measured as a function of hydrogen uptake by the palladium film. The sensor can also include angular measurement where a shift in the resonance angle,  $\theta_{sp}$  is measured. A decrease in the resonance angle indicates a reduction in the refractive index of palladium [72]. Chadwick and Gal [73] demonstrated the feasibility of the configuration shown in Figure 2.9 with a 20nm Pd coating. Using a polarised helium neon laser at 633nm (SPR is insensitive to the wavelength of light) they recorded a 90% change in reflected intensity for 5%  $H_2$  in  $N_2$ , at an incident angle of  $50^\circ$  with a response time of 30s.

Bevenot *et al* [75] eliminated the use of a bulky prism and developed a fibre optic based SPR sensor, where a MMF core with a large numerical aperture (0.48) was coated with 12nm Pd film along 15mm of stripped fibre length. A laser diode, at 670nm wavelength, was mounted on a rotation stage that allowed movements between  $0^\circ$  and  $30^\circ$ . 100%  $H_2$  in  $N_2$  was detected at an angle of incidence of  $15^\circ$  while 4%  $H_2$  in  $N_2$  was detected at  $12^\circ$ . The lowest concentration that the sensor was able to detect

was 0.8%  $H_2$  in  $N_2$  at room temperature with response times of 300s, whereas 100%  $H_2$  in  $N_2$  responded fast at 3s. The authors experimentally determined that the polarisation state of the laser emission had no measurable influence on the generation of the SPR wave due to the cylindrical geometry of the sensor head. The need for adjustment of the angle of light incidence makes this approach unsuitable for an embedded operation that requires long-term stability.

Perrotton *et al* [76] in 2013 demonstrated a fast and sensitive hydrogen sensor based on SPR, where 0.5cm of MMF (200 $\mu$ m core/230 $\mu$ m cladding) was stripped of cladding and coated in multiple layers of 35nm Au, 180nm  $SiO_2$  and 3.75nm Pd. The transmitted intensity was monitored in the wavelength range 500 to 800nm and the shifts in the SPR dips indicated a sensitivity of 0.5-4%  $H_2$  in Ar, with a response time of ~15s for 2%  $H_2$  in Ar and 3s for 4%  $H_2$  in Ar with a recovery of 10s for the latter concentration.

A SPW based refractive index sensing technique that already exists but has not yet been applied to hydrogen detection is the use of tapered fibre sensors coated in Au (which promotes SPW) film/particles. The resonant angle of the incident beam is determined by the tapered waist diameter. Typically 30-40 $\mu$ m tapered waist diameter in a MMF is coated in 30-50nm Au and operated in the visible wavelength range with a high sensitivity of 0.006 RIU (refractive index unit) [77, 78, 79]. Tapering a fibre can improve sensitivity, since the angular range of incidence can be broadened. A lower angle of incidence would mean a wider spread of evanescent waves and stronger coupling between evanescent wave and SPW and increased sensitivity. This could be applied to hydrogen detection by adding an extra coating of palladium on top of the Au layers.

### **2.3.4 Interferometer based**

Interferometers operate on the principle of superposition of two waves to create an interference pattern. As palladium expands on hydrogenation, the induced mechanical stress can result in changes in refractive index, optical path length and phase. Butler [80] demonstrated detecting very low concentrations of hydrogen down to 20ppb  $H_2$  in  $N_2$  in under ~30s using a Mach-Zehnder interferometer (MZI) and 0.5mW HeNe laser. One arm of the MZI had a 28cm section of SMF coated with 10nm Ti as the adhesive layer and 1 $\mu$ m Pd as the sensing layer. Palladium hydride with an expanded lattice constant stretched the fibre arm and caused changes in the optical path length, which in turn shifted the interference fringes. The shift was dependent on the hydrogen content. The configuration is shown in Figure 2.10.

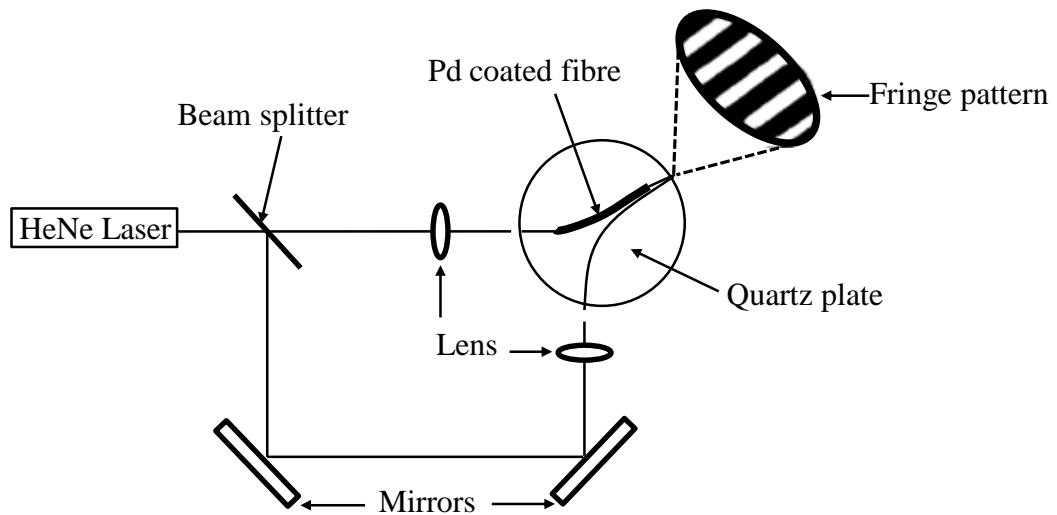


**Figure 2.10- Mach-Zehnder interferometer. Free space optics and a palladium coated fibre arm on a quartz plate. The fringe patterns shift as a function of hydrogen concentration. Diagram adapted from [9]**

The free space alignment of optics, and sensitivity to thermal changes and mechanical disturbances make this an impractical solution for this application for a micro sensor that has to be installed in situ.

Zeakes *et al* [81, 82] developed an extrinsic Fabry-Perot fibre sensor using the schematic shown in Figure 2.11. A cleaved single mode fibre was inserted in a glass tube opposite a cleaved reflective multimode fibre leaving an air gap of 50 $\mu$ m that formed a low finesse Fabry-Perot cavity. The components were held together by high temperature adhesive. A thick 2 $\mu$ m Pd layer was deposited on the glass tube so that its expansion upon hydrogenation changed the cavity size and thus the effective optical path length. The overall phase of the combined reflected intensities from the two sides of the air gap will shift as a function of hydrogen concentration. This sensor detected 0.5% H<sub>2</sub> in N<sub>2</sub> in under ~5s and had a minimum detection limit of 32ppm.

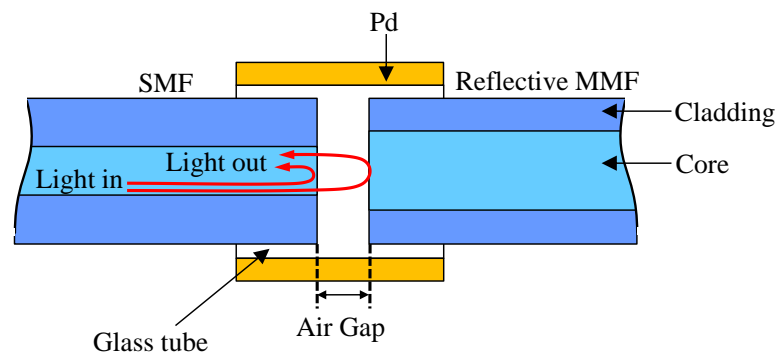


**Figure 2.11- Extrinsic Fabry-Perot cavity. A SMF and a reflective MMF end were separated by an air gap and held inside a glass tube coated with palladium. Palladium expands upon hydrogenation and causes shifts in the interference fringes. Adapted from [81]**



Photonic crystal fibres (PCFs) have recently emerged with interesting applications in gas sensing. These fibres have a solid core and many rings of air holes that run through the length of the fibre in the cladding and surround the core. Figure 2.12a shows the top view of a PCF.

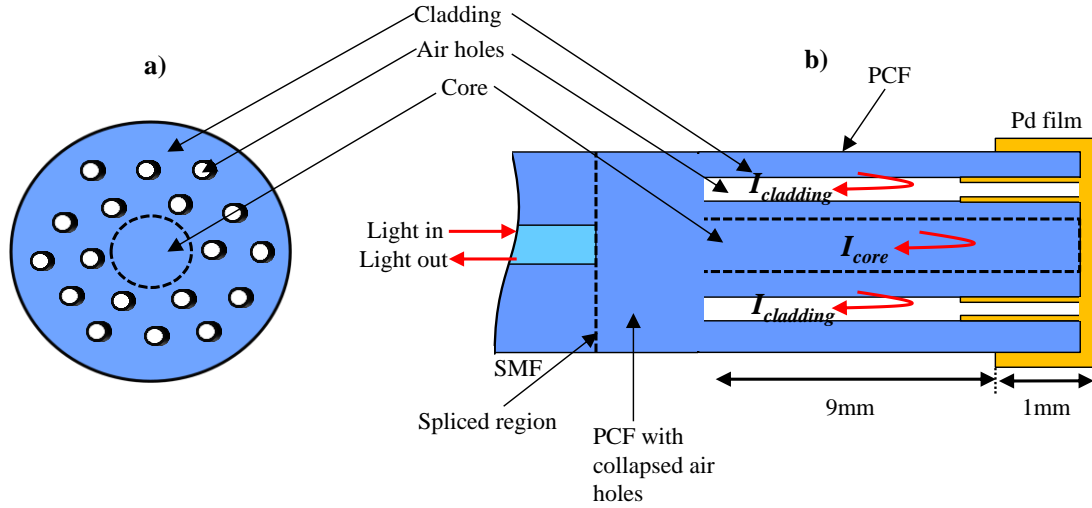


**Figure 2.12- Photonic crystal fibre (PCF) structure. a) Top view showing an array of air holes surrounding the core. The core is denoted by dashed lines. b) The side view of the PCF and its preparation as a  $H_2$  sensor.  $I_{core}$  and  $I_{cladding}$  are the intensities of the reflected fundamental and cladding modes respectively by the Pd mirror at the end. Diagram adapted from [83]**

Zhou *et al* [83] in 2014 introduced a new method for hydrogen sensing by developing a PCF in-line interferometer that was easy to produce in the lab, was cost-effective and had no tapering or etching of the fibre to weaken it. The schematic of the sensor head is shown in Figure 2.12b. A 10mm long PCF was spliced to a SMF fibre with matching cladding diameters of  $125\mu m$ . In the spliced region, the air holes collapsed to leave a region with an effectively uniform refractive index. When light travels from the SMF to the PCF, the SMF fundamental core mode excites multiple PCF core and cladding modes with different propagation constants. These modes are reflected at the end-face of the PCF, which recombine in the collapsed region and create interference. 1mm of the tip of the PCF was sputter coated with a 50nm Pd layer, covering the end face, the outer walls and part of the insides of the air holes as shown by Figure 2.12b. When exposed to hydrogen, the palladium film refractive index changes. The effective refractive index of the cladding modes decreases, causing the interference spectrum to shift to shorter wavelengths. The sensor was able to detect a 0.25nm and 1.25nm wavelength shift for 1% and 5%  $H_2$  in soybean oil respectively with a fast response time of 15 seconds. However the sensor's recovery time and repeatability were not investigated.

### 2.3.5 Fibre grating based

Fibre gratings are periodic modulations in refractive index that are etched in to the core of an optical fibre. A germanium doped silica fibre is photosensitive and when exposed to intense UV radiation, the refractive index changes. There are a number of other ways of modifying the refractive index of the

core: irradiation by femtosecond infrared lasers or CO<sub>2</sub> lasers, application of mechanical stress (eg- by tapering the fibre) or electrical discharges etc [84]. Long period gratings (LPGs) can be written in photonic crystal fibres by allowing periodic collapsing of the air holes using a CO<sub>2</sub> laser heat treatment [84]. Gratings with a short period of less than a few microns are called Fibre Bragg Grating (FBG). Light of wavelength  $\lambda_B$ , is reflected when it meets the Bragg condition given by equation (2.8).

$$\lambda_B = 2n_{eff}\Lambda \quad (2.8)$$

Where,  $\lambda_B$  is the Bragg wavelength,  $n_{eff}$  is the effective refractive index of the grating in the core and  $\Lambda$  is the grating period or the pitch. The Bragg period can change due to strain or thermal expansion in the fibre and from equation (2.8) it is evident that a change in the Bragg period will cause the reflected Bragg wavelength to shift, which can be measured to picometre accuracy. James and Tatam [84] reported FBGs that are capable of having sensitivities to strain and temperature of 1pm/ $\mu\epsilon$  and 13pm/K at 1300nm.

A hydrogen sensor based on fibre gratings typically has a thin coating of palladium deposited along the length of the fibre containing the grating. The schematic of a grating based hydrogen sensor is shown in Figure 2.13 along with plots of the incident, reflection and transmission spectra. The expansion of palladium due to hydrogenation will exert strain on the fibre which can be measured as a shift in the Bragg wavelength. The grating must be operated at a stable single temperature and have thermal packaging to reduce cross sensitivities from temperature variation as well as employing a mechanical strain-isolated reference grating.

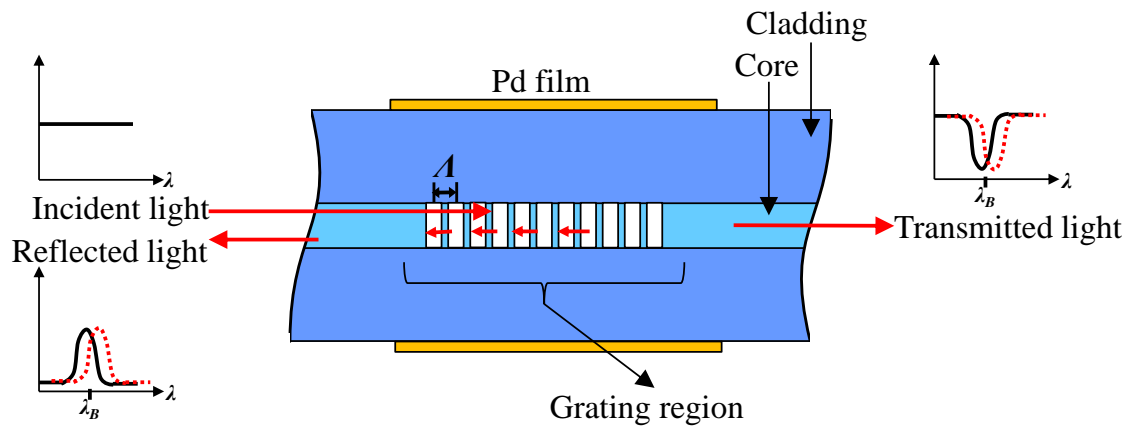


**Figure 2.13- Fibre Bragg gratings (FBG) based H<sub>2</sub> sensor. Fresnel reflected Bragg wavelength,  $\lambda_B$  shifts as the palladium hydride expands and changes the periodicity.**

Sutapan *et al* in 1999 [85] was the first to propose a grating based hydrogen sensor where the authors etched a 2-3cm grating region on single mode fibre and coated it with 560nm thick palladium. A fibre optic spectrometer in the wavelength range 800 to 1000nm was used to interrogate the sensor head. It was found to have a sensitivity of  $1.95 \times 10^{-2}$  nm/% vol H<sub>2</sub> and detected hydrogen in the range 0.3% to

1.8%  $H_2$  in  $N_2$ . For hydrogen concentrations higher than 1.8%, the palladium film peeled off. Multiple distinct FBGs with different Bragg wavelengths were used on one fibre piece so that the sensor could be multiplexed.

Maier *et al* [24] demonstrated 10ppm sensitivity where two 6.5mm long FBGs were used in sequence and a 1550nm broadband source used to interrogate the sequence in reflection. The first FBG was a strain sensor attached co-axially to a semi-circular palladium sensor tube that was 75mm long and 300 $\mu$ m thick. A hydrogen induced elongation of the tube of 0.0255 $\mu$ m for 10ppm  $H_2$  in  $N_2$  at 20°C was recorded with corresponding Bragg wavelength shifts of 0.7pm/ppm. The second FBG was a temperature monitoring sensor. The response times were long, ~16 days to reach 95% of signal saturation for 833ppm  $H_2$  in  $N_2$  due to bulk Pd reactions and slow diffusion rate constants. The thickness was chosen to provide good mechanical robustness and stability. It was also observed that  $H_2$  in  $N_2$  led to faster response times than  $H_2$  in air since the latter may have oxidised the Pd surface and blocked the sites for  $H_2$  adsorption. The recovery of the sensor in air (with 20%  $O_2$ ) took ~7 days whereas  $H_2$  removal in dry  $N_2$  failed. The presence of oxygen aided fast recovery of the sensor.

Recently an interesting combination of techniques was developed by Wang *et al* [86] where the sensor was an in-line Mach-Zehnder interferometer (MZI) and FBG coated with a 40nm Pd film. A schematic diagram of the sensor head is shown in Figure 2.14. An open air cavity of length 40 $\mu$ m was cut near a SMF core-cladding interface using a femto-second laser. Light from the core was split into two beams,  $I_{in1}$  and  $I_{in2}$ . One beam,  $I_{in2}$  travels through the core unaffected and the second beam,  $I_{in1}$  travels through the air cavity. When the beams are recombined at the end of the cavity, the beams  $I_{out1}$  and  $I_{out2}$  interfere from the phase difference induced by the refractive index mismatch between core and air cavity. The air cavity is followed by an 8mm FBG. When exposed to hydrogen, the palladium underwent volume expansion and the transmission spectrum showed changes in the resonant Bragg wavelength and the amplitude of the interference dip from the MZI. The sensor was used to demonstrate simultaneous detection of hydrogen in the range 0 to 8%  $H_2$  in air to eliminate temperature cross sensitivity. The hydrogen detection sensitivity was limited by the resolution of the optical spectrum analyser to 0.14%  $H_2$  in air.

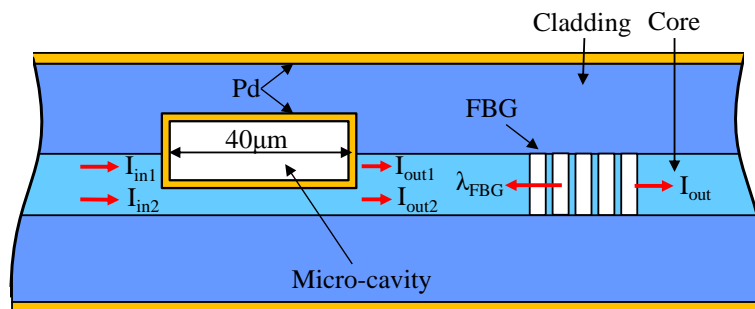


**Figure 2.14-** Schematic of the sensor head combining an in-line Mach-Zehnder interferometer (MZI) and FBG coated with Pd film. Taken from [86].

Long Period Gratings (LPGs) have a longer grating period in the range 100 $\mu\text{m}$  to 1mm (several times the light wavelength in the fibre) and promote coupling between the fundamental core mode with the multiple cladding modes propagating in the same direction [84]. This is shown in the schematic diagram in Figure 2.15. Light is coupled effectively under the phase matching condition given by equation (2.9) [84]:

$$\lambda_i = [n_{eff\_core}(\lambda) - n_{eff\_clad}^i(\lambda)]\Lambda \quad (2.9)$$

Where,  $\lambda_i$  is the  $i$ th cladding mode resonance wavelength,  $n_{eff\_core}$  and  $n_{eff\_clad}^i$  is the effective refractive index of the core and the  $i$ th cladding mode respectively and dependent on the light wavelength,  $\lambda$ . Since the cladding modes are rapidly attenuating, the transmitted spectrum from LPGs contains several minima instead of one big dip in the FBG transmission spectrum. The coupling of cladding modes is sensitive to changes in the refractive index of the surrounding medium in addition to temperature and strain. A LPG with a coating of palladium could promote the coupling of cladding modes to evanescent waves and surface plasmon waves and hence detect hydrogen [87].

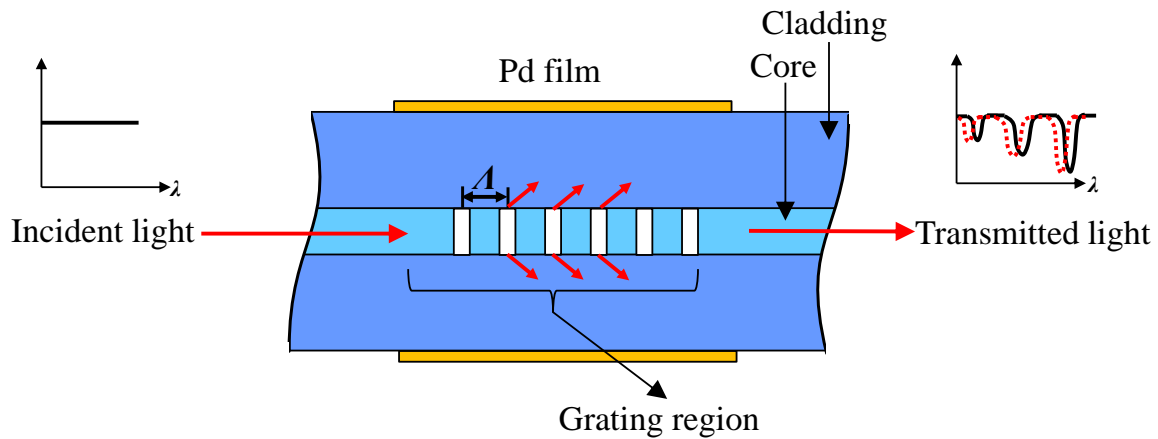


**Figure 2.15- Long period grating (LPG) based  $\text{H}_2$  sensor. Coupling of the fundamental core mode to cladding modes results in attenuation bands that shift when the Pd absorbs hydrogen and expands.**

Trouillet *et al* [87] first described a LPG based hydrogen sensor and compared its performance to an FBG. A FBG with a period of 0.5 $\mu\text{m}$  was written on one side of a fibre and coated with a 50nm thick Pd film using a 3cm length mask. It was able to detect a wavelength shift in the resonant wavelength (1550nm) as small as 14 pm for 4%  $\text{H}_2$  in  $\text{N}_2$  at room temperature. A fibre with an LPG with period between 200 and 700 $\mu\text{m}$  detected wavelength shifts of -5nm and -7nm in the two wavelength resonance peaks (1300nm and 1600nm) towards low wavelength for the same concentration. The authors found that the LPG was 500 times more sensitive than FBGs. The sensor response time and the stability were not reported.

Maier *et al* [14] reported a 40nm thick palladium film deposited on a LPG with a period of 450 $\mu\text{m}$  and 5cm in length. A superluminescent diode (SLD) at centre wavelength 1480nm was used to

illuminate the sensing region and the transmission spectrum recorded using an OSA. The authors were able to detect a wavelength shift of 9pm of the LPG spectrum in 10-20s at 75°C, which corresponded to a concentration of 625ppm H<sub>2</sub> in N<sub>2</sub>. However, the sensor's response was limited by cross-sensitivity to temperature, 1.4pm/°C. The authors measured this for 1% H<sub>2</sub> in N<sub>2</sub> in the temperature range, 26-75°C.

### 2.3.6 Other

Delepine-Lesoille *et al* [88] from the French National Radioactive Waste Management Agency developed a novel hydrogen sensor head for long term hydrogen level monitoring without the use of a palladium sensing material. It is based on Brillouin frequency variation with hydrogen diffusion and was inspired by the use of hydrogen loaded fibres to enhance photosensitivity before writing FBGs.

Brillouin scattering originates from the interaction between an electromagnetic wave and an acoustic wave (phonons). It is an inelastic scattering and the incident photon may lose energy (Stokes process) or gain energy (anti-Stokes process). The shift in the incident photon energy is the Brillouin shift in frequency and given by equation (2.10). It is equal to the energy released/absorbed by the phonon.

$$\nu_B = \frac{2n_{eff}V_A}{\lambda_0} \quad (2.10)$$

Where,  $n_{eff}$  is the effective refractive index of the optical mode,  $V_A$  is the sound velocity in silica and  $\lambda_0$  is the operating wavelength. The refractive index of the silica is modified as hydrogen diffuses in to form an OH species [89]. The Brillouin frequency is also dependent on temperature and strain, which necessitated the need for a reference fibre coated in carbon to eliminate hydrogen diffusion in harsh conditions such as high temperature and pressure.

The authors used two G652 single mode optical fibres and a Brillouin interrogation device with a spectral resolution of 1MHz and operating wavelength of 1550nm. The two fibres (one coated in carbon and the other without) were kept in a hydrogen chamber at 150bar pressure and 25°C and taken out periodically to make measurements. However, the hydrogen diffusion was slow and took 20hours for 1% hydrogen to diffuse into the core. A large response and recovery time makes this technique unsuitable for this project. With increasing refractive index of the core with increasing hydrogen concentration the Brillouin frequency,  $\nu_B$  shifted to higher frequencies and the shift was approximately linear. The hydrogen loading and unloading was a reversible process. The sensitivity of this technique was limited by the Brillouin device spectral resolution to 5% H<sub>2</sub>.

Recently, the group has reported further research [90] into developing optical fibres with palladium particles embedded into the silica cladding with the aim of preventing palladium film deterioration and to allow long length distributed gas sensing. PdO and SiO<sub>2</sub> powders were mixed and used in the

preform cladding material. The preform is heated under specific conditions and low pressure to control the reduction state of PdO to form metallic Pd particles into the Si cladding. They were successful in drawing multimode graded index fibres with a core diameter of 6  $\mu\text{m}$  and single mode PCF fibres with a core diameter of 8  $\mu\text{m}$  and air hole diameter of 2  $\mu\text{m}$ . The average distance between the core and the palladium particles were measured to be  $\sim 25 \mu\text{m}$  on average. As with the previous approach, the authors had issues with long response times for hydrogen loading and recovery.

### 2.4 Conclusion

Palladium reacts with hydrogen to form a palladium hydride with the composition  $\text{PdH}_x$ . The lattice structure of the palladium hydride expands to accommodate the hydrogen atoms. The volume of free electrons decreases which causes both the real and imaginary parts of the complex refractive index of the palladium coating to decrease as well and can be observed as a decrease in reflectivity. The palladium hydride can exist in two phases depending on the hydrogen content. Hysteresis in the region of co-existence of two phases ( $\alpha$  and  $\beta$ ) causes stress on the lattice structure, which is visible in the form of cracks or peeling. The cracking of the film may be reduced in two ways – choosing an optimum thickness of the palladium film between 25 and 100 nm (see Chapter 3 for the determination of the thickness) or using alloys of palladium. The palladium layer is generally used with an adhesive Ni layer and a capping protective layer (typically Pt) to eliminate carbon poisoning, oxidation or contamination of the surface.

The palladium-hydrogen reaction creates changes in refractive index, electrical, physical and mechanical properties. A transducer is used to transform these changes into an electrical signal. There are several existing hydrogen detection technologies such as semi-conducting metal oxide sensors, work-function based sensors, electrochemical cells, catalytic sensors, spectroscopic methods, optical fibre based sensors etc. All these sensor techniques, apart from optical fibre based sensors, require the passage of electricity to the sensor head, which could ignite a spark and cause an explosion. A fibre optic based hydrogen sensor is desirable for application in an explosive environment since the sensor network is based on dielectric materials and contains no energy storing elements that could lead to ignition. Also optical fibres are relatively unaffected by electromagnetic interference and the sensor heads are small in size and can be embedded for remote operation.

Fibre optic based hydrogen sensors are commonly coated with a palladium coating. The sensors reported in literature are summarised in Table 2-4 and are grouped based on their method of operation.

Intensity based sensors measure the change in transmitted/reflected intensity signal. The micromirror configuration with the tip of the fibre coated in palladium has a simple and robust design but offers a limited area for palladium deposition. Tapering, etching of fibres and exposing the core to access

evanescent waves and surface plasmons may cause the fibre to weaken, which would eventually compromise the longevity of the sensor. This is not an ideal solution in the search of a hydrogen sensor that would provide long term stability. However, these techniques are sensitive, respond fast and can be multiplexed along the length of the fibre. Although, interferometric techniques have demonstrated very low detection limits of hydrogen concentration, they display cross-sensitivity to temperature and strain that could lead to stability issues. Grating based sensors have similarly proven low detection limits and usefulness in multiplexing but display cross-sensitivity to temperature and strain effects on fibres. Gratings can also be used as a wavelength filter.

Judging the pros and cons of these methods, the micromirror based fibre optic technique has been chosen for the investigation of long-term stability of hydrogen sensors owing to its simplistic design that will be sensitive, robust, and can be self-referenced with infrequent need for calibration. It has the most potential to satisfy the design criteria outlined in Table 1-1.

**Table 2-4 – Summary of fibre optic hydrogen detection techniques based on intensity changes, interferometers and fibre gratings. This table is adapted from Silva *et al* review in 2012 [7] and updated with recent research techniques**

| Sensor details  | Limit of detection  | Response time   | Ref, Year                |
|---|---------------------|-----------------|--------------------------|
| <i>INTENSITY BASED: Pd refractive index decrease → decrease in Fresnel reflection</i> |                     |                 |                          |
| Micromirror on MMF<br>Coating: 10nm Pd  | 0.2% <sup>a</sup>   | 10min           | Butler, 1991 [62]        |
| Micromirror on GRIN lens<br>Coating: 10nm Ni /150nm PdAg / 25nm Pt                    | 50ppm <sup>b</sup>  | NS <sup>*</sup> | Butler, 1996 [29]        |
| Micromirror on MMF<br>Coating: 13nm Pd  | 1% <sup>a</sup>     | <5s             | Bevenot, 2000 [64]       |
| Evanescent wave on 1.5cm MMF core<br>Coating: 10nm Pd                                 | 0.2% <sup>a</sup>   | 30-20s          | Tabib Azar, 1999 [65]    |
| Tapered SMF and evanescent wave<br>Coating: 15mm long, 250µm φ, 12nm Pd               | 1.8% <sup>a</sup>   | <100s           | Villatoro, 2001 [66]     |
| Nano-tapered SMF and evanescent wave<br>Coating: 2mm long, 1300µm φ, 4nm Pd           | 500ppm <sup>a</sup> | 10s (4%)        | Villatoro, 2005 [67, 68] |
| Heterostructure MMF/SMF/MMF<br>Coating: 5mm SMF, 10nm PdAu                            | 0.2% <sup>a</sup>   | 15s (4%)        | Luna-Moreno, 2007 [69]   |
| Heterostructure MMF/SMF/MMF<br>Coating: alternate layers 1.4nm Pd and 0.6nm Au        | 0.8% <sup>a</sup>   | 6s (4%)         | Hernandez, 2009 [70]     |
| Side-polished SMF and evanescent wave<br>Coating: 40nm Pd                             | 4% <sup>a</sup>     | 100s            | Kim, 2007 [71]           |
| Surface Plasmon Resonance (SPR)   | 0.8% <sup>a</sup>   | 300-3s          | Bevenot, 2002 [75]       |

| Sensor details   | Limit of detection  | Response time       | Ref, Year                       |
|--|---------------------|---------------------|---------------------------------|
| Coating: 15mm MMF core 12nm Pd<br>Surface Plasmon Resonance (SPR)<br>Coating: 0.5cm MMF core 35nm Au /<br>180nm SiO <sub>2</sub> / 3.75nm Pd | 0.5% <sup>c</sup>   | 15s (2%)            | Perrotton, 2013 [76]            |
| <i>INTERFEROMETER BASED: Pd expansion → strain → increase in optical path length/ reduction in refractive index</i>                          |                     |                     |                                 |
| Mach-Zehnder interferometer<br>Coating: 10nm Ti / 1μm Pd   | 20ppb <sup>a</sup>  | <30s                | Butler, 1988 [80]               |
| Extrinsic Fabry-Perot SMF/50μm gap/MMF<br>Coating: 2μm Pd  | 32ppm <sup>a</sup>  | 5s (0.5%)           | Zeakes, 1994 [81]               |
| Photonic crystal fibre(PCF) and SMF<br>interferometer<br>Coating: 1mm of PCF tip in 50nm Pd  | 1% <sup>b</sup>     | 15s                 | Zhou, 2014 [83]                 |
| <i>FIBRE GRATING BASED: Pd expansion → strain → shift in transmission/reflection spectrum</i>  |                     |                     |                                 |
| 2.3cm Fibre Bragg Grating (FBG) on SMF<br>Coating: 560nm Pd  | 0.3% <sup>a</sup>   | NS <sup>*</sup>     | Sutapan, 1999 [85]              |
| FBGs in sequence<br>Coating: 6.5mm FBG, 75 mm Pd half-tube<br>and 300μm φ  | 10ppm <sup>a</sup>  | 16 days<br>(833ppm) | Maier, 2006 [24]                |
| Mach-Zehnder interferometer and FBG<br>Coating: 40μm air cavity and 8mm FBG in<br>40nm Pd  | 0.14% <sup>d</sup>  | NS <sup>*</sup>     | Wang, 2014 [86]                 |
| FBG and LPG<br>Coating: 50nm Pd  | 4% <sup>a</sup>     | 2 min               | Trouillet, 2006 [87]            |
| LPG, periodicity 450μm, 5cm long<br>Coating: 40nm Pd   | 625ppm <sup>a</sup> | 10-20s              | Maier, 2007 [14]                |
| OTHER  |                     |                     |                                 |
| Brillouin frequency shift of single mode G652<br>fibres in H <sub>2</sub>  | 5%                  | 30hours             | Delepine-Lesoille,<br>2012 [88] |
| Palladium particles embedded into silica<br>cladding   | NS <sup>*</sup>     | 60hours             | Leparmentier, 2014<br>[90]      |

*a* in N<sub>2</sub>; *b* in oil; *c* in Ar; *d* in Air; NS<sup>\*</sup> Not stated



## 2.5 References

- [1] Graham, T. (1867), "On the absorption and dialytic separation of gases by colloid septa", *Journal of the Chemical Society*, vol. 20, pp. 235-288.
- [2] Lide, D. R. (2013), *CRC Handbook of Chemistry and Physics*, 94th ed, CRC Press, Florida, US.
- [3] Lewis, F. A. (1967), *The palladium-hydrogen System*, 1st ed, Academic Press Inc, London.
- [4] Wicke, E., Brodowsky, H. and Züchner, H. (1978), "Hydrogen in palladium and palladium alloys", in Alefeld, G. and Völkl, J. (eds.) *Hydrogen in Metals II*, Topics in Applied Physics Volume 29 ed, Springer, pp. 75-155.
- [5] Flanagan, T. B. and Oates, W. A. (1991), "The palladium-hydrogen system", *Annual Review of Materials Science*, vol. 21, no. 1, pp. 269-304.
- [6] Kay, B. D., Peden, C. H. F. and Goodman, D. W. (1986), "Kinetics of hydrogen absorption by Pd(110)", *Physical Review B*, vol. 34, no. 2, pp. 817-822.
- [7] Silva, S. F., Coelho, L., Frazão, O., Santos, J. L. and Malcata, F. X. (2012), "A review of palladium-based fiber-optic sensors for molecular hydrogen detection", *IEEE Sensors Journal*, vol. 12, no. 1, pp. 93-102.
- [8] Frazier, G. A. and Glosser, R. (1980), "Characterization of thin films of the palladium-hydrogen system", *Journal of The Less-Common Metals*, vol. 74, no. 1, pp. 89-96.
- [9] Butler, M. A. (1984), "Optical Fiber Hydrogen Sensor", *Applied Physics Letters*, vol. 45, no. 10, pp. 1007-1009.
- [10] Smith, J. M., Van Ness, H. C. and Abbott, M. M. (2004), *Introduction to Chemical Engineering Thermodynamics*, 7th ed, McGraw-Hill, NY, US.
- [11] Maeland, A. and Flangan, T. (1966), "The hydrogen-palladium system", *Platinum Metals Review*, vol. 10, no. 1, pp. 20-23.
- [12] Worsham Jr, J., Wilkinson, M. and Shull, C. (1957), "Neutron-diffraction observations on the palladium-hydrogen and palladium-deuterium systems", *Journal of Physics and Chemistry of Solids*, vol. 3, no. 3, pp. 303-310.
- [13] Lacher, J. R. (1937), "A theoretical formula for the solubility of hydrogen in palladium", *Proceedings of the Royal Society of London. Series A, Mathematical and Physical Sciences*, vol. 161, pp. 525-545.
- [14] Maier, R. R. J., Jones, B. J. S., Barton, J. S., McCulloch, S., Allsop, T., Jones, J. D. C. and Bennion, I. (2007), "Fibre optics in palladium-based hydrogen-sensing", *Journal of Optics A: Pure and Applied Optics*, vol. 9, no. 6, pp. S45-S59.
- [15] Zalvidea, D., Díez, A., Cruz, J. L. and Andrés, M. V. (2006), "Hydrogen sensor based on a palladium-coated fibre-taper with improved time-response", *Sensors and Actuators, B: Chemical*, vol. 114, no. 1, pp. 268-274.
- [16] Wright, P. (1950), "The effect of occluded hydrogen on the electrical resistance of palladium", *Proceedings of the Physical Society*, vol. 63, no. 7, pp. 727.
- [17] Wicke, E. and Blaurock, J. (1986), "New experiments on and interpretations of hysteresis effects of Pd-D<sub>2</sub> and Pd-H<sub>2</sub>", *Journal of The Less-Common Metals*, vol. 130, pp. 351-363.

- [18] Ubbelohde, A. (1937), "Some properties of the metallic state. I. Metallic hydrogen and its alloys", *Proceedings of the Royal Society of London. Series A-Mathematical and Physical Sciences*, vol. 159, no. 897, pp. 295-306.
- [19] Lewis, F. A. (1995), "The palladium-hydrogen system: structures near phase transition and critical points", *International Journal of Hydrogen Energy*, vol. 20, no. 7, pp. 587-592.
- [20] Frazier, G. A. and Glosser, R. (1982), "Hydrogen induced changes in the electronic structure of the palladium-hydrogen system as measured by thermoreflectance", *Solid State Communications*, vol. 41, no. 3, pp. 245-250.
- [21] Cheng, Y. T., Li, Y., Lisi, D. and Wang, W. M. (1996), "Preparation and characterization of Pd/Ni thin films for hydrogen sensing", *Sensors and Actuators B-Chemical*, vol. 30, no. 1, pp. 11-16.
- [22] Noh, J. S., Lee, J. M. and Lee, W. (2011), "Low-dimensional palladium nanostructures for fast and reliable hydrogen gas detection", *Sensors (Basel)*, vol. 11, no. 1, pp. 825-851.
- [23] Fortunato, G., Bearzotti, A., Caliendo, C. and D'Amico, A. (1989), "Hydrogen sensitivity of Pd/SiO<sub>2</sub>/Si structure: a correlation with the hydrogen-induced modifications on optical and transport properties of  $\alpha$ -phase Pd films", *Sensors and Actuators*, vol. 16, no. 1-2, pp. 43-54.
- [24] Maier, R. R. J., Barton, J. S., Jones, J. D. C., McCulloch, S., Jones, B. J. S. and Burnell, G. (2006), "Palladium-based hydrogen sensing for monitoring of ageing materials", *Measurement Science and Technology*, vol. 17, no. 5, pp. 1118-1123.
- [25] Palik, E. D. (1998), *Handbook of Optical Constants of Solids*, 3rd ed, Academic press, NY, US.
- [26] Musket, R. G. (1976), "Effects of contamination on the interaction of hydrogen gas with palladium: A review", *Journal of The Less-Common Metals*, vol. 45, no. 2, pp. 173-183.
- [27] Butler, M. A. and Buss, R. J. (1993), "Kinetics of the micromirror chemical sensor", *Sensors and Actuators B: Chemical*, vol. 11, no. 1-3, pp. 161-166.
- [28] Gao, H., Lin, Y. S., Li, Y. and Zhang, B. (2004), "Chemical stability and its improvement of palladium-based metallic membranes", *Industrial and Engineering Chemistry Research*, vol. 43, no. 22, pp. 6920-6930.
- [29] Butler, M. A., Sanchez, R. and Dulleck, G. (1996), *Fiber Optic Hydrogen Sensor*, Sandia Reports SAND96-113, Sandia National Laboratories, Albuquerque, US.
- [30] Ohira, K., Sakamoto, Y. and Flanagan, T. B. (1996), "Thermodynamic properties for solution of hydrogen in Pd-Ag-Ni ternary alloys", *Journal of Alloys and Compounds*, vol. 236, no. 1-2, pp. 42-49.
- [31] Yun, S. and Ted Oyama, S. (2011), "Correlations in palladium membranes for hydrogen separation: A review", *Journal of Membrane Science*, vol. 375, no. 1-2, pp. 28-45.
- [32] Knapton, A. G. (1977), "Palladium alloys for hydrogen diffusion membranes", *Platinum Metals Review*, vol. 21, no. 2, pp. 44-50.
- [33] Pundt, A., Sachs, C., Winter, M., Reetz, M. T., Fritsch, D. and Kirchheim, R. (1999), "Hydrogen sorption in elastically soft stabilized Pd-clusters", *Journal of Alloys and Compounds*, vol. 293, pp. 480-483.
- [34] The Institution of Gas Engineers (1998), *Dealing with reported gas escapes*, IGE/SR/20 Edition 2, Institution of Gas Engineers and Managers, Kegworth, UK.

- [35] British Standards Institution (2007), *Explosive atmospheres - Part 28: Protection of equipment and transmission systems using optical radiation*, BSI EN 60079-28:2007, Cenelec, UK.
- [36] Hübert, T., Boon-Brett, L., Black, G. and Banach, U. (2011), "Hydrogen sensors - a review", *Sensors and Actuators, B: Chemical*, vol. 157, no. 2, pp. 329-352.
- [37] SIRA Technology Limited (2005), *Gas Detector Selection and Calibration Guide*, 1st ed, Witherby & Company Ltd, Livingston, UK.
- [38] Jardine, A. P. (2000), *Hydrogen sensors for hydrogen fuel cell applications*, , Darnell Group Inc., Valencia, CA.
- [39] Xu, T., Zach, M. P., Xiao, Z. L., Rosenmann, D., Welp, U., Kwok, W. K. and Crabtree, G. W. (2005), "Self-assembled monolayer-enhanced hydrogen sensing with ultrathin palladium films", *Applied Physics Letters*, vol. 86, no. 20, pp. 1-3.
- [40] Lundström, I., Shivaraman, S., Svensson, C. and Lundkvist, L. (1975), "A hydrogen-sensitive MOS field-effect transistor", *Applied Physics Letters*, vol. 26, no. 2, pp. 55-57.
- [41] Ito, K. (1979), "Hydrogen-sensitive Schottky barrier diodes", *Surface Science*, vol. 86, no. 0, pp. 345-352.
- [42] Abadi, M. S. H., Gholizadeh, M. and Salehi, A. (2009), "Modeling and simulation of a MOSFET gas sensor with platinum gate for hydrogen gas detection", *Sensors and Actuators B: Chemical*, vol. 141, no. 1, pp. 1-6.
- [43] Dura, H. G., Schöneberg, U., Mokwa, W., Hostika, B. J. and Vogt, H. (1992), "Performance of hydrogen-sensitive MOS capacitances with integrated on-chip signal conditioning", *Sensors and Actuators: B. Chemical*, vol. 6, no. 1-3, pp. 162-164.
- [44] Kumar, R. V. and Fray, D. J. (1988), "Development of solid-state hydrogen sensors", *Sensors and Actuators*, vol. 15, no. 2, pp. 185-191.
- [45] Korotcenkov, G., Han, S. D. and Stetter, J. R. (2009), "Review of electrochemical hydrogen sensors", *Chemical reviews*, vol. 109, no. 3, pp. 1402-1433.
- [46] Christofides, C. and Mandelis, A. (1990), "Solid-state sensors for trace hydrogen gas detection", *Journal of Applied Physics*, vol. 68, no. 6, pp. R1-R30.
- [47] Mandelis, A. and Christofides, C. (1990), "Photopyroelectric (P2E) sensor for trace hydrogen gas detection", *Sensors and Actuators: B. Chemical*, vol. 2, no. 1, pp. 79-87.
- [48] Miura, N., Minamoto, H., Sakai, G. and Yamazoe, N. (1991), "New-type calorimetric gas sensor using temperature characteristics of piezoelectric quartz crystal fitted with noble metal catalyst film", *Sensors and Actuators: B. Chemical*, vol. 5, no. 1-4, pp. 211-217.
- [49] Moseley, P. T. (1997), "Solid state gas sensors", *Measurement Science and Technology*, vol. 8, no. 3, pp. 223-237.
- [50] Bucur, R. V., Mecea, V. and Flanagan, T. B. (1976), "The kinetics of hydrogen (deuterium) sorption by thin palladium layers studied with a piezoelectric quartz crystal microbalance", *Surface Science*, vol. 54, no. 2, pp. 477-488.
- [51] Ho, C., Itamura, M., Kelley, M., Hughes, R. (2001), *Review of chemical sensors for in-situ monitoring volatile contaminants*, SAND2001-0643, Sandia National Laboratories, Albuquerque, US.

- [52] Yamanaka, K., Nakaso, N., Sim, D. and Fukiura, T. (2009), "Principle and application of ball surface acoustic wave (SAW) sensor", *Acoustical Science and Technology*, vol. 30, no. 1, pp. 2-6.
- [53] Wheeler, M. D., Newman, S. M., Orr-Ewing, A. J. and Ashfold, M. N. R. (1998), "Cavity ring-down spectroscopy", *Journal of the Chemical Society - Faraday Transactions*, vol. 94, no. 3, pp. 337-351.
- [54] Waechter, H., Litman, J., Cheung, A. H., Barnes, J. A. and Looock, H. -. (2010), "Chemical sensing using fiber cavity ring-down spectroscopy", *Sensors*, vol. 10, no. 3, pp. 1716-1742.
- [55] Vallance, C. (2005), "Innovations in cavity ringdown spectroscopy", *New Journal of Chemistry*, vol. 29, no. 7, pp. 867-874.
- [56] Mazurenka, M., Orr-Ewing, A. J., Peverall, R. and Ritchie, G. A. D. (2005), "Cavity ring-down and cavity enhanced spectroscopy using diode lasers", *Annual Reports on the Progress of Chemistry - Section C*, vol. 101, pp. 100-142.
- [57] Kasyutich, V. L., Martin, P. A. and Holdsworth, R. J. (2006), "Effect of broadband amplified spontaneous emission on absorption measurements in phase-shift off-axis cavity enhanced absorption spectroscopy", *Chemical Physics Letters*, vol. 430, no. 4-6, pp. 429-434.
- [58] Adlergolden, S. M., Goldstein, N., Bien, F., Matthew, M. W., Gersh, M. E., Cheng, W. K. and Adams, F. W. (1992), "Laser Raman sensor for measurement of trace-hydrogen gas", *Applied Optics*, vol. 31, no. 6, pp. 831-835.
- [59] Carlson, R. W. and Fenner, W. R. (1972), "Absolute Raman scattering cross-section of molecular-hydrogen", *Astrophysical Journal*, vol. 178, no. 2, pp. 551-556.
- [60] Oki, Y., Kawada, N., Abe, Y. and Maeda, M. (1999), "Nonlinear Raman spectroscopy without tunable laser for sensitive gas detection in the atmosphere", *Optics Communications*, vol. 161, no. 1-3, pp. 57-62.
- [61] Ingle, J. D. and Crouch, S. R. (1988), *Spectrochemical Analysis*, 1st ed, Prentice-Hall, Inc., New Jersey, USA.
- [62] Butler, M. A. (1991), "Fiber optic sensor for hydrogen concentrations near the explosive limit", *Journal of the Electrochemical Society*, vol. 138, no. 9, pp. L46-L47.
- [63] Michael A., B. (1994), "Micromirror optical-fiber hydrogen sensor", *Sensors and Actuators B: Chemical*, vol. 22, no. 2, pp. 155-163.
- [64] Bévenot, X., Trouillet, A., Veillas, C., Gagnaire, H. and Clément, M. (2000), "Hydrogen leak detection using an optical fibre sensor for aerospace applications", *Sensors and Actuators B: Chemical*, vol. 67, no. 1-2, pp. 57-67.
- [65] Tabib-Azar, M., Sutapun, B., Petrick, R. and Kazemi, A. (1999), "Highly sensitive hydrogen sensors using palladium coated fiber optics with exposed cores and evanescent field interactions", *Sensors and Actuators, B: Chemical*, vol. 56, no. 1, pp. 158-163.
- [66] Villatoro, J., Díez, A., Cruz, J. L. and Andrés, M. V. (2001), "Highly sensitive optical hydrogen sensor using circular Pd-coated singlemode tapered fibre", *Electronics Letters*, vol. 37, no. 16, pp. 1011-1012.
- [67] Villatoro, J., Luna-Moreno, D. and Monzón-Hernández, D. (2005), "Optical fiber hydrogen sensor for concentrations below the lower explosive limit", *Sensors and Actuators B: Chemical*, vol. 110, no. 1, pp. 23-27.
- [68] Villatoro, J. and Monzón-Hernández, D. (2005), "Fast detection of hydrogen with nano fiber tapers coated with ultra thin palladium layers", *Optics Express*, vol. 13, no. 13, pp. 5087-5092.

- [69] Luna-Moreno, D., Monzón-Hernández, D., Villatoro, J. and Badenes, G. (2007), "Optical fiber hydrogen sensor based on core diameter mismatch and annealed Pd-Au thin films", *Sensors and Actuators, B: Chemical*, vol. 125, no. 1, pp. 66-71.
- [70] Monzón-Hernández, D., Luna-Moreno, D. and Martínez-Escobar, D. (2009), "Fast response fiber optic hydrogen sensor based on palladium and gold nano-layers", *Sensors and Actuators, B: Chemical*, vol. 136, no. 2, pp. 562-566.
- [71] Kim, K. T., Song, H. S., Mah, J. P., Hong, K. B., Im, K., Baik, S. and Yoon, Y. (2007), "Hydrogen sensor based on palladium coated side-polished single-mode fiber", *IEEE Sensors Journal*, vol. 7, no. 12, pp. 1767-1771.
- [72] Sharma, A. K., Jha, R. and Gupta, B. D. (2007), "Fiber-optic sensors based on surface plasmon resonance: A comprehensive review", *IEEE Sensors Journal*, vol. 7, no. 8, pp. 1118-1129.
- [73] Chadwick, B. and Gal, M. (1993), "Enhanced optical detection of hydrogen using the excitation of surface plasmons in palladium", *Applied Surface Science*, vol. 68, no. 1, pp. 135-138.
- [74] Liedberg, B., Nylander, C. and Lunström, I. (1983), "Surface plasmon resonance for gas detection and biosensing", *Sensors and Actuators*, vol. 4, no. C, pp. 299-304.
- [75] Bévenot, X., Trouillet, A., Veillas, C., Gagnaire, H. and Clément, M. (2002), "Surface plasmon resonance hydrogen sensor using an optical fibre", *Measurement Science and Technology*, vol. 13, no. 1, pp. 118-124.
- [76] Perrotton, C., Westerwaal, R. J., Javahiraly, N., Slaman, M., Schreuders, H., Dam, B. and Meyrueis, P. (2013), "A reliable, sensitive and fast optical fiber hydrogen sensor based on surface plasmon resonance", *Optics Express*, vol. 21, no. 1, pp. 382-390.
- [77] Verma, R. K., Sharma, A. K. and Gupta, B. D. (2008), "Surface plasmon resonance based tapered fiber optic sensor with different taper profiles", *Optics Communications*, vol. 281, no. 6, pp. 1486-1491.
- [78] Banerjee, A., Mukherjee, S., Verma, R. K., Jana, B., Khan, T. K., Chakroborty, M., Das, R., Biswas, S., Saxena, A., Singh, V., Hallen, R. M., Rajput, R. S., Tewari, P., Kumar, S., Saxena, V., Ghosh, A. K., John, J. and Gupta-Bhaya, P. (2007), "Fiber optic sensing of liquid refractive index", *Sensors and Actuators B: Chemical*, vol. 123, no. 1, pp. 594-605.
- [79] Díez, A., Andrés, M. V. and Cruz, J. L. (2001), "In-line fiber-optic sensors based on the excitation of surface plasma modes in metal-coated tapered fibers", *Sensors and Actuators, B: Chemical*, vol. 73, no. 2-3, pp. 95-99.
- [80] Butler, M. A. and Ginley, D. S. (1988), "Hydrogen sensing with palladium-coated optical fibers", *Journal of Applied Physics*, vol. 64, no. 7, pp. 3706-3712.
- [81] Zeakes, J. S., Murphy, K. A., Elshabini-Riad, A. and Claus, R. O. (1994), "Modified extrinsic Fabry-Perot interferometric Hydrogen gas sensor", *IEEE LEOS Annual Meeting - Proceedings*, Vol. 2, pp. 235.
- [82] Maciak, E. and Opilski, Z. (2007), "Transition metal oxides covered Pd film for optical H<sub>2</sub> gas detection", *Thin Solid Films*, vol. 515, no. 23, pp. 8351-8355.
- [83] Zhou, F., Qiu, S. J., Luo, W., Xu, F. and Lu, Y. -. (2014), "An all-fiber reflective hydrogen sensor based on a photonic crystal fiber in-line interferometer", *IEEE Sensors Journal*, vol. 14, no. 4, pp. 1133-1136.
- [84] James, S. W. and Tatam, R. P. (2003), "Optical fibre long-period grating sensors: Characteristics and application", *Measurement Science and Technology*, vol. 14, no. 5, pp. R49-R61.

- [85] Sutapun, B., Tabib-Azar, M. and Kazemi, A. (1999), "Pd-coated elastooptic fiber optic Bragg grating sensors for multiplexed hydrogen sensing", *Sensors and Actuators, B: Chemical*, vol. 60, no. 1, pp. 27-34.
- [86] Wang, M., Wang, D. N., Yang, M., Cheng, J. and Li, J. (2014), "In-line Mach-Zehnder Interferometer and FBG with Pd film for simultaneous hydrogen and temperature detection", *Sensors and Actuators, B: Chemical*, vol. 202, pp. 893-896.
- [87] Trouillet, A., Marin, E. and Veillas, C. (2006), "Fibre gratings for hydrogen sensing", *Measurement Science and Technology*, vol. 17, no. 5, pp. 1124-1128.
- [88] Delepine-Lesoille, S., Bertrand, J., Lablonde, L. and Phéron, X. (2012), "Distributed hydrogen sensing with Brillouin scattering in optical fibers", *IEEE Photonics Technology Letters*, vol. 24, no. 17, pp. 1475-1477.
- [89] Canning, J. (2000), "Photosensitization and photostabilization of laser-induced index changes in optical fibers", *Optical Fiber Technology*, vol. 6, no. 3, pp. 275-289.
- [90] Leparmentier, S., Auguste, J. L., Humbert, G., Delaizir, G., Delepine Lesoille, S., Bertrand, J., Buschaert, S., Perisse, J. and Mace, J. R. (2014), "Palladium particles embedded into silica optical fibers for hydrogen gas detection", *In Proceedings of the SPIE Photonics Europe*, Vol. 9128, 2 May 2014, Bruxelles, Belgium.

# Chapter 3

## Experimental study of Pd film and instabilities

It has been discussed that palladium-hydride exhibits hysteretic properties during loading and unloading cycles of hydrogen due to lattice expansion and the exertion of additional strain and disorder. This can cause irreversible deformations that are manifested as cracks, pin-holes and peeling of the film. This can lead to reduced palladium reflectivity and thus deterioration in sensor performance. The thickness of the palladium film is also a factor that can contribute to surface delamination. In this chapter, the thickness of a palladium film and its dependency on reflectivity is modelled and the chosen optimum thickness discussed. Whilst the use of alloys can push the hysteresis effect to much higher concentrations of hydrogen, only palladium sensors were chosen for this study but with a hypothesis towards improving the sensor's long-term stability. It is expected that a larger sensor area would allow greater coverage for the palladium deposition, which can reduce the probability of catastrophic failure resulting from cracks and improve the predictability of the sensor's performance. The effects of using different sensing areas are investigated by completing a new statistical analysis.

### 3.1 Sensor coatings

#### 3.1.1 Pure palladium film thickness and reflectivity

In a micromirror sensor head, Figure 3.1a, palladium film is deposited at the tip of a fibre and light from the fibre is incident upon the film surface.

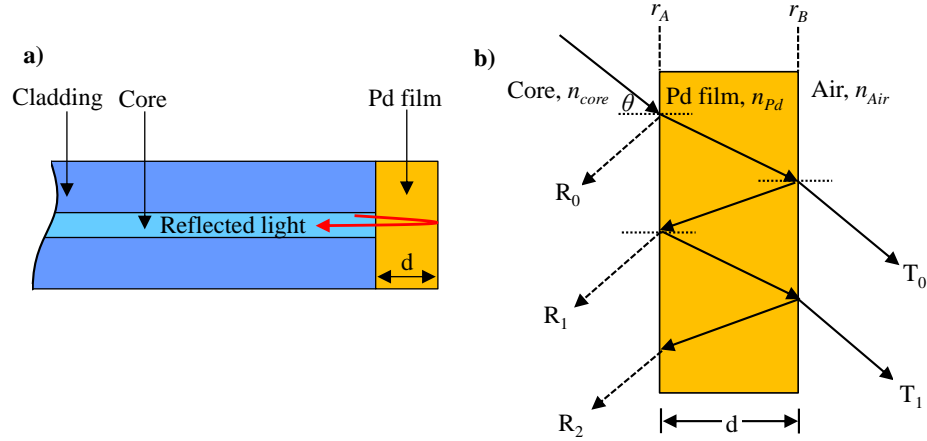


**Figure 3.1- a) Micromirror sensor head with a thin film of palladium deposited at the tip**  
**b) Thin film interference model used to model the reflectivity of palladium film [1].**

Suppose that the light reflects multiple times within the film and the thin-film interference model (as shown in Figure 3.1b) can be used to derive an equation for the reflectivity of the Pd film. The reflectivity,  $R_{Pd}$  is given by equation (3.1) [1].

$$R_{Pd} = \left| \frac{r_A + r_B e^{-2i\delta}}{1 + r_A r_B e^{-2i\delta}} \right|^2 \quad (3.1)$$

Where  $\delta$  is the phase shift and  $r$  is the reflection amplitude for light incident on an interface separating two media. Squares of the amplitudes give the intensity of the reflection at that interface, also known as the Fresnel reflection. Equation (3.1) is the final Fresnel reflection equation of a three layer system. The reflection amplitudes for the two layer system occurring at core/Pd and Pd/air interface are  $r_A$  and  $r_B$  respectively and shown in equations (3.2) and (3.3).

$$r_A = \frac{n_{core} - n_{Pd}}{n_{core} + n_{Pd}} \quad (3.2)$$

$$r_B = \frac{n_{Pd} - n_{Air}}{n_{Pd} + n_{Air}} \quad (3.3)$$



And  $n_{core}$  for a singlemode fibre core is 1.45 [2],  $n_{air}=1$  and  $n_{Pd}^*$  is the complex refractive index of palladium and has the form of equation (2.4), page 14.

The phase shift,  $\delta$  (for normal incidence) can be written as:

$$\delta = \frac{2\pi}{\lambda} \int_0^d n_{Pd}^*(x) dx \quad (3.4)$$

Where  $d$  is the thickness of the palladium film and  $\lambda$  is the wavelength of the incident light. This model also shows the dependency of the film's reflectance on the thickness of the palladium film. The relationship between reflectivity of the metal surface,  $R_{Pd}$ , and the thickness of the film,  $d$ , at 1550nm was modelled in MathCad (version 15, PTC softwares) when the real and imaginary refractive indices of palladium are:  $n_R = 2.95$  and  $n_I = 8.33$  respectively [3] to find the optimum thickness of the palladium film. The result is shown in Figure 3.2.

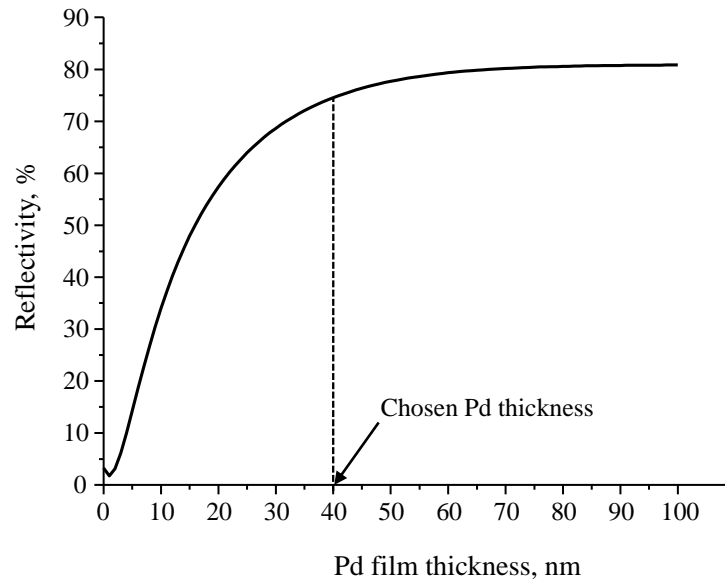


**Figure 3.2- Reflectivity of a palladium film deposited on the end of a singlemode fibre and held in air. The dashed line at 40nm marks the chosen thickness.**

Butler [4] experimentally determined the reflectivity of palladium films being deposited on a multimode fibre core using an 860nm LED and monitored the thickness using a quartz-crystal thickness monitor at 23°C. He obtained a curve shape similar to that shown in Figure 3.2. He concluded that the palladium film became optically thick after approximately 40nm. Films that are much thinner than 40nm are almost optically transparent since the light is able to reach the outer surface and respond to surface chemical reactions. For films thicker than 40nm, bulk chemical reactions determine the dynamics of the reflectivity and the reflectivity change plateaus as thickness increases.

However if the palladium film is too thin then the layer may not be continuously deposited and will produce inconsistent signals as Mandelis [5] found with a 5nm thin palladium film and Frazier [6] with a 25nm palladium film. Thin films also run the risk of saturating at low hydrogen concentrations [7]. Frazier [6] also reported that a palladium film thicker than 120nm stood a higher likelihood of peeling and delaminating. Chtanov and Gal [7] used a 40nm thick palladium film to test hydrogen concentration in the range 0.1% to 10% hydrogen in air.

The thickness chosen for this study was 40nm, based on past literature report that will provide a good compromise between response times, sensitivity and film adhesion.

### ***3.1.2 Adhesion of the palladium film***

Butler in 1994 [8] tested the hydrogen response from palladium films of different thicknesses from 10 to 80nm by cycling them in 10% H<sub>2</sub> in N<sub>2</sub> followed by flushing in air between the exposures. He noticed that the fractional change in reflectivity,  $(R_{\text{air}} - R_{\text{H}_2})/R_{\text{air}}$  measured from different palladium films with the same thickness varied. He categorised the responses into three cases where  $\Delta R/R_{\text{air}}$  was 0.8, 0.23 or 0.07. The inconsistency in response arose because the films sometimes adhered better to the substrate than at other times due to uncontrollable variations during the deposition technique.

In the case of  $\Delta R/R_{\text{air}}=0.8$ , a 15nm thick palladium film exposed to cycles of 10% H<sub>2</sub> in N<sub>2</sub> followed by air was examined under the microscope and revealed micro-blistering and micro-cracking on the surface. This was attributed to the  $\alpha$ - $\beta$  phase transition and the associated dimensional changes. These cracks were reversible when left in air. For a thicker 80nm film with the same  $\Delta R/R$  value, the cracks were irreversible and the film delaminated from the substrate resulting in no response from H<sub>2</sub> exposure in subsequent cycling. The  $\Delta R/R_{\text{air}}$  response value was independent of the film thickness size and Butler concluded that the response was in fact as a result of the cracking of the surface.

For a different 15nm thick palladium film that responded with  $\Delta R/R_{\text{air}}=0.07$ , the film showed little or no cracking or delamination. Butler proposed that a likely explanation for the reduced response was a ‘clamping’ effect of the palladium film to the substrate. Better adhesion would restrict lateral movements [9], yet stress would still be induced normal to the palladium film on hydrogen uptake. The additional mechanical energy associated with the adhesive bond alters the thermodynamics of the palladium-hydrogen reaction and manifests as a reduced response. The difference in  $\Delta R/R_{\text{air}}$  with or without adhesion is small for low concentrations of hydrogen. The adhesion hypothesis was further proved by Butler by depositing a few nanometres of Ni (between 1 and 3nm) on the substrate before a 10nm Pd film was deposited. The  $\Delta R/R_{\text{air}}$  response to 10% H<sub>2</sub> in N<sub>2</sub> coincided with  $\Delta R/R_{\text{air}}=0.07$  and was relatively independent of the thickness of the Ni layer. Butler further concluded that this response must be due to the changes in the optical constant of the palladium-hydride system.

The  $\Delta R/R_{\text{air}}=0.23$  case is the intermediate stage where the palladium film is not fully clamped to the substrate nor exhibits micro-blistering. Butler found that the probability of directly depositing a palladium film that will respond with  $\Delta R/R_{\text{air}}=0.23$  was higher than the previous two cases.

Butler's findings highlight the importance of adhesion, which was achieved with a nickel layer deposition between the palladium and the substrate for reproducibility of the response as well as reduced micro-blistering for enhanced film stability. For this study a 10nm Ni film was chosen for adhesion, to be followed by 40nm Pd. 10nm was the minimum thickness that could be deposited using the sputter coating machine (see section 3.2.1, page 47 for details)

### 3.1.3 Protection of the palladium film

Butler further discovered that the response kinetics of hydrogen uptake by a palladium or palladium alloy film on a fibre end was dependent on the carrier gas for the  $\text{H}_2$ . The presence of oxygen in air reduced the magnitude of response as well as reduced the rate of hydrogen uptake due to catalytic water formation reaction on the surface. Butler defined the rate of hydrogen uptake as  $\Delta R/t$ , where  $\Delta R$  was the maximum change in reflectivity with  $\text{H}_2$  and  $t$  as the time taken to reach the change [4].

The oxygen concentration had to be ten times larger than the hydrogen concentration to have a significant impact on the sensor performance. The difference in response size of a PdAg alloy sensor to 500ppm  $\text{H}_2$  in  $\text{N}_2$  with and without the presence of oxygen is shown in Figure 3.3 from Butler's experiments. The slower response is likely to arise from the oxygen blocking active adsorption sites on the palladium surface for hydrogen [4].

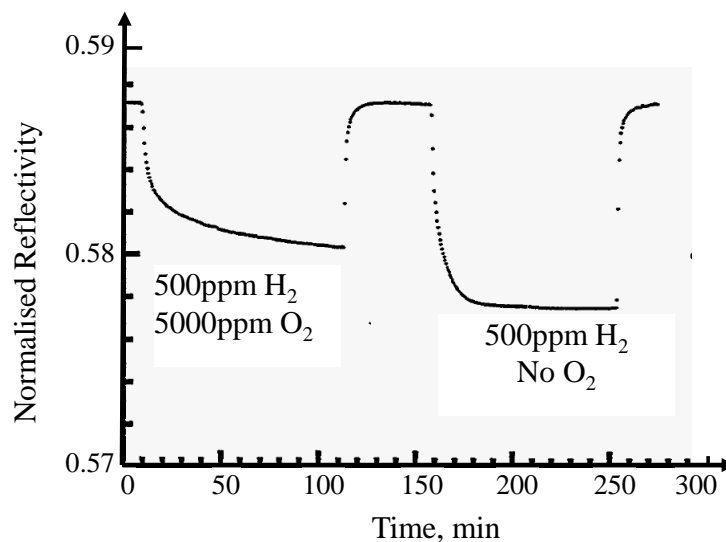


**Figure 3.3- Response of PdAg film to 500ppm  $\text{H}_2$  in  $\text{N}_2$  with and without the presence of  $\text{O}_2$ . Taken from [9]**

Butler tested the effects of different carrier gases on the rate of hydrogen uptake by a palladium film by exposing optically thin films of 10nm Pd deposited on multimode fibre to two environments: 10% H<sub>2</sub> in N<sub>2</sub> and in 10% H<sub>2</sub> in air [8]. Butler's experimental evidence is shown in Figure 3.4

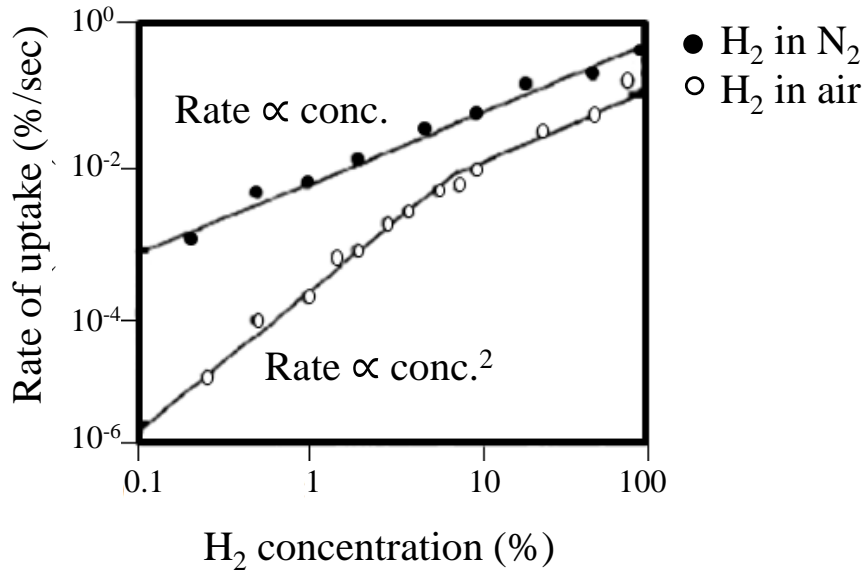
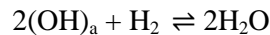
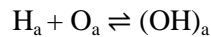
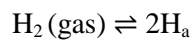


**Figure 3.4- Rate of hydrogen uptake by 10nm Pd film. Filled circles are data for H<sub>2</sub> in N<sub>2</sub> and the blank circles are for H<sub>2</sub> in air. Taken from Butler [4].**

At low H<sub>2</sub> concentrations ( $\leq 10\%$  H<sub>2</sub>), the rate of H<sub>2</sub> uptake was proportional to its concentration in N<sub>2</sub>, whereas the rate was proportional to the square of H<sub>2</sub> concentration in air. At higher hydrogen concentrations, the response kinetics was equivalent for N<sub>2</sub> and air. Adsorbed hydrogen, H<sub>a</sub> reacts with adsorbed oxygen, O<sub>a</sub> to form an adsorbed hydroxide (OH)<sub>a</sub> which reacts with the hydrogen gas to form desorbable water [10, 11].



The hydrogen removal is controlled by water desorption, which is proportional to the partial pressure of oxygen. Butler found that the cross-sensitivity to oxygen was minimised when the partial pressure of hydrogen was 0.5 times the partial pressure of oxygen.

Maier et al [12], Nave [13] and Butler [9] reported the oxidation of the palladium layer to form PdO<sub>2</sub> which is catalytically inactive. Nave tested pure palladium sensors with and without a protective Teflon coating. Uncoated sensors left in ambient air for an extended amount of time displayed an inverted response, where the reflectivity increased on exposure to hydrogen before resuming normal downward response. The increase in reflectivity was believed to be caused by formation of an oxide

layer. Once this was reduced to the metal by a number of hydrogen/air cycles, the reflectivity reached the standard response level. Butler [9] used a protective coating of 25nm Pt on a 250nm PdAg sensing layer. Palladium alloyed with silver oxidises more readily than pure palladium, so using a protective coating was important. Chtanov and Gal [7] used a 35nm Au protective layer on a 40nm palladium film deposited on a glass substrate.

In this project, air has been chosen as a carrier gas for hydrogen instead of nitrogen for safety reasons. A protective Au layer was also chosen due to the availability of a Au sputter target, with a thickness of 10nm, which was the lowest thickness that the sputter coater could deposit. The following section investigates the stability of the multilayer structure in a hydrogen environment.

### **3.2 Multilayer coating stability**

It has been discussed that the fibre sensor head would be coated with 10nm Ni as an adhesive layer, 40nm Pd as the sensing layer and 10nm Au as the protective layer. The multilayer structure was designed to eliminate some of the limitations of a simple Pd coating. Different combinations of the coatings on the fibre tip were tested in hydrogen and their responses analysed.

#### ***3.2.1 Sputter coating deposition***

Preliminary tests for hydrogen response were carried out at first using Ni/Pd coating at the tip of a bare fibre. The metal coatings on the end of the fibre were fabricated by AWE using a sputter coater (Emitech K575X) and I am grateful to Dr Alex Thompson for depositing the coatings. Sputtering is a physical vapour deposition process, where a solid pure metal target is bombarded with a stream of argon ions in vacuum to eject atoms from the target surface and provide omni-directional deposition of sputtered atoms, in order to create films that conform to shape changes of the substrate [14]. No shadowing was visible for overhangs of less than 1mm. The fibre tips were observed to have a metallic coating along the exposed section of fibre (approx. 1cm). The coating thickness was confirmed by a scanning electron microscope, SEM (FEI, XL30), analysis of flat glass substrates coated simultaneously, since the fibre tips were too small and delicate for SEM analysis. The coated glass substrate was prepared for SEM observation by coating the substrate with 3nm of Au/Pd alloy for conductivity and imaged using a BSE (Back Scatter Electron) detector at 160,000 times magnification. BSE images provide better information about the distribution of different elements in the sample in comparison to the ultra-high resolution TLD (Through the Lens Detector) and SE (Secondary Electron) mode. The SEM image of a Ni and Pd coated substrate is shown in Figure 3.5.

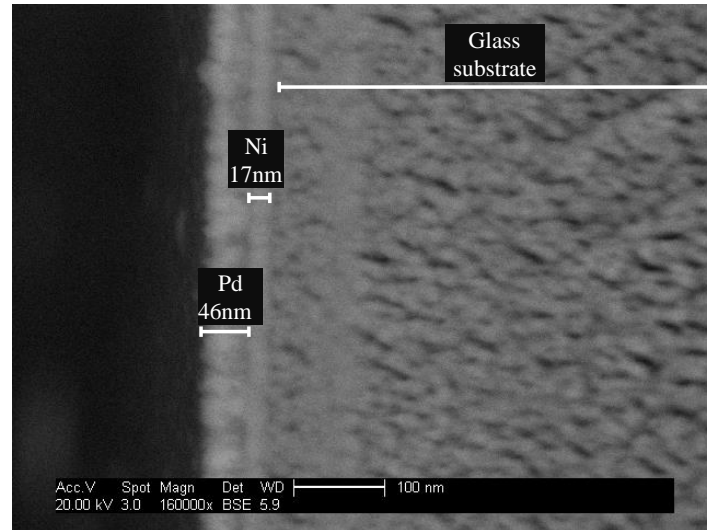


**Figure 3.5- SEM image of a cross-section through Ni and Pd layer deposited on a glass substrate**

The image shows relatively uniform deposition of the metal film layers. The thicknesses of the two layers were measured at five different points and the average taken. The thinner Ni layer measured  $17\text{nm} \pm 5\text{nm}$  and the palladium layer was  $46\text{nm} \pm 4\text{nm}$ . The measured thicknesses have high errors due to local variations in the deposition layer and also as a result of the SEM image not having sharp and well-defined edges.

### ***3.2.2 Coating stability tests in hydrogen***

The Fresnel reflectivity from the Ni/Pd coatings on bare fibre tips as a function of hydrogen concentration was measured using the interrogation system described in chapter 4. A drop in reflectivity was expected when hydrogen was introduced in the testing chamber, as reported in the literature and shown in Figure 3.3, and according to the theory discussed in chapter 2. However, an unusual sensor response was observed. The Ni/Pd sensor heads when left in ambient air for a few weeks gave an inverse response, whereby the reflectivity increased on exposure to hydrogen. The reflectivity versus hydrogen concentration chart in the range of 1% to 0.1%  $\text{H}_2$  in air is shown in Figure 3.6, where the red traces signify sensor response due to hydrogen. The voltage inversion is evident and it is interesting that the proportional change in reflectivity varies as a function of hydrogen concentration too.

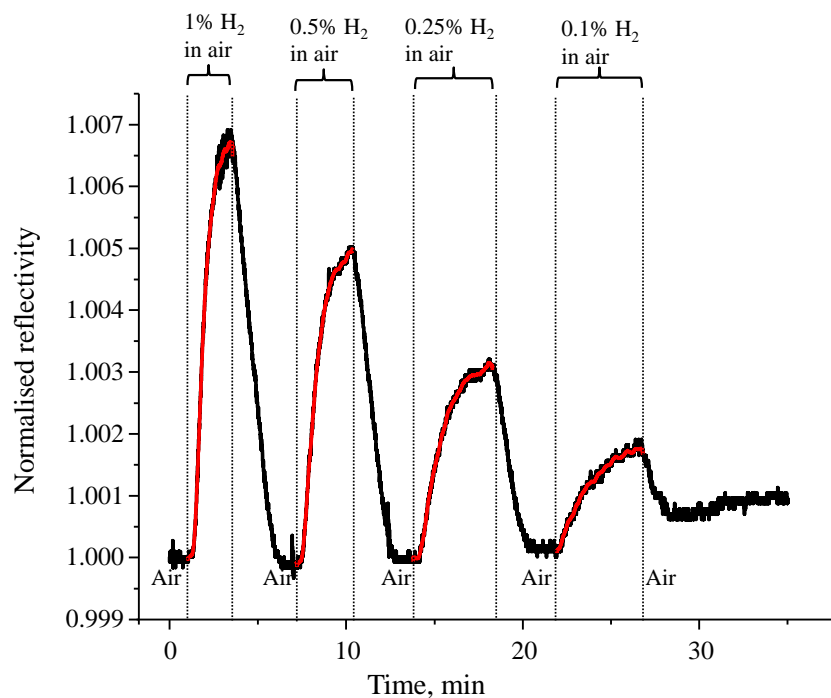


**Figure 3.6- Unusual hydrogen response from a Ni/Pd coated cleaved fibre where the reflectivity increases upon exposure to hydrogen in air. The red traces signify sensor response to hydrogen.**

Unlike Maier, Nave and Butler's reports where the reflectivity resumed to normal after a rise in reflectivity due to the formation of an oxide layer, these sensor heads did not. All five Ni/Pd coated fibres which were tested after being left in air for longer than 1 week showed an inverted response. This was consistent after multiple cycles of  $H_2$  and air. It was therefore decided to test combinations of the coatings deposited on the tip of a cleaved fibre to identify the possible metal coating responsible for the reflectivity inversion and to investigate the effects of introducing multiple layers. The sensing coatings tested were:

1. Pure Pd (40nm)
2. Ni (10nm) and Pd (40nm)
3. Ni (10nm), Pd (40nm) and Au (10nm)
4. Pd (40nm) and Au (10nm)

Three fibres per combination were coated and one from each set were tested in 500ppm  $H_2$  in air in the first week after being sputter coated. On the 4<sup>th</sup> week the first fibre was re-tested and a 2<sup>nd</sup> fibre tested for the first time to check for the response level and direction. The fibres with the four different coating layers tested on week 1 responded as expected, where the reflectivity decreased upon hydrogen exposure and the response levels are shown in Figure 3.7. The responses from the four fibres over 4 weeks are summarised in Table 3-1.

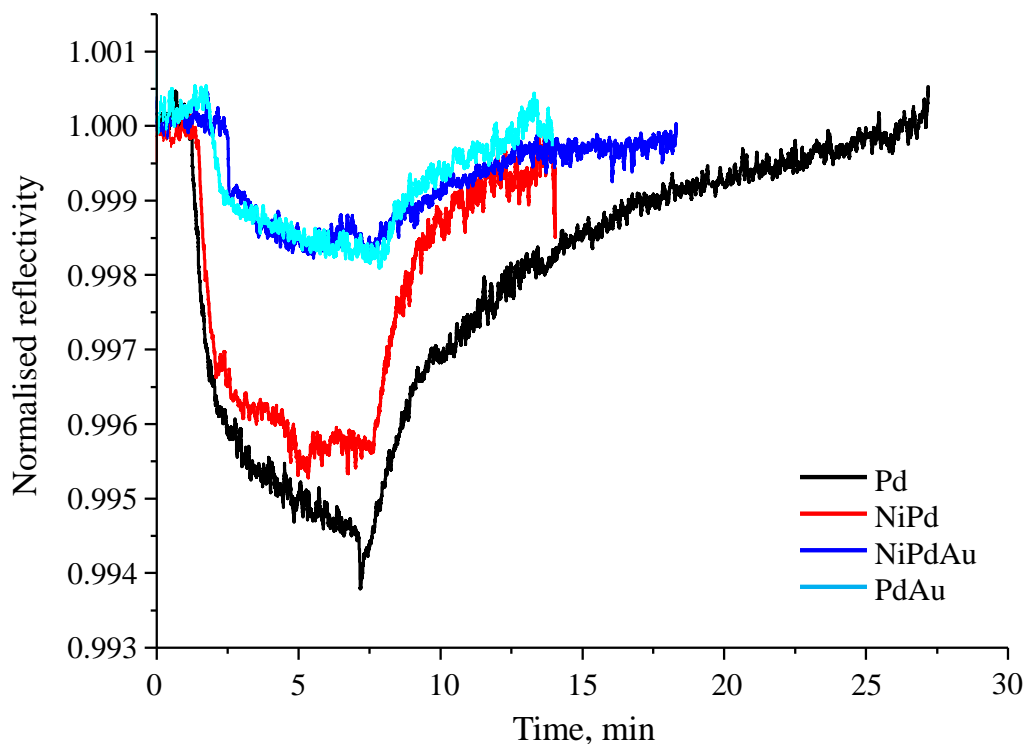


**Figure 3.7-** Comparison of the response sizes from cleaved SMF tips coated in Pd, Ni/Pd, Ni/Pd/Au and Pd/Au exposed to 500ppm H<sub>2</sub> in air on week-1 of the coating run.

The coatings on the fibres did not respond to hydrogen immediately. It was noticed that the fibres needed to be cycled in air-H<sub>2</sub> for about 5 or 6 cycles, where one cycle consisted of flowing air for 20 minutes followed by 10 minutes of hydrogen. This suggests that the coating surfaces were prone to collect impurities and adsorb other gases from ambient air. The sensor needs to be purged in air to allow the film surface to regenerate so that the adsorption sites were cleansed and available for reaction.

**Table 3-1 – Response from coating layers to 500ppm H<sub>2</sub> in air in the first week after being sputter coated and then again after three weeks. ‘Expected response’ means a reduction in Pd reflectivity and ‘Inverted response’ means an increase in Pd reflectivity**

| Coating layer | Week 1            |                   | Week 4            |  |
|---------------|-------------------|-------------------|-------------------|--|
|               | <i>Fibre-1</i>    | <i>Fibre-1</i>    | <i>Fibre-2</i>    |  |
| Pd            | Expected response | No response       | Expected response |  |
| Pd/Au*        | Expected response | Expected response | -                 |  |
| Ni/Pd         | Expected response | No response       | Inverted response |  |
| Ni/Pd/Au*     | Expected response | Inverted response | Expected response |  |

\* 4 out of 10 fibres coated with Au responded to hydrogen tests



Consistent with Butler's findings [8], which were discussed in section 3.1.2, page 44, the magnitude of response from the Ni/Pd sensor is slightly lower than the magnitude of response from the pure Pd sensor, due to adhesion or 'clamping' effects of the Ni layer. A Ni layer also seemed to aid the recovery speed of the sensor whereas the response speed was relatively similar for all sensor heads. Adding a protective Au layer reduced the response level by ~70%, which would restrict the sensor's detection limit.

All four fibres were left in ambient air for a further three weeks and tested in 500ppm H<sub>2</sub> in air again. The Pd fibre did not respond again on week-4 after several regeneration cycles. A possible explanation could be that the Pd layer on first exposure to hydrogen formed desorbable water, which contaminated the metal surface and prevented it from reacting further. A second new Pd fibre, which had been left in ambient air for four weeks, was tested and the response showed evidence of palladium oxidation in air, where the reflectivity increased briefly before the oxide was reduced to the metal and the reflectivity decreased again. When the Pd layer was coated with a Au protective layer, the sensor responded as expected after three weeks of being left in ambient air with the same magnitude of response as week-1. Thus it is evident that a protective layer preserves the palladium layer beneath it and protects it from contamination.

Similar to the Pd coated sensor head, the Ni/Pd coated fibre did not respond on week 4 after several cycles, possibly because of the exposed palladium layer becoming contaminated. However the second Ni/Pd sensor head, which had been in ambient air for four weeks, showed an inverted response whereby the reflectivity increased upon hydrogen exposure, and did not resume the usual decrease in reflectivity after subsequent cycling. With the addition of the protective Au layer, the first Ni/Pd/Au fibre tested after three weeks of being left in ambient air did respond although it also shared an inverted response. A second Ni/Pd/Au fibre was tested which had been left in ambient air and it responded in the expected direction.

It appears that the addition of the Ni layer affected the response and created unusual responses. Five cleaved fibres with a Ni underlayer were tested after being left in air for a period of time since deposition and they all displayed an inverted response. However, four ball lenses were later coated in Ni and Pd and two of the ball lenses gave the expected response over a period of 6 months, which made long term testing of the sensor heads possible. This is described in more details in chapter 5. The kinetics of hydrogen uptake and its dependency on the deposition techniques of the metal layers is not fully understood yet and needs further investigation. Alternatives to Ni as the adhesive layer should be tested. Nave and Anderson [13] observed improved adhesion using a 2nm Cr as an underlayer to 100nm Pd. Butler [15] used 10nm Ti as an adhesive layer for 1µm Pd film.

Although a protective gold layer prevented contamination of the Pd, only four out of ten fibres tested responded to hydrogen. This highlights the unreliability of the gold coatings and more samples need to be tested with varying thickness of the gold layer to find the optimum thickness at which the hydrogen will be able to pass through the gold layer. Alternatives such as platinum as the protective layer should also be tested. Based on these results it was decided that further experiments would be carried out using Ni/Pd coating structure as this was found to be more repeatable.

### 3.3 Palladium film cracking under high hydrogen pressure

Three glass substrates, which were deposited with Pd, Ni/Pd and Ni/Pd/Au simultaneously with the fibres in the sputter coater, were left in a gas chamber and exposed to 99% hydrogen at 70 bar pressure to accelerate failure. The substrates were taken out every 2 hours and observed under the microscope to study the progression of the cracks and the effects of the different coating layers on the crack development. The three substrates were exposed to hydrogen for a total of 40 hours. The first time the substrates were taken out for observation, moisture was noticed because of condensation. To eliminate peeling of the film from the substrate due to moisture, after all the hydrogen gas was purged out of the chamber, the coated substrates were left for a further 30 minutes to allow the contents of the chamber to reach thermal equilibrium prior exposure to air.

A high pressure and concentration hydrogen cylinder was connected to a gas chamber, shown in Figure 3.8a. The cylindrical gas chamber had a small inner diameter of 8cm and a depth of 4cm and is shown in the schematic diagram in Figure 3.8b. Due to limited space the substrates, wrapped in protective lens tissues, were left stacked on top of each other inside the chamber.

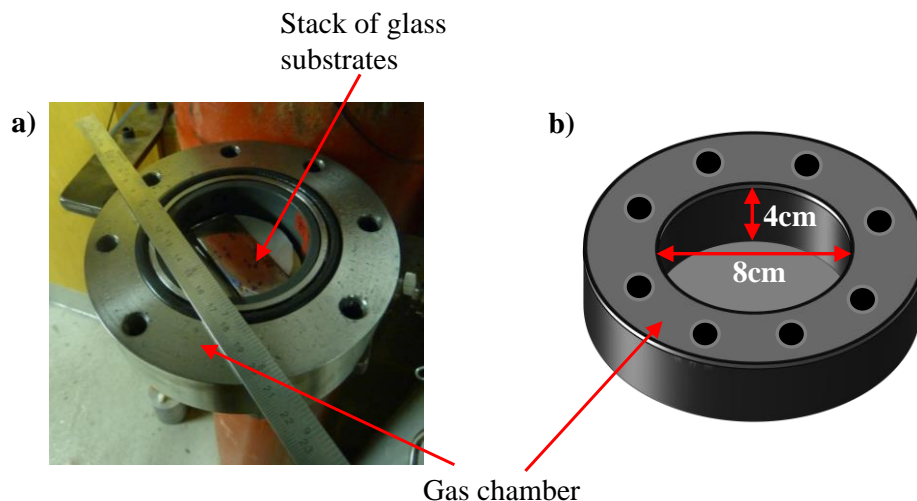


**Figure 3.8- a) Gas chamber, connected to the high pressure and concentration hydrogen cylinder, where the coated glass substrates were kept for accelerated ageing. b) Gas chamber has an inner diameter of 8cm and a depth of 4cm.**

The three glass substrates are shown in Figure 3.9 after 4 hours of hydrogen exposure. The coating on the edges of the substrates cracked first. The cracks near the edge were the largest and then smaller cracks progressed inwards as can be seen from Figure 3.9a. Crack development was more aggressive where the palladium layer did not have a protective layer. These cracks were permanent and did not disappear when left in air.

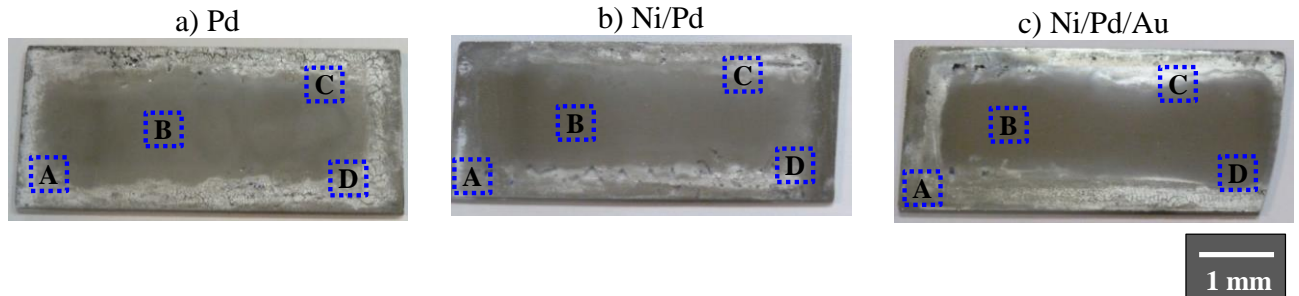


**Figure 3.9- Coated glass substrates a) Pd, b) Ni/Pd and c) Ni/Pd/Au exposed to 99% hydrogen for four hours. Four regions A, B, C and D on each substrate were studied periodically to observe the development of cracks.**

Four sections with different types of behaviour were identified as shown in Figure 3.9. Region A was chosen at a corner edge and B was in the centre of the substrate. Regions C and D are at the boundary between the edge and the centre coating to highlight the progression of the cracks from the edge.

When the substrates were not in the chamber, they were kept wrapped in lens cloth in ambient air. The coatings on the substrates did not show any signs of additional cracking when left in air, as was evident from coated control samples left in air for the duration of the testing.

The images of the substrate sections were taken using a microscope (Olympus, BX51) at 200X magnification (20X objective with 10X eyepiece) in transmission for qualitative analysis to highlight features such as cracks, wrinkles and pin-holes. These features of interest are shown in Figure 3.10. The high intensity pixels represent cracks and pin-holes where the film is no longer continuous, whereas the low intensity pixels are wrinkles in the film. The images are 8-bit greyscale whereby one pixel corresponds to an area of 15nm x 15nm on the film surface.

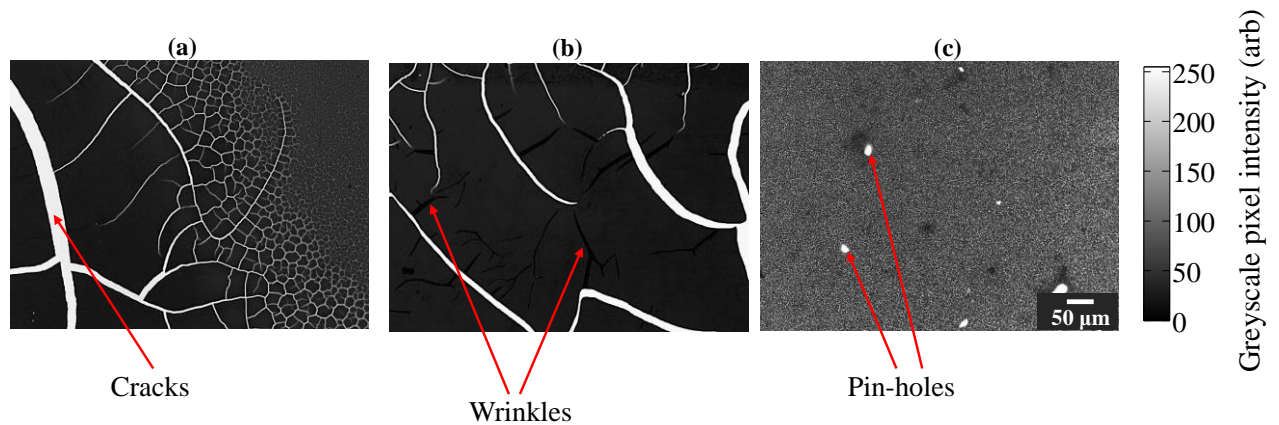


**Figure 3.10-** Examples of features of interest on the films: a) cracks b) wrinkles and c) pin-holes. The high intensity pixels correspond to cracks and pin-holes and the low intensity pixels to wrinkles.

The time progression of crack formation on the four sections of the Pd, Ni/Pd and Ni/Pd/Au coated substrates are shown in Figure 3.11, Figure 3.12 and Figure 3.13 respectively at 2, 4, 10, 22 and 40 hours in hydrogen. The substrates were taken out every two hours for observation but only selected results are presented. The contrast setting on the microscope was arbitrary for each observation but light pixels still correspond to flaws and dark pixels to wrinkles. A summary of observations is given below.

*Pd substrate:* Region A displayed mild cracking within the first two hours of exposure, which spread within 10 hours leading to delamination near the edge in the corner. Region B showed wrinkles on the film for the first 4 hours and then micro-cracks with the appearance of a fine web, which took up to 40 hours to develop. This means that the cracks from the edges had not propagated to the centre in 40 hours of exposure. C and D showed similar wrinkling to region B in the first 2 hours but then fine hair-like cracks developed and spread to form wider cracks and pin-holes started to appear.

*Ni/Pd substrate:* The crack formation on the Ni/Pd coated substrate appeared to be more aggressive than for Pd alone as shown in Figure 3.12. Region A showed severe cracking and peeling within 10 hours of exposure and hence there are no images at 22 and 40 hours. Regions B, C and D showed resistance to cracking and wrinkling in the first 2 hours, in contrast to the Pd coated substrate. B, in the centre, show reduced cracks and short, fine wisp-like cracks spread to form a web of cracks after 40 hours. Regions C and D showed deeper cracks developing and worsening within 10 hours of exposure.

*Ni/Pd/Au substrate:* The crack progression on the Ni/Pd/Au coated substrate over time is shown in Figure 3.13. Region A showed cracking and peeling within the first two hours of exposure and then micro-cracks spread without any delamination up to 40 hours. It is interesting to see that regions B

and D showed resistance to cracking even after 40 hours of exposure in contrast to the previous two coated substrates. Region C showed development of micro-cracks in the first two hours, which then spread and pin-holes started to develop.

### ***3.3.1 Discussion- Pd cracking under high hydrogen pressure***

It is evident from these tests that a Au capping layer protects the palladium. The formation of flaws and delamination is delayed and this is consistent with previous results that implied that Au prevents H<sub>2</sub> passage into the palladium layer. However, the substrate with an adhesive layer appeared to show worse delamination compared to the Pd substrate. This is in contrast to Butler's reports [8] on the 'clamping' effect of the palladium layer to the substrate, which should also reduce chances of delamination.

There are two likely explanations why regions C and D from the Ni/Pd substrate after 4 hours showed worse cracking than the Pd film. Firstly, because the regions were selected manually by eye, regions C and D on the Ni/Pd film may have been closer to the edge in comparison to the Pd film. Therefore the film deterioration may not be directly comparable. Secondly, the substrates were stacked on top of each other in the chamber with the Ni/Pd coated substrate at the top. The effects of hydrogen exposure may have affected the Ni/Pd film more than the Pd film. It was not possible to position the substrates next to each other due to space restrictions in the chamber and thus reach a definite conclusion.



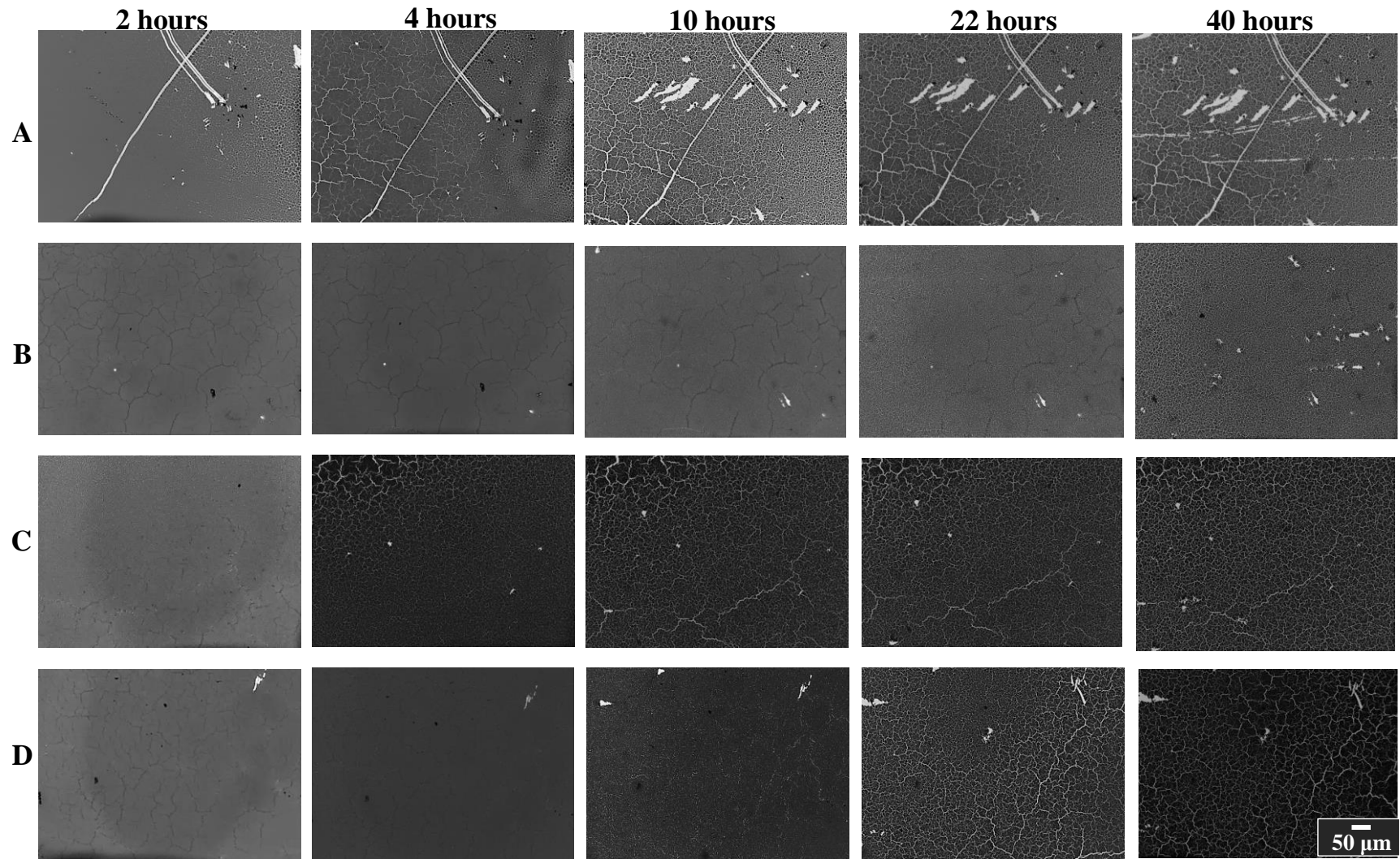


Figure 3.11- Pd coated glass substrate - four regions A, B, C and D observed at 2, 4, 10, 22 and 40 hours



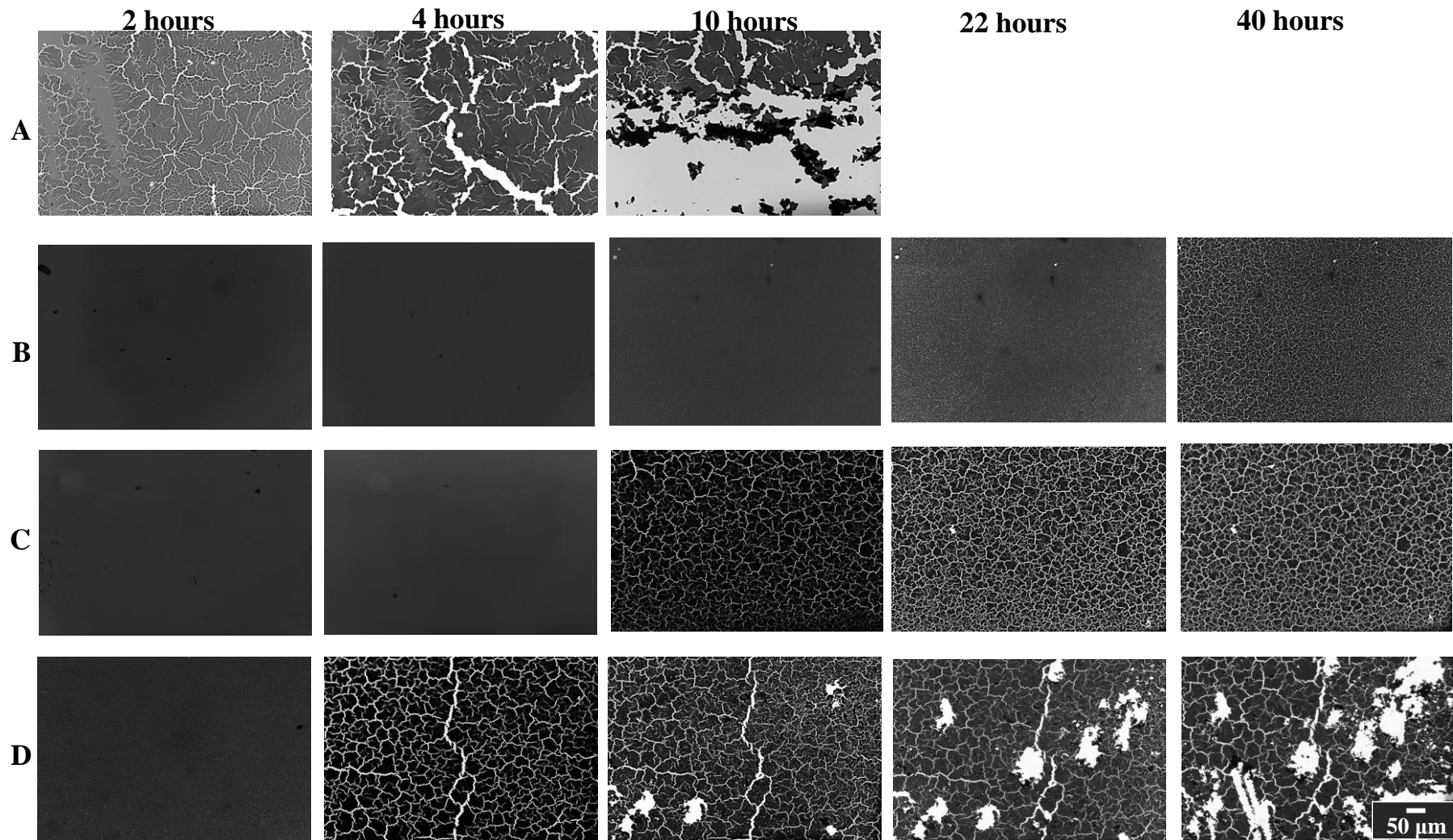


Figure 3.12- Ni/Pd coated glass substrate - four regions A, B, C and D observed at 2, 4, 10, 22 and 40 hours Images for region A at 22 and 40 hours were not available due to severe cracking and delamination

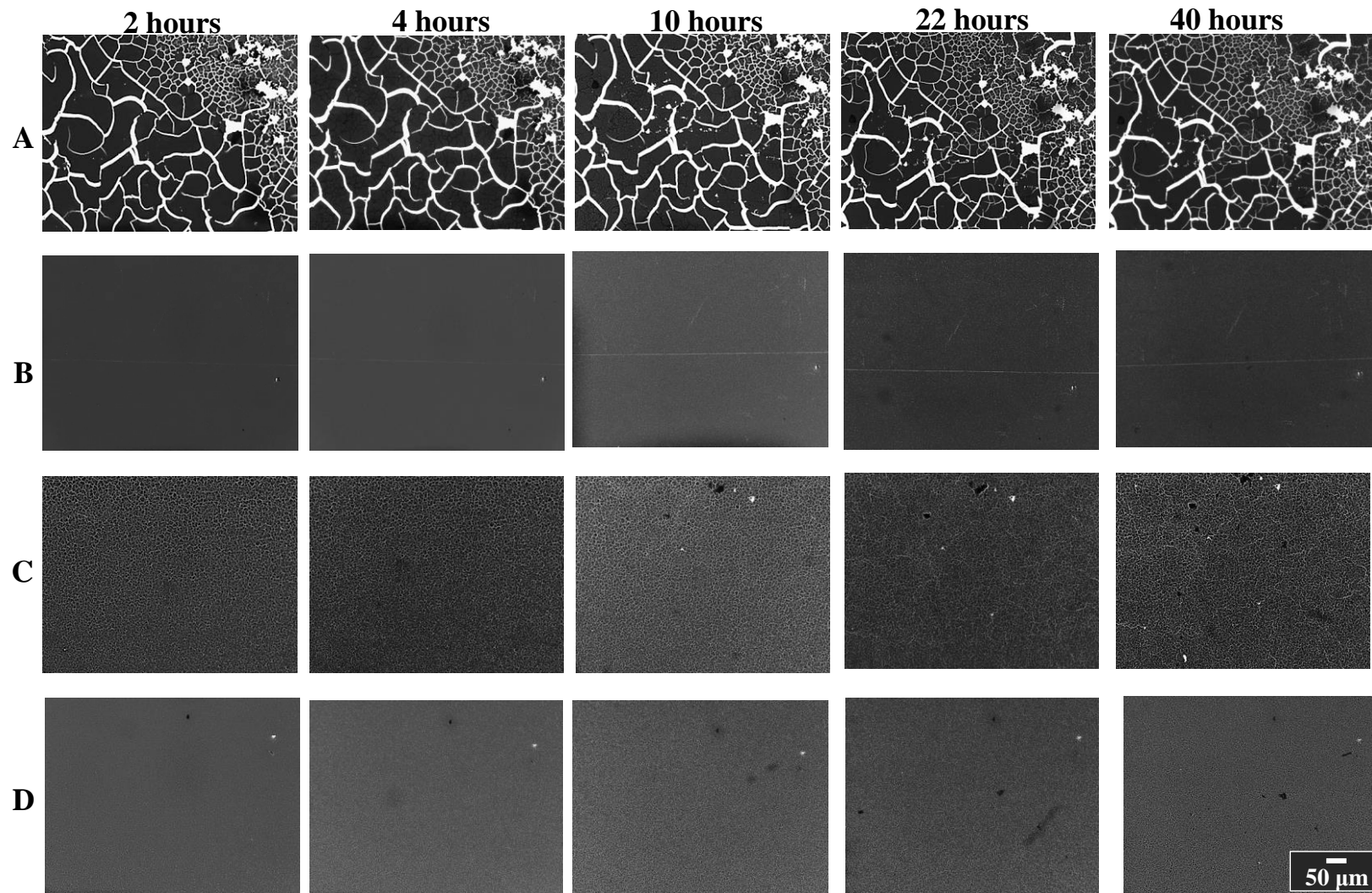
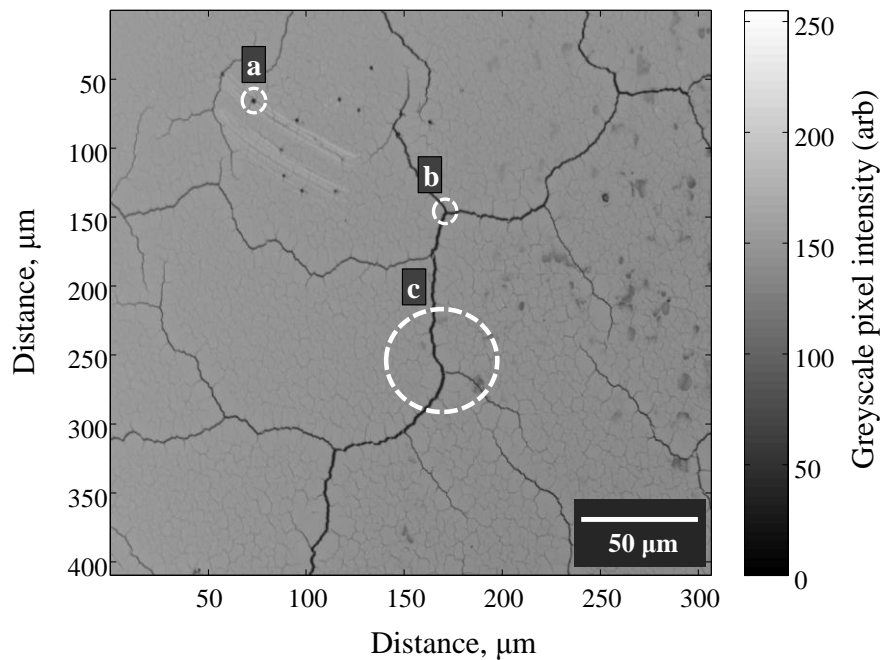


Figure 3.13- Ni/Pd/Au coated glass substrate - four regions A, B, C and D observed at 2, 4, 10, 22 and 40 hours



### 3.4 Statistical analysis of the cracking

For statistical analysis, the image of a cracked palladium film was taken in reflection because the image is representative of the mode of operation of the sensor heads. Figure 3.14 shows an 8-bit greyscale image, with an area of  $300\mu\text{m} \times 300\mu\text{m}$  (or  $20,000 \times 20,000$  pixels) in which the low intensity pixels show irreversible pin-holes and cracks. It is possible that a SMF core could coincide with an area affected by flaws, for example at positions *a* or *b* in Figure 3.14, resulting in catastrophic failure of the sensor. The dashed circles at *a* and *b* indicate hypothetical area of a SMF core ( $10.4\mu\text{m}$  in diameter).



**Figure 3.14-** Magnified image of a cracked 40nm Pd film on glass substrate, taken in reflection using an optical microscope after accelerated ageing of the film (99%  $\text{H}_2$ , 100 bar pressure, 48 hours). Circles indicate hypothetical sensors of different active areas at sites *a* and *b* (both  $10.4\mu\text{m}$  diameter) and *c* ( $47\mu\text{m}$  diameter).

Although a larger sensor area is known to be more reliable, this has not yet been quantified to the best of the author's knowledge. A larger sensor, as shown by circle *c* in Figure 3.14, is in fact more likely to have some cracks within this area, however the performance of the sensor head will be more predictable because the ratio of cracked to unaffected area is more likely to be consistent. This can be quantified by building an image histogram that can be treated as a discrete probability density function that defines the likelihood of a pixel intensity occurring within the image [16]. The pixel intensities correspond directly to the level of reflectivity that might be seen in a sensor. The low intensity pixels show the pin-holes and cracks.

The original image was divided into a series of windows of given area ( $x$ -by- $x$  pixels, where  $x$  is an integer). The average intensity was then calculated for each window in the entire image. The window intensities correspond to the average reflectivity that might be seen in a hypothetical sensor of the given area. The average window greyscale intensities and the number of windows with each intensity were plotted on a histogram. Figure 3.15a shows the result of averaging over a  $52 \times 52$  pixel window, which approximately corresponds to the area intersected by the single-mode fibre mode field diameter of  $10.4 \mu\text{m}$ . The pixel intensities ranged from 109 to 157, with a mean pixel intensity of 133. Figure 3.15b shows the result for a  $240 \times 240$  pixel window, which corresponds approximately to the area intersected by the  $47 \mu\text{m}$  diameter active region. The pixel intensity range is narrower from 131 to 153, with a mean pixel intensity of 142. As the window size increases, the number of low intensity pixels (that represent cracks) drops, resulting in a narrower histogram. Thus, larger area sensors are less likely to suffer catastrophic failure as a result of pin-holes and cracks.

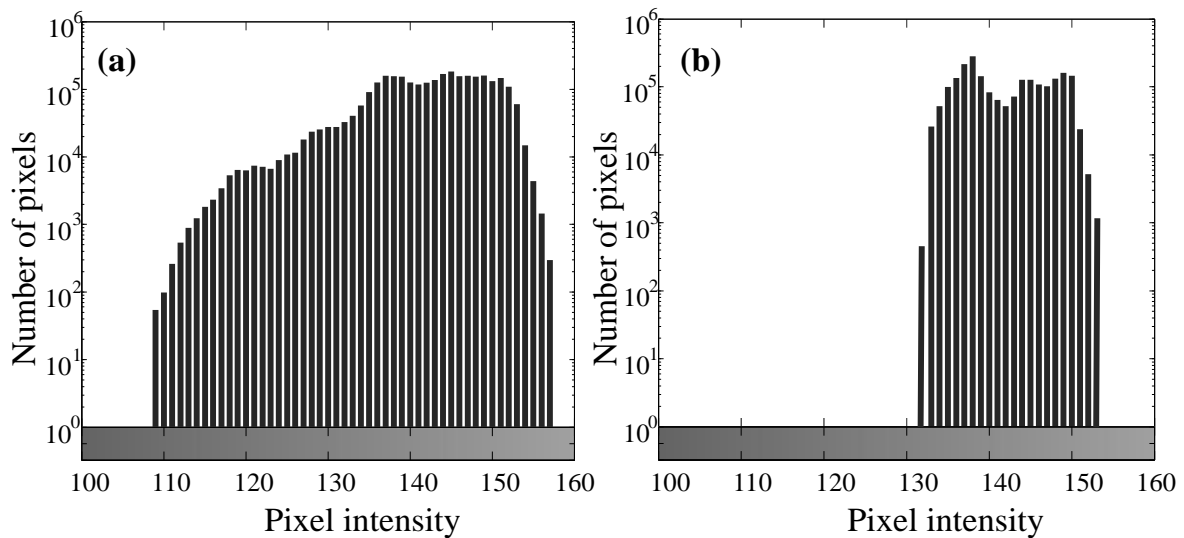


**Figure 3.15- Histogram analysis of image in Figure 3.14, following averaging over hypothetical area windows, showing relative numbers of windows with different intensity. The horizontal greyscale beneath each histogram gives a visual indication of reflected intensity. Averaging over a)  $52 \times 52$  and b)  $240 \times 240$  pixel windows, with equivalent area to  $10.4 \mu\text{m}$  and  $47 \mu\text{m}$  diameter circles respectively.**

With the proposed hypothesis that a larger sensor area with more palladium coverage will lower the risks of sensor failure due to cracking of the palladium film, new sensor designs were conceived that would be cost-effective, easily produced in the lab, with minimal alignment that will not cause any weakening of the fibre. The schematic designs in order of increasing sensing area are shown in Figure 3.16, where Figure 3.16b has a ball lens at the tip of a SMF and Figure 3.16c has a GRIN (GRaded INdex) lens attached to the end of a SMF.

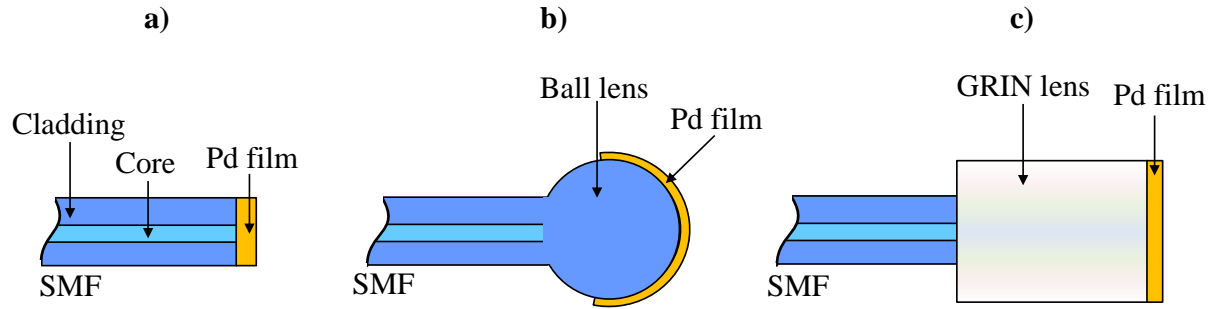


**Figure 3.16- Micromirror sensor heads in order of increasing sensing area. a) SMF core (~8.2 $\mu$ m) coated with palladium. b) A ball lens at the end of a SMF and coated in palladium. c) A GRIN lens attached to a SMF and the lens coated in palladium**

A ball lens was created by melting the tip of the fibre in a controlled process in a fusion splicer. The size of the ball lens was chosen to optimise the intensity of the Fresnel back-reflection from the outer surface of the ball lens that is coupled back into the singlemode fibre, using a Gaussian beam propagation model. This is discussed along with the ball lens production methods in the chapter 5. The GRIN lens assembly from Thorlabs spliced to the end of a SMF is also described. The resulting active sensor head areas were considerably larger than an SMF core.

### 3.5 Conclusion

The coating structure of the hydrogen sensor has been discussed. The ideal thickness of the Pd layer was determined to be 40nm using the thin film interference model. The film is optically thin at 40nm and the response is dominated by surface chemical reactions. If the film were thicker than 40nm then the reflectivity would be mainly due to bulk chemical reactions and the reflectivity change would become smaller. Thicker films also stand a higher likelihood of peeling and delamination.

The importance of an adhesive and a protective layer is highlighted in the literature. A thin adhesive layer of Ni is commonly used in between the substrate and the Pd layer for reproducibility of the response and to reduce micro-blistering. A 10nm Ni layer was chosen to be deposited which is optically transparent. A thin protective layer, commonly Au or Pt on top of the Pd layer prevents the Pd from contamination and oxidation in air, yet is understood to allow passage of H<sub>2</sub>. A 10nm Au layer was used. However the addition of multiple layers makes a complex structure and led to unusual sensor response where the reflectivity of the Pd increased on hydrogen exposure instead of decreasing. The interrogation system used to measure the reflectivity is described in chapter 4. It has been reported that the reflectivity of Pd left in air may increase at first due to the formation of PdO but the reflectivity should decrease as the PdO is reduced to the metal. A reduction in reflectivity was not observed even after prolonged exposure to hydrogen.

A number of coating combinations were deposited on cleaved fibres and were tested in hydrogen after being left in air for 4 weeks. The fibres were coated with i) pure Pd, ii) Ni and Pd, iii) Ni, Pd and Au and iv) Pd and Au. Fibres that had a Ni underlayer showed an inverted response. Five cleaved fibres tested from different coating runs, all showed an inverted response where the reflectivity increased upon hydrogen exposure. For future work several more fibres should be tested at regular intervals over a period of 4 weeks to identify trends in behaviour that may arise due to variation in the deposition technique. Also, sensors with thinner Ni layers need to be tested to find the optimum thickness. Alternative to Ni, such as Ti and Cr should also be tested. For this project, 10nm was the minimum layer thickness achievable using the sputter coater.

Although an Au protective layer prevented the Pd from contamination, only 4 fibres tested out of 10 responded to  $H_2$ . This means that variations in the deposition technique are likely to have an impact on the sensor performance. Although gold has been reported to allow the passage of hydrogen, it is possible that the adsorption sites on the Pd layer were blocked during the deposition process. More fibres need to be tested with varying thickness of Au to find the optimum thickness at which the hydrogen will be able to pass through the gold layer. Alternatives such as platinum as the protective layer should also be tested.

It was also found that the 2 out of 4 ball lenses coated in Ni/Pd showed the expected response over a period of 6 months. This is described in more detail in chapter 5. For this reason and combined with the unreliability of the gold coating, it was decided to carry out the experiments using a Ni/Pd coating structure as a proof of concept for a viable hydrogen sensor.

To further understand the effects of the various layers on the cracking of the films, three glass substrates coated with Pd, Ni/Pd and Ni/Pd/Au were kept in a high pressure and high concentration hydrogen chamber to accelerate failure. The substrates were taken out periodically and four regions were studied. The region nearest the edges showed the most severe cracking and peeling whereas the centre regions showed some resistance. The substrates coated with Ni/Pd/Au showed the most resistance to cracking after 40 hours, proving that the Au capping layer does indeed protect the palladium from aggressive cracking. The cracking of the films could have been exacerbated by a number of other factors besides hydrogen induced cracking – for example dirt on the substrate, uneven surface due to variation in deposition techniques exerting undue stress on isolated locations, moisture, stacking the slides on top of each other etc.

However, the peeling and the extent of cracking of the film deposited on larger surfaces may not be representative of the cracking of films deposited on micro-dimensional areas, such as coatings on fibre tips and lenses. Although a protective layer on top of the palladium delays the formation of flaws, it might also mean a delayed progression of hydrogen reaching the palladium surface as observed with non-responsive Ni/Pd/Au coated fibres.

A statistical analysis of the cracks led to the hypothesis that a larger area coated with the palladium sensing film would be less likely to fail catastrophically. Although a larger area has a higher likelihood of encountering flaws, the overall success rate of the sensor is more predictable because the ratio of cracked to unaffected area is more likely to be consistent. Sensor heads that will be bigger than the SMF cores are suggested for example – melting the tip of the fibre and forming a ball lens or attaching a GRIN lens to the fibre tip to increase the surface area. These different sensor heads are described in detail in chapter 5.

### 3.6 References

- [1] Heavens, O. S. (1955), *Optical properties of thin solid films*, 1st ed, General Publishing Company Ltd, Canada.
- [2] Corning Incorporated Optical Fiber (2002), *Corning Single-Mode Optical Fiber*, available at: <http://ece466.groups.et.byu.net/notes/smf28.pdf> (accessed 15/06/2012).
- [3] Palik, E. D. (1998), *Handbook of Optical Constants of Solids*, 3rd ed, Academic press, NY, US.
- [4] Butler, M. A. and Buss, R. J. (1993), "Kinetics of the micromirror chemical sensor", *Sensors and Actuators B: Chemical*, vol. 11, no. 1–3, pp. 161-166.
- [5] Mandelis, A. and Garcia, J. A. (1998), "Pd/PVDF thin film hydrogen sensor based on laser-amplitude-modulated optical-transmittance: Dependence on H<sub>2</sub> concentration and device physics", *Sensors and Actuators, B: Chemical*, vol. B49, no. 3, pp. 258-267.
- [6] Frazier, G. A. and Glosser, R. (1982), "Hydrogen induced changes in the electronic structure of the palladium-hydrogen system as measured by thermorefectance", *Solid State Communications*, vol. 41, no. 3, pp. 245-250.
- [7] Chtanov, A. and Gal, M. (2001), "Differential optical detection of hydrogen gas in the atmosphere", *Sensors and Actuators, B: Chemical*, vol. 79, no. 2-3, pp. 196-199.
- [8] Michael A., B. (1994), "Micromirror optical-fiber hydrogen sensor", *Sensors and Actuators B: Chemical*, vol. 22, no. 2, pp. 155-163.
- [9] Butler, M. A., Sanchez, R. and Dulleck, G. (1996), *Fiber Optic Hydrogen Sensor*, Sandia Reports SAND96-113, Sandia National Laboratories, Albuquerque, US.
- [10] Cheng, Y. T., Li, Y., Lisi, D. and Wang, W. M. (1996), "Preparation and characterization of Pd/Ni thin films for hydrogen sensing", *Sensors and Actuators B-Chemical*, vol. 30, no. 1, pp. 11-16.
- [11] Gao, H., Lin, Y. S., Li, Y. and Zhang, B. (2004), "Chemical stability and its improvement of palladium-based metallic membranes", *Industrial and Engineering Chemistry Research*, vol. 43, no. 22, pp. 6920-6930.
- [12] Maier, R. R. J., Jones, B. J. S., Barton, J. S., McCulloch, S., Allsop, T., Jones, J. D. C. and Bennion, I. (2007), "Fibre optics in palladium-based hydrogen-sensing", *Journal of Optics A: Pure and Applied Optics*, vol. 9, no. 6, pp. S45-S59.

- [13] Nave, S. E. (1997), *FY 97 Report on hydrogen sensors for enhanced surveillance program project LL-ESP96-13*, WSRC-RP--97-00904 ON: DE98050546, Westinghouse Savannah River Co., Aiken, SC, United States.
- [14] Yun, S. and Ted Oyama, S. (2011), "Correlations in palladium membranes for hydrogen separation: A review", *Journal of Membrane Science*, vol. 375, no. 1-2, pp. 28-45.
- [15] Butler, M. A. and Ginley, D. S. (1988), "Hydrogen sensing with palladium-coated optical fibers", *Journal of Applied Physics*, vol. 64, no. 7, pp. 3706-3712.
- [16] Gonzalez, R. C., Woods, R. E. and Eddins, S. L. (2009), *Digital image processing using MATLAB*, 2nd ed, Gatesmark Publishing, USA.

# Chapter 4

## Fresnel Refractometer

A micromirror Fresnel refractometer measures changes in refractive index of an external medium via measurement of the change in reflected intensity from an optical fibre end. The refractive index of a substance is a measure of how fast light propagates through that substance and in the Pd system is indicative of H<sub>2</sub> concentration. The principles behind an optical fibre Fresnel refractometer are discussed here and a simple self-referenced refractometer is designed and characterised for testing sensitivity to hydrogen detection.

## 4.1 Fresnel Refractometer

### 4.1.1 Background

When light is incident on a boundary separating two media with different refractive indices, it is reflected and refracted as shown in Figure 4.1. The amplitude of the reflected waves can be determined from the Fresnel equations as given by Equations (4.1) and (4.2) [1].

$$r_{\perp} = \frac{n_a \cos \theta_i - n_b \cos \theta_t}{n_a \cos \theta_i + n_b \cos \theta_t} \quad (4.1)$$

$$r_{\parallel} = \frac{n_b \cos \theta_i - n_a \cos \theta_t}{n_a \cos \theta_t + n_b \cos \theta_i} \quad (4.2)$$

Where  $r_{\perp}$  is the amplitude reflection coefficient for light whose electric field component is perpendicular to the plane of incidence (s-polarised),  $r_{\parallel}$  is the amplitude reflection coefficient for light whose electric field component is parallel to the plane of incidence (p-polarised),  $\theta_i$  is the angle of incidence of light at the medium with refractive index  $n_a$  and  $\theta_t$  is the angle of transmission in the medium with refractive index  $n_b$ . The refractive indices may be complex, in which case the full expression  $n_R - in_I$  (from chapter 2, equation (2.4), page 14) may be substituted.

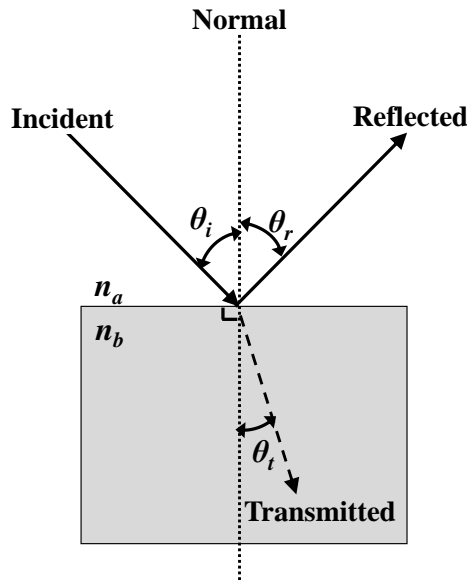


**Figure 4.1-** Light in medium with refractive index,  $n_a$  is incident on a plane boundary and a portion of the light gets reflected at an angle  $\theta_r$ . By the laws of reflection  $\theta_r$  is equal to the angle of incidence  $\theta_i$ . The rest of the light is transmitted at an angle  $\theta_t$  through the medium with refractive index  $n_b$  ( $>n_a$ ), towards the normal.



In a single-mode optical fibre, the light intercepts the fibre end at normal incidence and thus equations (4.1) and (4.2) can be simplified to:

$$r_{\perp(\theta=0)} = \frac{n_a - n_b}{n_a + n_b} \quad (4.3)$$

$$r_{\parallel(\theta=0)} = \frac{n_b - n_a}{n_a + n_b} \quad (4.4)$$

The Fresnel reflectance is given by the square of the amplitude reflection coefficient as shown by equation (4.5) :

$$R = |r|^2 = \frac{(n_a - n_b)^2}{(n_a + n_b)^2} \quad (4.5)$$

It can be seen from equation (4.5) that a change in refractive index of one of the media will cause the Fresnel reflected light intensity to change.

Kim and Su [2] designed a fibre optic system based on the principle of Fresnel reflection to measure the refractive index of various liquids. The experimental arrangement is shown in Figure 4.2.

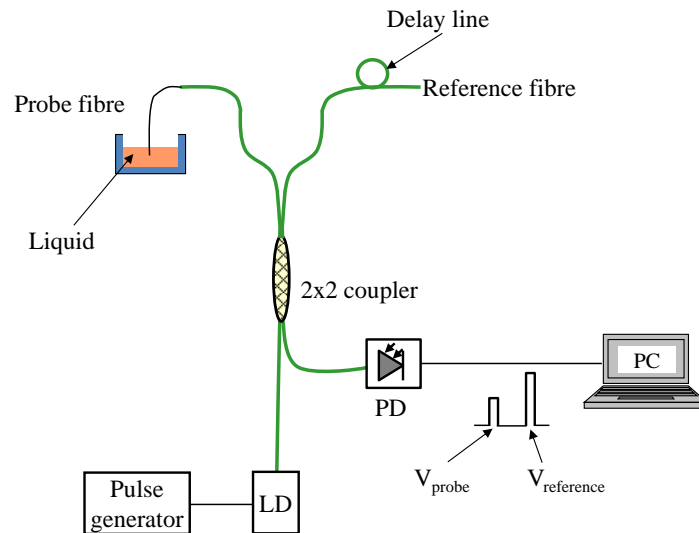


**Figure 4.2- Concept of a ratiometric fibre optic refractometer. Adapted from [2]**

Fresnel reflection signals from the fibre-air and fibre-liquid interface were measured by a photodetector amplifier. The voltage signal from the reference fibre-air interface,  $V_{\text{reference}}$  is proportional to (4.6):

$$V_{\text{reference}} \propto \frac{(n_{\text{core}} - n_{\text{air}})^2}{(n_{\text{core}} + n_{\text{air}})^2} \quad (4.6)$$

Where,  $n_{core}$  is the effective index of the fibre core, 1.45 at 1550nm [3] and  $n_{air}$  is the refractive index of air, 1 and is approximately 3.4% of the incident light intensity for a typical single mode fibre in air. The voltage signal from the probe fibre-liquid interface,  $(V_{probe})_l$  is proportional to (4.7):

$$(V_{probe})_l \propto \frac{(n_{core} - n_l)^2}{(n_{core} + n_l)^2} \quad (4.7)$$

Where,  $n_l$  is the refractive index of the test medium. Assuming that the constant of proportionality does not vary then the ratio of the voltages can be equated as shown in equation (4.8) and rearranged to find the refractive index of the liquid as shown in equation (4.9).

$$R \equiv \frac{V_{reference}}{R_{norm} \times (V_{probe})_l} = \left( \frac{n_{core} - n_{air}}{n_{core} + n_{air}} \right)^2 / \left( \frac{n_{core} - n_l}{n_{core} + n_l} \right)^2 \quad (4.8)$$

$$n_l = n_f \left\{ \frac{1 - \eta}{1 + \eta} \right\} \quad (4.9)$$

Where,

$$\eta = \frac{1}{\sqrt{R}} \left\{ \frac{n_{core} - n_{air}}{n_{core} + n_{air}} \right\} \quad (4.10)$$

In equation (4.8),  $R_{norm}$  is the normalised calibration factor taken by leaving the probe fibre in air,  $V_{reference}/(V_{probe})_{air}$ . The normalisation routine accounts for fluctuations in the laser output power and variations in the component performance. The reference and probe pulses were separated by an optical path time delay, where the probe path was much shorter than the reference path. To introduce a significant delay between the two pulses the reference arm must be very long, for example 150km of reference arm will be required for a 1ms delay between the pulses, calculated using  $t=(2l)/c$  where  $l$  is the length of the fibre and  $c$  is the free space speed of light. Or else, the technique would require fast pulse generation and detection equipment.

A simple optical fibre refractometer network based on Kim's principle was adapted by Dimopoulos *et al* [4], and used to monitor the refractive index of epoxy resin whilst it was being cured. This system was adopted for this project for the initial stages of scoping out a stable interrogation system.

The interrogation system's ability to detect small changes in refractive index was first characterised by immersing the test probe fibre in oils of known refractive index. It would have been ideal to use oils with high refractive indices that would match the refractive index of palladium to mimic the

system response from palladium. However, the highest refractive index oil available commercially (from Cargille Labs) was 1.8, above which the oil becomes toxic and harmful to health. A calibration chart using a range of refractive index oils was completed to establish the system's minimum detectable change in refractive index. The oil calibration test served as a proof of concept before using palladium coated test fibres. The experiments are discussed in detail in the following section.

## 4.2 Method 1: Single source, 2 paths and cleaved fibre in oil

The experimental arrangement shown in Figure 4.3a consists of a single source and two fibre branches that hold the reference fibre and the probe fibre. The dotted lines in the diagram show the electrical connections and the solid lines show the optical fibre network, all singlemode SMF28. This was adapted from [4]. Figure 4.3b shows a photograph of the experimental setup of an oil well on a temperature controlling Peltier heat sink.

The interrogation system was tested using two sources – a low coherence broadband SLD (super luminescent diode) source and a high coherence DFB LD (distributed feedback laser diode) source to compare the sensitivity and long term stability.

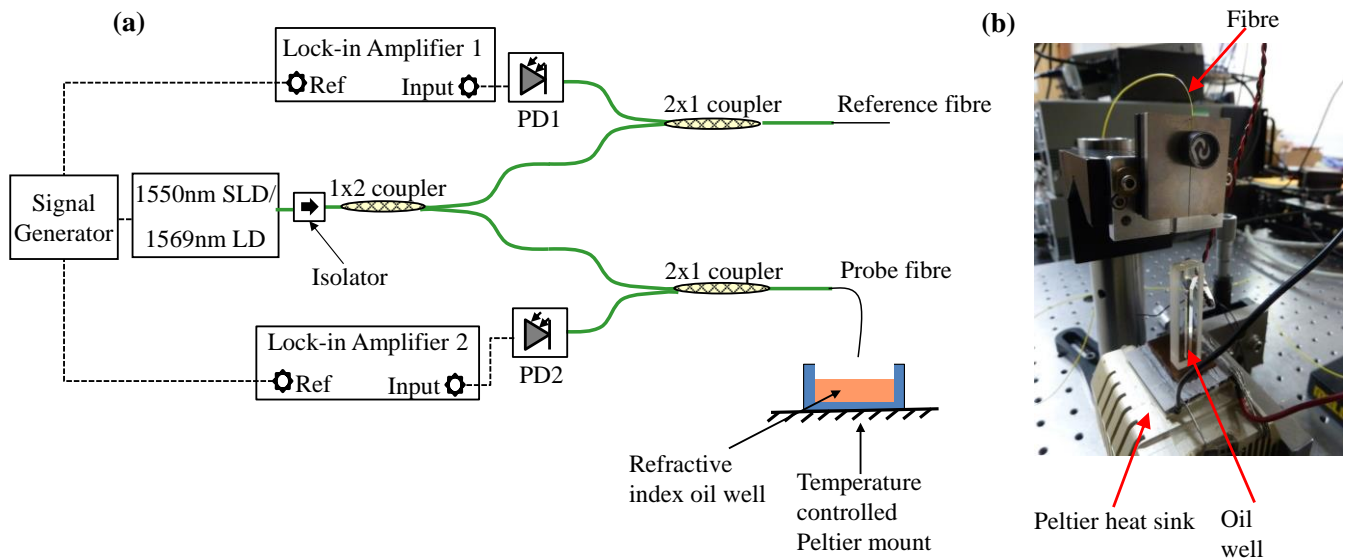


**Figure 4.3- a) Schematic of single source and 2 path configuration - the Fresnel reflections from the reference and probe arm were detected by photodetector amplifier PD1 and PD2 respectively and demodulated by matched lock-in amplifiers 1 and 2; b) experimental photograph of oil well on a Peltier heat sink**

The properties of the two sources were:

- The broadband SLD (Covega Corporation, SLD 1005) had a typical centre wavelength at 1550nm and FWHM (full width half maximum) of 50nm.
- The DFB laser diode (Laser Components, PL15BL0021FAB-A-1-01) was centred at 1569nm and had a narrow FWHM of  $\leq 15\text{pm}$ , measured using an OSA, (optical spectrum analyser) (Ando, AQ6370C). The FWHM measurement was limited by the resolution of the OSA.

The source spectra plotted on a semi-log scale are shown in Figure 4.4.

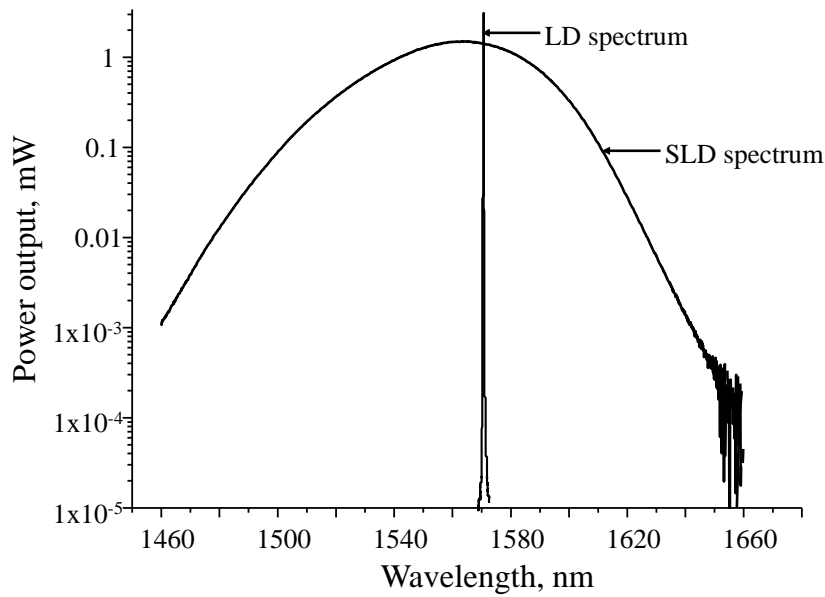


**Figure 4.4- Broadband SLD spectrum centred at 1550nm and linewidth of 50nm. DFB LD spectrum centred at 1569nm and linewidth of 0.015nm.**

The SLD was operated at an injection current of 600mA. A signal generator (Stanford Research, DS345) was used to modulate the SLD output intensity at 997Hz with a 0.2Vpp sine function and the resulting current modulation was  $\pm 7\text{mA}$ . The laser diode current was set to 40mA and modulated at 997Hz and 1.5Vpp sine function. The resulting current modulation on the laser diode driver was  $\pm 4\text{mA}$ .

A modulation frequency of 997Hz was chosen so that it was not a multiple of the mains noise frequency at 50Hz and an additional peak found at 60Hz, or their harmonics as shown by the spectrum in Figure 4.5, taken using an electrical spectrum analyser (Stanford Research, SR780). At 997Hz the noise baseline from the photodetector amplifiers ( $1.2\mu\text{Vrms}/\sqrt{\text{Hz}}$ ) reached was no better than at higher frequencies. Also, many acoustic noises occur at lower frequencies. So, a high enough frequency was chosen that was permitted by the detector bandwidth and ensured that any systematic distortion of the output signal was eliminated and cross talk between the communication equipment

was reduced. In later experiments, a higher modulation frequency was used to create pseudo broadband sources (see chapter 6 section 6.3, page 119).

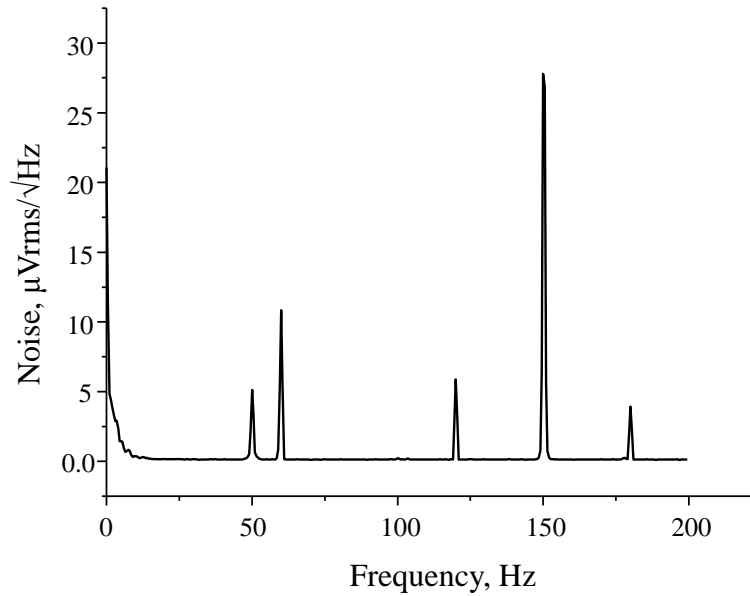


**Figure 4.5- Noise frequencies 50Hz and 60Hz, detected using an electrical spectrum analyser. A modulating frequency of 997Hz was chosen to avoid the harmonics.**

The pigtailed fibre from the light source was connected to a 1x2 3dB directional coupler that had a 50:50 split ratio and had a design centre wavelength of 1550nm and a bandwidth of 60nm (Laser2000, C-NS-AL-50-S-2210-15-AP/AP). Light from the first coupler was directed via the top 2x1 coupler to a cleaved reference fibre in air (see Figure 4.3). The remaining light was directed via the bottom 2x1 coupler to a cleaved probe fibre for immersion in test oils of varying refractive indices. The Fresnel reflections from the reference channel (fibre-air interface) and the probe channel (fibre-oil interface) were detected using photodetector amplifiers, PD1 and PD2 (Thorlabs, PDA10CS-EC) respectively and demodulated by matched, phase-sensitive lock-in amplifiers (Stanford Research, SR850). An integration time period (defined by the time constant of the lock-in amplifiers) of 100ms was used. For data acquisition a GPIB (General Purpose Interface Bus) adapter (National Instruments, GPIB-USB-HS) was used to read the lock-in amplifier voltages and the ratio of the reference and probe voltages were written to a text file using a LabView program. The signal was further averaged over 10s in the computer to reduce the noise on the output to a minimum.

#### ***4.2.1 Results 1: Single source, 2 paths and cleaved fibre in oil***

The cleaved probe fibre was immersed in oils of known refractive indices in the range 1.72 to 1.78 (Cargille Labs, Series M) measured at 589nm and 25°C. The oils have an average temperature coefficient,  $dn/dT \sim -0.0007$  (15-35°C). To improve the repeatability of the measurements, the oils were mounted on a Peltier element to maintain a constant temperature of 25°C using a thermoelectric

heat pump. The temperature was controlled using a transducer type temperature sensor (Thorlabs, TED200). A Cauchy dispersion equation (provided by the manufacturer) was used to calculate the approximate refractive index of the oils at the wavelength of the light source and at 25°C. The error on the approximated Cauchy refractive index value was stated to be  $\pm 0.005$ .

Data collection in oil and in air was run for 4 minutes and the averaged ratio of the voltages was used in equation (4.8) to calculate the refractive index of the oil. Three refractive index measurements were made per oil –  $n_1$ ,  $n_2$  and  $n_3$  and the average of the three measurements,  $n_{avg}$  per oil was taken. This was repeated for all eight oils tested. The average refractive index,  $n_{avg}$  was plotted against their corresponding calculated Cauchy values on a calibration chart, shown in Figure 4.6. The error on the experimental data points was calculated by taking the standard deviation,  $n_{stdev}$  of the three measurements per oil.

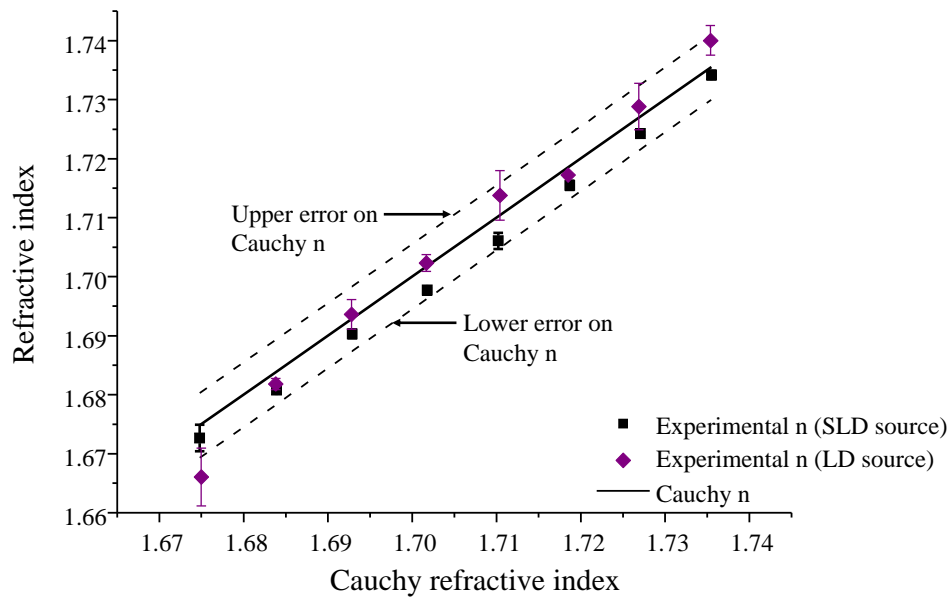


**Figure 4.6-** Calibration chart showing the Cauchy refractive index (marked as a line with upper and lower error limits) and experimentally determined refractive index using SLD (marked as squares) and using LD (marked as diamonds) with error bars.

It can be seen that the experimentally measured values using both the SLD and LD lie within the error bars of the approximated Cauchy values and have a residual error of 1%. The uncertainty in the data set given by  $n_{stdev}$  can be said to be the minimum resolvable change in refractive index. Thus the repeatability,  $\Delta n$  was calculated from the average of  $n_{stdev}$  for the eight tested oils. The repeatability of the system using the SLD source was  $\Delta n = 0.0009$  and for the LD source was  $\Delta n = 0.003$ , calculated to  $1\sigma$ . The SLD source gave ten times better sensitivity to detecting small changes in refractive index compared to the LD source. The larger error bars on the measured refractive index using the LD source arises because of the noise levels in the signal as explained in the following section.

### 4.2.2 Discussion 1: Single source, 2 paths and cleaved fibre in oil

The sensitivity of the system using the LD was compromised because the reflected voltage output from the lock-in amplifiers was very noisy, where the variation in the noise within  $1\sigma$  of the mean of the data set was  $\pm 6\%$  and two orders of magnitude worse than the noise level using the SLD source. The noise levels relative to the output reflectivity are summarised in Table 4-1. The laser diode had a much narrower linewidth compared to the SLD ( $>3000$  times) and hence a longer coherence length of  $>160\text{mm}$  (see section 6.2, page 113). As a result, it was possible for light to reflect multiple times within unwanted etalons in the system, such as the gap between fibre connectors, which would be manifested as interference fringes in the output signal.

**Table 4-1 – Noise levels relative to the output intensity at the reference channel in air and probe channel in air and oil using different sources**

| Source | Reference channel | Probe channel |               |
|--------|-------------------|---------------|---------------|
|        |                   | <i>In air</i> | <i>In oil</i> |
| SLD    | 0.02%             | 0.02%         | 0.6%          |
| LD     | 6%                | 5%            | 13%           |

It can be noticed that the overall signal to noise ratio when using a LD gets worse as the probe channel is immersed in oil because the reflectivity drops by  $\sim 80\%$  and the signal has a higher proportion of noise, as shown in Figure 4.7.

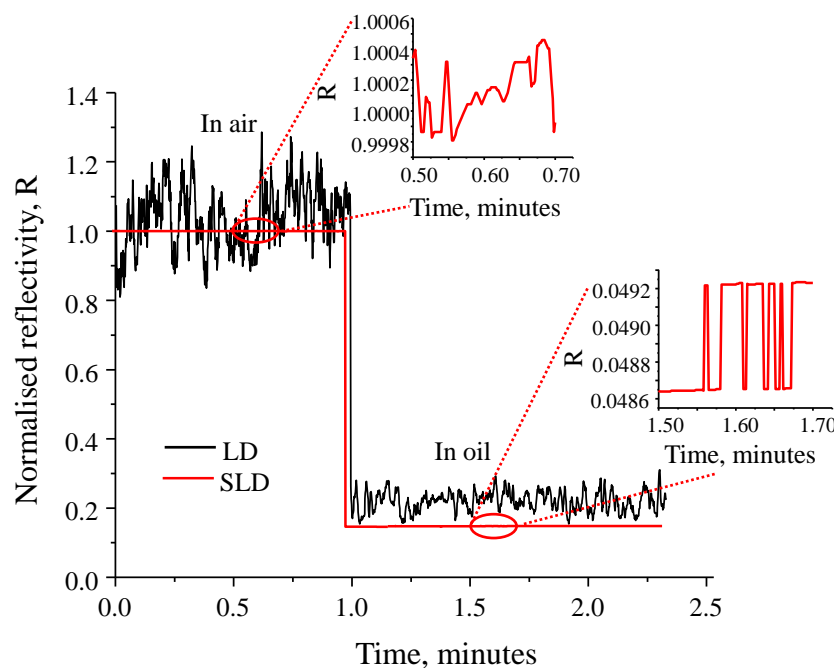


**Figure 4.7- Change in reflectivity as the probe fibre is immersed in oil. The reflectivity measured using a LD has high noise levels compared to SLD measurements.**

Due to a marked improvement in sensitivity from using a broadband source, it was decided that the single source and 2 path experiment would be conducted using the SLD source.

### 4.3 Method 2: Single source, 2 paths and Pd coated cleaved fibre in H<sub>2</sub>

After establishing the refractive index detection capability of the interrogation system using the broadband SLD source, hydrogen tests were carried out on a cleaved probe fibre freshly coated with a 10nm Ni adhesive layer and a 40nm Pd sensing layer (as described in section 3.2.1, chapter 3, page 47). The probe fibre was inserted into a 125cm<sup>3</sup> volume cylindrical gas trial vessel, designed and manufactured by AWE, as shown in Figure 4.8a. Cross-sections of the vessel are shown in Figure 4.8b and c.

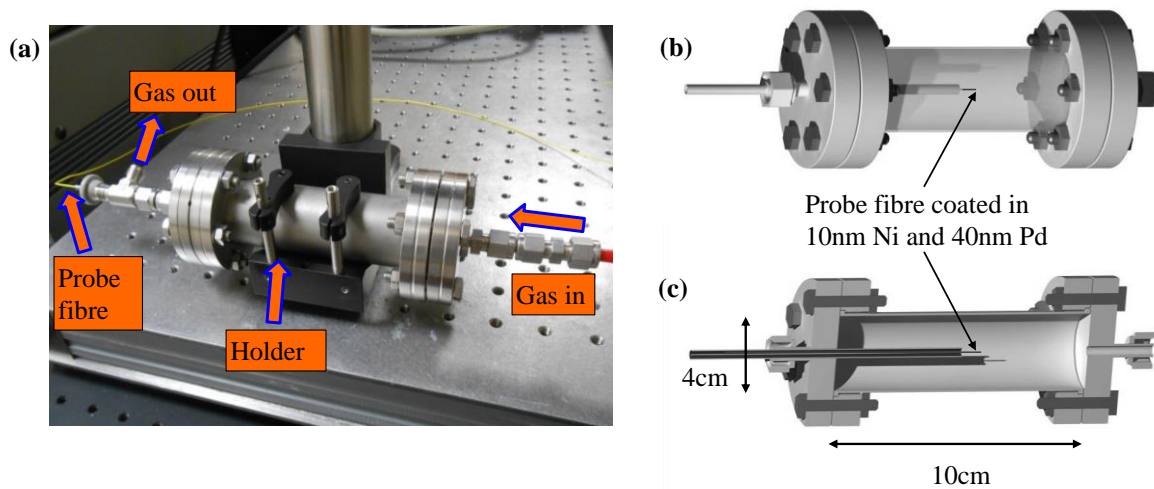


**Figure 4.8- a) Trial vessel used to supply test gases b) Transparent view of a model of the vessel showing the probe fibre. c) Cross-section of the vessel.**

It is important to notice that the Fresnel reflected intensity from a palladium coated fibre is 22 times larger than the Fresnel reflected intensity from an uncoated fibre held in air, as shown in Table 4-2 calculated using equation (4.5).

**Table 4-2 – Fresnel reflected intensities between a fibre ( $n_{\text{fibre}}=1.45$ ) and test medium**

| Interface              | Refractive index, $n$<br>of test medium  | Fresnel Reflectivity |
|------------------------|--|----------------------|
| Fibre – Air            | $n_{\text{air}} = 1$                     | 3.4%                 |
| Fibre – Oil            | $n_{\text{oil}} = 1.72 \text{ to } 1.78$ | 0.7%                 |
| Fibre – 40nm Palladium | $n_{\text{Pd}} = 2.95 - i8.33$           | 74%                  |

A balanced interrogation network was setup so that the amount of light reaching the reference and the probe fibre was equalised as much as possible. The first 1x2 directional coupler with a 50:50 split



ratio in Figure 4.3 was replaced with a 90:10 split ratio directional coupler, where 90% of the light was directed to the reference fibre and 10% to the probe fibre. This is discussed in section 4.3.2.

The test gases were supplied from certified cylinders (BOC) with concentrations of 0 ppm (+1/-0 ppm) and 998 ppm ( $\pm 1$  ppm)  $H_2$  in air. Here, “air” refers to a synthetic mixture of nitrogen and oxygen, substantially free of other trace gases. Gas from the cylinders was fed into a bank of mass flow controllers (Teledyne Hastings HFC-302 with THPS-400 controller) with ranges of (i) 0-1000  $cm^3/min$ , (ii) 0-1000  $cm^3/min$ , (iii) 0-100  $cm^3/min$  and (iv) 0-10  $cm^3/min$ . This system was used to control flow rates from the two cylinders, with downstream mixing generating a series of mixtures of different concentrations in the range 0-1000 ppm  $H_2$  in air. For each step change in concentration applied, a total of 6 minutes was allowed for passage of gas down the connecting pipework, diffusion into the cell and settling of the lock-in amplifiers before taking readings.

At each concentration step, signals from the probe and reference channels were recorded simultaneously and the normalised signal calculated according to equation (4.8). The values of  $(V_{reference})_{air}$  and  $(V_{probe})_{air}$  used to normalise the measurement were established in the same way by supplying air to the trial vessel prior to each gas measurement and again taking readings simultaneously on both channels.

#### ***4.3.1 Results 2: Single source, 2 paths and Pd coated cleaved fibre in $H_2$***

The response of the sensor head to 500ppm  $H_2$  in air was shown in the previous chapter 3, in section 3.2.2, page 48.

Extension of these measurements to other concentrations results in the data shown in Figure 4.9, as the normalised change in reflectivity as a function of hydrogen concentration on a log-log plot. The repeatability was estimated to be 10ppm  $H_2$  in air ( $1\sigma$ ). This was established as 1 standard deviation of each of two series of change in reflectivity measurements made at 0ppm  $H_2$  and 10ppm  $H_2$ . It can be seen that the response was linear in the range 0-1000ppm hydrogen in air, when the palladium hydride is understood to be in the  $\alpha$  phase for a thin palladium film at these concentrations [5]. There is a small amount of zero drift for the 10ppm  $H_2$  measurement and is exaggerated on the log-log plot.

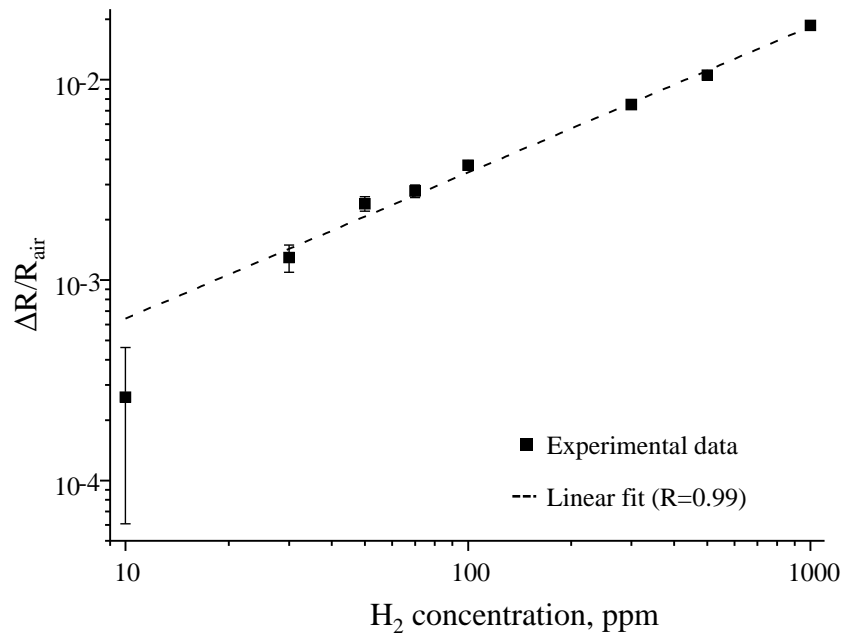


**Figure 4.9-** Normalised change in reflectivity from the cleaved probe fibre coated with 40nm Pd as a function of hydrogen concentration on a log-log plot. The dashed line shows a linear fit for the data points

#### 4.3.2 Discussion 2: Single source, 2 paths, Pd coated cleaved fibre

The system using the 50:50 split ratio coupler was left running in air for a period of 24 hours to allow the palladium coating to regenerate. Over that period it was observed that although both the reflected intensity outputs followed the same trend, the normalised signal displayed significant downward drift and sinusoidal modulations. The normalised graph obtained when using a 50:50 coupler is shown in Figure 4.10a. It was thought that this may have been because of an unsymmetrical network where the reflected intensity from the fibre-Pd interface (probe channel) was 22 times larger than that of the reference channel. The first 1x2 50:50 split ratio coupler was then replaced with a 90:10 split ratio coupler, where 90% of the incident light was directed to the reference channel and 10% to the probe channel. The new setup was run again for 24 hours. However the normalised graph showed an identical downward drift with modulations. This meant that the drift and the modulations were not an artefact of an unbalanced system with mismatched light intensities at the channel ends.

The modulations in the normalised output were attributed to differential temperature effects experienced by the reference and the probe fibre. Thermal responses are likely to arise due to thermal expansion/contraction of the fibre and the associated change in refractive index,  $dn/dT$  (where  $n$  is the refractive index and  $T$  is the temperature). The single source and 2 paths system has a common path up to the first 1x2 coupler in Figure 4.3a. Thermal effects on the first fibre and the first coupler will be compensated during the normalisation routine. Differential temperature effects could affect the split ratios of the two 2x1 couplers on separate arms or on the reference and probe fibre. The fibre couplers

have a high thermal stability as per manufacturer's datasheet [7] and will have negligible impact on the result. For silica fibre, the  $dn/dT$  is  $\sim 11 \times 10^{-6}/^{\circ}\text{C}$  [8] at 1530nm. This would cause the Fresnel reflection to vary by  $\sim 0.004\%$ . Figure 4.10b shows the lab temperature, which was recorded simultaneously using an iButton® DS1923 temperature logger that had a resolution of  $0.5^{\circ}\text{C}$  and an offset of  $0.13^{\circ}\text{C}$  on the temperature accuracy. The peaks in the output coincide with drops in the temperature. Where no temperature change is observed (because it is too small to be detected using a low resolution temperature recorder), the amplitude of the modulations are reduced. For a  $0.5^{\circ}\text{C}$  (maximum) change in temperature, the normalised reflectivity changes by approximately  $0.05\%$ .

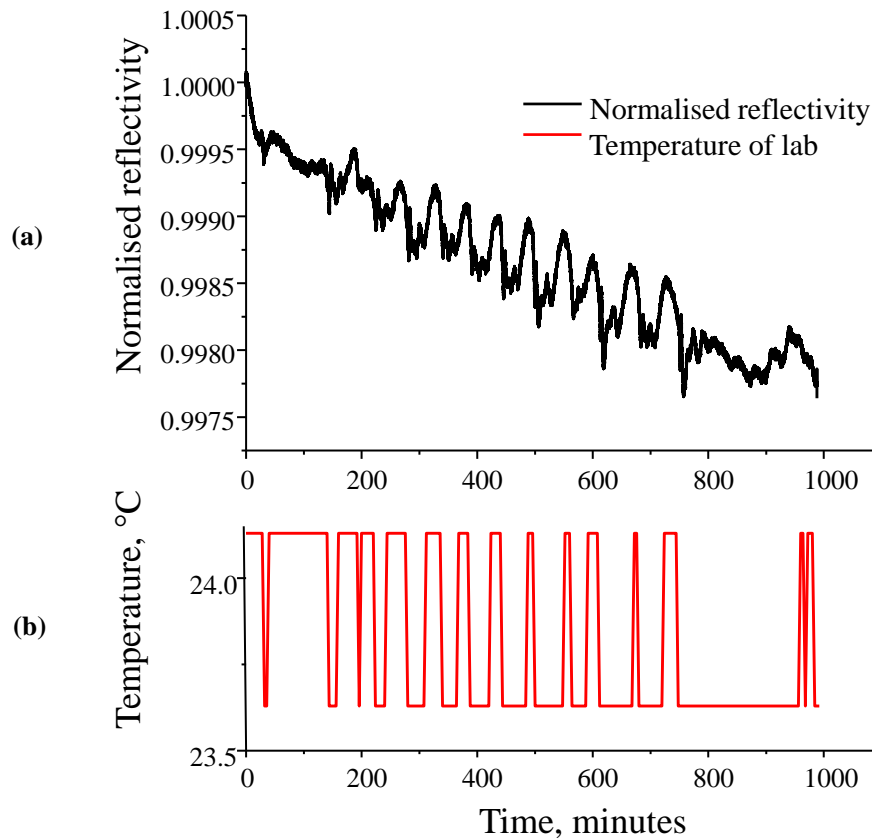


**Figure 4.10- Normalised reflectivity from a long term running experiment using a 50:50 split ratio 1x2 coupler and in lab temperature. Fluctuations in the reflectivity coincide with changes in the lab temperature.**

It is also likely that the differential change in reflectivity is due to changes in palladium refractive index. Temperature effects on palladium's reflectivity can be roughly estimated. Palladium has a low thermal expansion coefficient of the order  $10^{-6}/^{\circ}\text{C}$  [9]. Assuming that the thermally induced lattice expansion of palladium is equivalent to hydrogen induced lattice expansion and also that the expansion is linear in the 0-2% volume hydrogen then from Table 2-1, page 11, it can be said that an exposure of 1000ppm (0.1%) volume hydrogen will cause the palladium lattice to expand by  $2.6 \times 10^{-5}$ . An equivalent thermal expansion of the lattice will occur for a temperature change of  $26^{\circ}\text{C}$  (using palladium's thermal expansion coefficient). If a thermally induced expansion of the palladium lattice

due to a temperature change of  $26^{\circ}\text{C}$  is equivalent to hydrogen induced expansion of the lattice at 1000ppm  $\text{H}_2$ , then it can be said that  $0.5^{\circ}\text{C}$  change in temperature will cause the reflectivity of the probe fibre to change according to 20ppm  $\text{H}_2$ . From Figure 4.9, this roughly accounts for the 0.05% change in reflectivity.

The temperature instabilities could be reduced by using an interrogation method where both the reference and the probe signal would travel down a common path. Such a system has been investigated and described in detail in chapter 6.

Meanwhile, to improve the performance of the current setup, the reference and the probe fibre arms were kept in close thermal contact by taping them together and the entire fibre network was mounted on an insulating polystyrene base. A cardboard box lined with polystyrene was used to cover the fibre network and achieve thermal equilibrium inside the box. The setup is shown in Figure 4.11.

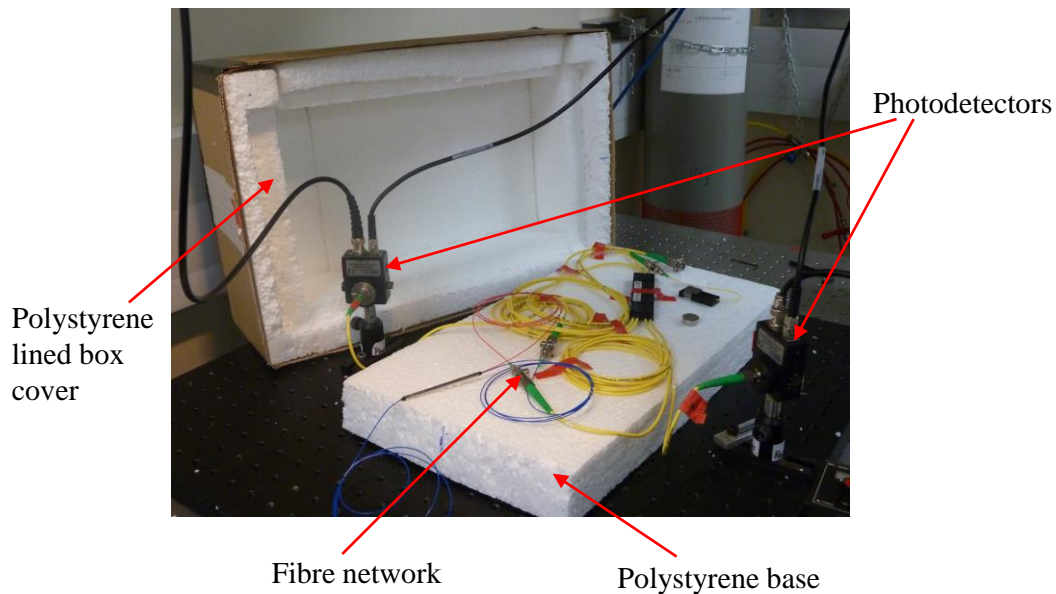


**Figure 4.11- Fibre network kept inside an insulating polystyrene box to reduce temperature fluctuations.**

Two thermocouple temperature loggers (Pico, USB TC-08) with a better resolution of  $0.01^{\circ}\text{C}$  were used to record the temperature for this experiment. One thermocouple was attached to the inside of the box and the second was left outside the box to record the lab temperature. The two temperature recordings are shown in Figure 4.12. The logged temperature of the lab showed rapid fluctuations, whereas the temperature inside the box showed reduced short term fluctuations. Both temperatures follow the same trend of rising in temperature and then reducing temperature subsequently, which coincides with the lab temperature regulator switch on/off schedule. However, this rise and fall in temperature is still partially reflected in the normalised reflectivity.

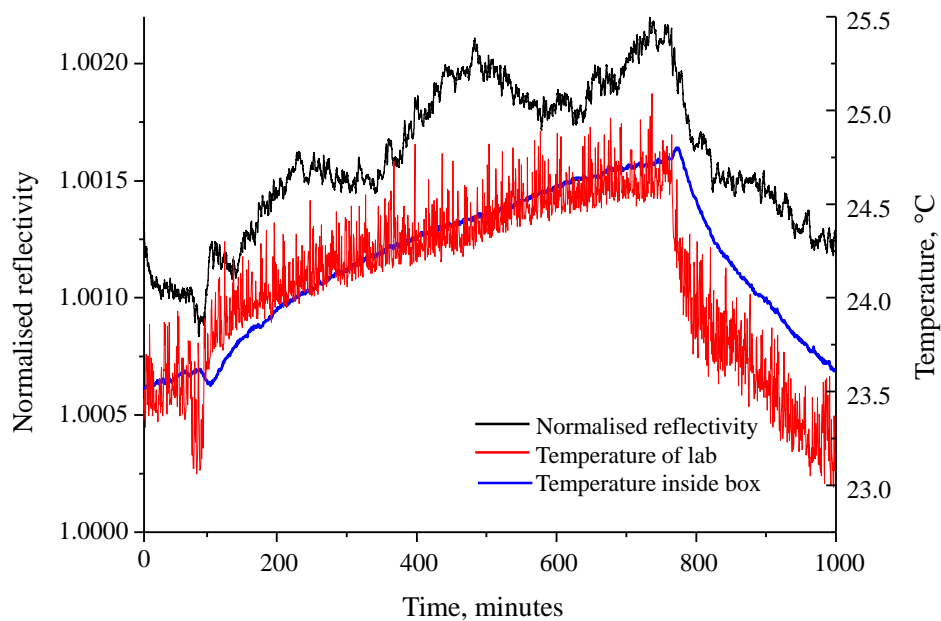


**Figure 4.12- Normalised reflectivity from a long term running experiment using a 90:10 split ratio 1x2 coupler and in an insulating polystyrene box. The box helps reduce fluctuations in temperature in the short term.**

#### 4.4 Conclusion

The concept of a micromirror Fresnel refractometer has been introduced in this chapter, where the reflectivity from the tip of a fibre changes depending on the external medium to which the fibre is exposed. The reflectivity is related to the refractive index of the external medium. Therefore, a change in the reflectivity is a direct indication of the presence of the species that interacts with the fibre tip. This system can be used to determine the level of hydrogen concentration in the environment using a palladium sensing film, which has a high natural affinity for absorbing hydrogen and changes its refractive index.

An interrogation system consisting of a single source and two paths for a reference and probe fibre is reported in this chapter. The probe fibre is placed in contact with the test medium and the reference fibre is left in air. The signal from the reference fibre normalises the signal from the probe fibre to account for fluctuations in the laser output power and variations in the performance of some components. Before hydrogen testing was conducted, the system was characterised for sensitivity and stability using two different sources and a range of test oils of known refractive index. The properties of the sources and the results obtained are summarised in Table 4-3 and show that the system performance is dependent on the type of source used.

**Table 4-3 – Summary of source properties and corresponding sensitivity results**

| Source, $\lambda$ | Linewidth, nm | Minimum detectable $\Delta n$ | Minimum detectable change in reflectivity* |
|-------------------|---------------|-------------------------------|--|
| SLD, 1550nm       | 50            | 0.0009                        | 0.3%                                       |
| LD, 1569nm        | $\leq 0.015$  | 0.003                         | 13%  |

\*In oil

Although both sources demonstrated measurements of the test oil refractive index within 1% residual error, the noise levels in the normalised reflectivity using a LD source led to a compromise in the minimum change in refractive index detection limit,  $\Delta n$  because of the presence of noise consistent with interference fringes.

An interrogation system using the broadband SLD source and a cleaved probe fibre coated with 10nm Ni adhesive layer and a 40nm Pd sensing layer was used to test for hydrogen sensitivity. The Fresnel reflection from a fibre-palladium interface was 22x the Fresnel reflection from the fibre-air reflection. Minor adjustments to the interrogation system were made to balance the amount of light reaching the reference and the probe fibre. The first 1x2 directional coupler with a 50:50 split ratio was replaced with a 90:10 split ratio directional coupler, where 90% of the light was directed to the reference fibre and 10% to the probe fibre. This resulted in an improved intensity ratio between the reference and the probe, at 1:3. The repeatability of the system was established to be 10ppm  $H_2$  in air. The change in reflectivity response plotted against  $H_2$  concentration on a log-log scale was linear in the range 0-1000ppm  $H_2$  in air and the  $PdH_x$  system is assumed to be in the  $\alpha$  phase.

Differential temperature effects on the reference and the probe fibre were demonstrated, which appeared as a result of the two fibres being physically separate. Thermal responses arise due to differential thermal expansion/contraction of the fibre material and the associated temperature dependent refractive index. The normalised reflectivity displayed a downward drift and sinusoidal modulations. The results were consistent with changes in temperature affecting the reflectivity but it is difficult to draw definite conclusion since the temperature logger had a poor resolution. Enclosing the fibre network inside an insulating polystyrene box eliminated the short term rapid fluctuations in temperature but the long term drift related to the lab temperature regulator was still present. The rise and drop in temperature was partially reflected in the normalised reflectivity.

The temperature dependence of the single source and two path interrogation system calls for the need for a system where the reference and probe signals have a common path and multiplexing allows the signals to be separated. The investigation of such a system is reported in chapter 6.

## 4.5 References

- [1] Hecht, E. (1998), *Optics*, 3rd ed, Addison-Wesley Publishing Company, New York, USA.
- [2] Kim, C. B. and Su, C. B. (2004), "Measurement of the refractive index of liquids at 1.3 and 1.5 micron using a fibre optic Fresnel ratio meter", *Measurement Science and Technology*, vol. 15, no. 9, pp. 1683-1686.
- [3] Corning Incorporated Optical Fiber (2002), *Corning Single-Mode Optical Fiber*, available at: <http://ece466.groups.et.byu.net/notes/smf28.pdf> (accessed 15/06/2012).
- [4] Dimopoulos, A., Buggy, S. J., Skordos, A. A., James, S. W., Tatam, R. P. and Partridge, I. K. (2009), "Monitoring cure in epoxies containing carbon nanotubes with an optical-fiber Fresnel refractometer", *Journal of Applied Polymer Science*, vol. 113, no. 2, pp. 730-735.
- [5] Frazier, G. A. and Glosser, R. (1980), "Characterization of thin films of the palladium-hydrogen system", *Journal of The Less-Common Metals*, vol. 74, no. 1, pp. 89-96.
- [6] Libbrecht, K. G., Black, E. D. and Hirata, C. M. (2003), "A basic lock-in amplifier experiment for the undergraduate laboratory", *American Journal of Physics*, vol. 71, no. 11, pp. 1208-1213.
- [7] Laser 2000 (2013), *Fibre Optic Components*, available at: <http://www.laser2000.co.uk/pdfs/download/2013/Fibre-Optic-Components.pdf> (accessed 08/2015).
- [8] Wray, J. H. and Neu, J. T. (1969), "Refractive index of several glasses as a function of wavelength and temperature", *Journal of the Optical Society of America*, vol. 59, no. 6, pp. 774-776.
- [9] Lide, D. R. (2013), *CRC Handbook of Chemistry and Physics*, 94th ed, CRC Press, Florida, US.

# Chapter 5

## Probe sensor heads

It was hypothesized in chapter 3 that the use of a larger sensor head would improve a system's long-term stability and performance. In this chapter two sensor heads, one with a spherical ball lens and the other with a GRIN lens at the end of a singlemode optical fibre are presented. These sensor heads are larger than the SMF core, which would allow greater coverage for the palladium sensing layer, which could reduce the probability of catastrophic failure resulting from pin-holes/cracks and improve the predictability of the sensor's performance. The production of the sensor heads and their sensitivity characterisation using the single source and 2 path interrogation system is presented.



## 5.1 Optical fibre probe sensor heads

### 5.1.1 Background

Swanson *et al* [1] proposed several structures of fibre based optical probes in his patent, for example fibre GRIN (GRAded INdex) lenses and fibre ball lenses at the tip of optical fibres. Fibre ball lenses as a probe have garnered interest recently and have found applications in biomedical imaging. Prince *et al* [2] describe the use of ball lenses in delivery of light for laser angioplasty. The smooth tips minimised the chances of perforation of artery walls. Using a ball lens attached at the end of the fibre, the authors noted that the spot size at the end of the penetration depth into the sample was smaller than the ball diameter. The spot size was varied by varying the fibre input coupling and the numerical aperture. A multi-mode fibre, MMF with a 400 $\mu\text{m}$  core diameter was melted at the tip using an oxy-methane flame/ $\text{CO}_2$  laser to form a tapered section that forms into a ball. A schematic of this sensor head is shown in Figure 5.1. The tapered region allowed the beam to expand to a larger spot size. The tapered region was protected inside a stainless steel housing and wrapped with heat shrink Teflon. However, tapering the tip of the fibre with repeatable results was challenging.

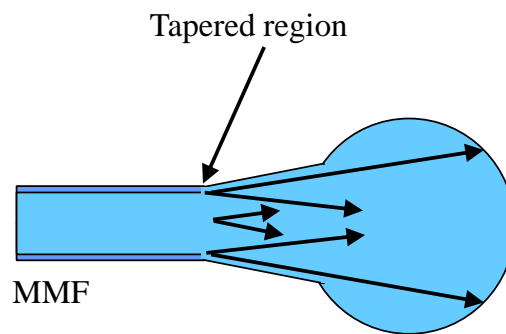


**Figure 5.1- Multimode fibre (MMF) with a tapered section and a ball lens to allow the beam to expand to a larger spot size. Schematic adapted from [2]**

Mao *et al* [3] used ball and GRIN fibre lens probes in OCT (optical coherence tomography) for biomedical imaging of tissue microstructure at a resolution close to cellular level. Similarly to Prince *et al* [2], the authors had difficulty increasing the imaging distance and the spot size because of the small mode field diameter of a standard Corning SMF-28 single mode fibre. The authors took a different approach by allowing the beam to expand first as it propagated from the core through a small piece of fibre spacer. Fibre spacers are pure silica without a core and have a uniform refractive index. The probes were made by splicing a fibre spacer to SMF-28 fibre with a matching diameter of 125 $\mu\text{m}$  and the fibre spacer accurately cleaved to a specific length. For a ball fibre lens probe, an extra 0.2mm of the fibre spacer was used to form a ball shape using a fusion arc. For a GRIN fibre lens probe, an off the shelf multimode GRIN fibre with a core of 100 $\mu\text{m}$ , outer diameter of 140 $\mu\text{m}$  and core refractive index of 1.487 was used to fuse to the fibre spacer. For minimum back reflection, the fibre spacer, centre of GRIN/ball fibre lens and the SMF-28 core were index matched. The ball lens

gave a larger spot size in comparison to the GRIN lens. A 0.55mm long fibre spacer and a ball lens diameter of 150 $\mu$ m achieved a depth of field of 3.6mm in air and a spot size at the tissue of 50 $\mu$ m at an operating wavelength of 1300nm. A 0.48mm of fibre spacer and 140 $\mu$ m length of the GRIN lens achieved 2mm depth of field and 45 $\mu$ m spot size at the tissue. These probes were used in transmission and the ball lens achieved a slightly larger sensing area on the target material.

Recently in 2012 Zhao *et al* [4] described a similar ball lens probe structure to Mao *et al* for OCT for corneal and retinal imaging but used a high refractive index sapphire ball ( $n=1.75$ ), shown in Figure 5.2, which was intended to improve the focussing power. An SMF, followed by an air gap or UV epoxy spacer ( $n=1.5$ ) and finally a sapphire ball lens of diameter 500 $\mu$ m formed the probe sensor head. A common path interrogation system was used with a 1310nm swept source with a tuning range of 100nm. The reference signal for the interferometric measurement came from the fibre distal tip. Using an epoxy spacer of length 169 $\mu$ m and an imaging distance of 1221 $\mu$ m gave a spot size of 18 $\mu$ m.

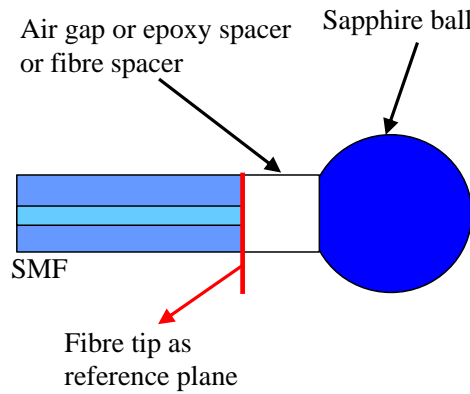


**Figure 5.2- Singlemode fibre (SMF) followed by an air gap or epoxy spacer or fibre spacer allows the beam to expand before entering a ball lens. Schematic adapted from [4]**

Harun *et al* [5] reported a different use for a ball lens that would measure the glucose concentration in ionised water. The ball lens was formed by an arcing technique using a fusion splicer at the tip of a cleaved SMF microfibre coupler. A mirror reflector was fixed perpendicular to the ball lens at a distance of 1.5mm, to form a Fabry-Perot interferometer. The setup is shown in Figure 5.3. Reflection from the ball lens inner wall and the reflection from the mirror interfered inside the ball and the reflected power was measured using an optical spectrum analyser. The experiment used a 1550nm laser source. As the glucose concentration increased, the refractive index of the solution increased and the overall peak power reduced due to a reduced index contrast.

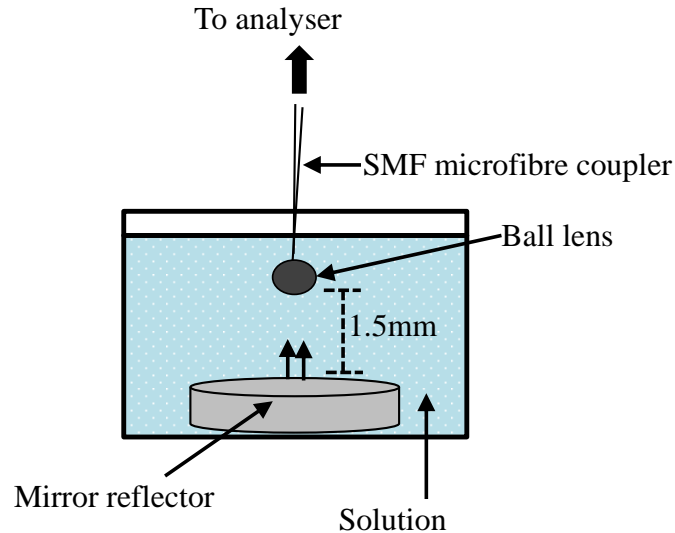


**Figure 5.3- Interferometric technique using a ball lens and a mirror to measure concentration of glucose in the solution. Schematic adapted from [5].**

GRIN fibre lenses have appeared in imaging of tissues using low-coherence interferometry. Owing to their small size, the lenses can be inserted into the body using hypodermic needles. Reed *et al* [6] describes drawing their own fibres out of a Ge-doped GRIN preform to form fibres with a range of outer diameters between 100 and 125 $\mu\text{m}$  and a GRIN core diameter between 70-125 $\mu\text{m}$ . By splicing the GRIN fibre to SMF-28 they were able to achieve a spot size of  $\sim 33\mu\text{m}$  on the target material. Since the GRIN fibres had little cladding, the splice to SMF-28 required positioning of the heat at an offset from the junction by 50-100 $\mu\text{m}$  to avoid glass viscosity mismatch. Minimum insertion loss was found when the GRIN fibre was cleaved at  $\frac{1}{2}$  wavelength pitch length. The authors were able to produce SMF-GRIN probes that were automatically aligned. Another version of their probes had a small piece of coreless quartz rod with an angle cut fused to the top end of the GRIN lens. The beam would exit off-axis and trace a cone when the fibre was rotated for rotation scanning of the tissues. This allowed high NA focussing since a single GRIN fibre lens cannot focus a collimated beam at a shorter distance than its initial waist.

Optical fibre probes have mainly found uses in medical applications due to their micro-dimensional size allowing easy insertion in the body. In this thesis an application for such small probes have been found that can be permanently installed in a small materials testing chamber. Whilst most of the described sensors are used in transmission for imaging samples at a distance from the probe tip, in this project a model for light reflected by the final end face of the probe tip back into the core has been developed. The ball lens production method is similar to the approach used by Harun *et al* [5] using a fusion splicer and is described in detail in sections 5.2.2 and 5.2.3.

## 5.2 Ball lens sensor head

Laser light emitted from a single mode fibre will expand radially in the direction of travel,  $z$  with a Gaussian profile in a homogenous medium [7]. The beam radius increases as the beam expands and can be focused back into the single mode fibre core using a spherical lens. Thus a ball lens acting as a mirror with a radius of curvature that matches the wavefront curvature will allow beam expansion to a larger beam spot radius compared to a SMF spot radius and then reflect this back into the core. This is illustrated in Figure 5.4. The theory of Gaussian beam expansion is described in section 5.2.1 and a model for choosing the optimum size of the ball lens.

### 5.2.1 Theory of Gaussian beam expansion

The beam starts to propagate at  $z = 0$  (at the output of the fibre) from a minimum beam waist radius or spot radius,  $\omega_0$  where the beam intensity has fallen to  $1/e^2$  (13.5%) of its peak and the wavefront is planar with an infinite radius of curvature,  $R(z)=\infty$ . The radius of curvature passes through a minimum at a finite  $z$  and increases as  $z$  is further increased.

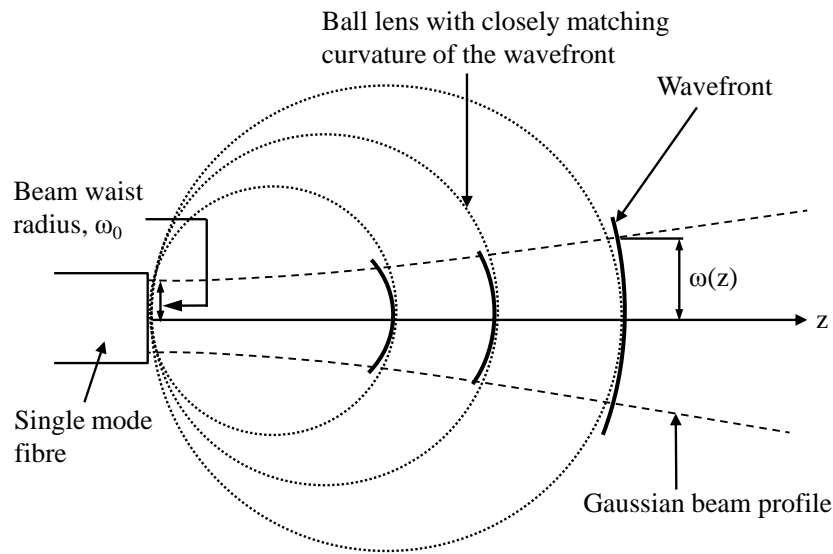


**Figure 5.4-** Gaussian beam propagation from the output of a single-mode fibre. Construction lines representing ball lenses of various sizes are presented as well as representations of diverging wavefronts to illustrate the optimum ball lens size at which the coupling efficiency of reflected light back into the core will be maximized.

The radius of wavefront curvature,  $R(z)$  is defined by equation (5.1) for beam expansion in the ball lens medium [7].

$$R(z) = z \left[ 1 + \left( \frac{n_{ball} \pi \omega_0^2}{\lambda z} \right)^2 \right] \quad (5.1)$$

The ball lens is assumed to have a uniform refractive index  $n_{ball}$ ,  $\omega_0$  is the beam waist radius, ( $5.2\mu\text{m}$  for SMF-28 fibre) at  $z = 0$  and  $\lambda$  is the operating wavelength ( $1550\text{nm}$ ).

For the optimum curvature of the ball lens, at which most of the reflected light will be coupled back into the core, the wavefront radius of curvature,  $R(z)$  must be equal to the radius of the ball lens,  $z/2$ . This condition would ensure that the beam would be normally incident on the ball lens surface, and we would expect a Fresnel reflection from the latter that is dependent on the refractive index of the external medium. Figure 5.5 shows the change in ball lens radius,  $z/2$  and the wavefront radius,  $R(z)$  with increasing propagation distance  $z$ , calculated using equation (5.1). There is no point of intersection between the two traces that would allow maximised coupling of reflected light back into the fibre. It was therefore chosen to work with ball lenses at the upper end of the range supported by the fusion splicer, in order to maximise the illuminated area of the ball lens. The reflectivity of the ball lens as a function of its diameter is shown in sections 5.2.2 and 5.2.3.

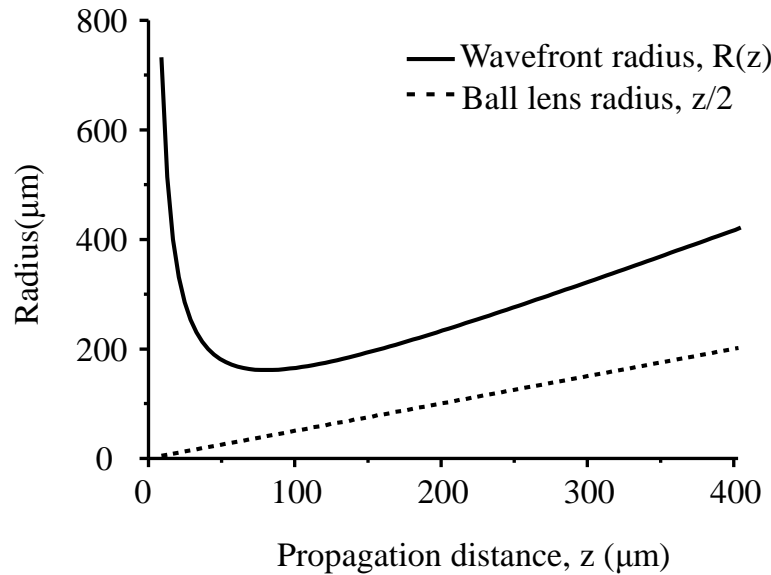


**Figure 5.5- Change in ball lens radius,  $z/2$  and the wavefront radius increasing with propagation distance,  $z$  for a Gaussian beam exiting the singlemode fibre.**

The evolution of the beam waist radius as a function of propagating distance,  $\omega(z)$  is defined by equation (5.2) and displayed graphically in Figure 5.6.

$$\omega(z) = \omega_0 \left[ 1 + \left( \frac{\lambda z}{n_{ball} \pi \omega_0^2} \right)^2 \right]^{1/2} \quad (5.2)$$

The beam waist radius  $\omega_0$  for wavelength  $\lambda$  is given by equations (5.3) and (5.4) [8].

$$\omega_0^2 = \frac{d^2}{\ln v^2} \quad (5.3)$$

$$v = \frac{2\pi d}{\lambda} \sqrt{2(n_{core} - n_{clad})n_{core}} \quad (5.4)$$

Where  $d$  is the core radius of SMF-28 (4.1  $\mu\text{m}$ ),  $v$  is the normalised wave number,  $n_{core}$  and  $n_{clad}$  are the refractive indices of the fibre core and cladding respectively. It can be noted here that the  $v$  value is responsible for the number of modes that a fibre can guide. For  $v < 2.405$  at wavelength  $\lambda$ , the fibre can guide only a single spatial mode of light making single-mode fibres.

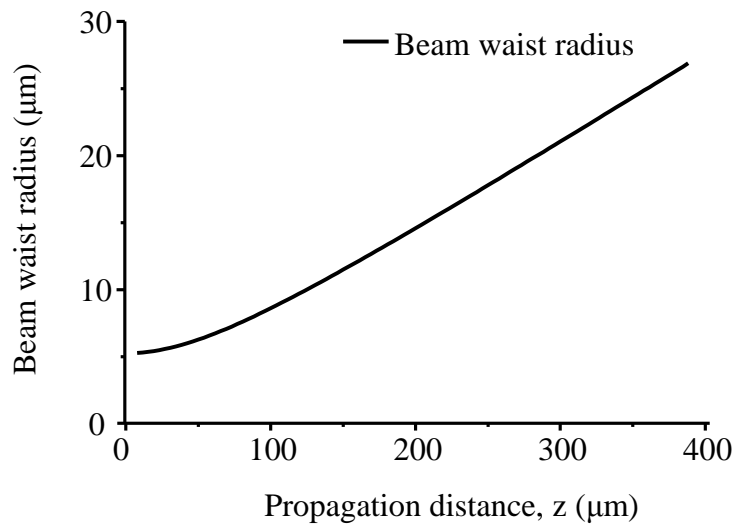


**Figure 5.6-** The beam waist radius increase with propagation distance,  $z$ .

### 5.2.2 Ball lens preparation A: Manual

Ball lenses were made in a fusion splicer (Fujikura, FSM-100P) by clamping the cleaved tip of a singlemode fibre (Corning SMF28) near the electrodes where the electric arc is produced. The tip melts in the arc and forms into a ball under the surface tension. The geometry of the ball lens was dependent on three parameters – i) arc current, ii) arc time (melting time) and iii) position of the fibre relative to the electrodes. Three sets of experiments were carried out where the fibre was fixed 500  $\mu\text{m}$  to the left of the centre of the electrode, fixed at the centre and 1000  $\mu\text{m}$  to the right of the centre of the electrode. These were the maximum distances that the splicer stage motors could manoeuvre. For each experiment, the arc current and the arc time were increased to increase the diameter of the ball lens formation.

Using an arc current of 24mA and the fibre 500  $\mu\text{m}$  to the left of the electrodes, as shown in Figure 5.7a, the resulting ball lens was small in size. A 4s melting time was insufficient to melt the tip into a ball and instead formed a rounded dome shape (Figure 5.7b). For an increased melting time of 120s, the fibre tip started to form a ball shape with a diameter of 165  $\mu\text{m}$  (Figure 5.7c).

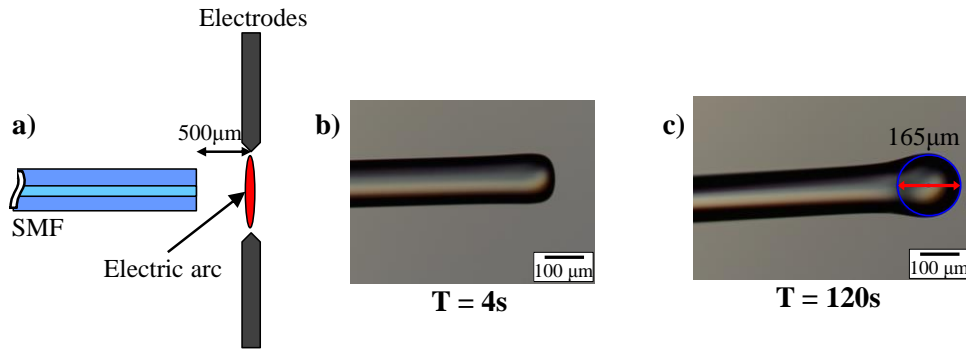


**Figure 5.7- Manual ball lens production a) fibre positioned 500 $\mu$ m to left of centre of electrodes b) low melting time of 4s gives a rounded dome at the tip c) 120s melting time forms a small diameter, 165 $\mu$ m, ball.**

To make the ball lens bigger, the arc current was increased to 40mA and the fibre was fixed at the centre of the electrode (Figure 5.8a). Using a 4s melting time the ball lens diameter grew by 70% to 280 $\mu$ m as shown in Figure 5.8b.

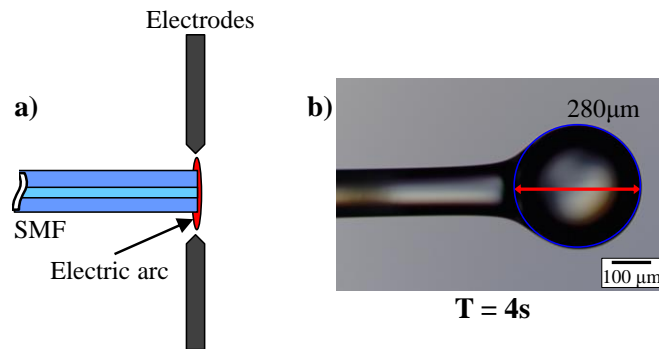


**Figure 5.8- Manual ball lens production a) fibre positioned at centre of electrodes b) a 4s melting times forms a larger diameter, 280 $\mu$ m, ball lens.**

To further increase the size of the ball lens, the fibre tip was positioned 1000 $\mu$ m to the right of the centre of the electrodes (Figure 5.9a) so that more of the fibre was available for melting. This resulted in bigger ball lenses with diameters of 360 $\mu$ m for 4s and 370 $\mu$ m for 9s, which are shown in Figure 5.9b and Figure 5.9c respectively.

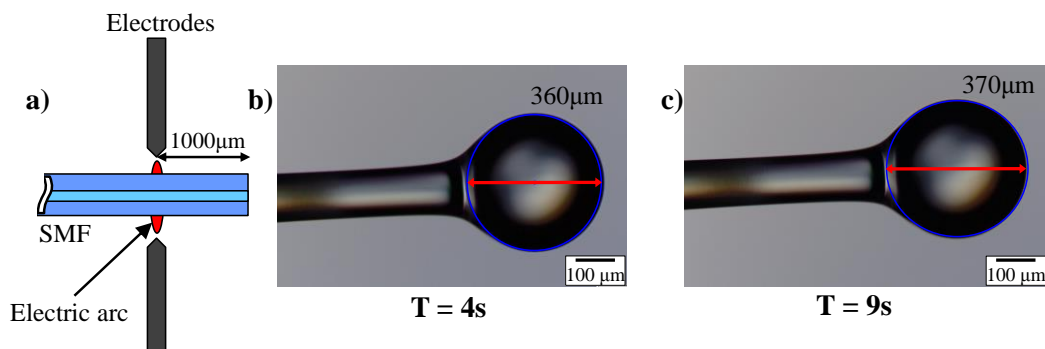


**Figure 5.9- Manual ball lens production a) fibre positioned 1000 $\mu$ m to right of centre of electrodes b) a 4s melting time forms a larger ball of diameter 360 $\mu$ m c) increasing the melting time to 9s makes a bigger ball lens with diameter, 370 $\mu$ m.**

Reflected power measurements from the tip of these fibres were made using the single source and two path refractometer described in chapter 4. The reflected power for the different ball lens sizes is summarised in Table 5-1 and shown graphically in Figure 5.10, where the experimental data has been fitted with a polynomial curve.

**Table 5-1 – Summary of ball lens sizes and their reflected power relative to a cleaved control fibre**

| Settings                           | Shape         | Curvature diameter ( $\mu\text{m}$ ) | Propagation distance, $z$ ( $\mu\text{m}$ ) | Reflectivity %* |
|------------------------------------|---------------|--------------------------------------|---|-----------------|
| None                               | Cleaved fibre | $\infty$                             | 3   | 100             |
| L-500 $\mu\text{m}$ , 23.7mA, 4s   | Arc/dome      | 60                                   | 40  | 55              |
| L-500 $\mu\text{m}$ , 23.7mA, 120s | Small ball    | 165                                  | 165   | 4               |
| Centre, 40mA, 4s                   | Ball          | 280                                  | 280   | 1               |
| R-500 $\mu\text{m}$ , 40mA, 4s     | Ball          | 328                                  | 328   | 6               |
| R-1000 $\mu\text{m}$ , 40mA, 4s    | Ball          | 360                                  | 360   | 20              |
| R-1000 $\mu\text{m}$ , 40mA, 9s    | Ball          | 370                                  | 370   | 31              |

\* Reflectivity relative to cleaved fibre

Similar to the Gaussian beam propagation model, the  $x$ -axis for the graph in Figure 5.10 uses the propagation distance,  $z$  as being equivalent to the distance travelled by light along the diameter of the ball lens. For a cleaved fibre with infinite curvature at  $z = 0$ , the reflectivity was maximum. When the melted tip was in the shape of an arc or a small ball, the light reflectivity dropped to a minimum for a ball lens with diameter of 240 $\mu\text{m}$  and then starts to increase again for increasing ball lens size.

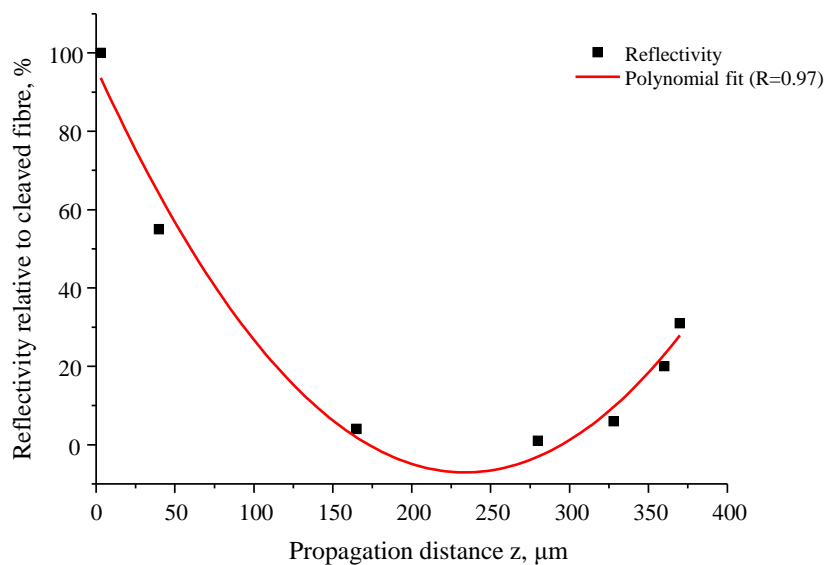


**Figure 5.10- Variation in reflected light intensity by the ball lens inner wall after propagating a distance  $z$  inside the ball lens. The data is fitted with a polynomial curve fit.**



However, the production of the ball lens using the manual setting has its limitations, especially the positioning of the fibres shown in Figure 5.8 and Figure 5.9. The clamps that held the fibres in position were very close to the electric arc and suffered the risk of burning. Instead, an automated process to make the ball lenses was adopted, which is described in the following section.

### 5.2.3 Ball lens preparation B: Automated

Ball lens preparation was automated using Fujikura's proprietary software [9] linking to the fusion splicer. The software allowed production of ball lenses safely up to a maximum diameter of 400 $\mu\text{m}$ . The software required a few input design parameters for the ball lens geometry and depending on the defined parameters, the software could control the movement and rotation of the fibre holders in the splicer, the heat power and the melting time. The parameters that need to be defined by the user are: i) required ball lens diameter,  $\varphi$  ii) fibre diameter, iii) offset, which allows fine adjustment of the distance between the splice point and centre of the ball lens, and iv) distance  $b$ , which is the separation between the splice point/offset value point and the centre of the ball lens. These parameters are highlighted in bold and blue font in Figure 5.11. The value  $b$  and the offset value allows production of a ball lens using a spliced section of a different fibre.

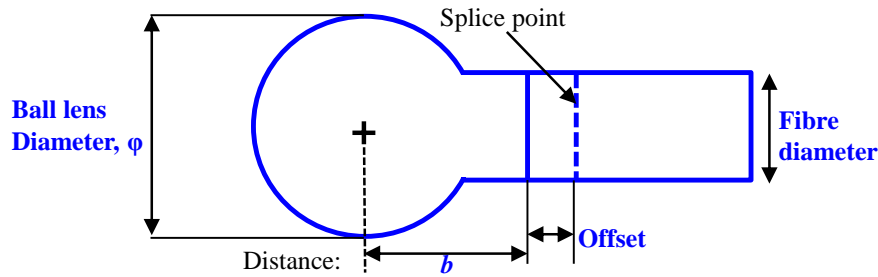


**Figure 5.11- Parameters that define the geometry of a ball lens – ball lens diameter, fibre diameter, distance between the centre of the ball lens and splice point and an offset value for fine adjustments.**

For a ball lens diameter  $\varphi$  set to 350 $\mu\text{m}$ , and the offset and value of  $b$  set to zero, the software specified an arc current of 20mA and a melting time of ~65s. The ball lens was created at the tip of SMF-28 fibre and viewed after fabrication through immersion oil that matches the refractive index of the cladding, to allow better visibility of the core. The image is shown in Figure 5.12a. It can be observed that the core was still present and its orientation has been affected by gravity. A rotation speed of 10°/s ensured even heat distribution during the melting process and this corrected the bending of the core, as shown in Figure 5.12b. The reflected light levels were similar to the values in Table 5-1. However, the reflected light can still be guided by the core, which invalidates the use of Gaussian beam expansion model in a homogeneous medium. For a ball lens diameter  $\varphi$  set to 400 $\mu\text{m}$  and with rotation applied during the melting, the core spun and appeared twisted, which is shown in Figure 5.12c. It is possible that the rotational speed was too low for this ball lens size and

consequently the geometry of the ball is not symmetrical. This ball lens did not reflect any light back into the core.

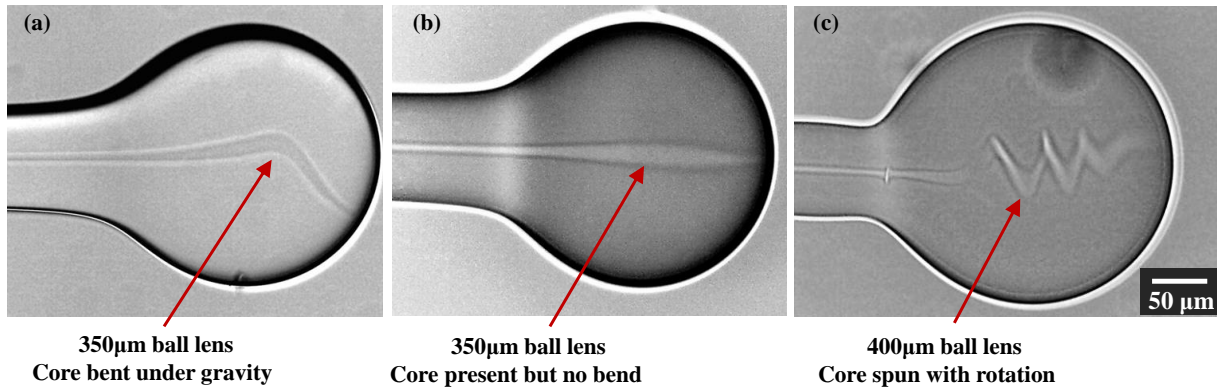


**Figure 5.12-** a) SMF28 tip melted with no rotation to form a 350µm diameter ball lens. The core is still present and its orientation affected by gravity. b) Rotating the fibre during melting corrects the bending. c) 400µm diameter ball lens with a spun core. The fibres are viewed through an immersion oil that allows better contrast to see the core

To eliminate the presence of the core in the ball lens, a short length of coreless silica fibre (FiberCore, MM125) with a matched cladding diameter of 125µm and a refractive index of 1.444 was spliced to the SMF-28. The production sequence is shown in Figure 5.13.

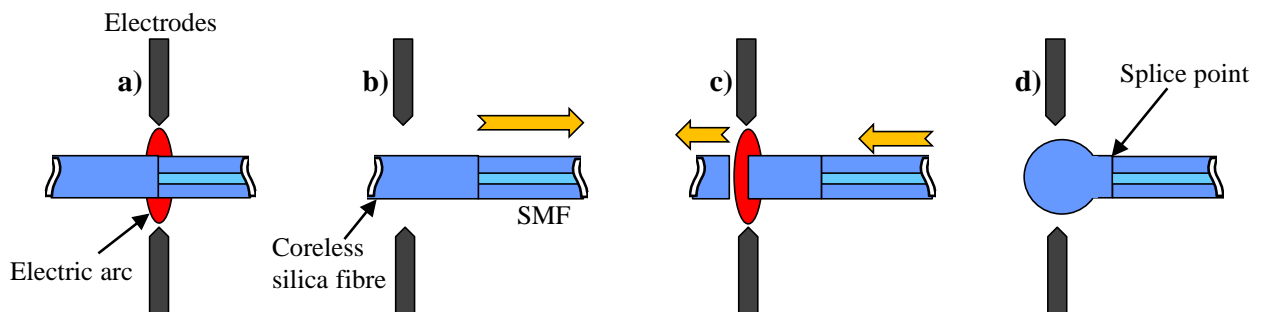


**Figure 5.13-** Illustration for the automated process of a) splicing a SMF-28 and coreless silica fibre, b) shifting spliced fibre to leave an appropriate length of the coreless silica fibre to form a ball lens, c) breaking and d) ball-lensing.

The MM125 fibre is spliced to the SMF-28 and then shifted to acquire an appropriate length of the coreless silica fibre required to form a ball lens with the user-defined geometry, before breaking off the fibre on the left. The fibre tip is then melted with an arc power that is 30% more than that for splicing. The splicer captures images and applies a geometry based algorithm to measure the ball lens diameter. A 350µm diameter ball lens of pure silica, assumed to have uniform refractive index at the tip of the SMF-28, is shown in Figure 5.14.

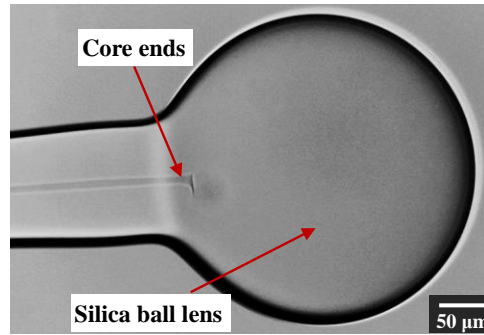


**Figure 5.14-** Pure silica ball lens formed at the tip of a single mode fibre.

The core ends right before the formation of the ball lens, as set by the value  $a$ . But it can be seen that the core tapers slightly and then fans out. This was a feature of the ball lensing process, possibly affected during the melting of the coreless fibre close to the SMF28 core during the production sequence shown in Figure 5.13c.

A range of ball lens sizes was tested experimentally and reflectivity measurements were made using the single source and 2 path refractometer described in chapter 4. Some of these measurements are summarised in Table 5-2. A pattern was observed where the reflectivity was dependent on the accuracy of the measured diameter (difference between the set diameter and the measured diameter), with an approximate error between  $\pm 0.3\%$  and  $\pm 0.5\%$  of the set diameter such that the set value of  $b$  is half the set diameter. The reflectivity was also dependent on the symmetry of the ball and the tapering of the core. Qualitative assessments of the symmetry and the tapered core were performed by observation. The tapering helped reduce the numerical aperture of the core and forced the beam to expand, which in turn improved the reflectivity from the ball lens end. The quality of the accuracy, symmetry and taper is flagged using red (poor), orange (medium) and green (good) colours in Table 5-2. The accuracy of the measured diameter and the repeatability could be improved with frequent calibration of the splicer in between ball lens production.

**Table 5-2 – MM125 ball lens (BL) of varying diameter produced using the automated software and the corresponding reflectivity. The quality of the accuracy, symmetry and the taper is flagged using red (poor), orange (medium) and green (good) colours.**

| Set $\phi$<br>( $\mu\text{m}$ ) | Measured $\phi$<br>( $\mu\text{m}$ ) | Set $b$<br>(mm) | Reflectivity<br>(%)* | BL chosen for<br>experiments | Qualitative assessment |          |       |
|---------------------------------|--------------------------------------|-----------------|----------------------|------------------------------|------------------------|----------|-------|
|                                 |                                      |                 |                      |                              | Accuracy               | Symmetry | Taper |
| 335                             | 336.7                                | 0.17            | <b>1.5</b>           | B (Chap 6 & 7)               |                        |          |       |
| 335                             | 340.5                                | 0.17            | <i>nd</i>            |                              |                        |          |       |
| 349                             | 348.6                                | 0.18            | <b>4</b>             |                              |                        |          |       |
| 349                             | 348.7                                | 0.18            | <b>0.3</b>           |                              |                        |          |       |
| 349                             | 348.9                                | 0.18            | <b>10</b>            |                              |                        |          |       |
| 349                             | 349.9                                | 0.18            | <b>0.5</b>           |                              |                        |          |       |
| 350                             | 350.2                                | 0.18            | <b>0.4</b>           |                              |                        |          |       |
| 350                             | 350.8                                | 0.18            | <b>4</b>             |                              |                        |          |       |
| 349                             | 351.8                                | 0.18            | <i>nd</i>            |                              |                        |          |       |
| 349                             | 352                                  | 0.18            | <i>nd</i>            |                              |                        |          |       |
| 350                             | 353.8                                | 0.18            | <i>nd</i>            | A (Chap 5 & 7)               |                        |          |       |
| 400                             | 402.1                                | 0.2             | <i>nd</i>            |                              |                        |          |       |
| 400                             | 408.6                                | 0.2             | <i>nd</i>            |                              |                        |          |       |
|                                 |                                      |                 |                      |                              |                        |          |       |

\*: Reflectivity measured as a % of cleaved control fibre

*nd*: not detected; minimum detectable power 0.2%

The reflectivity measured as a percentage of the cleaved control fibre for SMF28 ball lenses shown in Table 5-1 was much higher than the reflectivity of the MM125 ball lenses. This could be the influence of the core being present and guiding the returning light back. The SMF28 ball lenses had better reproducibility and increased reflected signal, however the spot size was smaller than the MM125 ball lens (discussed below). The close refractive index matching of the core and the silica ball means that the Fresnel reflection at that interface was negligible ( $\sim 0.01\%$ ) and it can be assumed that a portion of the reflected light has reached the final end face of the sphere and interacted with the palladium.

The optimum diameter of the MM125 ball lens was  $349 \pm 1\mu\text{m}$ . Given that this does not correspond to a match between ideal ball lens radius and ideal wavefront curvature, as indicated in Figure 5.5, these results may indicate either that there is a slight distortion in the ball lens curvature created during fabrication, or that there is some distortion of the wavefront at the end of the single mode fibre core. Also, the original Gaussian model is not representative of the light reflected into the core due to the tapering of the core at the tip. From the limited testing done, the  $350\mu\text{m}$  ball lens gave more successful results than the  $400\mu\text{m}$  ball lens. However, this does not mean that a  $400\mu\text{m}$  diameter ball lens will not reflect light back into the core. More ball lenses with bigger diameters need to be tested.

The spot sizes of the SMF-28 bare fibre and  $349\mu\text{m}$  diameter MM125 ball lens were imaged under a microscope with 200x magnification. A 532nm green DPSS (diode pumped solid-state) laser (Photop Suwtech, model DPGL-3010F, 10 mW output power) was used for this work as the camera associated with the microscope is not sensitive to the 1550nm design wavelength of the fibre. Figure 5.15a shows the side view of an illuminated  $349\mu\text{m}$  MM125 ball lens under the microscope and the spot

size of the ball lens from the top view is shown in Figure 5.15b. The much smaller spot size originating from an SMF28 core is shown in Figure 5.15c. The spot size of a 35 $\mu$ m SMF28 ball lens is also shown in Figure 5.15d for comparison. The spot area is relatively smaller than an MM125 ball lens of same size.

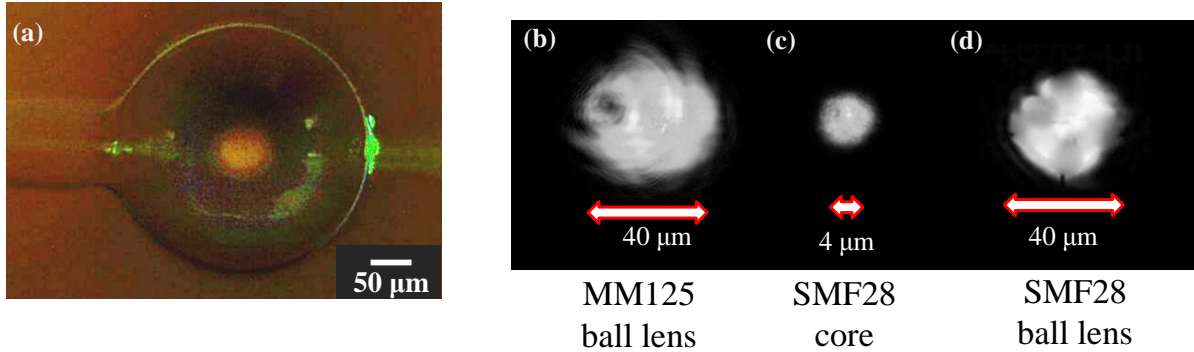


**Figure 5.15-** Images taken of the illuminated fibre from the side and from the top ends when connected to a 532nm laser source, using an optical microscope focused onto the fibre tip. a) Side view of an illuminated 349 $\mu$ m diameter MM125 ball b) End view of a 349 $\mu$ m diameter MM125 ball lens; c) End view of bare SMF28 fibre core; d) End view of a 350 $\mu$ m diameter SMF28 ball lens. Calculated spot diameters at 532nm are shown by the arrows.

At 532nm wavelength the calculated spot diameter of the cleaved SMF-28, using equations (5.3) and (5.4), is 4 $\mu$ m and that of the ball lens is 40 $\mu$ m. It was not possible to measure from the image the spot diameter where the beam intensity falls to  $1/e^2$  but the calculated values are consistent with the images and within the measured diameter from the image

At 1550nm, the spot diameters of the SMF-28 core and the 349 $\mu$ m diameter ball lens were calculated to be 10.4 $\mu$ m and 47 $\mu$ m respectively (from Figure 5.6), with sampling areas of 87 $\mu$ m<sup>2</sup> and 1720 $\mu$ m<sup>2</sup>.

In an ideal case, the maximum coupling efficiency of reflected light back into the core will occur at a ball lens radius that is equal to the wavefront radius. However, there is no ideal size of ball lens at which wavefront radius and ball lens radius intersect. Nevertheless, a ball diameter of 349 $\mu$ m was found to provide an acceptable level of reflectivity to permit sensor development. With the radii of curvature no longer matching, the effective sampling area of the spot size therefore becomes somewhat uncertain; we can assess the illuminated area of the sensor head, but not which parts of this area reflect light back into the core. The SMF ball lens is worth re-investigating since it provided improved and consistent reflectivity for the same size of a MM125 ball lens with a marginally smaller spot size.

### 5.3 Method 1: Single source, 2 paths and ball lens in oil

The sensitivity of the ball lenses as sensor heads was first characterised using oils of known refractive index using the single source (1550nm SLD) and 2 paths (where the first 1x2 directional coupler had a 50:50 split ratio) interrogation system as described previously in chapter 4, section 4.2, Figure 4.3, page 69.

#### 5.3.1 Results 1: Single source, 2 paths and ball lens in oil

The uncoated ball lens with diameter 350.8 $\mu$ m from Table 5-2 (ball lens A), was immersed in oils of known refractive index in the range 1.60 to 1.68 (Cargille Labs, Series M) measured at 589nm and 25°C. A Cauchy dispersion equation (provided by the manufacturer) was used to calculate the refractive index of the oils at 1550nm and 25°C. The resulting error in the calculated refractive index was  $\pm 0.005$  according to the manufacturer. The oils were mounted on a Peltier element to maintain a constant temperature of  $25 \pm 0.1^\circ\text{C}$ . The refractive index of the oils,  $n_i$ , were determined from equation (4.9) in chapter 4, page 68.

The oil calibration chart shown in Figure 5.16 shows the experimentally determined refractive index using the ball lens refractometer against the calculated Cauchy refractive index values at 1550nm and 25°C. The refractive index of each oil was experimentally measured three times and the average value plotted. The error on each data point is the standard deviation of the repeated set. This is explained in more detail in section 4.2.1, page 71. The Cauchy and experimental values match closely for each oil (with 1% residual) and lie within the expected error as quoted by the manufacturer. The minimum detectable change in refractive index,  $\Delta n$  is 0.0012 ( $1\sigma$ ).

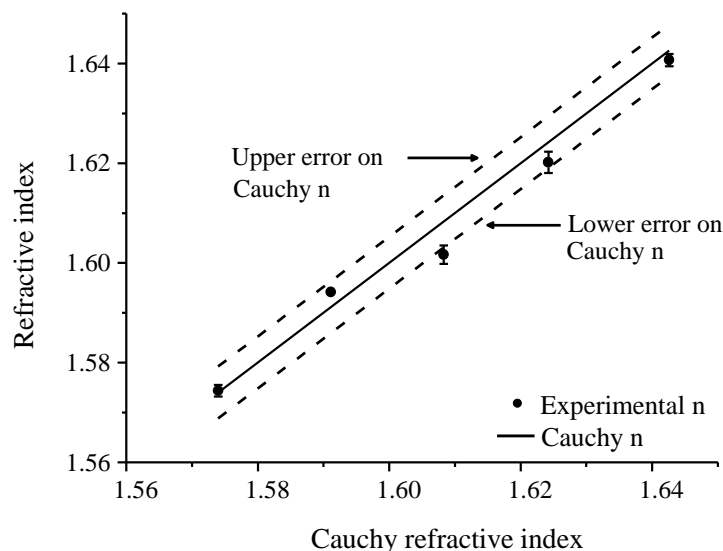


**Figure 5.16-** Calibration chart showing the Cauchy refractive index (marked as a line with upper and lower error limits) and experimentally determined refractive index (marked as circles) with error bars

### 5.4 Method 2: Single source, 2 paths and Pd coated ball lens in H<sub>2</sub>

Ball lens A from Table 5-2, with a reflectivity of 4% relative to a cleaved fibre and a diameter of 350.8µm, was coated with 40nm Pd with an underlayer of 10nm Ni and tested in hydrogen in the trial vessel. The trial vessel was shown previously in Figure 4.8 in chapter 4, page 74. The measurements were taken using the single source (1550nm SLD) and 2 path interrogation system described in section 4.2, page 69. The sensor head was tested three times in six months under different circumstances, which are summarised in Table 5-3.

**Table 5-3 – Summary of ball lens testing conditions over 6 months**

| <b>Date</b> | <b>System configuration*</b> | <b>Time in vacuum</b> | <b>Range of H<sub>2</sub> conc. (ppm)</b> | <b>Cycling period</b>                  |
|-------------|------------------------------|-----------------------|---|--|
| Month 1     | 50:50 coupler                | -                     | 0 – 10,000                                | 2mins in H <sub>2</sub> , 3mins in air |
| Month 4     | 50:50 coupler                | 1 month               | 0 – 1000                                  | 3mins in H <sub>2</sub> , 6mins in air |
| Month 6     | 90:10 coupler                | 1.5 months            | 0 – 1000                                  | 3mins in H <sub>2</sub> , 6mins in air |

\*: Single source (1550nm SLD) and 2 path configuration with a different first coupler

In the first two tests, a 50:50 split ratio coupler was used as the first directional coupler. The third test used a 90:10 split ratio coupler to improve the symmetry of light reaching the reference and the probe fibre (90% reaching the reference fibre and 10% reaching the probe fibre). The sensor head was left in a vacuum chamber in between its testing as it was realised that the palladium coating will re-generate faster as well as reduce oxidation and contamination from exposure in air. After the sensor was tested in hydrogen in Month 1, it was stored in air for 2 months and then kept in a vacuum chamber at AWE plc for a month before it was tested again in Month 4. The second time round, the sensor was stored in air for 2 weeks before being transported to the vacuum chamber at AWE plc. It was left in vacuum for 1.5 months.

The first test, carried out in Month 1, used test gases supplied from certified cylinders (BOC) with concentrations of 0 ppm (+1/-0 ppm) and 10,000 ppm (±100 ppm) H<sub>2</sub> in air, whereas the remaining tests focussed on a smaller concentration range of 0 ppm (+1/-0 ppm) and 998ppm (±1 ppm) H<sub>2</sub> in air. Here, “air” refers to a synthetic mixture of nitrogen and oxygen, substantially free of other trace gases. A bank of mass flow controllers (described in section 4.3, page 74) was used to control flow rates from the two cylinders to generate a different concentrations in the range 0-10,000 ppm H<sub>2</sub> in air or 0-1000 ppm H<sub>2</sub> in air.

### 5.4.1 Results 2: Single source, 2 paths and Pd coated ball lens in $H_2$

A typical sensor response for a range of hydrogen concentrations is shown in Figure 5.17. It can be observed that the signal from the sensor in air does not return to the starting baseline and this is attributed to extended recovery times (see section 5.4.2).

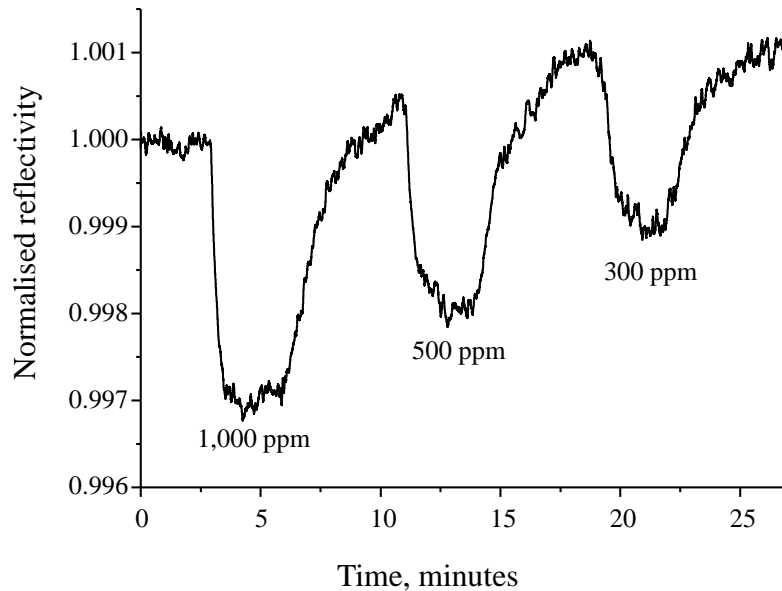


**Figure 5.17- Normalized reflectivity measured from 40nm Pd coated 350.8 $\mu$ m diameter ball lens in Month 4 (using the single source, 2 path configuration and 50:50 coupler) exposed to various concentrations of  $H_2$  in air. The system was flushed with air between exposures.**

The response time of the sensor to hydrogen was estimated at  $t_{50}$  and  $t_{90}$  where  $t_{50}$  is the time at which the signal changed by 50% of the full step, and  $t_{90}$  is the time at which the signal changed by 90% of the full step. For a change between 0 and 1000ppm  $H_2$  in air,  $t_{50} = 18$ s and  $t_{90} = 40$ s. For a change between 0 and 500ppm  $H_2$  in air,  $t_{50} = 24$ s and  $t_{90} = 80$ s. These times include the filling time of the test vessel and the response time of the hydrogen mass flow controller being switched on. The recovery time was estimated at approximately 8 minutes but is difficult to estimate because of the drift in baseline. The normalised change in reflectivity for a range of hydrogen concentrations for the experiments listed in Table 5-3 are shown on a log-log plot in Figure 5.18. The data for the cleaved fibre, from chapter 4, Figure 4.9, page 76, is also shown as a comparison.



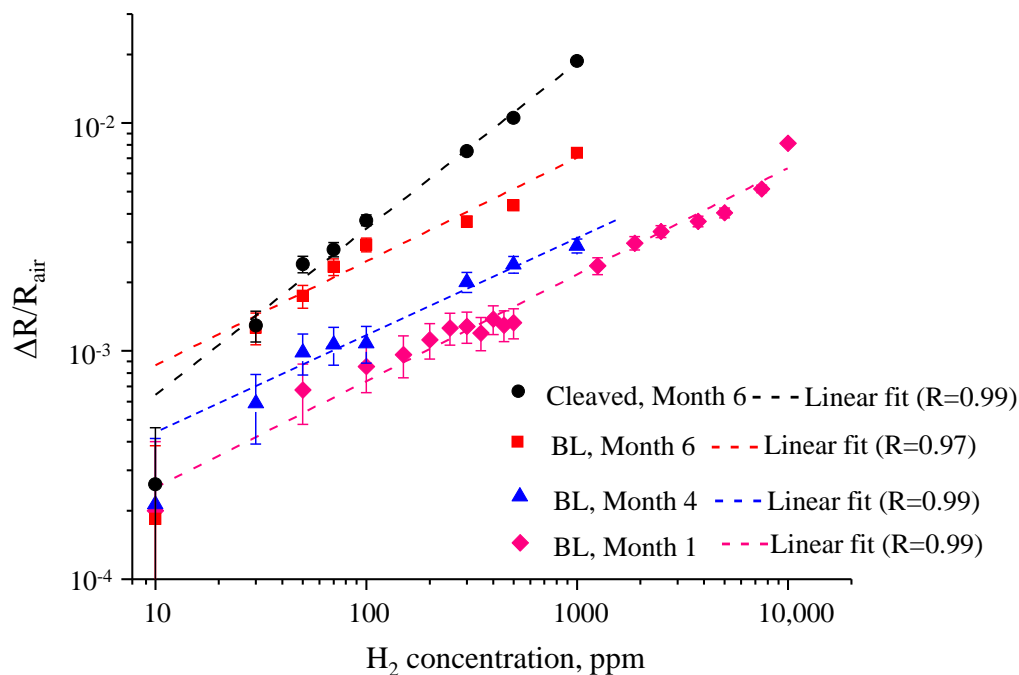


**Figure 5.18-** Normalised change in reflectivity from a 40nm Pd coated ball lens (BL) as a function of hydrogen concentration on a log-log plot. The reflectivity measurements were made in Month 1 (marked as diamonds), Month 4 (marked as triangles) and Month 6 (marked as squares). Control measurements using a 40nm Pd coated cleaved fibre are marked as circles. The dotted lines show linear fits for the data points, using the least squares method.

The limit of detection was estimated to be 10ppm  $H_2$  in air ( $1\sigma$ ) in all the experiments. There is a small amount of zero drift for the 10ppm  $H_2$  measurement and is exaggerated on the log-log plot. Although the response is linear, the proportional change in reflectivity with respect to hydrogen concentration varied for each experiment, with the cleaved fibre showing the best responsivity,  $\Delta R/R_{air}$ . The values for the change in reflectivity are summarised in Table 5-4.

It can be seen that the gradient of the normalised reflectivity and concentration curve for the ball lens curves are similar but the normalised change in reflectivity increases from Month 1 to Month 6. The normalised change in reflectivity values obtained from the 'BL, Month 4' experiment is ~30% higher than the reflectivity values for 'BL, Month 1.' However, the reflectivity measurements for 'BL, Month 6' experiment is significantly larger at ~250% compared to 'BL, Month 1' experiment.

Although the ball lens and the cleaved fibre are expected to show the same responses, inconsistent results may have arisen due to a number of reasons- i) the test procedure had changed over the period of testing, for example a longer cycling period and leaving the sensor in a vacuum chamber for palladium coating re-generation may have improved the  $\Delta R$  response (see section 5.4.2, page 100 for a discussion); ii) all fibres were coated at different times and the sensing layers may not have been identical, which could have led to different responses; iii) an offset in the absolute response levels may have arisen due to a certain amount of light not reaching the end face of the palladium covered ball lens, and iv) light is incident on the final end face of the ball lens at a range of angles of

incidence, whereas the Fresnel equations assume normal incidence, and the tapered core facilitated the coupling of the off-axis rays back into the core.

**Table 5-4 – Normalised change in reflectivity,  $\Delta R/R_{\text{air}}$  for a range of hydrogen concentrations.**

| Concentration(ppm) | BL (Month 1) | BL (Month 4) | BL (Month 6) | Cleaved (Month 6) |
|--------------------|--------------|--------------|--------------|-------------------|
| 10,000             | 0.0081       | -            | -            | -                 |
| 1000               | 0.0022       | 0.0029       | 0.0074       | 0.019             |
| 100                | 0.00086      | 0.0011       | 0.0029       | 0.0037            |
| 10                 | 0.00021      | 0.00022      | 0.0018       | 0.00026           |

#### 5.4.2 Discussion 2: Single source, 2 paths and Pd coated ball lens in $H_2$

The change in reflectivity of coating upon exposure to hydrogen depends partly on the recovery time allowed for the palladium hydride to return to the metallic phase. This recovery could be assisted by flushing the sensor head in air or by leaving the sensor head in a vacuum chamber. If sufficient recovery time is not allowed, the proportional change in reflectivity will be underestimated. This is demonstrated in Figure 5.19.

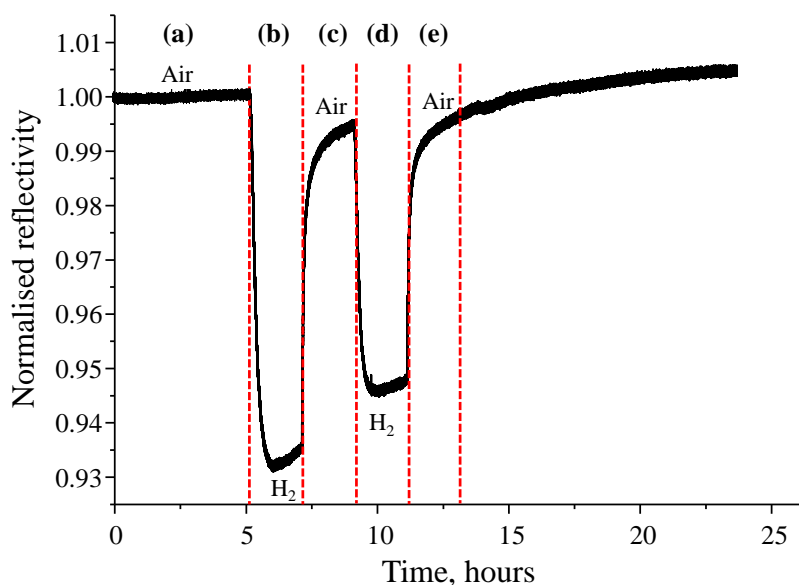


**Figure 5.19- Ball lens sensor head exposed to 998ppm  $H_2$  in air. Long term recovery of sensor head in air observed over 20 hours. The overall change in reflectivity due to hydrogen is underestimated by 20% due to insufficient time allowed for recovery in air (phase c).**

The ball lens sensor head was initially left in synthetic air for 5 days to allow maximum regeneration of the pure palladium phase of the film (only the last five hours are shown at the beginning of the graph in region (a) in Figure 5.19 to establish the baseline). It was then exposed to 998ppm ( $\pm 1$ ppm)  $H_2$  in air at a low flow rate of 15sccm/min for 2 hours as shown by region (b). The signal reached a minimum and stabilised in 40 minutes. This response time is different to the  $t_{90}$  time, shown in Figure

5.17b, which was in the order of seconds, due to the low flow rate used in this experiment in comparison to the vessel volume of  $125\text{cm}^3$ . The sensor head was then exposed to air at a flow rate of  $100\text{sccm/min}$  for 2 hours as shown by region (c). It can be seen that the reflectivity has not reached the original baseline after 2 hours. When a second identical hydrogen flow was started in region (d), the change in reflectivity was 20% smaller than the first cycle. The sensor head was left in air, and once again region (e) shows that 2 hours recovery is not sufficient to reach baseline. The sensor head was kept in air for a further 12 hours and it can be seen that the reflectivity reached the baseline level after 4 hours, however an upward drift is observed.

It can be concluded that a number of parameters need to be controlled in future experiments to obtain repeatable results, such as:

- Consistent test methodology, including long recovery periods of at least 30 minutes in air in between testing for hydrogen response (if using a flow rate of  $500\text{sccm/min}$  or the equivalent of at least 4 times the volume of the testing vessel)
- Factors that affect ball lens quality such as regular calibration of the splicer to form spheres within  $\pm 0.5\%$  of the specified diameter, tapering of the core and the symmetry of the sphere
- Coating deposition technique

The Gaussian beam expansion theory is not the ideal model for the behaviour of light inside the ball lens, due to the distorted core. The Fresnel equations used so far assumed normal incidence on the palladium surface. However the beam of light, after expanding inside the silica ball, could be incident on the end face at a range of angles of incidence. Additionally the illuminated area responsible for detecting hydrogen induced changes in palladium is uncertain.

### 5.4.3 Data modelling to find $n_{Pd}$ of $\text{PdH}_x$

In an attempt to gain an understanding of how the complex refractive index of palladium,  $n_{Pd}^*$  changes with hydrogen content, a model of the reflectivity based on equation (3.1), page 42 was used to fit the experimental data based on different combinations of the real and imaginary refractive index values.

Starting with Sievert's law in equation (2.2), page 11, the equation may be re-written in terms of refractive index of palladium and hydrogen concentration. Suppose that the refractive index changes linearly with  $x$ , the amount of hydrogen absorbed by palladium for low concentrations of hydrogen in the range 0 to 1% in air. And the partial pressure of hydrogen is proportional to hydrogen concentration. The new forms of Sievert's law are then shown by equations (5.5) and (5.6):

$$n_R = \Delta n_R \sqrt{[H_2]} + 2.94951 \quad (5.5)$$

$$n_I = \Delta n_I \sqrt{[H_2]} + 8.3321 \quad (5.6)$$

Where  $[H_2]$  is the hydrogen concentration between 0 and 1%, and  $\Delta n_R$  and  $\Delta n_I$  are the changes in the real and imaginary part of the refractive index respectively.

Goddard *et al* [10] measured the complex refractive index of a 27nm Pd film at 1550nm. This was the only reported measurement found in literature. He found that  $\Delta n_R$  changed by -0.033 for 1%  $H_2$  in  $N_2$  but found that  $\Delta n_I$  increased by 0.067 for the same  $H_2$  concentration. This is contrary to scientific consensus (explained in section 2.1.2, page 14), where the imaginary part is expected to decrease with hydrogen.

Substituting Goddard's  $\Delta n_R$  and  $\Delta n_I$  values in equations (5.5) and (5.6), a range of reflectivity values for a 40nm Pd film was calculated using equation (3.1), page 42. The modelled reflectivities did not fit the experimental data using Goddard's values of increasing  $\Delta n_I$  – in fact,  $\Delta n_I$  had to decrease. Using a method of trial and error, it was found that the modelled reflectivities showed a best fit to the experimental data for  $\Delta n_R = -0.01 \pm 0.02$  and  $\Delta n_I = -0.4 \pm 0.05$  for 1%  $H_2$  in air. The modelled response fitting the experimental data using a ball lens (Month 6 experiment) is shown in Figure 5.20. This fit between the modelled reflectivity and experimental data was confirmed using the method of least squares as described by Squires [11]. The gradient of the modelled response was calculated to be  $0.50 \pm 0.0003$ , which is within the error limits of the gradient of the least squares fit,  $0.45 \pm 0.04$ .

It is interesting to notice that the imaginary refractive index had to decrease with increasing hydrogen concentration for the model to fit. This is consistent with the scientific consensus and contrary to Goddard's findings. It is also interesting that the change in  $\Delta n_I$  was the dominant factor affecting the curve fit, implying that the absorption process of light by the palladium film has a greater influence than the reflection process.

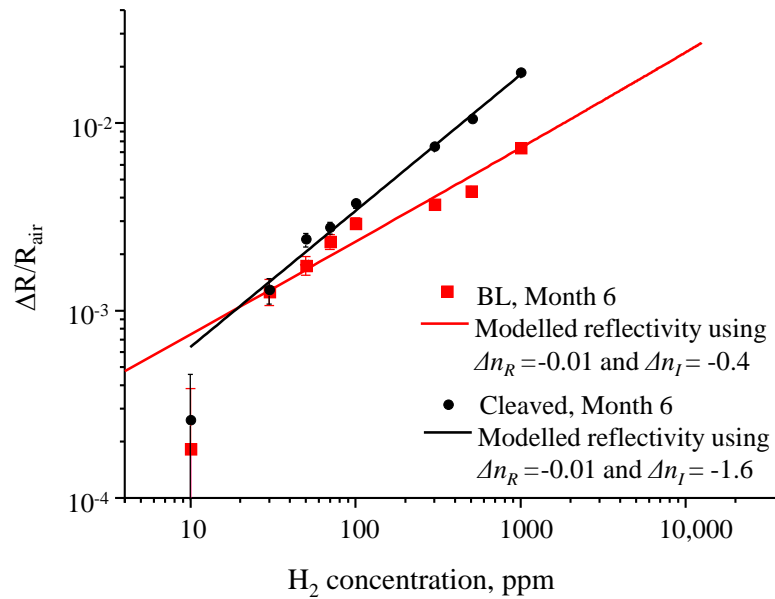


**Figure 5.20-** Fitting a model, based on calculating palladium-hydride's change in reflectivity using equations 5.5 and 5.6, to the experimental data from the ball lens to find an estimation for the change in the complex refractive index of palladium hydride.

However the fit for the 'Cleaved, Month 6' data had a different gradient to the 'BL, Month 6' data and was not fitted by Sievert's law. Instead, the change in reflectivity was fitted using an equation for the complex refractive index of palladium of the form,  $n = \Delta n[\text{H}_2]^{0.7} + n$ . The model gave a value of  $\Delta n_R = -0.01 \pm 0.02$  and  $\Delta n_I = -1.6 \pm 0.2$  for 1%  $\text{H}_2$  in air. The value of  $\Delta n_I$  was found to be higher than the 'BL, Month 6' model.

These values are somewhat speculative and presented here as an alternative method of investigating how  $n_{\text{Pd}}^*$  varies with hydrogen content and therefore are by no means definite. Further experimental investigation is needed to validate these estimated values.

### 5.5 Method 3: Single source, 2 paths and GRIN lens in oil

An off-the-shelf GRIN lens was used as a sensor head at the tip of a singlemode fibre (Corning SMF28) as shown in the schematic diagram in Figure 5.21a. The GRIN lens assembly consisted of a pigtailed glass ferrule (Thorlabs, SMPF0115) and a quarter wavelength pitch GRIN lens (Thorlabs, GRIN2315A) designed to collimate the light and not focus it at an operating wavelength of  $1550\text{nm} \pm 15\text{nm}$ . Both the GRIN lens and the glass ferrule had matching  $8^\circ$  face cut to minimise back reflections. It was noticed that an index matching medium applied between the angle cuts improved the light coupling and made it easier to align the components. The ferrule and lens were inserted into a protective glass sleeve (Thorlabs, 51-2800-1800) and the angle cut faces aligned under a microscope. The GRIN lens was 4.43mm long and had a face diameter of 1.8mm. Optical adhesive (Norland Products, NOA63) was used to secure the ferrule and the lens in place and cured using a UV gun (Norland Products, Opticure 4 Light Gun) for 1.5 minutes.

To characterise the sensitivity of the system using the GRIN lens, the single source (1550nm SLD) and 2 paths (with a 90:10 split ratio of the first directional coupler) interrogation system was used. The GRIN lens was immersed in different oils with known refractive index, where the oil well was placed on a Peltier heat sink to keep the oils at a constant temperature. The oil well on the Peltier heat sink and the GRIN lens setup is shown in Figure 5.21b.

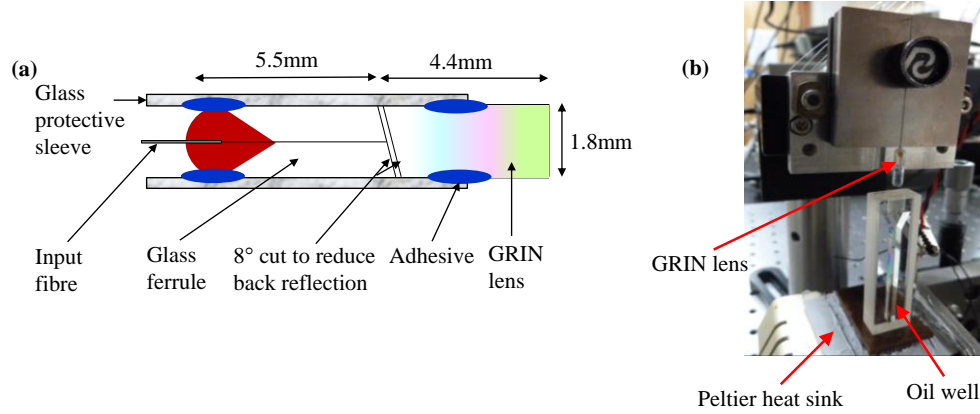


**Figure 5.21-** a) Schematic of the GRIN lens sensor head assembly b) GRIN lens immersed in an oil well, which is resting on a Peltier heat sink to maintain a constant temperature.

### 5.5.1 Results 3: Single source, 2 paths and GRIN lens in oil

Similarly to previous oil calibration experiments, the GRIN lens was immersed in oils of known refractive index in the range 1.60 to 1.68 (Cargille Labs, Series M) measured at 589nm and 25°C. The refractive index of the oils,  $n_l$ , were determined from equation (4.8) in chapter 4 (page 68), with modification to the  $(V_{probe})_l$  expression. The Fresnel reflection equation at the GRIN lens and oil interface, shown by equation (5.7), was used instead.

$$(V_{probe})_l \propto \frac{(n_{GRIN} - n_l)^2}{(n_{GRIN} + n_l)^2} \quad (5.7)$$

Where,  $n_{GRIN}$ , the effective refractive index of the GRIN lens is equal to 1.5901. The oil calibration chart of experimentally determined refractive index against the calculated Cauchy refractive index values at 1550nm and 25°C is shown in Figure 5.22. Each experimental value is the average of three repeated measurements.

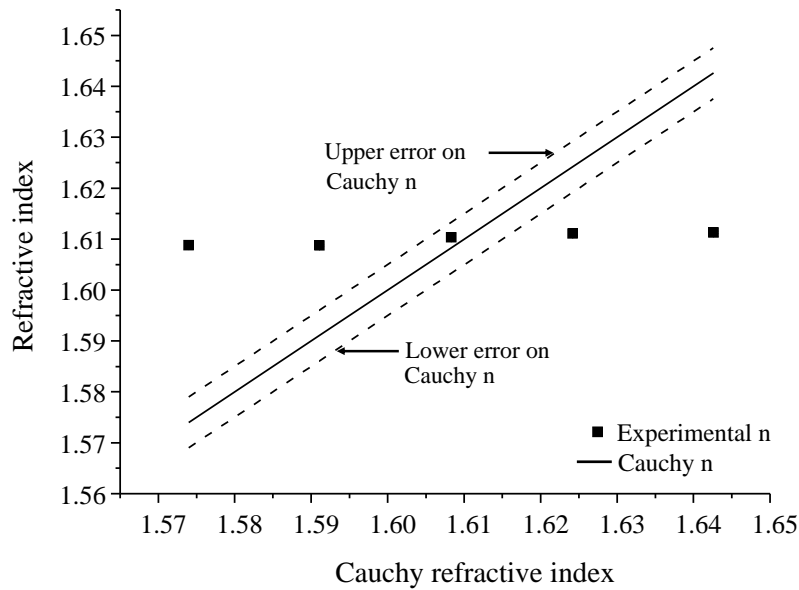


**Figure 5.22- Oil calibration chart obtained using the GRIN lens shows that the sensor head is unable to detect changes in refractive index.**

It can be seen that the GRIN lens was unable to detect any changes in refractive index. There are a number of possible reasons for this. The GRIN lens bought from Thorlabs had an anti-reflection (AR) coating. These off-the-shelf products were intended to be used in transmission and the AR coating was designed to minimise Fresnel reflections between the glass-air interface. The use of a customised GRIN lens without the AR coating was not possible for this project. The coating could be polished off the top in-house, but with a shortening of the pitch length. Secondly, it was noticed that the glue holding the GRIN lens in the protective sleeve was absorbing the oils, because the transparent glue was observed to turn a faint shade of yellow during the experiment. The oils were removed by cleaning the GRIN lens in acetone, in which the oils were soluble. This in turn softened the glue holding the alignment together. It would be ideal to use GRIN lenses that require no glue and without an anti-reflection coating.

In this case, practical issues with the oils and cleaning solvents meant that using refractive index oils was not the appropriate method of assessing the GRIN lens' sensitivity. A palladium coated GRIN lens was tested in hydrogen to investigate for its sensitivity, since palladium has high reflectivity and was expected to reflect back a reasonable proportion of the incident light. This is described in the following section.

## 5.6 Method 4: Single source, 2 paths and Pd coated GRIN lens in H<sub>2</sub>

Two coating combinations on the GRIN lens, with and without a gold protective layer were tested in hydrogen – i) 10nm Ni and 40nm Pd, ii) 10nm Ni, 40nm Pd and 10nm Au. The lenses were tested within three days of being coated. A coated GRIN lens is shown in Figure 5.23. The same

experimental procedure, using the single SLD source and 2 paths interrogation system with a first coupler with a 90:10 split ratio, described in section 5.4, page 97 was followed.

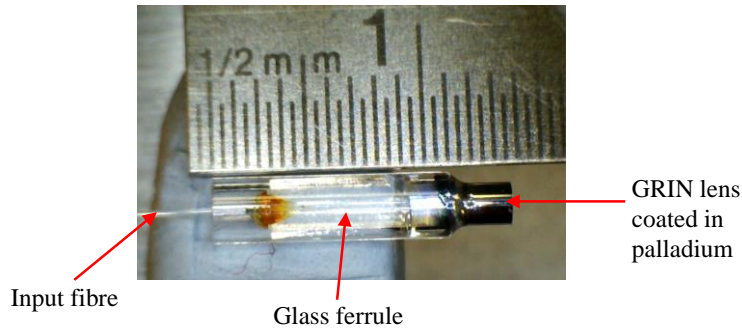


**Figure 5.23- Metallic palladium coated GRIN lens as a hydrogen sensor head.**

### ***5.6.1 Results 4: Single source, 2 paths and Pd coated GRIN lens in $H_2$***

The GRIN lenses coated in Ni/Pd and Ni/Pd/Au were tested in  $H_2$  in air and an inverse response was observed for both. The inversion phenomenon was discussed in chapter 3, section 3.2.2, page 48, however it was observed with Ni/Pd coatings that had been left in ambient air for a period of time and did not have an Au layer to protect the palladium from contamination and oxidation. In contrast, an inverse response was not expected from the Ni/Pd/Au coated GRIN lens. The GRIN lens with Ni/Pd coating was exposed to 1%  $H_2$  in air and the reflectivity inversion response is shown in Figure 5.24a. The recovery time was extended to 10 minutes, without full baseline recovery. The GRIN lens with Ni/Pd/Au coating was exposed to cycles of 500ppm  $H_2$  in air and its response is shown in Figure 5.24b. The reflectivity increased with hydrogen concentration, but there was little recovery in air. The same behaviour was observed for a second hydrogen exposure. It is possible that the anti-reflection coating was responsible for a different reflection response where the effective refractive index of the multi-layer system was higher than palladium causing a reflectivity inversion.



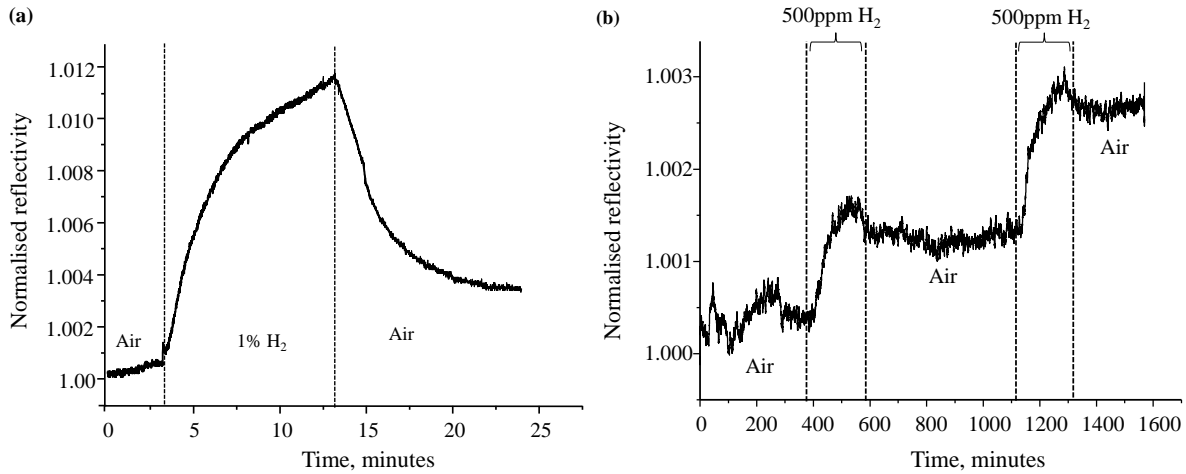


**Figure 5.24- a) Hydrogen response from a Ni/Pd coated GRIN lens. The reflectivity increased upon hydrogen exposure, which is contrary to expectations. The reflectivity decreases in air without reaching the original baseline b) A similar reflectivity inversion obtained using a Ni/Pd/Au coated GRIN lens. There was little recovery in air.**

The change in reflectivity from the graphs in Figure 5.24 for 1% and 500ppm H<sub>2</sub> in air seem to take a similar form from the ball lens experiment conducted in Month 1.

## 5.7 Conclusion

Two sensor heads are presented that have an active area that is larger than a single mode fibre core- a ball lens and a GRIN lens at the tip of a SMF. The larger area allows a greater coverage of palladium and thus provides resilience to hydrogen induced cracking of the palladium film. Similar fibre tips have previously found applications in the field of medical imaging. The use of these probes in a reflectivity study to detect gas concentrations is a novel approach that is investigated here.

The ball lens was initially produced by melting the tip of a SMF in an electric arc in a fusion splicer. When the ball lens was observed under an immersion fluid with matching refractive index of the cladding, the core was still present. The ball lens was designed assuming that the light emitted from the SMF will expand radially with a Gaussian profile to a bigger spot size. The presence of the core invalidates this assumption. Therefore, a short piece of coreless silica fibre with matched SMF diameter that was spliced to the SMF, was melted to form a pure silica ball lens. The Gaussian beam expansion model was at first used to determine the optimum curvature of the ball lens at which most of the reflected light will be coupled into the core. This is most likely to happen if the curvature of the radial wavefront coincided with the curvature of the ball lens. There was no point of intersection between the two curves and it was decided to work with ball lenses near the upper end of the range supported by the fusion splicer, between 350µm and 400µm diameter. Further experimenting with ball lenses of various sizes revealed that the optimum diameter was in the region 349±1µm. The amount of light reflected back depended on the accuracy of the measured ball lens diameter in comparison to the set diameter, tapering of the core before the ball lens and the symmetry of the sphere. The trial and

error method of producing these ball lenses highlights the difficulty in controlling the aforementioned parameters despite the use of control software and producing ball lenses with reproducible quality. The illuminated area of the sensor head can be assessed, but it is difficult to say which parts of the ball lens is reflecting light back. Although the spot area of a ball lens head was 20 times larger than the spot area of a single mode fibre, it is difficult to demonstrate conclusively that a larger sensing area has been achieved by using a ball lens. The tapering of the SMF core before the silica ball implies that the Gaussian beam expansion model may not be an appropriate model for these ball lenses. Modelling the light behaviour in a sensor with a larger area coupled to a fibre is an issue especially when the refractive index profile at the core end is not known.

The illuminated area of the sensor head can be assessed, but not which parts of this area reflect light back into the core and it is therefore uncertain whether a larger sensor area has actually been achieved.

The sensitivity of the ball lens was first characterised by immersing it in a range of oils with known refractive index. The measured refractive indices of the oils were calculated from the change in reflected signal. The minimum detectable change in refractive index was 0.0012 ( $1\sigma$ ). A coated ball lens (10nm Ni and 40nm Pd) was then successfully tested in hydrogen on three occasions over a period of six months. The repeatability was estimated to be 10ppm  $H_2$  in air ( $1\sigma$ ) for all the experiments with a  $t_{90}$  response time of 40s for 1000ppm  $H_2$  in air. The ball lenses were kept in a vacuum chamber between tests to maximise palladium surface regeneration and to prevent contamination. However, the change in reflectivity for the hydrogen concentrations differed with each experiment. This difference may be attributed to insufficient recovery of the palladium hydride to the metallic phase when left in air.

The best result was obtained with the final symmetrical interrogation system where equal amounts of light reached the reference and probe arms and with a relatively long recovery period of 6 minutes in air allowed in experiments. Ideally, a longer recovery period of at least 15 minutes would ensure more consistent and repeatable results. The experimental results of the reflectivity change were fitted with a model calculated from the change in reflectivity of palladium-hydride by adjusting estimated values of its complex refractive index. The refractive index was fitted using Sievert's law and the closest fit of reflectivity the model to the experimental data was obtained for  $\Delta n_R = -0.01 \pm 0.02$  and  $\Delta n_I = -0.4 \pm 0.05$  for 1%  $H_2$  in air. It is interesting that  $\Delta n_I$  was much higher than  $\Delta n_R$  indicating a dominant absorption process of light by the palladium film. Further experimental investigation would be needed to validate these estimated values, for example by using an ellipsometry method.

It is reasonable to expect that the change in reflectivity from a Pd coated ball lens and a Pd coated cleaved fibre for a particular hydrogen concentration will be the same. However, the change in

measured intensities was not the same. The gradient of the normalised reflectivity change with hydrogen concentration for the cleaved fibre was higher than that of the ball lens. This difference may have arisen for a number of reasons. Firstly, the fibres were coated at different times and the sensing layers were not identical. Secondly, there may have been an offset in the absolute response levels from the ball lens probe tip due to a certain amount of light not reaching the end face of the palladium covered ball lens but still being reflected back into the interrogation system. Thirdly, it was assumed that light is incident normally on the end face of the ball lens. Light may be incident at a range of angle of incidences the off-axis reflected light coupled back into the core facilitated by the tapering.

A second sensor head that made use of a GRIN lens was assembled in the lab. The GRIN lens used was standard off-the shelf product that came with an anti-reflection coating on the top surface. This coating was designed to minimise the Fresnel reflection between a glass and air interface. However, when characterising the GRIN lens' sensitivity by immersing in oils, it was found unable to detect any changes in refractive index. In addition, the optical adhesive that was holding together the GRIN lens alignment became contaminated with the oil when immersed in it. Another disadvantage of the AR coating was discovered during the testing of coated GRIN lenses in hydrogen. Sensing layers of 40nm Pd with a 10nm Ni adhesive layer were deposited with and without the Au protective layer and tested in hydrogen. For both sensor heads, a reflectivity inversion was observed. With multiple coating layers, the effective refractive index of the composition may have been higher. The effect of this would be increase in reflectivity upon exposure to hydrogen.

From the characterisation of the ball lens and the GRIN lens as sensor heads, it was decided that the ball lens offered a better solution in terms of stability at this stage. The anti-reflection coating on the GRIN lenses may have been responsible in creating unusual responses during the hydrogen testing. However for future work the GRIN lenses may offer a larger surface area and it would be ideal to have customised GRIN lenses without the AR coating. Although the unknown behaviour of light inside the ball lens makes the sensor area coverage uncertain, currently the ball lens has the advantage over the GRIN lens that it is seamless, has a less complex structure and can be produced using ordinary lab equipment.

## 5.8 References

- [1] Swanson, E., Petersen, C. L., McNamara, E., Lamport, R. B. and Kelly, D. L. (eds.) (2002), *Ultra-small optical probes, imaging optics, and methods for using same*, US Patent No. 6445939 B1.
- [2] Prince, M. R., LaMuraglia, G. M., Seidlitz, C. E., Prahl, S. A., Athanasoulis, C. A. and Birngruber, R. (1990), "Ball-tipped fibers for laser angioplasty with the pulsed-dye laser", *IEEE Journal of Quantum Electronics*, vol. 26, no. 12, pp. 2297-2304.
- [3] Mao, Y., Chang, S. and Flueraru, C. (2010), "Fiber lenses for ultra-small probes used in optical coherent tomography", *Journal of Biomedical Science and Engineering*, vol. 3, pp. 27-34.
- [4] Zhao, M., Huang, Y. and Kang, J. U. (2012), "Sapphire ball lens-based fiber probe for common-path optical coherence tomography and its applications in corneal and retinal imaging", *Optics Letters*, vol. 37, no. 23, pp. 4835-4837.
- [5] Harun, S. W., Jasim, A. A., Rahman, H. A., Muhammad, M. Z. and Ahmad, H. (2013), "Micro-ball lensed fiber-based glucose sensor", *IEEE Sensors Journal*, vol. 13, no. 1, pp. 348-350.
- [6] Reed, W. A., Yan, M. F. and Schnitzer, M. J. (2002), "Gradient-index fiber-optic microprobes for minimally invasive in vivo low-coherence interferometry", *Optics Letters*, vol. 27, no. 20, pp. 1794-1796.
- [7] Kogelnik, H. and Li, T. (1996), "Laser Beams and Resonators", *Applied Optics*, vol. 5, no. 10, pp. 1550-1567.
- [8] Lee, D. L. (1986), *Electromagnetic principles of integrated optics*, 1st ed, Wiley & Sons, Canada.
- [9] Fujikura AFL Telecommunications, ( 2013), *SpliceLab User's Guide - Fiber Ball-lens software Version 2.0*, 2nd ed., AFL, USA.
- [10] Goddard, L., Kai, Y. W., Garg, A., Behymer, E., Cole, G. and Bond, T. (2008), "Measurements of the complex refractive index of Pd and Pt films in air and upon adsorption of H<sub>2</sub> gas", *Lasers and Electro-Optics Society 21st Annual Meeting-LEOS*, Acalpuco, pp. 569-570.
- [11] Squires., G. L. (2001), *Practical physics*, 4th ed, Chapter 4, Page 39, Cambridge University Press, Cambridge, UK.

# Chapter 6

## Advanced Fresnel Refractometer

A simple micromirror Fresnel refractometer was previously discussed in chapter 4. The design employed reference and probe channels on separate optical branches, which meant that the signals were susceptible to differential temperature changes between the two arms. A relative change between the two channels may be mistaken for a refractive index induced change in signal. As a solution to this issue, a common path design for the reference and probe signal was investigated and is presented in this chapter. The common path would allow the reference signal to compensate for thermally induced changes, bend losses in the fibre and changes to the coupler split ratio. Two single wavelength sources were used and the wavelengths were separated by a filter/FBG to label one wavelength a reference and the second a probe signal. Time division multiplexing was applied to identify the detected wavelength.

## 6.1 Introduction

Butler *et al* in 1996 [1] originally proposed using a common path, self-referencing fibre optic network to detect hydrogen using the same reflectivity principle as chapter 4. He used two LEDs at wavelengths 810nm and 880nm, modulated at 10kHz to inject 25 $\mu$ W of power into a multimode fibre network. A high pass filter with a cut-off at 840nm was deposited on a quarter wavelength pitch GRaded INdex (GRIN) lens. The filter had 39% reflectivity and reflected the 810nm light, which was used as the reference wavelength. The 880nm light was transmitted towards a palladium based sensing layer and was used as the probe wavelength. The end face of the GRIN lens was coated with a 10nm optically transparent adhesive layer of Ni to bond the palladium alloy film to the lens, followed by a 150nm optically thick sensing layer of PdAg and finally a 25nm capping layer of Pt to protect the silver from oxidation, yet allow hydrogen to diffuse through. The configuration is shown in Figure 6.1.

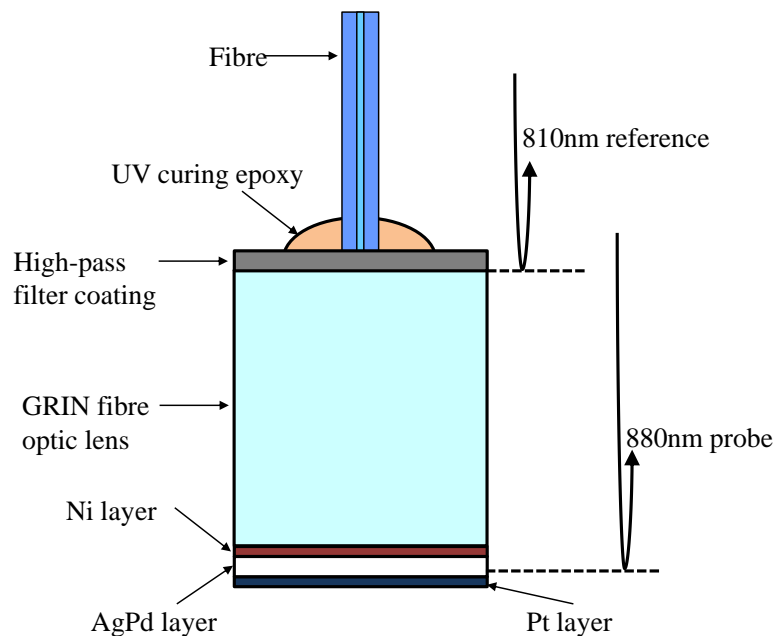


**Figure 6.1- Hydrogen sensor configuration using GRIN lens to support the sensing coatings and wavelength selective filter. Modified from Butler *et al* [1].**

Butler chose to deposit the layers on a GRIN lens rather than a multimode fibre core to provide larger area support for the multiple sensing layers from a practical and engineering perspective. He also noticed that depositing the sensing layers on top of the filter generated stress points that led to peeling, thus he chose to coat the filter and sensing layers on opposite ends of the GRIN lens. The LEDs were switched on/off sequentially to generate sequential pulses at the respective wavelengths and the signals were ratioed to correct for optical losses and variations in environmental factors.

However, Butler was unable to carry out field tests using prototypes of this sensor head due to unreliability issues with the coating layers. Since the objective of Butler's work was to prove the

concept of a fibre optic hydrogen sensor in transformer oil, he instead tested a fibre tip coated in just PdAg and demonstrated a detection capability of 50ppm  $H_2$  in transformer oil at room temperature.

Despite the results, shown previously in section 5.5.1, disproving the GRIN lens' ability to sense changes in the refractive index, it was decided to investigate Butler's idea of GRIN lens and a filter sensor head assembly. It was expected that using a filter would assist in greatly improving the reflectivity from the filter and test medium interface.

## 6.2 Method 1: Dual wavelength, common path, GRIN lens and filter in oil

The experimental arrangement shown in Figure 6.2 is an adaptation of Butler's configuration, whereby two wavelengths travel down a common path and are separated by a filter fitted at the end of the sensor head. The light sources were time-division multiplexed so that the output wavelength at the photodetector amplifier was always known. The dotted lines in the diagram show the electrical connections and the solid lines show the optical network.

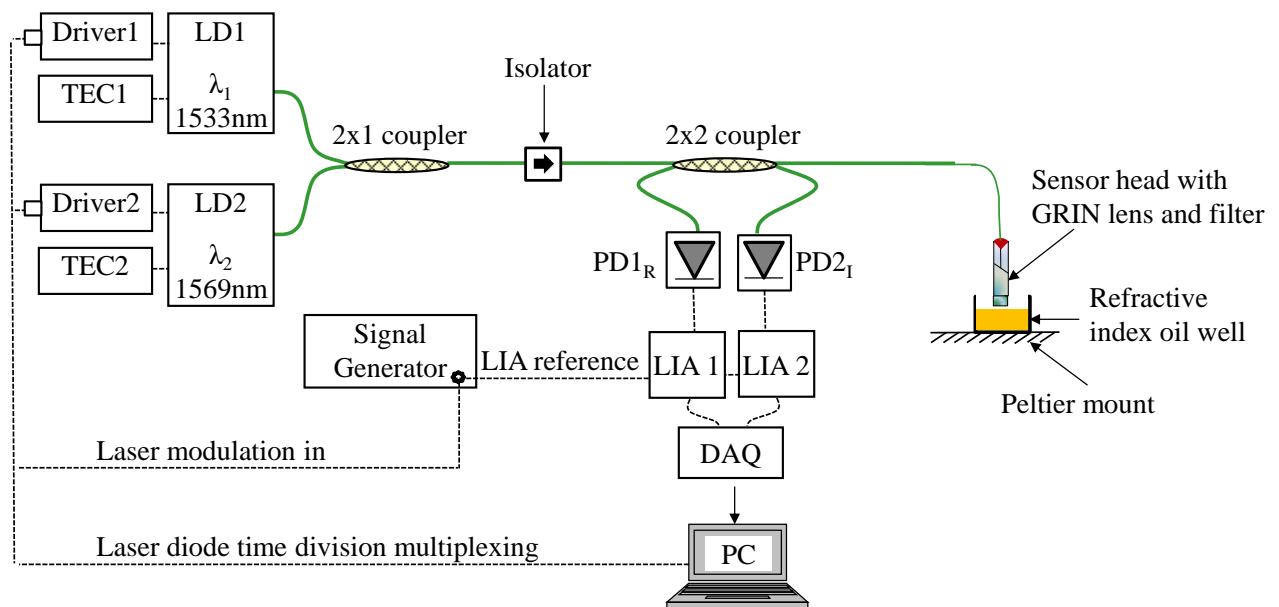


**Figure 6.2- Dual wavelength, common path system using a 1533nm laser diode, LD1 as a probe beam and a 1569nm laser diode, LD2 as a reference beam. The reflected intensity was picked up by photodetector amplifier, PD1<sub>R</sub> and the initial intensity of the beams was picked up by photodetector amplifier, PD2<sub>I</sub> and demodulated by matched lock in amplifiers LIA1 and LIA2. The measurements were recorded using a data acquisition adapter (DAQ) and a lab computer.**

Two DFB (distributed feedback) laser diodes were used, at 1533nm (Laser Components, PL15BM0021FAB-A-1-01) and 1569nm (Laser Components, PL15BL0021FAB-A-1-01). Laser diodes were chosen, rather than Butler's choice of LEDs, because they have a narrow linewidth and the separation between the two wavelengths could be reduced and therefore both would fall within the passband of the couplers ( $1550\text{nm} \pm 30\text{nm}$ ). The use of laser diodes is likely to result in a poorer

performance, but the smaller separation between the wavelengths means that the system is as common path as possible. Using the telecommunications wavelength range meant that a commercial off-the-shelf filter could be used to separate the wavelengths. The laser diode spectra are shown in Figure 6.3. The linewidth or FWHM (full width at half maximum) of the spectra were measured using an optical spectrum analyser (Ando, AQ6370C). The linewidths for laser diodes were measured to be  $\leq 15\text{pm}$ , which is the stated resolution limit of the spectrum analyser. The actual linewidth is probably less than  $15\text{pm}$  and a confocal Fabry-Perot interferometer could be used to determine the linewidth more precisely. The lower limit of the coherence length,  $l_c$  at the respective wavelength,  $\lambda$  can be calculated using equation (6.1), where  $(\Delta\lambda)_{FWHM}$  is the linewidth at FWHM. The coherence length is  $> 160\text{mm}$ .

$$l_c = \frac{\lambda^2}{(\Delta\lambda)_{FWHM}} \quad (6.1)$$

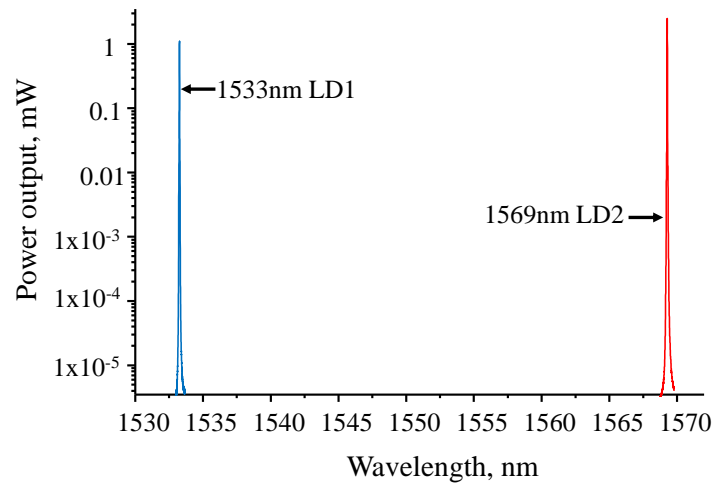


**Figure 6.3- DFB laser diode spectra with centre wavelengths at 1533nm and 1569nm taken with an optical spectrum analyser (Ando, AQ6370C).**

The laser diode currents were set to  $40\text{mA}$ . A signal generator (Stanford Research, DS345) was used to modulate the laser output intensities at  $997\text{Hz}$  with a  $1.5\text{Vpp}$  sine function. The resulting current modulation on the laser diode driver was  $\pm 4\text{mA}$ . The choice of  $997\text{Hz}$  as the modulation frequency was discussed in chapter 4, section 4.2, page 69 and was made because it avoids overlap with harmonics of the noise frequency peaks at  $50\text{Hz}$  and  $60\text{Hz}$ . The laser diodes were controlled using a pair of laser diode current drivers (Thorlabs, T-Cube LD Controller TLD001) and temperature drivers (Thorlabs, T-Cube APT TEC Controller TTC001). These drivers were mounted on a USB controlling hub (Thorlabs, T-Cube USB Controller Hub TCH001). The T-Cube hub was connected to the PC to directly control the laser diodes' current and temperature and could be switched on and off using a LabView program. Photodetector amplifier,  $\text{PD}_{2\text{I}}$  measured the incoming optical signal whereas photodetector amplifier 1,  $\text{PD}_{1\text{R}}$  received the back reflected light from the sensor head. The



photodetector signals were demodulated by matched lock-in amplifiers 1 and 2 (Stanford Research Systems, SR850), termed LIA2 and LIA1 respectively using a time averaging constant of 100ms.

Time-division multiplexing of the two laser diodes was automated by a LabView program as shown by the time sequence in Figure 6.4. When the sequence was initiated, the laser diode took 2s to switch on and reach a stable signal level (as shown by the red curve in the first LD1 pulse) and then the data collection started and continued for 1s (10 data points). The power to the first laser diode was switched off and there was a period of one second when both sources were switched off before the second laser diode was switched on and the cycle continued. The data sets were averaged over 10 data points and it was assumed that the whole system was a ‘black box’ that gave a reading every 7s. This was the optimum switching frequency of the configuration given the soft key start/stop of the laser diodes governed by the laser diode controllers. The laser diode signal voltage data was written to a text file along with a time-stamp (see section 6.3.2).

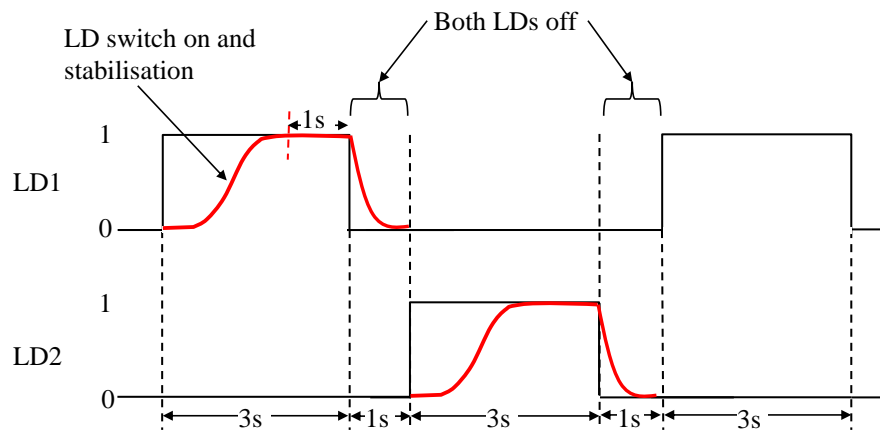


**Figure 6.4- Time division multiplexing sequence. A current modulation at 997Hz was also imposed while each laser diode was active.**

The commercial filter (Iridian Spectral, BMP000001) used to separate the wavelengths transmitted the 1533nm beam as the probe wavelength but reflected the 1569nm beam as the reference wavelength. The transmission specification curve of the filter given by the manufacturer is shown in Figure 6.5 with an overlay of the laser diode spectra and all fitting within the coupler bandwidth. Details of the filter and the sensor fabrication process are given in section 6.2.1.

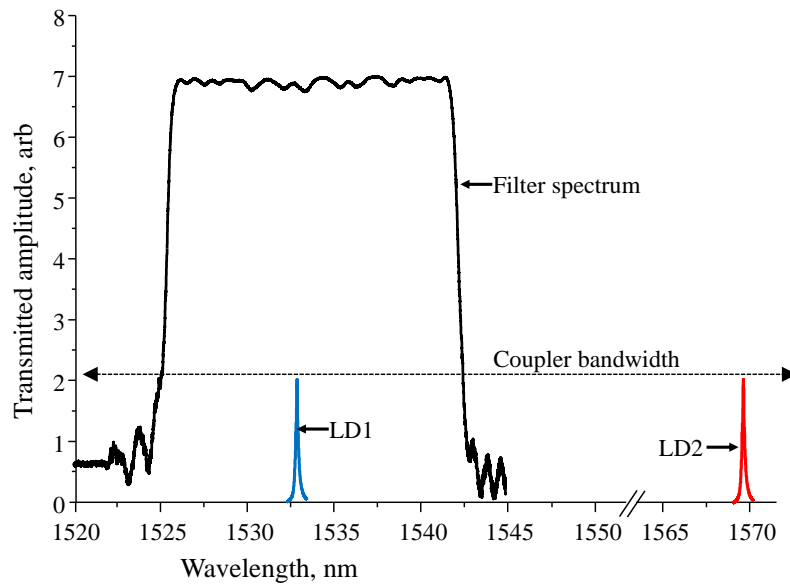


**Figure 6.5- Filter transmission spectrum. Transmits the 1533nm LD1 wavelength and reflects the 1569nm LD2 wavelength and falls within the coupler bandwidth**

### 6.2.1 Sensor head: GRIN lens and filter

Similar to Butler's [1] configuration, a sensor head using a GRIN lens and a filter was fabricated. The schematic diagram of the sensor head is shown in Figure 6.6a and the assembled sensor head is shown in Figure 6.6b. The components of the GRIN lens assembly and its fabrication was described previously in chapter 5, section 5.5, page 103.

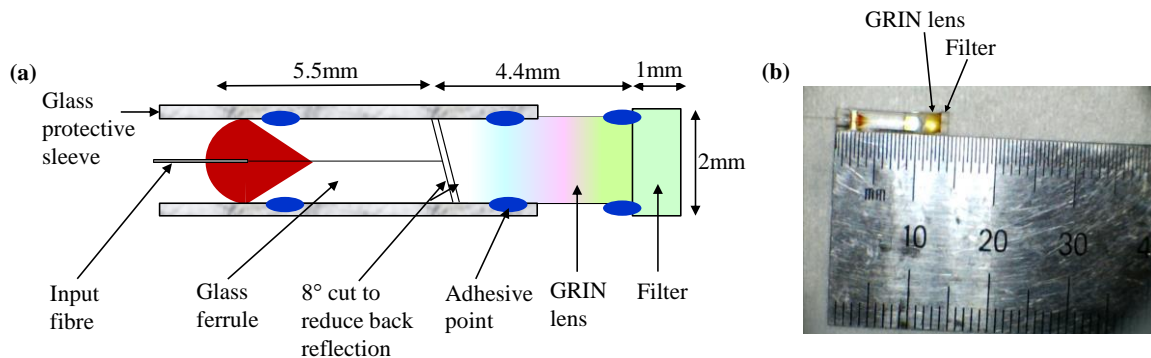


**Figure 6.6- a) Schematic of sensor head assembly used for the double wavelength configuration  
b) assembled sensor head**

Unlike Butler's configuration where the filter was directly deposited on the GRIN lens, a commercial off-the-shelf edge pass filter (Iridian Spectral, BMP000001) deposited on a 2x2x1mm glass substrate was used. Aligning the GRIN lens and the filter was very difficult. The GRIN lens was held vertically and the filter aligned from the top with minor rotational adjustments. The reflected light intensity was monitored until it reached a maximum and then the adhesive was UV-cured.

The 1533nm Fresnel reflection intensity output changed with time and had a variation of  $\pm 2\%$  ( $1\sigma$ ). This is evidence for the presence of a multi-pass Fabry-Perot cavity present in the sensor assembly, causing a path length imbalance. A further disadvantage of this approach was that the curing of the glue over-time misaligned the filter and the GRIN lens and caused the 1569nm reflected intensity to drop by 96%.

The presence of the cavity was investigated using an OBR, optical backscatter reflectometer (Luna Technologies, OBR 4400). The OBR is an interferometer that measures the Rayleigh backscatter caused by changes in the refractive index along the length of a fibre. It uses a tunable laser with a sweep scan of emitted wavelengths in the range 1525-1605nm. The GRIN lens and filter sensor head, attached to a 2m long fibre, was connected to the OBR as shown in Figure 6.7a. Figure 6.7b shows the reflectivity measurements in the space domain. The spike at 0m is due to fibre insertion loss and the second spike occurs around  $\sim 2$ m, which corresponds to the sensor head at the end of the fibre. A Fast Fourier Transform of the second spike is shown in Figure 6.7c. In the 1533nm region, the fringes confirm the presence of a cavity in the sensor head with a peak separation or free spectral range,  $(\Delta\lambda)_{FSR}$ , of 3nm. The cavity size was determined using equation (6.2) [2].

$$(\Delta\lambda)_{FSR} = \frac{\lambda^2}{2nd} \quad (6.2)$$

Where,  $\lambda$  is the operating wavelength,  $n$  is the refractive index (1.5) and  $d$  is the length of the cavity. At 1530nm the cavity size was calculated to be 1mm, which matches the depth of the edge-pass filter. Therefore, the low signal to noise ratio can be attributed to the presence of a cavity in the sensor head.

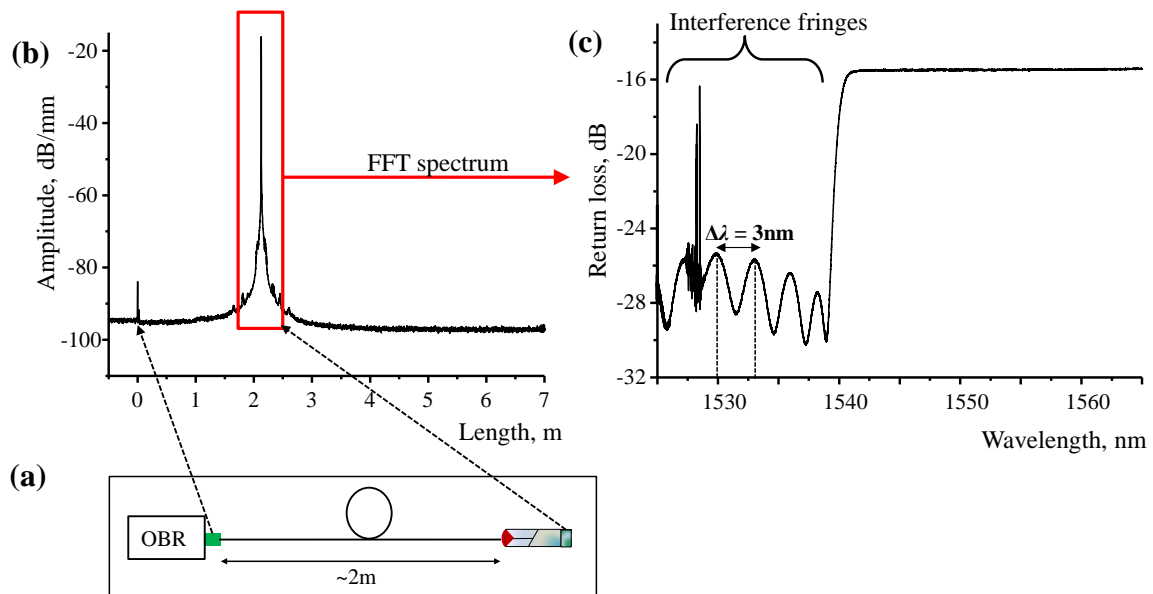


**Figure 6.7- a) OBR and sensor head setup b) Reflectivity from sensor head in the space domain at 0m and 2m c) Fast Fourier Transform of spike at 2m shows interference fringes from a cavity**

From Figure 6.7c, the return loss of the 1569nm wavelength was measured to be -14dB which corresponds to a reflectivity of 4%.

Further work was completed to reduce the interference effects by angle polishing matching  $8^\circ$  cuts on the filter and GRIN. The angled cuts made the alignment more difficult. The assembly setup is shown in Figure 6.8a and b. The schematic of the sensor head is shown in Figure 6.8c.

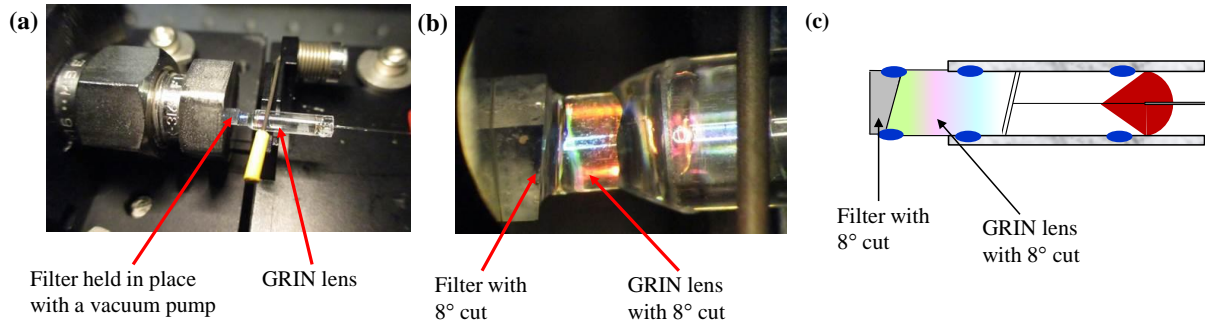


**Figure 6.8- a) and b) GRIN lens sensor head assembly with matching  $8^\circ$  cuts on the filter and GRIN lens c) schematic of the sensor head from Figure 6.6a.**

The filter was held in place by a vacuum pump and the GRIN lens rotated whilst the reflected light was monitored. Once again the gluing of the filter to the GRIN lens and the curing process led to a drop of filter efficiency until no power output from the filter was observed. This active alignment work was completed at the University of Southampton and I am grateful to Dr James Gates for his assistance.

Despite using these techniques, it was not possible to maintain a reflected output for the reference wavelength. Mechanical issues with this alignment process ultimately led to the adoption of an alternative to separate the wavelengths. This is described in section 6.3, where a fibre Bragg grating (FBG) is used instead of a filter. A bare fibre was used instead of a GRIN lens for simplicity to test this option.

Ideally, a broadband LED source would reduce the interference effects. In the absence of a second SLD source, the linewidth of the existing laser diodes were broadened by modulating them at a higher frequency using a second signal generator, so as to shorten the coherence length. The intention was to average out the interference fringes and improve the signal to noise ratio. Oils with lower refractive indices were used to characterise the sensor head to avoid contamination. The new experimental setup is described in section 6.3.

### 6.3 Method 2: Dual wavelength, common path, FBG and bare fibre in oil

The improvements made to the previous setup were:-

- A second signal generator was implemented that operated at 15kHz with a 4.4Vpp triangular wave.
- A summing operational amplifier was used to combine the 15kHz and 997Hz waveforms before injection into the laser diodes.
- A fibre Bragg grating (FBG) was used instead of a filter. A bare fibre was used instead of a GRIN lens for simplicity

The new configuration is shown in Figure 6.9.

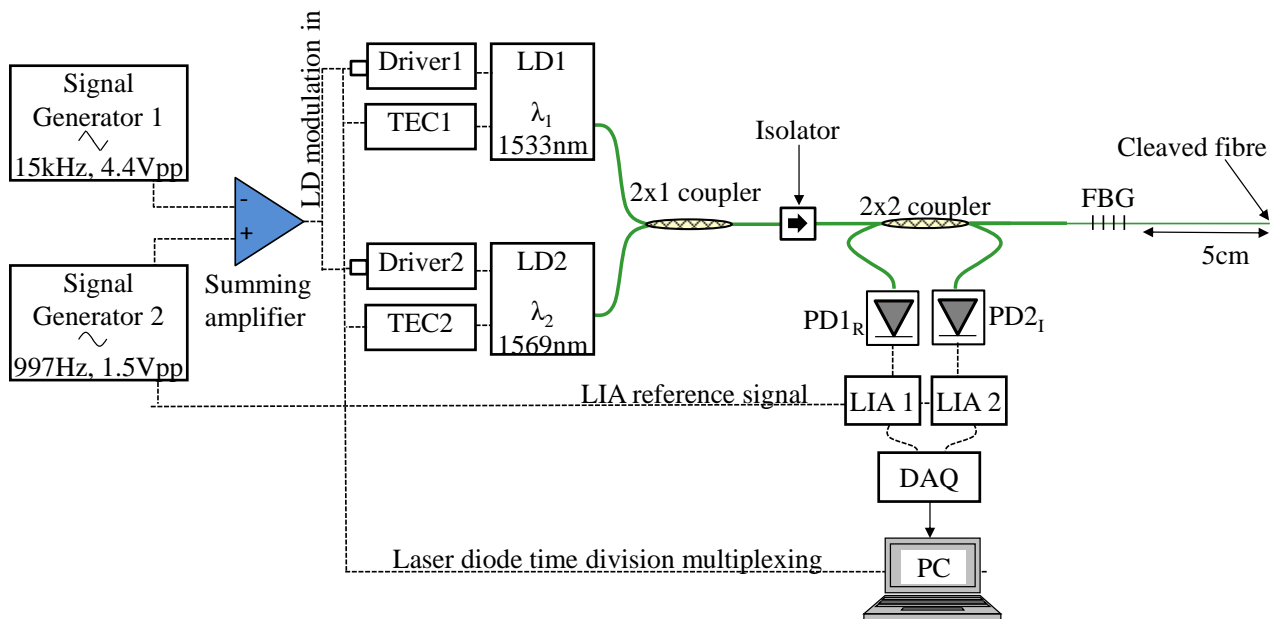


**Figure 6.9- Modified dual wavelength configuration that combines a high modulation frequency from a second signal generator. The dotted lines represent electrical connection and the solid lines represent the optical network. LD is laser diode, PD is photodetector amplifier, LIA is lock-in amplifier and DAQ is data acquisition adapter.**

A triangular wave was used for broadening the linewidth of the laser diodes, the waveform ensuring that the wavelengths were scanned linearly across the waveform. The optimum modulating parameters of 15kHz and 4.4Vpp amplitude were chosen by observing the pseudo broadband output on the OSA. The laser diodes' linewidth broadened to  $(\Delta\lambda)_{FWHM} = 0.1\text{nm}$  which gave a shorter coherence length in the range 22-25mm from equation (6.1) compared to the >160mm from the unbroadened source. A summing operational amplifier was used to combine the 15kHz and 997Hz signals before applying to the laser diode driver input and the details of the circuit are given in section 6.3.1. The 997Hz sine waveform still acted a reference for the lock-in amplifiers. The resulting pseudo broadband spectra are shown in Figure 6.11.

An FBG fabricated at Cranfield University, Department of Engineering Photonics was used. The FBG had a reflective Bragg wavelength of 1533.9nm, a linewidth of 0.77nm and a reflectivity of 47.5% to separate the wavelengths. The FBG was written in SMF-28 fibre, which had been hydrogen loaded at 100bar for a few weeks, using a 266nm frequency quadrupled Nd:YAG laser. The grating was 3mm long. Unlike the previous experiment, the 1533nm wavelength was now the reference pulse and the 1569nm wavelength the probe. The distance between the FBG and the end of the fibre was 5cm and the optical path length difference,  $\sim 15\text{cm}$ , was much longer than the coherence length of the modulated source so that there would be no cavity between the FBG and the sensor head. The optical path length difference,  $\Delta$  is described by equation (6.3) and is dependent on the refractive index of the cavity  $n$  (1.45), size of the cavity  $d$  (5cm) and the angle of incidence  $\theta$  (normal incidence).

$$\Delta = 2nd \cos \theta \quad (6.3)$$

The laser diodes have a wavelength dependent temperature coefficient of  $0.1\text{nm}/^\circ\text{C}$  as specified by the manufacturer. The temperature on the 1533nm laser diode controller was adjusted to  $33 \pm 0.2^\circ\text{C}$  (from the original  $25^\circ\text{C}$ ) so that the LD peak shifted to  $1533.8 \pm 0.1\text{nm}$  and coincided with the FBG peak. The laser diodes were tested separately initially. The 1533nm broadened LD was used to monitor the initial and Fresnel reflected intensities of the reference pulse. Figure 6.10 shows an improvement in the signal to noise ratio with the application of the additional 15kHz signal. With no high frequency modulation, the variation in the signal is  $\pm 6\%$  ( $1\sigma$ ) in region **a**. With the application of the 15kHz modulating frequency the variation in the signal reduced to  $\pm 0.7\%$  ( $1\sigma$ ) in region **b**. Although the amplitude of the fringes has reduced, residual fringes persisted at a smaller amplitude as shown in region **b** (see the enlarged inset). This could be because of small back reflections from the gap between the angle-polished connectors on the couplers that join the fibres, which could be eliminated by splicing the network together. Other sources of noise could be instrumental: phase noise from summing amplifier (unknown), LDs (negligible, not detectable on an electronic spectrum analyser), photodetector amplifier noise ( $1.2\mu\text{Vrms}/\sqrt{\text{Hz}}$ ) and lock-in amplifier noise (negligible at  $5\text{nVrms}/\sqrt{\text{Hz}}$ ). At 1kHz lock-in amplifier bandwidth, the detector noise would appear as  $\pm 10^{-5}\text{Vrms}$  on the reflectivity scale.

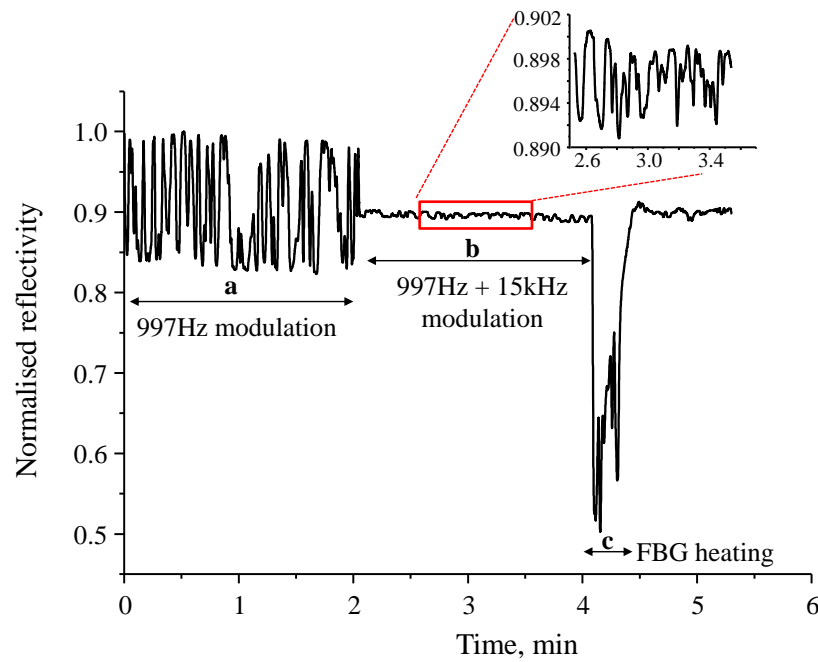


**Figure 6.10- Reflected intensity from the 1533nm wavelength from the FBG before and after the application of a high frequency modulation on the laser diode (regions a and b); and the effects of temperature on the FBG (region c)**

Fringes arising from cavities are likely to shift due to thermal expansion and contraction of the cavity and so the fibre arm containing the FBG and the cleaved end was heated using a heat gun to locate the temperature dependent components. The temperature of the heat gun reached  $85^{\circ}\text{C} \pm 5^{\circ}\text{C}$ . The output signal dropped sharply only when the FBG was heated as shown by region **c** in Figure 6.10 and not when potential cavities were heated, e.g. between the FBG and the sensor head or the rest of the fibre network. This is expected since the grating is temperature dependent. The FBG spectrum shifted relative to the LD spectrum by 0.6nm, such that the reflective peaks were not aligned and the apparent reflectivity dropped. This shift corresponds to a temperature sensitivity of  $10\text{pm}/^{\circ}\text{C}$  and is in agreement with the measurement made by James and Tatam [4]. The returned optical power from the LD and the FBG were recorded using an optical spectrum analyser (Ando, AQ6370C) and the shift in spectrum is shown in Figure 6.11.

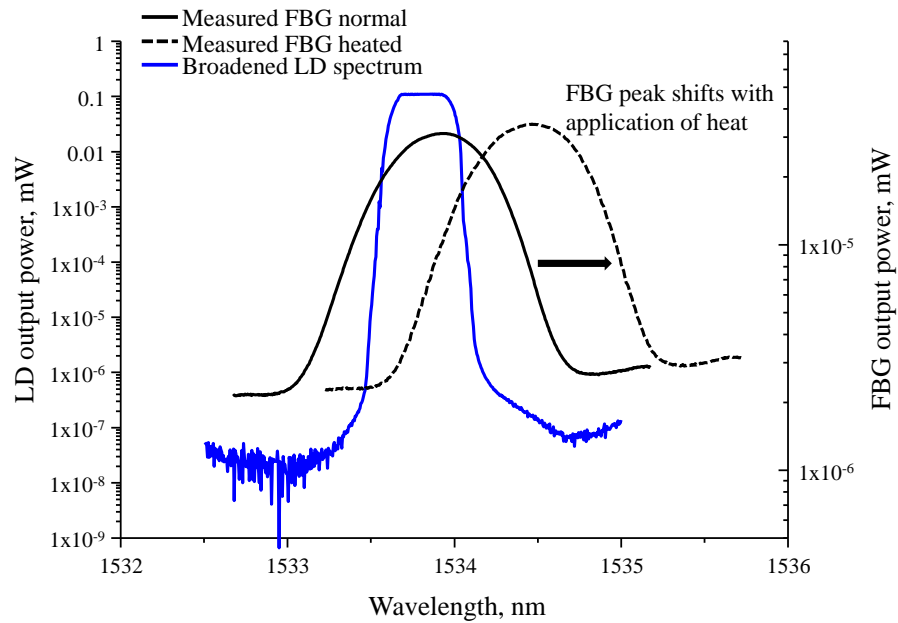


**Figure 6.11- Returned optical power from broadened 1533nm LD and FBG recorded using an OSA.**

Secondly, the 1569nm laser diode was used to monitor the initial and the Fresnel reflection intensities of the probe pulse. Similar improvements to the signal to noise ratio was observed using the 15kHz modulation frequency. Heating the FBG had no significant impact on the output intensity, which confirms that the probe signal was well separated from the FBG.

### ***6.3.1 Summing operational amplifier***

The summing amplifier combined the two input waveforms,  $V_{1in} = 15\text{kHz}$  and  $4.4\text{Vpp}$  and  $V_{2in} = 997\text{Hz}$  and  $1.5\text{Vpp}$ , into a single output waveform,  $V_{out}$ . The electric circuit diagram is shown in Figure 6.12. Where  $R_1$ ,  $R_2$  and  $R_3$  have a resistance value of  $10\text{k}\Omega$  and  $R_4$  is  $3.3\text{k}\Omega$ , which is the equivalent resistance of  $R_1$ ,  $R_2$  and  $R_3$  being in parallel.  $C_1$  and  $C_2$  have capacitance values of  $0.1\mu\text{F}$ . For demonstration purposes the circuit was implanted on a breadboard and I am grateful to Mr Steve Staines for his assistance in the design and building of this circuit.



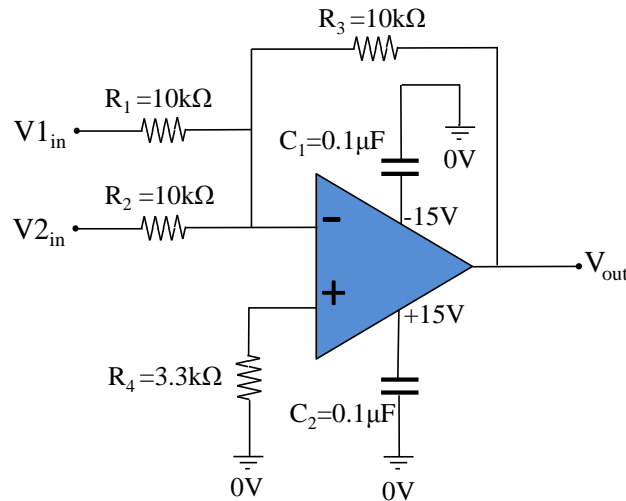


**Figure 6.12- Circuit diagram of the summing operational amplifier.**

The overall gain of this amplifier was unity and so the output voltage equals the sum of the input voltages. The output voltage was recorded using an oscilloscope (Tektronix, DPO2014) and the trace is shown in Figure 6.13, where the amplitude is  $\sim 6\text{Vpp}$ . However, since the two input frequencies are not multiples of each other, the waveforms were not phase-locked and this may have contributed to phase noise.

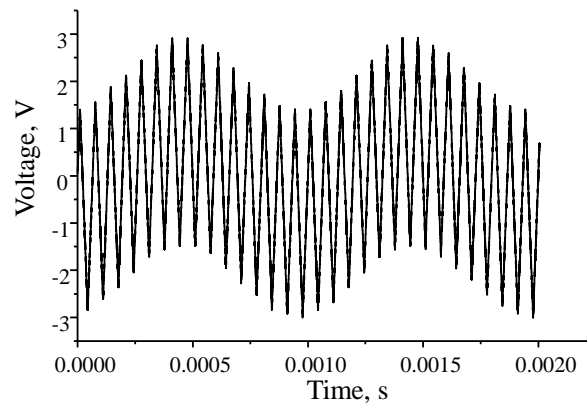


**Figure 6.13- Output from the summing amplifier (sum of 15kHz and 997Hz). The combined output voltage has a frequency of 15kHz and amplitude  $\sim 6\text{Vpp}$ .**

It would have been preferable to use a higher modulation frequency than 15kHz in order to separate the two frequencies, but this was the maximum that the laser diode controllers could handle with a triangular waveform.

### 6.3.2 Calculation of refractive index

The bare fibre was immersed into the oils of known refractive index and four sets of voltages were recorded by the LabView program. The data set is presented in a matrix,  $M$  shown in equation (6.4):

$$M = \begin{pmatrix} PD1_{R,\lambda_1} & PD2_{I,\lambda_1} \\ PD1_{R,\lambda_2} & PD2_{I,\lambda_2} \end{pmatrix} \quad (6.4)$$

Where,  $PD1_R$  is the reflected intensity,  $PD2_I$  is the initial intensity,  $\lambda_1$  is the 1569nm probe signal reflected by the test oil/sensor interface and  $\lambda_2$  is the 1533nm reference signal reflected by the FBG. The reflectivity of the FBG was measured from the transmission spectrum as shown in Figure 6.14, where there is a dip in reflectivity around 1533.9nm.

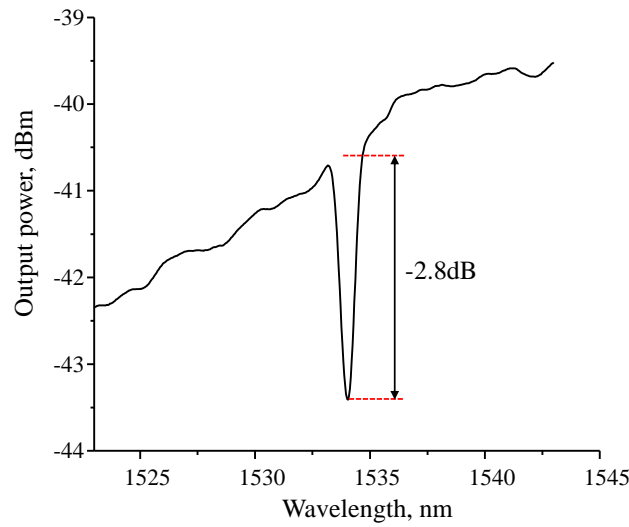


**Figure 6.14- Transmission spectrum of the FBG with a reflectivity dip centred at 1533.9nm**

The depth of the reflective peak, measured in transmission was -2.8dB. This corresponded to a reflectivity of 47.5% at the peak wavelength, 1533.9nm. It is appreciated that the FBG reflectivity will not be 47.5% across the entire spectrum of the broadened 1533nm LD source. For a more accurate estimate of the FBG reflectivity, the common area where the broadened LD and FBG spectra overlap could be integrated. The effective reflectivity is then expected to be less than 47.5%, which is likely to introduce systematic errors to the calculations.

The sensor head using an inefficient FBG means that a portion of the reference signal is able to reach the end of the probe and get reflected back. It is no longer a true reference as its reflectivity will change as a function of hydrogen concentration. Multiple interfaces at the sensor head also makes the derivation of an expression to calculate the refractive index of oil complex and this is outlined in detail in Appendix A. The final equation that was used to calculate the refractive index of oil,  $n_{oil}$  is given by equations (6.5) and (6.6).

$$n_{oil} = n_{core} \left( \frac{1 - \eta}{1 + \eta} \right) \quad (6.5)$$

Where,

$$\eta = \frac{R_{FBG,reference}}{\sqrt{\left( \frac{V_{reference}}{V_{probe}} \right) - R_{norm} + \left( \frac{R_{FBG,reference}}{R_{air,probe}} \right)}} \quad (6.6)$$

In equations (6.5) and (6.6),  $n_{core}$  is the refractive index of the fibre core, 1.45.  $V_{reference}$  is the normalised average  $(PD1_{R, \lambda 2})/(PD2_{I, \lambda 2})$  and  $V_{probe}$  is the normalised average of the data when the sensor head was immersed in oil  $(PD1_{R, \lambda 1})_{oil}/(PD2_{I, \lambda 1})$  and  $R_{norm}$  is the normalised scaling factor, taken from the average voltage data where the sensor head had been left in air (see Appendix A).  $R_{FBG,reference}$  is the efficiency of the FBG in reflecting the 1533nm pulse as the reference.

### 6.3.3 Results 2: Dual wavelength, common path, FBG and bare fibre in oil

Oils of known refractive index in the range 1.60 to 1.68 (Cargille Labs, Series M) measured by the manufacturers at 589nm and 25°C, were used to characterise the sensor head. Lower refractive index oils were used, since they were soluble in acetone unlike the high refractive index oils. This made the cleaning of the oil easier to avoid contamination. A Cauchy dispersion equation provided by the manufacturer was used to find an approximation of the refractive index at the operating 1569nm wavelength and 25°C. The resulting error on the calculated approximate value of the refractive index was  $\pm 0.005$  according to the manufacturer.

The method used was similar to that for the previous oil calibration charts, where three repeated air/oil measurements were made per oil. The average of the three measurements was plotted against the calculated approximate Cauchy values and is shown in Figure 6.15a. The error on the data points was calculated by taking the standard deviation of the three repeated measurements. The bare fibre with FBG was capable of detecting changes in refractive index as low as  $\Delta n = 0.003$  ( $1\sigma$ ), which is the repeatability of the measurements and is determined by taking the average of the standard deviations of the repeated set per oil. However, the experimental values are underestimated because of systematic errors and low reflectivity of the FBG, (see equation (A.9), page 164). Figure 6.15b shows the systematic errors in the measurements calculated from the residual values (difference between the Cauchy approximated values and the experimentally determined values). The average systematic error is 0.03 RIU.

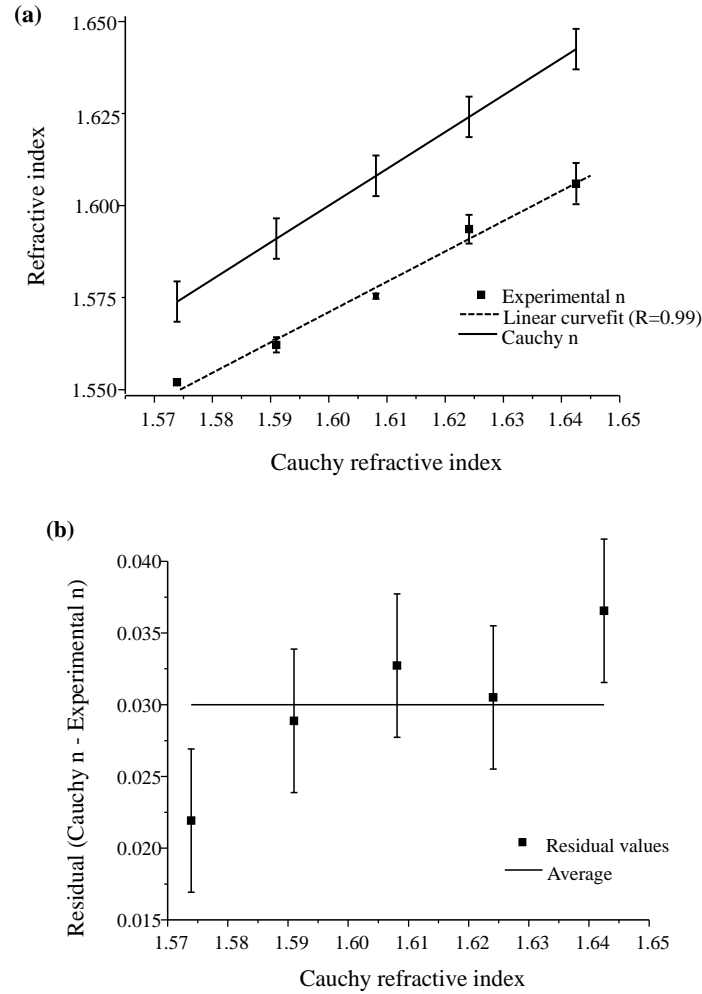


**Figure 6.15- a) Calibration chart showing the Cauchy refractive index, marked as a line with error bars and experimentally determined refractive index b) Systematic errors between the Cauchy approximate value and the experimentally determined value.**

### 6.3.4 Discussion 2: Dual wavelength, common path, FBG and bare fibre in oil

It has been demonstrated that a common path interrogation system was able to detect changes in refractive index down to  $\Delta n = 0.003$  RIU using a bare fibre and FBG as a sensor head. The experimentally determined values are underestimated because of the low reflectivity from the FBG. This was confirmed by substituting higher values of FBG reflectivity in equation (6.6), which brought the experimental values closer to the Cauchy values. An FBG with at least 70% reflectivity is desirable to reduce the systematic error. Temperature induced shift of the FBG spectrum relative to the broadened LD spectrum, as shown in Figure 6.11, means that the effective reflected probe signal will vary, which is likely to contribute to the systematic error.

A limiting factor on the  $\Delta n$  detection limit was that the reflected intensities of the two wavelengths being demodulated by LIA1 were very different. The 1533nm reflected intensity from the FBG was

~20 times bigger than the Fresnel reflected intensity from the cleaved fibre in air at 1569nm, because the FBG reflected ~47.5% of the incident light whereas the cleaved fibre reflected 3.4% (see chapter 4, Table 4-2, page 74) of the incident light from the core-air interface. When immersed in oil, the reflected intensity reduced by a further ~20 times. The gain setting on PD1<sub>R</sub> was optimised to prevent signal saturation for the larger 1533nm reflected intensity and this determined the full scale sensitivity of the corresponding lock-in amplifier, LIA1. Although PD1<sub>R</sub> and LIA1 were optimised for the 1533nm reference wavelength, the probe 1569nm reflected intensity was small when measured with the large sensitivity scale on LIA1. Digitisation was therefore an issue. For example if the sensitivity input voltage range was set from -200mV to 200mV on LIA1, the 1533nm reflected intensity spanned across 98% of the positive range scale, whereas the 1569nm Fresnel reflected intensity from the oil interface covered only 0.25% of the positive range scale (Fresnel reflected intensity from fibre-air interface covered 5% of the scale). The lock-in amplifiers have an 18bit A/D converter that allows quantisation of the signal to  $2^{18}$  output levels. This would give a minimum voltage resolution of 1.5 $\mu$ V per bit for the specified full scale range. Therefore, the 1569nm probe signal appeared digitised (see section 6.4.1 for signal data) and restricted the resolvable  $\Delta n$  limit.

Although, a highly efficient FBG would be ideal to create a true reference, the difference between the reflected intensities at 1533nm and 1569nm could then be even larger. This will further limit the  $\Delta n$  detection limit and hence, the hydrogen detection capabilities.

The purpose of this experiment was to demonstrate the viability of this interrogation system as a refractometer. The following section demonstrates its capability as a hydrogen detector using a palladium coated ball lens sensor head. Palladium has ~20 times higher reflectivity (chapter 4, Table 4-2, page 74) than an uncoated fibre in air and should ideally reduce the gap between the two different reflected intensities.

### **6.4 Method 3: Dual wavelength, common path, FBG and Pd coated ball lens in H<sub>2</sub>**

It was proposed previously in chapter 5 that the ball lens sensor configuration would provide an advantage with a larger sensing area over the restricted core diameter of a cleaved single-mode fibre. The larger area would allow a greater coverage for the palladium deposition, which could reduce the probability of catastrophic failure resulting from cracks on the film surface and improve the predictability of the sensor's performance in the long run.

The cleaved fibre in the common path system (Figure 6.9) was replaced with the best performing ball lens, B, with a reflectivity of 10%, as shown in chapter 5, Table 5-2, page 94. Therefore, the reflected light intensity was ~2.5 times more than the ball lens sensor head with 4% reflectivity used in the single source, 2 paths system experiments in chapter 4. The lock-in amplifier integration time constant

was set to 100ms. The ball lens sensor head was coated in 40nm palladium with an adhesive under layer of 10nm Ni. The test gas vessel, shown in Figure 4.8, page 74 was used for hydrogen testing and mixtures of different concentrations in the range 0-1000 ppm  $H_2$  in air were passed through the vessel. For each hydrogen step change in concentration applied, a total of 30 minutes was allowed for passage of gas down the connecting pipework, diffusion into the vessel and settling of the lock-in amplifiers before taking readings. This was followed by ~60 minutes of supplying just air to the vessel to allow the sensor to dehydrogenate and return to base line. Intensities from the probe and reference wavelengths were recorded simultaneously for each air/hydrogen cycle and the normalised signal calculated.

#### ***6.4.1 Results 3: Dual wavelength, common path, FBG and Pd coated ball lens in $H_2$***

The sensor head was exposed to cycles of 1000ppm, 500ppm and 300ppm hydrogen in air and the resulting probe signal at 1569nm is shown in Figure 6.16a. There are clear dips in the air baseline level when the sensor head was exposed to hydrogen. The probe wavelength intensity was small compared to the reference wavelength intensity. Although a palladium coated fibre should have 20x more reflectivity than the Fresnel reflection from an uncoated end, the reference signal from the FBG at 1533nm was ~20 times larger than the probe signal from the ball lens. This difference is in fact greater than that the experiment in section 6.3. The reflectivity of the ball lens started off as being 10% of the Fresnel reflection of a cleaved fibre, but the reflectivity dropped to 4%. It is possible that the reflectivity deteriorated during the transport of the fibre to/from the coating chamber or due to contamination of the surface during the handling, packaging and coating process.

Therefore the probe wavelength signal appeared digitised with an approximate step size of  $2 \times 10^{-3}$ . The signal was averaged over 10s (100 data points) to smooth the digitisation steps.

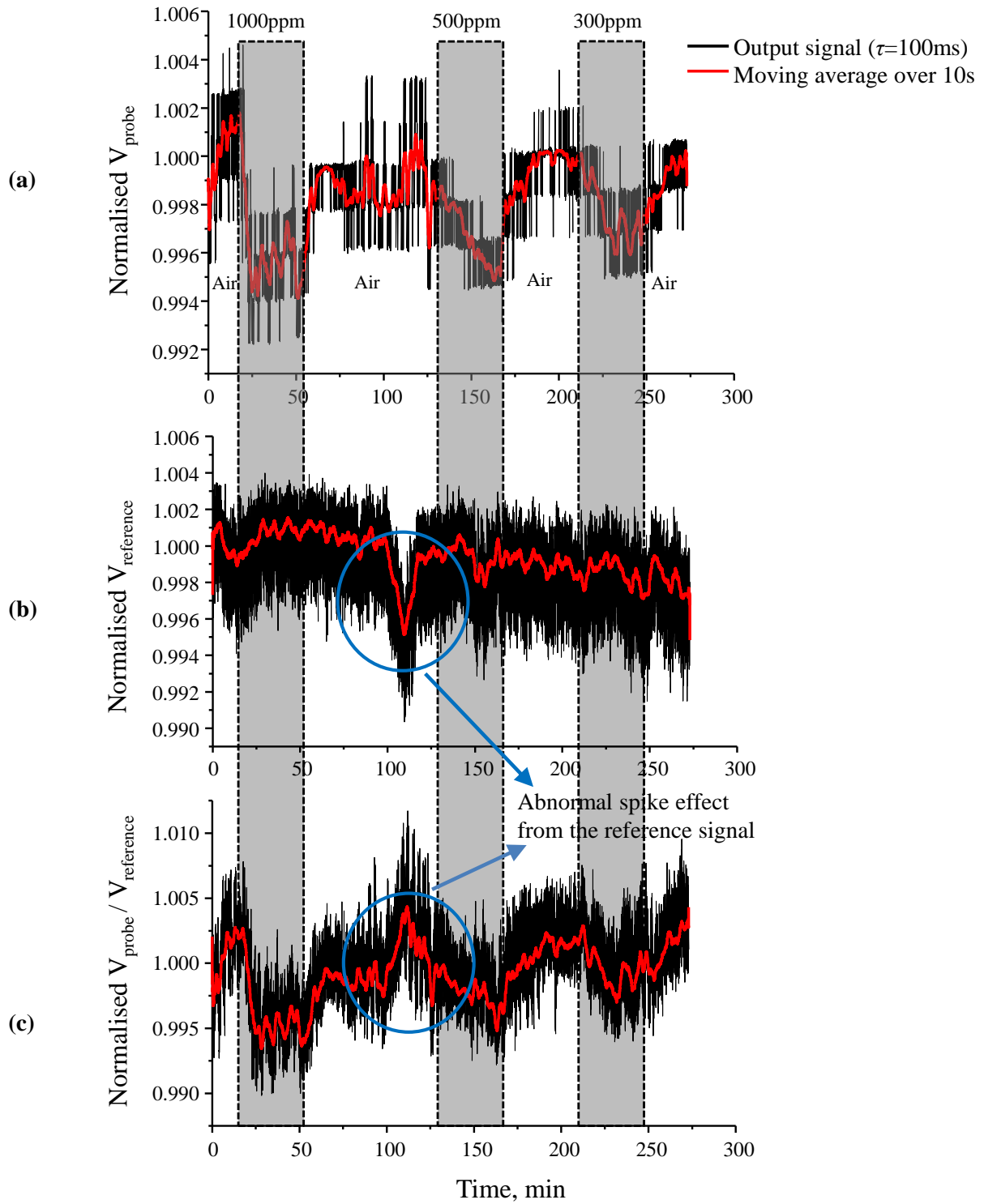


**Figure 6.16-** a) Hydrogen response from the 1569nm probe wavelength for different concentrations of hydrogen in air. The output was averaged over 10s to smooth the digitisation steps b) Reference signal from the 1533nm wavelength c) Normalised hydrogen signal. The noise on the reference signal dominates the output.

The reference signal was larger than the probe signal from the ball lens but the noise level was proportionally larger too, as shown in Figure 6.16b. So, when the probe signal in Figure 6.16a was normalised by the reference signal, the overall spectrum was noisier and introduced large error bars to the hydrogen measurements. The final normalised signal is shown in Figure 6.16c.

The response and recovery times were estimated as  $t_{90}$ - $t_{10}$  where  $t_{10}$  is the time at which the signal changed by 10% of the full step, and  $t_{90}$  is the time at which the signal changed by 90% of the full step. For a change between 0 and 500ppm  $H_2$  in air, the response time was estimated to be 18 min and the recovery time was estimated at approximately 20 min.

The hydrogen measurements were repeated twice. The change in reflectivity as a function of hydrogen concentration was calculated for the normalised signal and the average of the repeated set taken. This is shown in Figure 6.17 and the error bars on each point is the standard deviation of the repeated measurements. The repeatability using the dual wavelength, common path and ball lens as sensor head was estimated at 300ppm  $H_2$  in air ( $1\sigma$ ). However, there appears to be a zero drift, i.e.- the linear curve fit does not extrapolate to the origin where no change in reflectivity is expected in the absence of hydrogen gas. For an accurate curve fitting result more data points are needed.

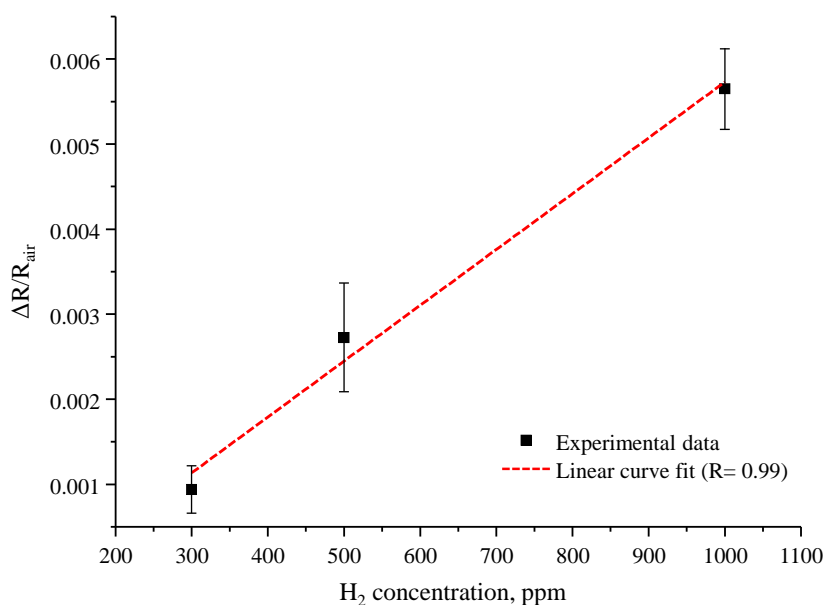


**Figure 6.17- Normalised change in reflectivity from the 40nm Pd coated ball lens as a function of hydrogen concentration. The dotted line shows a linear fit for the data points.**

To understand the importance of optimising the photodetector amplifier and the lock-in amplifier for the 1569nm probe wavelength intensity, the experimental setup was conducted at 1569nm wavelength alone. The PD1<sub>R</sub> setting was optimised to maximum possible signal to noise ratio, such that there was a 3 times improvement than the previous setup. The ball lens sensor head was exposed to 1000ppm  $H_2$  in air, followed by just air to allow the sensor head to recover. Whilst the proportional normalised



change in reflectivity ( $\Delta R/R_{\text{air}}$ ) was approximately the same for both the dual wavelength system and the optimised probe channel, the change in signal for the optimised probe channel was 23 times larger. The change in signal as the sensor head is exposed to hydrogen was calculated from the difference in voltages,  $V_{\text{Air}} - V_{\text{H}_2}$ . For example – using the dual wavelength system, the signal change for 1000ppm  $\text{H}_2$  in air was calculated to be 0.03mV, whereas using the optimised 1569nm source the signal change was found to be 0.7mV, which would improve the hydrogen sensitivity by an order of magnitude to approximately 30ppm.

#### ***6.4.2 Discussion 3: Dual wavelength, common path, FBG and Pd coated ball lens in $\text{H}_2$***

It is useful to compare these results with those obtained by Butler. Butler developed a prototype of a hydrogen sensor, consisting of the GRIN lens and the multi-layer structure (Figure 6.1), that would be commercially available at low cost and detect hydrogen in oil in the temperature range 20°C to 120°. He also developed a prototype of a temperature sensor to enable correction of the hydrogen sensor data for temperature fluctuations – a 500nm silicon film deposited on a cleaved end of a multimode fibre and followed by 100nm of Ni as a protective layer and as an optical seal. The silicon film acted as an interferometer and changed reflectivity with temperature. The dual wavelength and common path system was used to obtain a response to temperature from both wavelengths – increase in reflectivity with increasing temperature at 880nm and decreasing reflectivity with increasing temperature at 810nm. Ratios of the reflected signals would eliminate additional environmental effects. Butler was able to measure temperature with an accuracy of 1.5°C. The hydrogen sensor and temperature sensor were connected to an optical switch array.

However, Butler was not able to carry out field tests using these prototype sensors due to reliability issues with the multi-layer structure and the coating deposition techniques. Instead, he did tests with fibres coated in just PdAg immersed in transformer oil to prove the feasibility of detecting hydrogen in oil and was able to detect 50ppm  $\text{H}_2$  in oil. He carried out long term stability test of the sensor head by leaving it in 100ppm  $\text{H}_2$  in oil for over a month and noticed no degradation in sensor response. It is unclear from the report whether the interrogation system used to get these results consisted of two sources and a filter to separate the wavelengths.

In this project, Butler's dual wavelength interrogation system with a FBG and 40nm palladium coated ball lens as a sensor head was successfully implemented to detect hydrogen down to 300ppm  $\text{H}_2$  in air. This detection limit was compromised by unbalanced reflected intensities from the reference and probe wavelength. If the system was optimised for just the probe 1569nm wavelength intensity, the hydrogen detection limit would be as low as 30ppm  $\text{H}_2$  in air. This could be achieved by using a variable attenuator to reduce the intensity of the reference wavelength source.

## 6.5 Conclusion

A dual wavelength and common path interrogation system has been investigated as a refractometer and based on Butler's system [1]. Two laser diodes at 1533nm and 1569nm and a commercial filter deposited on a glass substrate to separate the wavelengths were used. The sources were time division multiplexed by a LabView code. The optimum data collection cycle, given the soft key start/stop of the laser diodes, was 7s between the first LD switching off, second LD switching on/off and then the first LD switching back on again, stabilising and recording 10 data points. The data set was averaged over 10 data points and the system was assumed to be a 'black box' that gave a reading every 7s. A faster data collection cycle would be ideal so that a true reference channel can compensate for time varying fluctuations in the signal. An alternative method to overcome this would be to use frequency division multiplexing of the sources, as explained in section 8.3.1, page 154. The sensor head was an off-the-shelf GRIN lens at the tip of a SMF28 fibre. An edge pass filter was placed at the end face of the GRIN lens, however there were a number of mechanical issues with the alignment of the filter to the GRIN lens, where the intensity of the reflected reference wavelength decreased during the adhesive curing process. The signal displayed interference effects due to the presence of a cavity formed between the two sides of the filter in the sensor head. An alternative interrogation system was designed whereby an additional high frequency modulation was applied to the laser diodes to broaden their effective linewidths and shorten the effective coherence length, so as to minimise the interference fringes originating from the cavity. The sensor head configuration was altered such that the filter was replaced with a fibre Bragg grating to alleviate alignment problems. This new design was successful in reducing the noise levels by a factor of 10.

Calibration was performed using different oils of known refractive indices. The change in reflected light intensity is a direct measure of change in refractive index and system was able to detect small changes in refractive index down to 0.003RIU. However, the experimentally determined values of the oils were an underestimation because the overall reflectivity of the FBG was  $\leq 47.5\%$  across the spectrum. Also, the FBG was temperature sensitive and so the reflected intensity varied with temperature changes in the lab. All these factors could have contributed to systematic errors in the measurement of the refractive indices of the oils.

The interrogation system was used to measure the sensitivity of a palladium coated ball lens as the sensor head in hydrogen. The uncoated ball lens had a diameter of 348.9 $\mu\text{m}$  and 10% reflectivity. However the use of a common path design also meant that the system had unbalanced levels of reflected light intensity for the two wavelengths. PD1<sub>R</sub> and LIA1 were used to detect both the reflected intensities of the 1533nm reference pulse and the 1569nm probe pulse. The reference signal reflected by the FBG was 20 times bigger than the probe signal reflected by the ball lens. PD1<sub>R</sub> and LIA1 were optimised for the bigger reference pulse. This meant that the LIA1 sensitivity settings

were not optimised to resolve small changes in the probe wavelength intensity and the resulting output appeared digitised. The resulting output had a significant source of uncertainty. This restricted the system's hydrogen detection limits and it was only able to detect 300ppm  $H_2$  in air. For a change between 0 and 500ppm  $H_2$  in air, the  $t_{90}$  response time was estimated to be 18 min and the recovery time was estimated at approximately 20 min. If the system had been optimised just for the 1569nm probe wavelength intensity, then the system's sensitivity limit of detection would improve to 30ppm  $H_2$  in air.

The response and recovery time for this experiment is higher in comparison to that of the ball lens sensor head and the single source, 2 paths system (40s response and 8mins recovery for 500ppm  $H_2$  in air) as described in chapter 5, section 5.4.1, page 98. This difference may be attributed to different ageing of the palladium and oxidation of the surface or due to differences in the deposition technique because the ball lenses were coated at separate times under nominally same coating conditions and film thicknesses.

If a highly reflective FBG were used with at least 70% reflectivity, this would reduce the systematic errors on the measurements since the reference wavelength would not see any changes in the refractive index. However this would lead to a bigger difference in the reflected intensity levels from the reference and the probe wavelength. A solution to this problem could be using a variable attenuator to turn down the intensity of the reference wavelength source. To be able to optimise both the wavelength pulses, separate photodetector amplifiers with reflective wavelength gratings and lock-in amplifiers could be used. However, this would further compromise the common path nature of the interrogation system. Or the sensitivity scale of the lock-in amplifiers could be changed using a LabView program corresponding to the respective LD switch on/off. However this would make the time-division multiplexing cycle sequence longer. The reference measurement would no longer be a true reference since it would not be able to sample simultaneous voltage changes and would fail to correct for time varying fluctuations in the optical components and the surrounding temperature.

The dual wavelength and common path interrogation system was designed to provide a self-referencing technique that will compensate for time varying changes in optical components as well as thermal fluctuations. However, the common path configuration for the wavelengths was breached by using a temperature dependent FBG as a filter to separate the reference wavelength from the probe. In addition, the temperature dependent changes in palladium's refractive index was indicated in section 4.3.2, page 76. The associated variation in reflectivity will not be compensated for since only the probe wavelength senses changes in the palladium layer. These limitations meant that the temperature compensation effect could not be demonstrated.

Improvements to the dual wavelength and common path system could be made using an athermalised FBG with a broader and more flat-topped spectrum and broadband swept tunable laser sources. These are discussed in the future work section in chapter 8. Palladium's reflectivity dependence on temperature can be characterised and corrected for in the hydrogen response measurements.

## 6.6 References

- [1] Butler, M. A., Sanchez, R. and Dulleck, G. (1996), *Fiber Optic Hydrogen Sensor*, Sandia Reports SAND96-113, Sandia National Laboratories, Albuquerque, US.
- [2] Hecht, E. (1998), *Optics*, 3rd ed, Addison-Wesley Publishing Company, New York, USA.
- [3] Pedrotti, F. L. and Pedrotti, L. S. (1987), *Introduction to optics*, 1st ed, Prentice-Hall International, Inc, New Jersey.
- [4] James, S. W. and Tatam, R. P. (2003), "Optical fibre long-period grating sensors: Characteristics and application", *Measurement Science and Technology*, vol. 14, no. 5, pp. R49-R61.

# Chapter 7

## Long term stability tests

Both Fresnel refractometer interrogation systems – (i) single source, 2 paths and (ii) dual wavelength, common path – were tested over a week to assess the stability in terms of white noise (from equipment) and long term drift (from systematic errors such as temperature effects) in the reflected intensity. These features can be quantified using Allan deviation statistical analysis. Based on this analysis, the best interrogation system was chosen and further tested over a period of a month to characterise longer term stability.

## 7.1 Allan deviation

### 7.1.1 Background

Allan deviation plots are useful to characterise the stability of a system, which also means characterising how the system is varying over time [1]. The plot helps analyse the noise and drift in signal over time. White noise can be reduced to zero if averaged over an infinite number of data points. However, there are other types of noise that may cause the signal to drift by large amounts in the long term and do not average out over time. Sources of these noises may be in the form of temperature fluctuations or DC offsets [1]. The Allan deviation is calculated from a time series data set. For the refractometers presented here, the reflected intensity from the fibre/sensor head tip was monitored over a period of ten hours with an averaging period of 100ms as shown in Figure 7.1a.

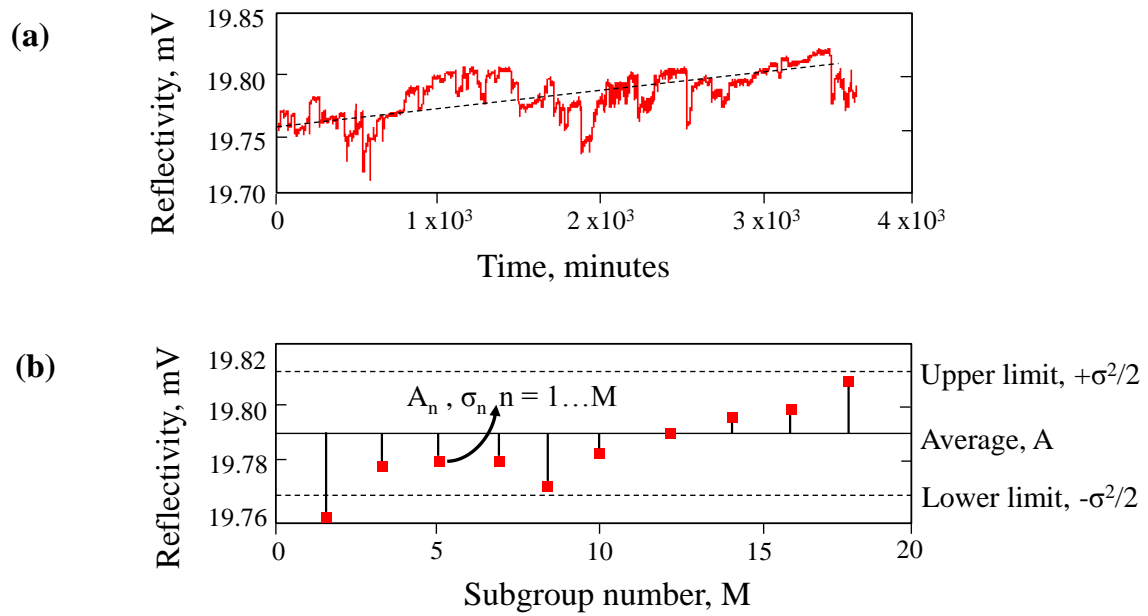


**Figure 7.1-** a) Reflectivity signals collected over time with a positive drift b) The time series is binned into  $M$  subgroups and the average of the  $n$ th subgroup,  $A_n$  and the standard deviation of that subgroup,  $\sigma_n$  was calculated and each are shown by the red squares.

The signal is noisy and has a positive linear drift, as shown by the dotted line in Figure 7.1a. Suppose there are a total of  $N$  data points and  $x_i$  refers to the individual points on the time series and  $i = 1, 2 \dots N$ . The average value,  $A$  of the data set can be calculated using equation (7.1) and is shown by the solid line in Figure 7.1b. The approach described mathematically below is the so-called Allan-deviation adopted by Werle *et al* [1].

$$A = \frac{1}{N} \sum_{i=1}^N x_i \quad (7.1)$$

The variance  $\sigma^2$  is defined by equation (7.2) and gives the highest and lowest level of the data spread. The upper and lower limits are shown by the dashed lines in Figure 7.1b; they are labelled from the average value and thus have values of  $\pm\sigma^2/2$  [1].

$$\sigma^2 = \frac{1}{N-1} \sum_{i=1}^N (x_i - A)^2 \quad (7.2)$$

The square root of the variance is the standard deviation,  $\sigma$  which represents the closest 68% spread of the data from the average. The variance of the mean is  $\text{Var}(A) = \sigma^2/N$ .

The data set is divided into  $M$  subgroups consisting of  $k$  elements such that  $M=N/k$ . Each subgroup is averaged over the  $k$  elements, and the average  $A_n$  (where  $n = 1, 2, \dots, M$ ) and the standard deviation  $\sigma_n$  of the subgroup is calculated using equations (7.3) and (7.4) and is shown in Figure 7.1b. The subgroup averages highlight drift in the reflected intensity. The length of the new data set is now  $M$ , with  $M$  data points. The factor of half in equation (7.4) gives the deviation from the average value.

$$A_n = \frac{1}{k} \sum_{l=1}^k x_{(n-1)k+l} \quad (7.3)$$

$$\sigma_n^2 = \frac{1}{2(k-1)} \sum_{l=1}^k (x_{(n-1)k+l} - A_n)^2 \quad (7.4)$$

The average and the variance are functions of the subgroup with a bin-size,  $k$ . The  $k$  value can be between 1 and  $N/2$ , since the minimum length of the resized data set,  $M$  can be 2 (recalling  $k=N/M$ ). Two consecutive average values are needed to calculate the variance of the resized data, as shown by equation (7.5), in which the variance is a function of  $M$  (number of groups) and  $\tau$  (integration time).

$$\sigma_A^2(M, \tau) = \frac{1}{2(M-1)} \sum_{n=1}^M (A_n - A_{n-1})^2 \quad (7.5)$$

The variance of the means,  $\sigma_A^2$  is the well-known ‘Allan Variance’ of the resized data, and a set of  $\sigma_A^2$  values can be calculated for a range of  $M$  values. For our analysis of the systems, the Allan deviation  $\sigma_A$  was plotted on a log-log scale against the averaging time period  $\tau = kt$ , where  $t$  is the time interval over which data is collected or the lock-in amplifier integrating time constant in the experiments. The Allan deviation gives the mean expected uncertainty from an instrument whose output is averaged over  $\tau$ . The log-log plot generally takes the form of a ‘V’ curve, where at short timescales white noise is averaged down to a minimum point and the rising curve at longer timescales shows the effects of drift. This is illustrated in Figure 7.2. The turning point in the data set at the lowest point (a) occurs at the optimum averaging time period. An analysis of the gradient of the drift curve, the rising plot on

the right of (a), can provide an insight into the stability of the overall interrogation system. It should be noted that Allan deviation plots do not all strictly follow the ‘V’ pattern due to statistical aberrations in the data when collected over an extended period of time or differences in the type of drift.

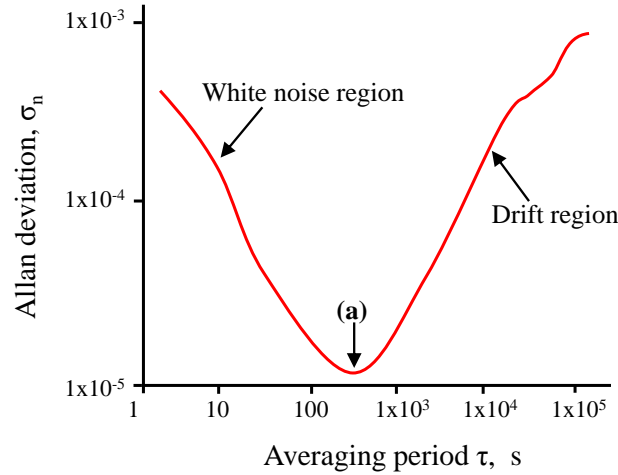


**Figure 7.2-** The normalised Allan deviation,  $\sigma_n$  against averaging time period on a log-log plot. A decreasing trend is expected for white noise, where it reaches a minimum at point (a) at an optimum averaging period. The rising trend indicates drift.

## 7.2 Single source, 2 paths and Pd coated cleaved fibre (24 hours)

The single source and 2 paths system described in chapter 4 that used either the 1550nm SLD or the 1569nm LD source were tested for long term stability over a period of 12 and 24 hours in air and at room temperature. The 1550nm SLD system used a 1x2 directional coupler with a 90:10 split ratio and a cleaved fibre coated with 10nm Ni and 40nm Pd as the probe fibre. The probe fibre was left in the testing vessel with synthetic air flowing in from the cylinder at a flow rate of 100sccm/minute. Reflectivity signals from the reference and probe channels using the SLD source were first collected over approximately 12 hours. The laboratory the air conditioning unit controlled the lab temperature to  $\pm 1^\circ\text{C}$  and the time series data is shown in Figure 7.3.

The long term tests were chosen to be conducted in air and not hydrogen due to limited supply of hydrogen. It was expected that most effects would be dominated by the interrogation system rather than the palladium sensing layer. Once a sufficiently stable interrogation system has been established, it will be worthwhile conducting long term experiments in hydrogen to compare with the air data.



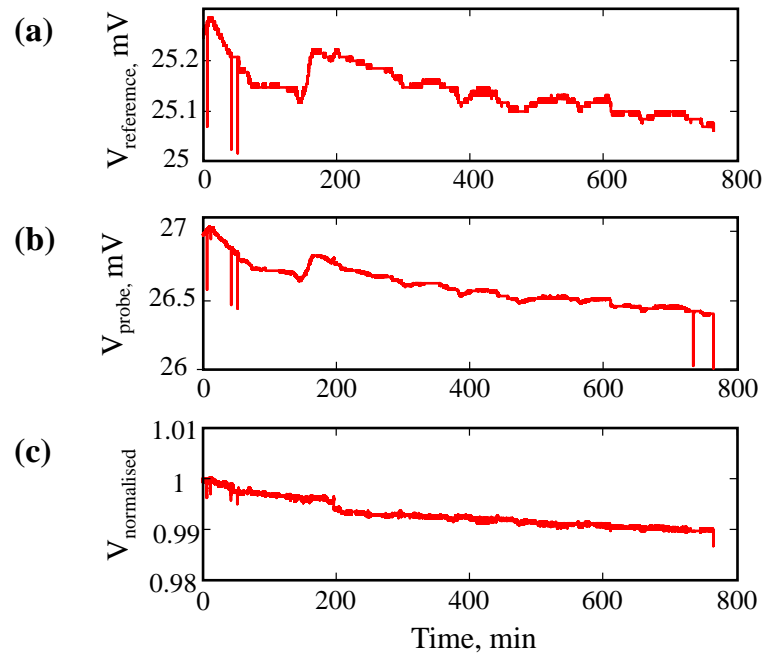


**Figure 7.3-** Time series data from the single SLD source and 2 path interrogation system running in air for 12 hours a) data from reference cleaved fibre b) data from probe cleaved fibre coated in palladium c) normalised signal,  $V_{\text{probe}}/V_{\text{reference}}$ .

The lock-in amplifier time averaging constant was set to 100ms. The 90:10 split ratio coupler was used to achieve a balanced interrogation network so that the amount of light reaching the reference and the probe fibre was equalised as far as possible, and there was symmetry in the photodetector amplifier and lock-in amplifier gain settings. The matched reflected intensities are shown in the raw data from the reference and probe fibre in Figure 7.3a and b. Spikes in the data were caused by the opening/closing of the lab door and the lights switching on. The Allan deviation was calculated based on the normalised reflectivity in Figure 7.3c and the plot is shown in Figure 7.4. It can be seen that the standard deviation of the dataset due to white noise gets averaged to a minimum at approximately 10s and rises upwards due to drift in the system and then appears to plateau. The unusual ‘wavy’ trend at the start of the Allan deviation plot is possibly due to statistical aberrations arising from the changes in reflectivity signal. A second Allan deviation plot was calculated for the data collected over 24 hours and the plot is shown in red in Figure 7.4. The 24 hour data captures a full cycle of temperature changes when the air conditioner unit was switched on during the day and then off outside working hours. The long term drift has a significantly sharper upward gradient and this is attributed to the rapid changes in signal due to temperature fluctuations.

An Allan deviation plot for a 12 hour experiment using the 1569nm LD system and a 50:50 split ratio coupler is also shown in Figure 7.4 (blue plot) for comparison. The plot highlights the system’s instability arising from signal variations due to interference fringes. The local minimum occurs at a much higher standard deviation of  $>0.01\text{mV}$ , reflecting the uncertainty in the data set.

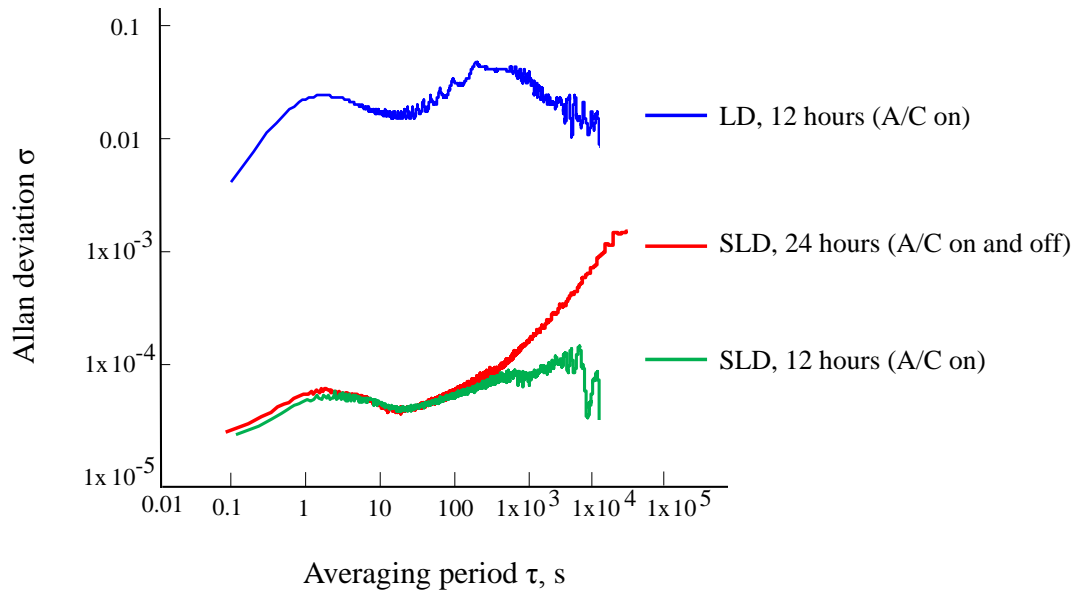


**Figure 7.4- Allan deviation plot of the single source and 2 path system using palladium coated cleaved probe fibre. The experiment was run for 24 hours using the SLD and for 12 hours using the LD with and without A/C (air conditioning).**

The interrogation system that used the SLD showed a marked improvement in sensitivity, with a minimum resolvable standard deviation of the order  $10^{-5}$  that allowed a repeatability value of 10ppm hydrogen in air to be achieved (see chapter 4). The SLD system showed better stability compared to the LD system. Furthermore long term experiments on sensor heads were therefore carried out using the single source and 2 paths system used the 1550nm SLD and the 90:10 split ratio coupler.

### 7.3 Single SLD source, 2 paths and Pd coated ball lens (4 days)

A palladium coated (10nm Ni and 40nm Pd) ball lens A from chapter 5, Table 5-2, page 94 was used as the probe fibre in the SLD source and 2 paths system long term experiment. The GRIN lens was not chosen for this study because of unsuccessful attempts in characterising its potential as a suitable sensor head (see chapter 5). The same experimental procedure as section 7.2 was followed, but the experiment was run for longer – 4 days. The fibre optic network was also placed inside a thermally insulating polystyrene box. The matched reflected intensities are shown in the time series data from the reference and probe fibre in Figure 7.5a and b. The temperature inside the box was logged in this instance every two minutes using an iButton® (DS1923) device, which had a resolution of  $0.5^\circ\text{C}$  with an offset of  $+0.13^\circ\text{C}$  and is shown in Figure 7.5d. The insulating box helped to reduce the short term temperature fluctuations but did not eliminate them.

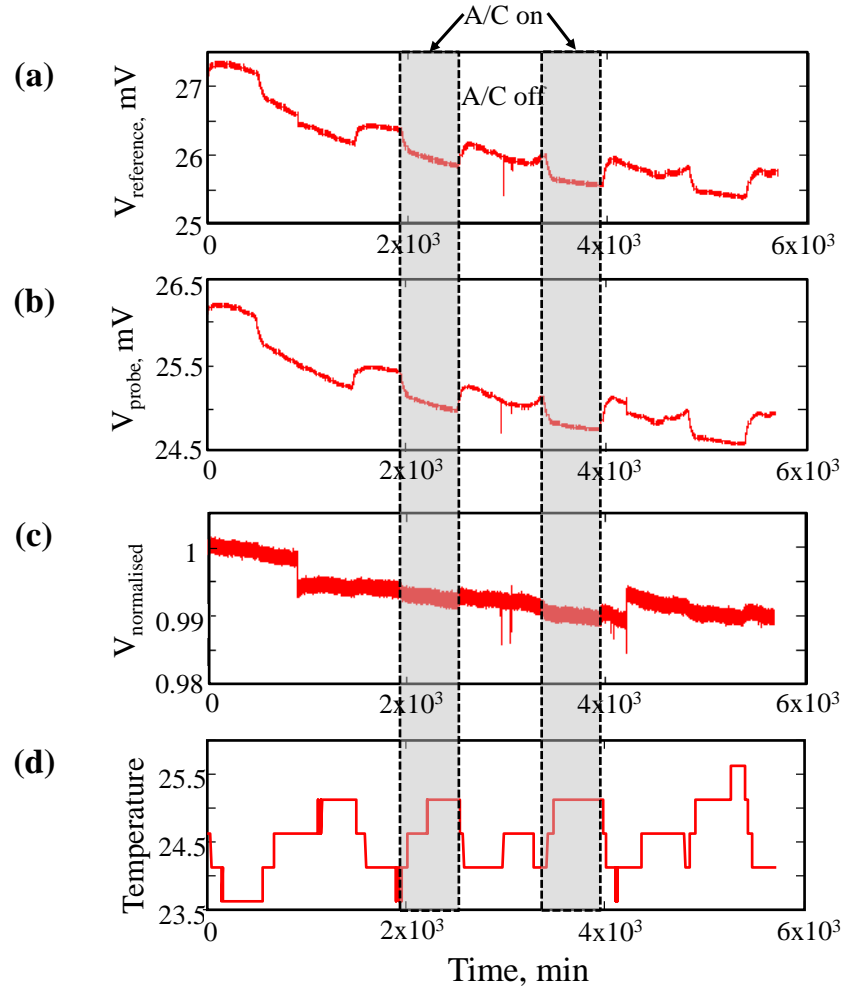


**Figure 7.5-** Time series data from the single SLD source and 2 path interrogation system running in air for 4 days a) data from reference cleaved fibre b) data from palladium coated ball lens probe fibre c) normalised signal,  $V_{\text{probe}}/V_{\text{reference}}$  d) temperature data. Shaded regions represent the lab air conditioner being switched off and the unshaded region where the lab air conditioner was on .

It can be seen that the reflected signal increases and decreases in a cyclic fashion and this coincides with the air conditioner switch on/off cycle. The experiment was carried out in September. When the air conditioner was switched off between 10pm and 7am, the temperature of the lab dropped. This was reflected as a rise in reflectivity during those times and is shown by the shaded regions in Figure 7.5. And the opposite is true when the temperature increased during the day time. So the change in reflected signal level appeared anti-correlated with the temperature.

The normalised signal in Figure 7.5c was not drift free, even though the probe and reference signals followed the same trend, due to differential temperature changes seen by the two paths. The Allan deviation was calculated for the normalised reflectivity and is shown in Figure 7.6.

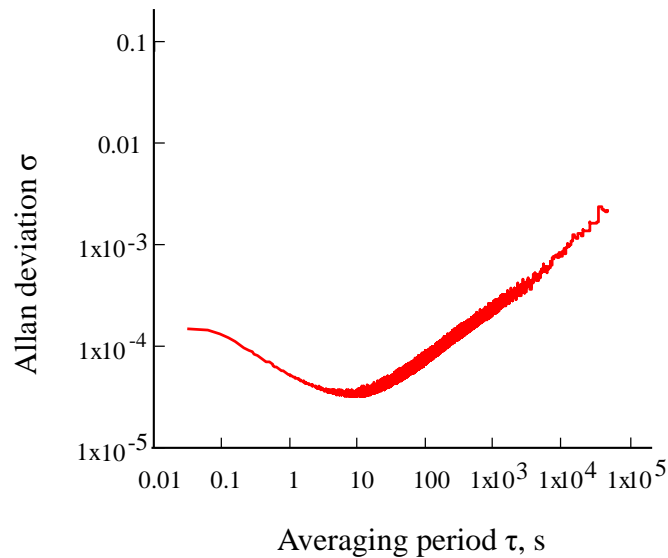


**Figure 7.6-** Allan deviation plot of the single SLD source and 2 path system using a palladium coated ball lens probe fibre. The experiment was run for 4 days.

The white noise was averaged to a minimum after approximately 10s and the uncertainty rose upwards due to drift at longer averaging periods, in a similar manner to the plot for the palladium coated cleaved fibre shown in Figure 7.4.

#### 7.4 Dual wavelength, common path and Pd coated ball lens (4 days)

The stability of the dual wavelength, common path interrogation system was tested with a palladium coated (10nm Ni and 40nm Pd) ball lens B and FBG as the sensor head as described in Table 5-2, page 94. Similar testing to the conditions described in section 7.3 was followed but without the insulating box, since the common path design for the reference and probe signals was believed to compensate for thermal fluctuations. The long term experiment was run for 4 days. Figure 7.7a and b shows the real time data from the reference 1533nm wavelength and the probe 1569nm wavelength source respectively. The probe reflected intensity was noisy but remained stable, whereas the reference wavelength intensity appeared unstable, possibly because of FBG sensitivity to temperature variations. Experiments that demonstrated the FBG's reflectivity dependence on temperature variation were discussed previously in chapter 6, page 121. The temperature data was collected every two minutes using the iButton® (DS1923) device and is shown in Figure 7.7d. Any correlation between the temperature and reflectivity is difficult to discern because of the poor resolution (0.5°C) of the temperature logger. The time interval used to plot the data was taken from the time division multiplexing sequence (Figure 6.4). It was shown that it takes 7s between the first LD switching off, second LD switching on/off and then the first LD switching back on again, stabilising and recording 10 data points. The data sets were further averaged over 10 data points and for the purpose of this analysis the whole system was assumed to be a 'black box' that gave a reading every 7s, which was

the time interval used to plot the Allan deviations. Although this was the optimum switching frequency given the soft start/stop key of the laser diodes, it is not ideal to wait 7s between the data collection since temporal variations in the signals will not be compensated for.

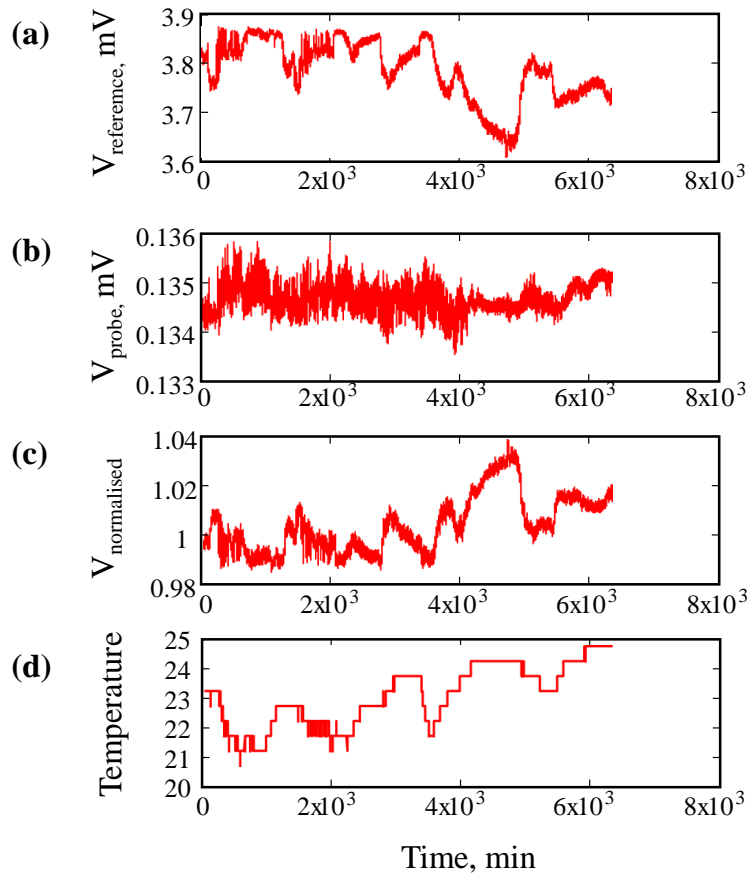


**Figure 7.7- Time series data from the dual wavelength, common path system running in air for 4 days a) data from reference cleaved fibre b) data from palladium coated ball lens probe fibre c) normalised signal,  $V_{\text{probe}}/V_{\text{reference}}$  d) temperature data**

The fluctuations in the reference signal appear in the normalised signal, shown in Figure 7.7c. An Allan deviation plot calculated based on the normalised signal is shown in Figure 7.8.

The Allan deviation plot for the dual wavelength, common path system has a different starting point relative to the plot obtained using single source and 2 path system (the plot for the latter is shown on Figure 7.8 for comparison), because of the different time intervals chosen for data acquisition, 7s and 100ms respectively. The first data point of the dual wavelength, common path graph has a standard deviation of  $\sim 10^{-3}$  mV, which is approximately an order of magnitude larger than the first data point of the single source, 2 paths graph in Figure 7.6. Whilst the white noise levels in the single source, 2 paths system signal are averaged to a minimum in 10s at point A, it is difficult to say where the local minimum point of the dual wavelength, common path system lies. If the minimum is at point A, then the averaging time period could be  $\sim 1000$ s. If a 100ms time interval was chosen, then this averaging period could go down to 10s. The rising plot represents the low frequency noise in the form of

temperature dependence. The noise from the dual wavelength, common path system appears to reach a maximum towards the end of the plot in comparison to the rising noise from the single source, 2 paths experiment plot in Figure 7.6.

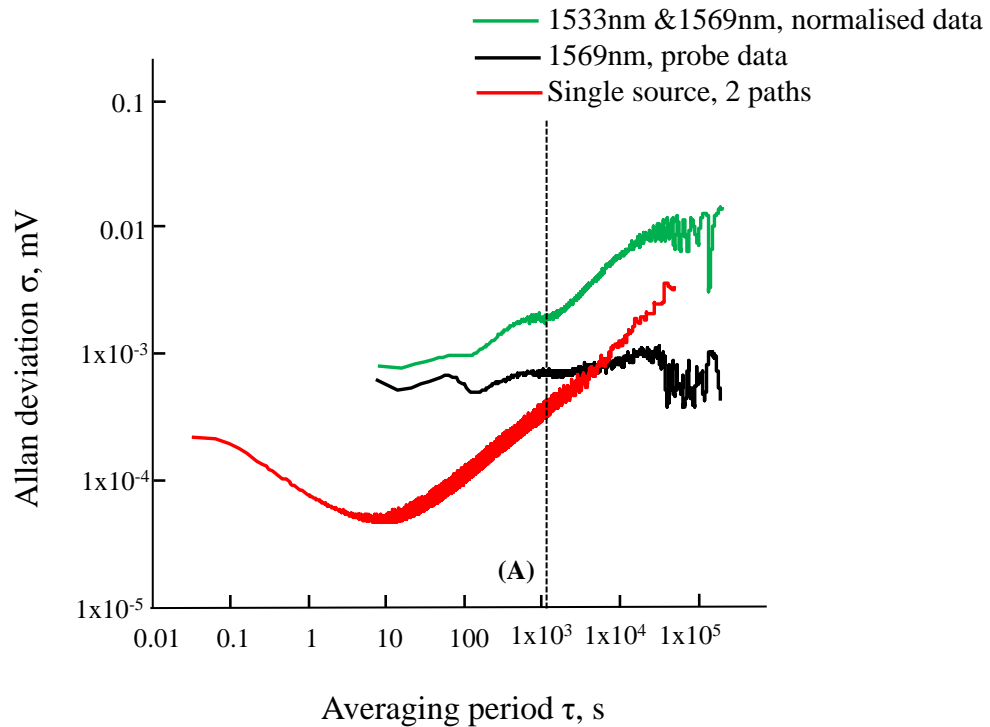


**Figure 7.8-** Allan deviation plot of the dual wavelength, common path system after running for 4 days. Allan deviation plot for the probe signal, where (A) marks the minimum. The plot obtained using the single SLD source and 2 path system using a palladium coated ball lens probe fibre is shown for comparison.

Another Allan deviation plot was computed for the probe data (1569nm wavelength, Figure 7.7b) to isolate the temperature dependent variations of the reference signal on the final normalised reflectivity. This is shown for comparison in Figure 7.8. The starting standard deviation of the data set is smaller than the dual wavelength, common path plot as the reflected signal is more stable, and the minimum is more obvious at 100s with less drift compared to the dual wavelength, common path plot.

This illustrates that the common mode path system has potential to improve the system's susceptibility to drift in the long term. Although the FBG's temperature dependence is an issue, it could be minimised by using an athermalised FBG and implementing an FBG with a broader top-hat spectrum in comparison to the source linewidth. However the sensitivity of the dual wavelength and common path system was an order of magnitude worse than the signal source and 2 paths system. This would affect the system's ability to detect hydrogen at safe and low levels and fails to satisfy the sensor requirements laid out in chapter 1, Table 1-1, page 4. For this reason, the final system that was chosen for a month long stability study was the single SLD source and 2 paths system using a ball lens as the sensor head. This is described in section 7.5.

### 7.5 One month stability of the final system (4 weeks)

The characteristics of the final system that was tested are summarised as follows:

- 1550nm SLD source with a linewidth of 50nm
- 90:10 split ratio coupler to send 10% of the light to the probe arm and 90% to reference to provide symmetry in light intensity and detector equipment settings
- Reference arm consisting of a cleaved fibre
- Probe arm consisting of a 348.9 $\mu$ m diameter ball lens with the highest achievable light reflectivity (10%)
- Probe fibre kept in the trial vessel with synthetic air supplied at a low flow rate of 100sccm/min.
- Lock-in amplifier time averaging constant set to 1s
- Fibre optic network kept inside an insulating polystyrene box
- A thermocouple temperature logger (USB TC\_08, Pico) with a resolution of 0.01°C

The time series data taken over a period of 4 weeks is shown in Figure 7.9. The probe and reference reflected signal spectra shown in Figure 7.9a and b had an approximately inverse correlation to the temperature fluctuations shown in Figure 7.9d. For a reduction in temperature, the signals are seen to increase and vice versa. The normalised signal in Figure 7.9c is not free from the temperature destabilisation but there is an improvement gained by using an insulating box as was shown in Figure 4.11, chapter 4, page 78.

An Allan deviation plot was calculated based on the normalised signal and shown in Figure 7.10. The 4 day plot from Figure 7.6 is also shown for comparison.

Once again the graphs start at different points because of different time intervals used during data acquisition. The minimum for the 4 day plot occurs at 10s (with 100ms time interval) and for the 4 week plot it occurs at 100s (with 1s time interval). A longer time interval was used for the long term testing for practical reasons concerned with storing and saving large volumes of data. The graphs overlap if they have the same starting point. The rising plots for both graphs showed approximately the same gradient. The 4 week plot has not reached a maximum at long time intervals and therefore larger drift effects might be expected over longer timescales.

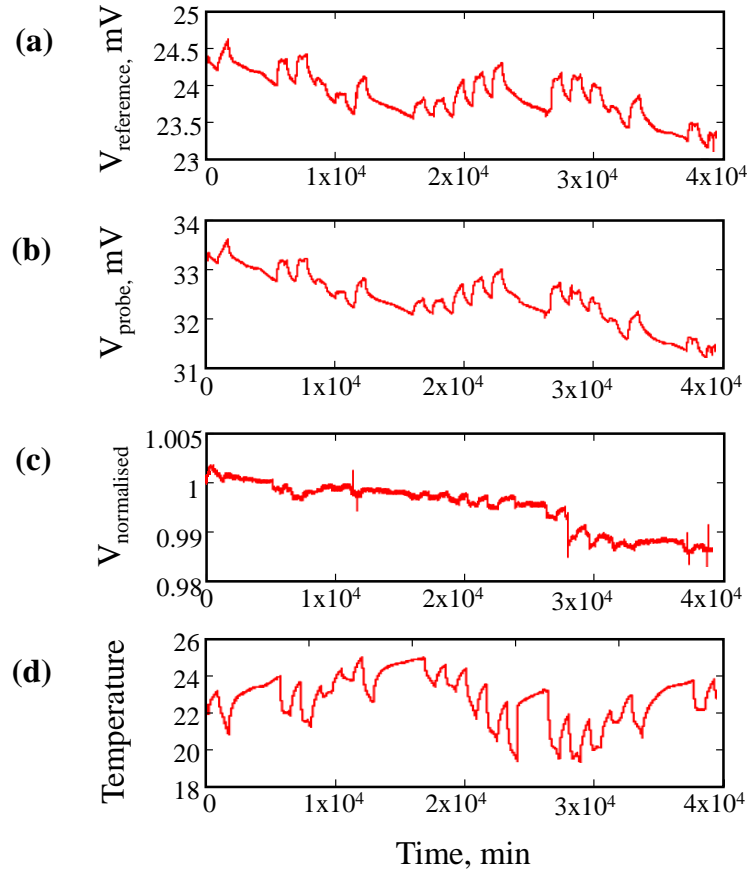


**Figure 7.9-** Time series data from the single SLD source, 2 paths system running in air for 4 weeks a) data from reference cleaved fibre, b) data from palladium coated ball lens probe fibre, c) normalised signal,  $V_{\text{probe}}/V_{\text{reference}}$ , d) temperature data

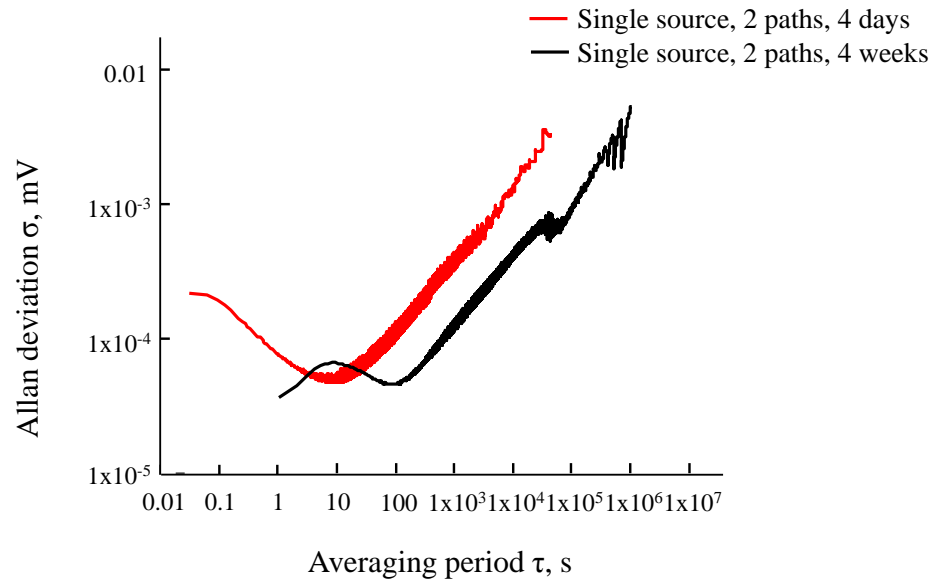


**Figure 7.10-** Allan deviation plot of single SLD source and 2 path system using a palladium coated ball lens probe fibre run for 4 weeks (black plot), with the plot for 4 days (red plot) for comparison.



## 7.6 Conclusion

The five long term experiments that were carried out under different conditions are summarised in Table 7-1.

**Table 7-1 – Summary of long term experiments**

| System configuration                  | Sensor head*                         | Time interval | $\sigma^\dagger$ , mV | Length of test | Comments   |
|---------------------------------------|--------------------------------------|---------------|-----------------------|----------------|--|
| 1569nm LD, 50:50 coupler, 2 paths     | Cleaved fibre                        | 100ms         | 0.01                  | 12hrs          | Noisy and unstable   |
| 1550nm SLD, 90:10 coupler, 2 paths    | Cleaved fibre                        | 100ms         | $10^{-5}$             | 12hrs, 24hrs   | SLD improves noise levels and stability                      |
| 1550nm SLD, 90:10 coupler, 2 paths    | 350.8 $\mu$ m BL<br>4% reflectivity  | 100ms         | $10^{-5}$             | 4 days         | Low noise levels but drifts over time                        |
| 1569nm and 1533nm LD FBG, common path | 348.9 $\mu$ m BL<br>10% reflectivity | 7s            | $10^{-3}$             | 4 days         | High noise levels but drift reaches a maximum                |
| 1550nm SLD, 90:10 coupler, 2 paths    | 348.9 $\mu$ m BL<br>10% reflectivity | 1s            | $10^{-5}$             | 4 weeks        | Best system that allows low $H_2$ detection limit but drifts |

\*: Coated in 10nm Ni and 40nm Pd and left in synthetic air supplied at a low flow rate

$\dagger$ : Allan deviation at which white noise averages to minimum

The lesson learnt from these sets of experiments are as follows- firstly using a broadband source instead of a narrow linewidth laser diode source reduced the noise and drift arising from interference fringes in the signal.

Secondly, temperature affects the reflectivity as observed when the experiments were run overnight. Temperature and reflectivity appear to be anti-correlated. This was noticed in the single source and 2 paths experiment, even after putting the fibre network in a thermally insulating box. The dual wavelength and common path system also showed effects of the temperature on the normalised ( $V_{\text{reference}}/V_{\text{probe}}$ ) signal, but as a result of the temperature-sensitive FBG that separated the reference and probe wavelengths. The reference signal appeared destabilised by temperature whereas the probe signal remained relatively immune. Allan deviation plots calculated for the normalised signal and the probe signal highlighted the presence of temperature related drift in the normalised signal. The dual wavelength, common path system drift showed a flatter gradient in the long term than the single source, 2 paths system, implying that the system's tolerance to drift may be better at longer time averaging constants but had a higher standard deviation or noise levels. This would affect the system's ability to detect low concentrations of hydrogen. Further improvements could be made to this system, such as using two broadband sources, athermalised FBG, FBG with a broader spectrum

etc, and these are described in chapter 8. Meanwhile, from these experiments it can be concluded that the SLD source and 2 path system that used a ball lens was the best system due to its low hydrogen detection capability of 10ppm H<sub>2</sub> in air, which meets the hydrogen sensor specifications laid out in Table 1-1, page 4.

Thirdly, under-sampling by using large time intervals between data acquisition increased the time taken to average the white noise.

However, the temperature may not only affect just the interrogation system but also the fibre/Pd interface as discussed in section 4.3.2. Differential changes in reflectivity may occur due to thermally induced expansion of the palladium lattice and therefore changes in its refractive index. A variation of 0.5°C in the lab temperature will cause the reflectivity to decrease by an amount that would be equivalent to the palladium being exposed to 20ppm H<sub>2</sub> in air.

Also, a general uncertainty related to long term testing is that two experiments will not have been exposed to the same conditions because of potential inconsistency of temperature changes. For future long term tests, the experiments should be conducted in low concentrations of hydrogen for long periods of time (a week or more) and a comparison of the Allan deviation plots, of experiments run both in air and hydrogen, be drawn.

## 7.7 References

- [1] Werle, P., Mücke, R. and Slemr, F. (1993), "The limits of signal averaging in atmospheric trace-gas monitoring by tunable diode-laser absorption spectroscopy (TDLAS)", *Applied Physics B Photophysics and Laser Chemistry*, vol. 57, no. 2, pp. 131-139.

# Chapter 8

## Conclusions and future work

This thesis has presented for the first time the investigation of the stability of a palladium coated optical fibre hydrogen sensor head and its associated interrogation system. This chapter summarises the conclusions drawn from the work presented in the previous chapters and suggests some possibilities for future work.

## 8.1 Summary

A summary of successfully implemented interrogation systems that were used to detect hydrogen is shown in Table 8-1. The single source, 2 paths system using a broadband SLD source centred at 1550nm showed repeatability of 10ppm H<sub>2</sub> (1 $\sigma$ ) in air with a response time at  $t_{90}$  for 500ppm H<sub>2</sub> in air of 80s and a recovery time of approximately 8 minutes. The dual wavelength, common path system that used two pseudo broadband sources centred at 1533nm and 1569nm showed a repeatability of 300ppm H<sub>2</sub> in air. The  $t_{90}$  response time for 500ppm H<sub>2</sub> in air was 18 minutes and a recovery time of 20 minutes. The differences in the response/recovery times may be attributed to different ageing of the palladium and oxidation of the surface or due to differences in the deposition technique because the ball lenses were coated at separate times under nominally same coating conditions and film thicknesses.

**Table 8-1 – Summary of hydrogen detection techniques and their limits of detection**

| Interrogation system         | Sec #    | Source                    | Sensor head <sup>‡</sup> | Modulation    | $\Delta n^*$       | H <sub>2</sub> detection limit |
|------------------------------|----------|---------------------------|--------------------------|---------------|--------------------|--------------------------------|
| Single source, 2 paths       | 4.2, 4.3 | SLD (1550nm)              | Cleaved fibre            | 997Hz         | 0.0009             | 10ppm                          |
| Single source, 2 paths       | 5.3, 5.4 | SLD (1550nm)              | Ball lens                | 997Hz         | 0.001              | 10ppm                          |
| Dual wavelength, common path | 6.3, 6.4 | LD (1533nm) & LD (1569nm) | Ball lens and FBG        | 15kHz & 997Hz | 0.003 <sup>†</sup> | 300ppm                         |

<sup>‡</sup>: coated in 10nm Ni and 40nm Pd;

\*: determined from oil calibration chart;

<sup>†</sup>: determined using cleaved fibre (with FBG) as sensor head in oil

It can also be noted that  $\Delta n$  for the dual wavelength, common path system is only three times larger compared to the single source, 2 paths system. However, this worsened the hydrogen detection limit by 30 times. It can be explained using the unoptimised probe channel argument. Had an optimised probe channel been implemented, then the limit of detection could be predicted to be as low as 30ppm H<sub>2</sub> in air.

The single source, 2 paths system was susceptible to differential changes in temperature experienced by the reference and probe fibres on two separate arms and this appeared as drift in signal when the experiment was run for long periods of time. The dual wavelength, common path system was designed to provide a self-referencing technique to compensate for thermal variations as both the reference and probe wavelength signal travel down the same path. Time-division multiplexing of the sources was applied and an FBG as a wavelength filter was used to separate the wavelengths to reflect the reference wavelength before the sensor head and pass the probe wavelength to reach the sensor head. However, a common network constructed using the components available meant that the system

was unbalanced. The reflected intensity from the reference signal was 20 times bigger than the probe signal and the same photodetector amplifiers were being used to detect both signals. Thus the system components were optimised for the larger reference signal and this restricted the system's capability to resolve small changes in the probe signal. As a result, the dual wavelength and common path system sensitivity was compromised. In addition, the FBG is temperature sensitive and thermal fluctuations of the lab were reflected in the normalised signal.

The final sensor head chosen was a ball lens where an appropriate section of a coreless silica fibre is attached to a singlemode fibre and melted under an electric arc to form a pure silica sphere. The area of the spot covered by a ball lens head is 20 times larger than the spot area of a single mode fibre. This would provide a wider coverage of the palladium for the ball lens sensor head. In this thesis a hypothesis has been proposed that would prolong the lifetime of an operating sensor head – that a larger area coated with the palladium sensing film, compared to a singlemode fibre area, is less likely to fail catastrophically because of hydrogen embrittlement from repeated hydrogen loading/unloading into a stressed palladium lattice. Although a larger area has a higher chance of encountering flaws, the overall performance of the sensor would be more predictable because the ratio of cracked to unaffected area is more likely to be consistent.

A second sensor head was also tested where a commercial GRIN lens was attached to the tip of a singlemode fibre. The GRIN lens had an end face diameter of 2mm, which would provide an even larger palladium coverage compared to the ball lens. However mechanical issues with alignment of a glass filter (to separate wavelengths in the dual wavelength, common path system) with the GRIN lens and an anti-reflection coating on the GRIN lens meant that this sensor head could not be characterised.

The ball lens was designed assuming that the light emitted from the SMF will expand radially with a Gaussian profile to a bigger spot size. The optimum curvature of the ball lens at which most of the reflected light will be coupled into the core is that for which the curvature of the radial wavefront coincided with the curvature of the ball lens. However, there was no ball lens diameter for which this occurred. A trial and error method of experimenting with different sizes of ball lens concluded that the optimum diameter was in the region of  $349 \pm 1 \mu\text{m}$ . The amount of light reflected back depended on the symmetry of the ball, accuracy of the measured ball lens diameter in comparison to the set diameter, and tapering of the core before the ball lens, which would permit additional expansion. Although the production concept of ball lens was simple and provided a robust, seamless design, the disadvantage was the difficulty in controlling the accuracy, tapering and symmetry, which were artefacts of the ball fabrication process using the fusion splicer. This affected the ball lens' reproducible quality each time.

There are further issues concerning the ball lenses. The tapering of the core before the silica ball implies that the Gaussian beam expansion model may not be the appropriate model for ball lenses. It

is also difficult to say which parts of the ball lens are reflecting light back. The illuminated area of the sensor head could be assessed, but not which parts of this area reflect light back into the core and it is therefore uncertain whether a larger sensor area was achieved.

The results for the change in reflectivity at respective hydrogen concentrations were not the same for the Pd coated ball lens and the Pd coated cleaved fibre using the single (SLD) source, 2 paths interrogation system. The change in normalised reflectivity for the Pd coated cleaved fibre was higher. This difference may have arisen for a number of reasons. It could be because the fibres were coated at different times and the sensing layers were not identical, or there was an offset in the absolute response levels from the ball lens probe tip due to a certain amount of light not reaching the end face of the palladium covered ball lens, or because of the assumption that light is incident normally on the end face of the ball lens. Light may be incident at a range of angles of incidence and the off-axis reflected light coupled back into the core is facilitated by the tapering.

It was originally decided that a thin 10nm adhesive layer of Ni would be used in between the substrate and the Pd layer to promote adhesion of the Pd layer to reduce micro-blistering. The Pd layer would be further followed by a thin 10nm protective layer of Au to protect the Pd from contamination and oxidation in air and yet allow passage of H<sub>2</sub>. 10nm was the minimum thickness achievable using the available sputter coater. However the addition of multiple layers made a complex structure and led to an unusual sensor response where the reflectivity of the Pd increased on hydrogen exposure instead of decreasing. It has been reported in literature that the reflectivity of Pd left in air may increase at first due to the formation of PdO but should subsequently decrease as the PdO becomes reduced to the metal. A reduction in reflectivity was not observed even after prolonged exposure to hydrogen.

It was found that freshly coated fibres with i) pure Pd, ii) Ni and Pd, iii) Ni, Pd and Au and iv) Pd and Au showed the expected response (reduction in reflectivity upon hydrogen exposure) when tested within the first week of being coated. Fibres that had a Ni underlayer showed an inverted response (rise in reflectivity upon hydrogen exposure) after being left in ambient air for 4 days. A Au capping layer prevented contamination in the case of Pd/Au coated fibre after 4 weeks of being left in air. However a Au capping layer in the combination Ni/Pd/Au did not prevent an inverted response from the fibre in the 4<sup>th</sup> week, suggesting that the response inversion may arise due to chemical reactions in the Ni layer. It was also observed that only 4 fibres tested out of 10, with a top coating of Au, responded to H<sub>2</sub> at all. This highlights the unreliability of the gold coating. Although gold has been reported to allow the passage of hydrogen, it is possible that the adsorption sites on the Pd layer were blocked during the deposition process. In order to prove a concept of a hydrogen sensor interrogated using a refractometer, all sensor heads used in experiments were coated with Ni and Pd.

For future work, several more sensor heads should be tested at regular intervals over a period of 4 weeks to identify trends in behaviour that may arise due to variation in the deposition technique. Also,

sensors with thinner Ni layers need to be tested to find the optimum thickness, as well as alternatives to Ni such as Ti and Cr. More fibres need to be tested with varying thickness of Au to find the optimum thickness at which the hydrogen will be able to pass through the gold layer. Alternatives such as Pt as the protective layer should also be tested.

It was also found that the 2 out of 4 ball lenses coated in Ni/Pd showed the expected response over a period of 6 months. This further highlights the lack of understanding of the chemical reactions in the complex coating structure and why some coatings responded correctly to hydrogen whereas the rest responded in an opposite manner.

The working ball lenses were used on three occasions over a period of six months using the single source, 2 paths system and 90:10 coupler to ensure equal amounts of light reached the reference and the probe fibre. The best result was obtained where the hydrogen cycling allowed longer recovery period of 6 minutes in air. Ideally, a longer recovery period of at least 15 minutes would ensure more consistent and repeatable responsivity results. This highlights the need for following the same test procedure in sensor head characterisation in future experiments, so that results can be compared with repeated measurements. This will allow an estimation of the accuracy and drift in the results separated by time.

Long term experiments were completed, where the two interrogation systems were left running in air:

- i) Single (1550nm SLD), 2 paths and 90:10 coupler interrogation system using a ball lens
- ii) Dual wavelength pseudo broadband sources (1569nm LD and 1533nm LD) and common path interrogation system using a ball lens

The systems were initially assessed for long term stability for 4 days. The single source, 2 paths system showed low noise levels but displayed temperature induced drift that increased over time. The dual wavelength, common path system showed high noise levels but the drift averaged out eventually over time. In terms of stability the dual wavelength, common path system demonstrated resistance to drift and hence improved long term stability, however the system's hydrogen detection capability was outside the specification range of 10ppm H<sub>2</sub> in air, from Table 1-1, page 4. There is potential for the dual wavelength, common path system in being the ultimate stable interrogation system but improvements need to be made, discussed in section 8.3, before it is suitable for use as a hydrogen concentration monitor in a potentially explosive environment. For these reasons, the single source, 2 paths system was chosen to be the best system from these sets of experiments.

## 8.2 Conclusions

The long term stability of a fibre optic hydrogen sensing system- in terms of the sensor head and the interrogation system- has been assessed for the first time.

A novel application of a ball lens created at the tip of a fibre has been demonstrated, where the ball is coated in a thin film of palladium and used as a hydrogen sensor. It has been proposed that a larger active area on the sensor head will improve the sensor's resistance to catastrophic failure due to hydrogen induced pin-holes and cracks. This will therefore increase the sensor's long term stability and durability.

Two self-referencing interrogation systems have been characterised for hydrogen sensing. The systems were quantified in terms of noise and drift using an Allan deviation statistical plot and compared. This approach of evaluating the system has been applied for the first time.

## 8.3 Future work

### *8.3.1 Dual wavelength and common path system*

The dual wavelength and common path configuration has the potential to be a stable interrogation system with a combination of some of the following ideas:

- i. Two broadband SLD sources could be used instead of two LDs modulated at high frequency to mimic broadband sources. The SLDs would provide a wider and flatter optical spectrum. An FBG with a wide linewidth and a flat top spectrum coinciding with the source spectrum would provide a true reference signal in case the FBG spectrum shifts with temperature fluctuations.
- ii. A swept wavelength tunable laser source could be used. These use external cavity semiconductor lasers and are able to sweep the lasing wavelength over a wide spectral range. These sources use a temperature stabilised acousto-optic tunable filter to ensure consistent stability of output emissions during the laser lifetime. Two photodetector amplifiers could be used, one each for collecting the reflected reference and probe signal. One reference fibre would have an FBG/filter to reflect the probe wavelength and the probe wavelength would have an FBG/filter to reflect the reference wavelength. This will eliminate the need for time division multiplexing and the reference and probe data will be collected simultaneously, however this design will stray from the common path design.
- iii. If a single source is used in conjunction with an edge pass filter at the sensor head, then the wavelength of the source,  $\lambda$  could be modulated with an amplitude,  $A$  after the 3dB edge of the filter such that the output response has a larger amplitude. This is demonstrated in Figure



- 8.1. The output will be partially transmitted or reflected depending on the slope,  $dV/d\lambda$  slope of the filter.
- iv. The problem of the reference signal being 20 times larger than the probe signal could be resolved by using a variable attenuator to turn down the output power of the reference source. This could provide a balanced network and improve the hydrogen detection sensitivity of the system.
  - v. An FBG is temperature sensitive and to eliminate effects of fluctuating temperature an athermalised FBG could be used, where the FBG is encased in a Teflon tube with aspiratory holes drilled into the surface to maintain an ambient temperature inside the tube [1]. An alternative to an FBG would be to directly deposit an appropriate filter on top of a GRIN lens with no anti-reflection coating. Also, if the FBG spectrum were more flat topped and wider than the relevant source, there would be a greater tolerance to wavelength changes.
  - vi. The two sources could be frequency division multiplexed rather than time division multiplexed, where both sources are run simultaneously but modulated at different frequencies that are not multiples of each other. Two lock-in amplifiers would demodulate the two signals at the corresponding reference frequencies and be separated using an athermalised interference filter or FBG. This would ensure continuous real time measurement of the reference and probe signal, which would improve short term noise, compensation for optical/temperature fluctuations and enhance signal to noise ratio.

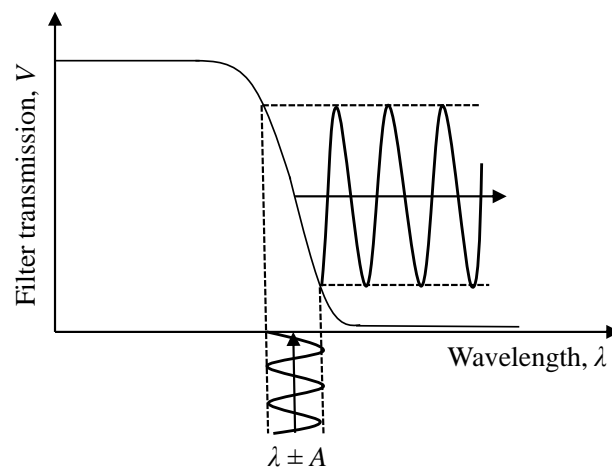


**Figure 8.1-** Modulating the source output wavelength,  $\lambda$  with a modulation amplitude  $A$  near the edge of the filter. The output response has larger amplitude. A portion of the output is transmitted and the rest reflected.

### 8.3.2 Sensor heads

The optimum diameter of the MM125 ball lens was determined to be in the region  $349 \pm 1 \mu\text{m}$ . More ball lenses were tested around the  $350 \mu\text{m}$  region than around the  $400 \mu\text{m}$  region, with a high success

rate determined by high levels of light reflected back into the core. This does not mean that 400 $\mu$ m diameter ball lenses would not reflect light back into the core. More ball lenses with bigger diameters need to be tested. The Fujikura, FSM-100P had an upper range of ball lens diameter of 400 $\mu$ m. For even larger ball lenses, an upgraded model of the Fujikura splicer, LZM-100 could be used that uses a CO<sub>2</sub> laser as a heating element. Advantages of melting using a CO<sub>2</sub> laser source are – 1) the splicer requires little maintenance and less frequent calibration due to absence of electrodes; 2) the heat source eliminates metal oxide contaminant particles and, 3) the heating area is adjustable and with the implementation of feedback control the CO<sub>2</sub> laser power is very stable and allows uniform heating [2]. A schematic of the CO<sub>2</sub> laser beam heating a fibre is shown in Figure 8.2. The feedback control method uses a power meter to measure 2% of the output beam power and two CMOS (complementary metal-oxide semiconductor) cameras, X and Y to measure the fibre luminescence. A maximum diameter of 2.5mm for the ball lens is possible using this splicer.

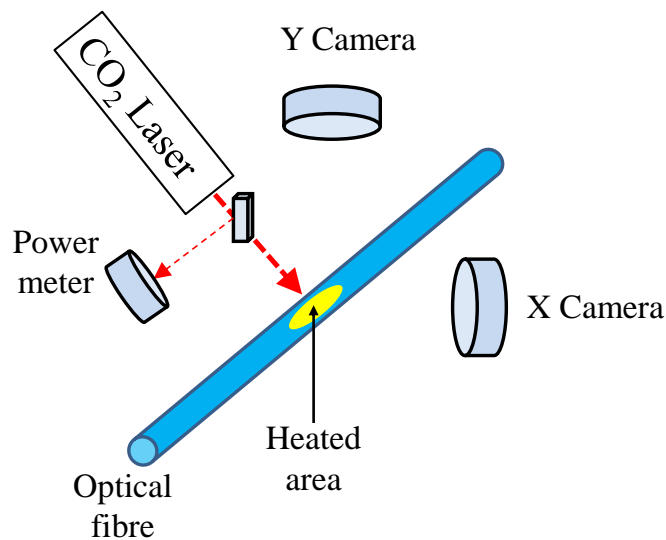


**Figure 8.2- CO<sub>2</sub> laser beam melting an optical fibre. Schematic adapted from [2]**

It was discussed that the optimum curvature of the ball lens, at which most of the reflected light will be coupled back into the core, will occur when the wavefront radius of curvature is equal to the radius of the ball lens. However, it was not possible to achieve this. To match the wavefront curvature to the ball lens geometry, the end face of the ball lens could be carefully polished to increase the ball lens' radius of curvature as shown in Figure 8.3.

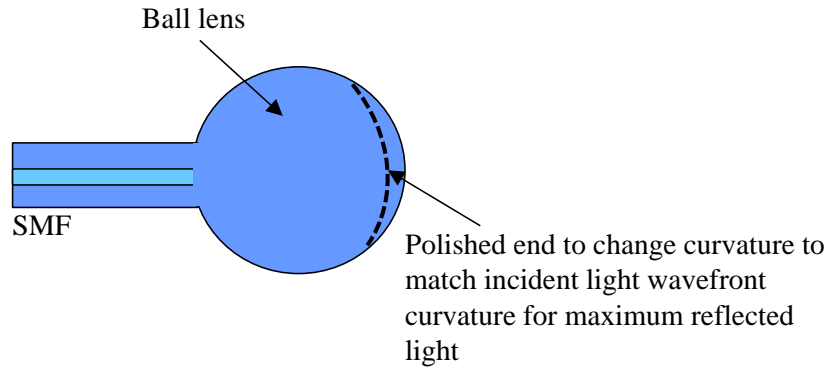


**Figure 8.3- Ball lens with a polished end to match the wavefront curvature of incident light to ensure maximum reflected light back into the core.**

This arrangement is likely to ensure that the beam is normally incident on the ball lens surface and uncertainties about which parts of the illuminated area is responsible for reflecting light back into the core will be reduced.

Alternative sensor head ideas would be (i) multimode fibre where the core diameter is large and in the range 50-60 $\mu\text{m}$  or (ii) an integrating sphere/rod. Figure 8.4a shows a ball lens created at the tip of a SMF, where a short section of pure silica fibre was spliced and melted under an electric arc. If the surface of the ball lens is roughened and coated with a thin palladium film, it will act as a solid integrating sphere. The same principle may be applied to a solid integrating rod, where a short section of pure silica fibre is spliced to the tip of a SMF as shown in Figure 8.4b. Light incident on the inner surface of the sphere/rod undergoes multiple scattering and after a few passes across the cell to remove local effects of launch geometry, the irradiance is uniform inside across the surface [3, 4]. This ideally means that light will be sampling a larger palladium covered area and thus supports the hypothesis that the performance of a larger sensor head is more likely to remain predictable in case of hydrogen embrittlement effects on the palladium surface.

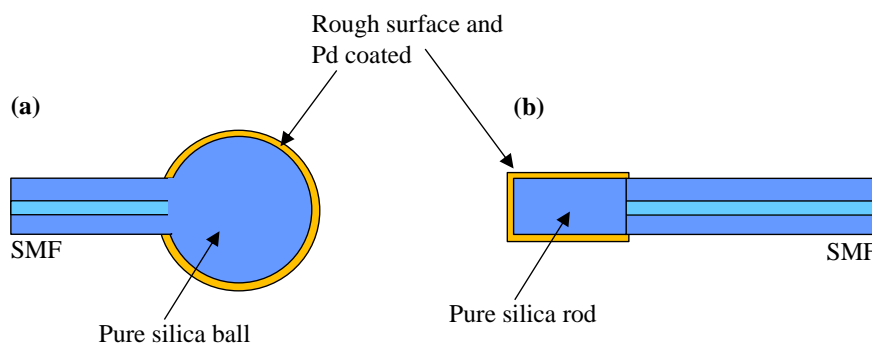


**Figure 8.4- Integrating solid geometry sensor head ideas with a roughened out surface and coated with a thin palladium film – a) ball lens at tip of SMF, b) silica rod spliced to SMF**

The GRIN lens is still attractive as a potential sensor head since they would allow a larger surface for palladium coverage, however custom made GRIN lenses without anti-reflection coatings will be

needed for future work. In order to complete the project within the budget available, commercial filters deposited on glass substrates were used in the separation of wavelengths in the dual wavelength, common path system. There were mechanical issues with the alignment of the GRIN lens and the filter block in the absence of ultra-precision engineering tools. It will be beneficial to deposit a filter film directly on the GRIN lens, similar to Butler in his original sensor [5].

An alternative to using filters and FBGs to separate two wavelengths into reference and probe signals, may be to use a transreflective nano-wire grid polariser as a spatial filter as described by Feng *et al* [6]. The wire grid has a period smaller than the wavelength of incident light and the grid reflects the TE-mode (where the electric vector is parallel to the grid) and transmits the TM-mode (where the electric vector is perpendicular to the grid). The authors used a period of 200nm with an operating wavelength of 1500nm. The working principle of the grid is demonstrated in Figure 8.5.

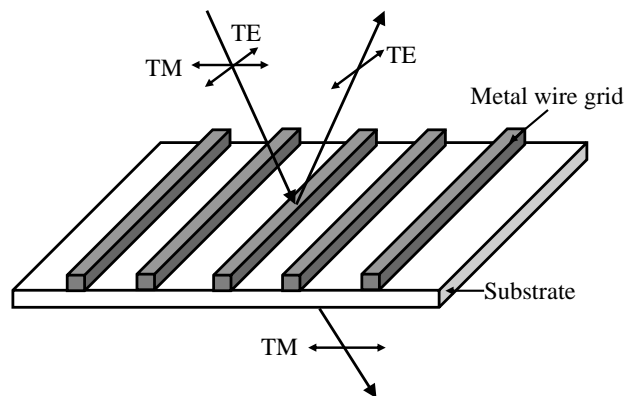


**Figure 8.5-** Schematic of a wire grid polariser taken from [6]

The authors described a fabrication process where the tip of a SMF fibre was coated with 70nm gold, which acted as the polariser, and used a focussed ion beam to etch a grid. This concept may be applied to a hydrogen sensor where the SMF tip is coated first in palladium and then gold for the polariser. The changes in the Fresnel reflected intensity of the TM-mode can be detected using the common path design but using two photodetectors with attached polarisers.

It is worth mentioning that the effects of varying the adhesive Ni layer thickness on sensor response should be tested. A 10nm Ni film was used in this project because that was the minimum thickness permissible using the sputter coater. Thinner films should be tested if they can be fabricated. It is unclear whether the inverse response from the palladium sensing layer was due to an inappropriate ratio between the Ni and Pd layer thicknesses. Also, a Pt layer as the protective capping layer should be tested instead of Au to test the response difference.

### 8.3.3 Packaging

In order to prevent the palladium coated sensor heads from breakage and contamination during transport and handling, the sensor heads should be packaged in a metal/Teflon housing. An idea for a metal housing derived from fibre connectors is shown in Figure 8.6.



**Figure 8.6- Sensors in a protective housing. Idea taken from [7]**

Multiple sensor heads may be packaged as one unit, and each sensor head could be interrogated using an optical switch. An optical switch would allow greater flexibility in terms of comparing long term performances in multiple experiments at the same time.

Recently, the use of 3D printers in science has become common. Therefore a 3D printed cage for the fibre sensor heads may also be another alternative.

## 8.4 Summary

This chapter summarises the findings of this research project. A novel hypothesis towards improving a palladium coated hydrogen sensor's performance in the long run has been presented. Sensor heads larger than a small singlemode fibre core, in the shape of a 350µm ball diameter or a GRIN lens with a face diameter of 2mm were tested. The ball lens design was successfully proven to be able to detect 10ppm H<sub>2</sub> in air with fast response and recovery times. The interrogation system used was a single broadband source with two optical branches for the reference and probe signal for normalisation purposes. This system was susceptible to differential temperature changes between the two arms that influenced the drift in signal over time. A common path interrogation system using dual wavelength sources was suggested as an alternative. This system was only able to detect 300ppm H<sub>2</sub> in air and had relatively longer response and recovery times, which may have been related to the use of different ball lens, different coating run or the use of a different interrogation system. However the stability was better in comparison to the single source, 2 paths system. Potential improvements to the dual wavelength, common path system to further enhance its sensitivity and stability are presented in this chapter, along with suggestions for various size sensor heads.

## 8.5 References

- [1] Mamidi, V. R., Kamineni, S., Sai Prasad Ravinuthala, L. N., Thumu, V. and Pachava, V. R. (2014), "Method to athermalize a long-period fiber grating for interrogation of fiber Bragg grating-based sensors", *Optical Engineering*, vol. 53, no. 9.
- [2] Zheng, W., Sugawara, H., Mizushima, T. and Klimowych, W., ( 2013), *Heating power feedback control for CO<sub>2</sub> laser fusions splicers*, 1st ed., Fujikura, AFL global, Fujikura, Japan.
- [3] Hodgkinson, J., Masiyano, D. and Tatam, R. P. (2009), "Using integrating spheres as absorption cells: Path-length distribution and application of beer's law", *Applied Optics*, vol. 48, no. 30, pp. 5748-5758.
- [4] Manojlovic, L. M. and Marinic, A. S. (2011), "On the integrating cavity transfer function and decay time", *Measurement Science and Technology*, vol. 22, no. 7.
- [5] Butler, M. A., Sanchez, R. and Dulleck, G. (1996), *Fiber Optic Hydrogen Sensor*, Sandia Reports SAND96-113, Sandia National Laboratories, Albuquerque, US.
- [6] Feng, J., Zhao, Y., Lin, X. -, Hu, W., Xu, F. and Lu, Y. -. (2011), "A transfective nano-wire grid polarizer based fiber-optic sensor", *Sensors*, vol. 11, no. 3, pp. 2488-2495.
- [7] Fiber Optics for Sale Co. (2012), *Expanded beam connectors*, available at: <http://www.fiberoptics4sale.com/wordpress/what-is-expanded-beam-connector/> (accessed August, 2015).

# List of Publications

## Peer-reviewed journal publications

- 1) Chowdhury, S. A., Correia, R., Francis, D., Brooks, S. J., Jones, B. J. S., Thompson, A. W. J., Hodgkinson, J. and Tatam, R. P. (2015), "An optical fibre hydrogen sensor using a palladium coated ball lens", *Journal of Lightwave Technology*, vol. 33, no. 12, pp. 2535-2542.

## Peer-reviewed conference publications

- 2) Chowdhury, S. A., Correia, R., Francis, D., Brooks, S. J., Jones, B. J. S., Thompson, A. W. J., Hodgkinson, J. and Tatam, R. P. (2014), "Palladium coated ball lens for optical fibre refractometry based hydrogen sensing", *23<sup>rd</sup> Conference on Optical Fibre Sensors [OFS-23]*, Santander, Spain, *Proceedings of SPIE - The International Society for Optical Engineering*, Vol. 9157.

## Conference publications

- 3) Chowdhury, S. A., Chehura, E., Correia, R., Francis, D., Hodgkinson, J. and Tatam, R. P. (2013), "Stability comparison between two optical refractometer techniques", *Sensors & their Applications XVII*, Dubrovnik, Croatia, *Journal of Physics: Conference Series*, Vol. 450.

## Planned publications

- 4) Chowdhury, S. A., Chehura, E., Correia, R., Francis, D., Hodgkinson, J. and Tatam, R. P. (2015), "Long term Allan deviation stability comparison between two optical refractometer techniques", Planned for *Measurement Science and Technology*.
- 5) Chowdhury, S. A., Correia, R., Francis, D., Brooks, S. J., Jones, B. J. S., Thompson, A. W. J., Hodgkinson, J. and Tatam, R. P. (2015), "Fibre optic palladium coated sensor heads for hydrogen sensing", Planned for *Measurement Science and Technology*.

# Appendix A

## Refractive index calculation

The refractive index calculation of the dual wavelength, common path system is complex because of reflection/transmission at multiple interfaces and because of the inefficiency of the FBG in reflecting the reference wavelength. In the case of the bare fibre and the sensor head assembly, the ray diagram is shown in a simplified model in Figure A.1, assuming that the transmission of the fibre and the effective split ratio of the coupler is the same for both wavelengths.

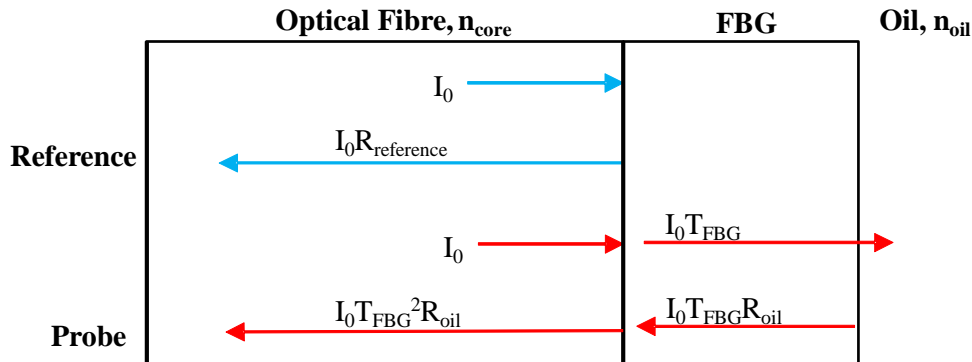


**Figure A.1-** Simple ray diagram model for the bare fibre and FBG sensor head, showing light reflectivity at multiple interfaces, where  $I_0$  is the intensity reaching the fibre and FBG interface,  $T_{\text{FBG}}$  is the transmission of the FBG,  $R_{\text{reference}}$  is the reflectivity of the FBG and  $R_{\text{oil}}$  is the reflectivity of the oil

The FBG is assumed to be 100% efficient in transmitting the probe wavelength, so the signal from the probe wavelength is proportional to equation (A.1).

$$V_{\text{probe}} \propto I_0 T_{\text{FBG},\text{probe}}^2 R_{\text{oil},\text{probe}} \quad (\text{A.1})$$



Where  $I_0$  is the intensity reaching the fibre and FBG interface,  $T_{\text{FBG, probe}}$  is the transmission of the FBG and  $R_{\text{oil, probe}}$  is the Fresnel reflection of the fibre and oil interface. However, the reflection efficiency of the FBG is not 100% and so part of the reference wavelength will reach the oil interface, so the signal from the reference wavelength is proportion to equation (A.2)

$$V_{\text{reference}} \propto I_0 R_{\text{FBG,reference}} + I_0 T_{\text{FBG,reference}}^2 R_{\text{oil,reference}} \quad (\text{A.2})$$

Assuming that  $T_{\text{FBG,probe}}$  is 100%, the ratio of equations (A.1) and (A.2) can be simplified and written as  $R$  in equation (A.3):

$$\frac{V_{\text{reference}}}{V_{\text{probe}}} = R = \frac{R_{\text{FBG,reference}} + T_{\text{FBG,reference}}^2 R_{\text{oil,reference}}}{R_{\text{oil,probe}}} \quad (\text{A.3})$$

Further assuming that the reflectivity of the oil is the same for both the reference and the probe wavelength, equation (A.3) can be simplified to equation (A.4), where the constant denotes the transmission of the reference wavelength by the filter.

$$\frac{V_{\text{reference}}}{V_{\text{probe}}} = R = \frac{R_{\text{FBG,reference}}}{R_{\text{oil,probe}}} + \text{constant} \quad (\text{A.4})$$

After each oil measurement, the sensor head was cleaned in acetone and isopropyl alcohol and exposed to air to establish a baseline and normalise the oil readings. The normalising factor can be defined as equation (A.5).

$$R_{\text{norm}} = \frac{R_{\text{FBG,reference}}}{R_{\text{air,probe}}} + \text{constant} \quad (\text{A.5})$$

Equations (A.4) and (A.5) can be solved simultaneously to remove the constant

$$\frac{V_{\text{reference}}}{V_{\text{probe}}} - R_{\text{norm}} = R_{\text{FBG,reference}} \left( \frac{1}{R_{\text{oil,probe}}} - \frac{1}{R_{\text{air,probe}}} \right) \quad (\text{A.6})$$

Where,  $R_{\text{air,probe}}$  can be calculated using equation (A.7). The refractive index of the fibre core,  $n_{\text{core}}$  is 1.45 and the refractive index of air,  $n_{\text{air}}$  is 1.

$$R_{\text{air,probe}} = \left( \frac{n_{\text{core}} - n_{\text{air}}}{n_{\text{core}} + n_{\text{air}}} \right)^2 \quad (\text{A.7})$$

And, the expression for  $R_{oil,probe}$  as given by equation (A.8) contains the unknown refractive index of oil,  $n_{oil}$ .

$$R_{oil,probe} = \left( \frac{n_{core} - n_{oil}}{n_{core} + n_{oil}} \right)^2 \quad (A.8)$$

Equation (A.6) can be rearranged to calculate  $n_{oil}$ .

$$n_{oil} = n_{core} \left( \frac{1 - \eta}{1 + \eta} \right) \quad (A.9)$$

Where,

$$\eta = \sqrt{\frac{R_{FBG,reference}}{\left( \left( V_{reference} / V_{probe} \right) - R_{norm} + \left( R_{FBG,reference} / R_{air,probe} \right) \right)}} \quad (A.10)$$

The value of  $R_{FBG,reference}$  was measured to be 47.5%.